

Thermo-mechanical design, realization and testing of screen-printed deformable mirrors

Dissertation

zur Erlangung des akademischen Grades

Doktoringenieur
(Dr.-Ing.)

vorgelegt der
Fakultät für Maschinenbau der
Technischen Universität Ilmenau

von Frau

Dipl.-Ing. Claudia Reinlein

(geb. Bruchmann)

geboren am 07.06.1980 in Erfurt / Deutschland

Univ.-Prof. Dr.-Ing. habil. Martin Hoffmann
Prof. Dr. rer. nat. habil. Andreas Tünnermann
Dr. rer. nat. Stefano Bonora

urn:nbn:de:gbv:ilm1-2012000191

Zusammenfassung

Die primäre Zielstellung dieser Dissertation ist die Entwicklung ungekühlter, unimorph deformierbarer Spiegel (DM) zum Ausgleich thermischer Linsen in Hochleistungslasersystemen. Die sekundäre Zielstellung ist die Entwicklung eines Herstellungsprozesses für deformierbare Spiegel, der hauptsächlich auf Waferleveltechnologien beruht und somit manuelle Prozesse reduziert.

Der DM besteht aus einem Spiegelsubstrat auf dessen Rückseite eine piezoelektrische Schicht zwischen zwei Elektroden aufgebracht ist. Diese Art von Spiegeln wurde bereits erfolgreich in Hochleistungslasersystemen eingesetzt. Eine weitere Erhöhung der Laserleistungsdichte erfordert jedoch neue thermische Kompensationstechniken, bei der die Spiegelperformance nicht durch Temperaturschwankungen in der Spiegelbaugruppe vermindert wird.

Ein während der Untersuchung entwickeltes Mehrlagendesign integriert mehrere Schichten in den Spiegelaufbau, dessen thermo-mechanische Parameter sich vom Substrat und der piezoelektrischen Schicht unterscheiden. Mittels analytischen Methoden und der Methode der finiten Elemente wurde eine Optimierung im Hinblick auf großen piezoelektrischen Hub und optimierte thermisch-induzierte Deformation durchgeführt. Diese wird entweder durch eine homogene Temperaturveränderung in der Spiegelmembran oder durch Absorption von Laserstrahlung generiert. Die dabei hervorgerufenen Veränderungen werden abhängig von Diskontinuitäten der piezoelektrischen Schicht, den mechanischen Randbedingungen, der spiegelnden Kupferschichtdicke und der Spiegelfassungsmaterialien simuliert.

Ein aus sechs Arbeitsschritten bestehende Herstellungsprozess eines DMs mit siebgedruckter piezoelektrischer Aktorstruktur wurde entwickelt. Fünf Schritte sind davon auf Waferlevel prozessierbar. Einzig die Bearbeitung der Spiegelfläche mittels eines ultrapräzisen Drehprozesses ist keine Serienfertigung. Im Gegensatz zum Stand der Technik für DM ist die elektrische Verdrahtung der strukturierten Elektroden auch auf Waferlevel prozessierbar und das Spiegelsetup ist monolithisch.

Thermisch induzierte Deformationen durch homogene Temperaturveränderung kann durch eine sog. *zero deflection* Konfiguration ausgeglichen werden. Laser-induzierte Deformationen werden mit gegenläufigen, thermisch homogen induzierten Deformationen kompensiert. Dieser Ansatz wird als Compound

loading bezeichnet und in einem praktischen Spiegelaufbau umgesetzt. In diesem deformierbaren Spiegel wird eine Deformation, induziert durch 1.3 W absorbierte Laserleistung, über eine homogene Temperaturerhöhung um 34 K kompensiert. Damit wird gezeigt, dass die entwickelten und vorwiegend mit parallelen Fertigungstechnologien hergestellten Spiegel für Hochleistungslaseranwendungen geeignet sind.

Abstract

The primary objective of this thesis is the development of non-cooled deformable unimorph mirrors (DM) for thermal lensing compensation in high-power laser systems. The secondary objective is the development of a manufacturing regime that consists mainly of batch-fabrication and reduced manual processes.

The DM consists of a mirror substrate with a piezoelectric layer sandwiched between two electrodes, bonded on the mirror's rear surface. These types of mirror have been successfully integrated into high-power laser systems; however, further increase in laser power requires new thermal compensation techniques in which the DMs performance is not affected by temperature changes in the mirror assembly.

To achieve this objective, a multi-layer design was studied. The multi-layer design integrates several layers with thermo-mechanical parameters that differ from the substrate and the active layer into the mirror set-up. Beginning with this set-up, an optimization is performed with regard to the required large piezoelectric stroke and low thermally-induced deflection by analytical and finite element modelling. The thermally-induced deflection of the multi-layer is distinguished by their source into homogeneous thermal loading and inhomogeneous laser loading. The mirror response upon piezoelectric activation and both thermal loadings was simulated with respect to piezoelectric layer discontinuity, different mechanical boundary conditions, reflective copper-layer thickness, and mirror mount materials.

The manufacturing regime of screen-printed piezoelectric DM is developed. The manufacturing process comprises six steps out of which five are batch-fabrication techniques. The mirror surface finishing by means of an ultraprecise turning process alone does not involve batch fabrication. In contrast to state-of-the-art deformable mirror technologies, the electric wiring of the addressing electrodes of the deformable mirror is also batch-fabricated and the mirror set-up is monolithic.

The thesis presents possible concepts to compensate for thermally-induced mirror deformation. Thermally-induced deformation by homogeneous loading is balanced by the *zero deflection* configuration of the multi-layer. The compensation for laser-induced deformation can be achieved by homogeneous

thermal loading that can compensate as the deformation caused by the loading opposes the laser-induced deformation. This approach is referred to as compound loading, and it is investigated in a practical mirror set-up. Here, a 1.3-W absorbed laser power is compensated by a 34-K homogeneous loading. It is concluded that the developed and mainly batch-fabricated DM are suitable for high-power laser applications.

Table of content

Zusammenfassung	i
Abstract	iii
Table of content	v
List of Acronyms/Abbreviations	vii
1 Introduction	1
2 Physical technical fundamentals	7
3 Deformable mirror architectures	15
3.1 <i>Segmented mirrors</i>	15
3.2 <i>Mirrors with discrete actuators</i>	18
3.3 <i>Deformable mirrors</i>	20
3.4 <i>Modular / hybrid mirror architecture</i>	26
3.5 <i>MEMS mirrors</i>	27
3.6 <i>Discussion of the state of the art solutions</i>	30
3.7 <i>Objectives of this thesis</i>	36
4 Screen-printed piezoelectric deformable unimorph mirrors	38
4.1 <i>Piezoelectricity</i>	38
4.1.1 <i>Large-signal activation</i>	39
4.1.2 <i>Temperature effects</i>	43
4.1.3 <i>Mathematical description of piezoelectricity: piezoelectric equations</i>	43
4.2 <i>Layer deposition</i>	47
4.2.1 <i>Jointing of piezoelectric disks</i>	47
4.2.2 <i>Direct thick film application</i>	47
4.2.3 <i>Screen printing</i>	48
4.3 <i>Evaluation of screen-printed material characteristics</i>	50
4.3.1 <i>Experimental investigation of screen-printed layer characteristics</i>	53
4.3.2 <i>Stress effects on screen-printed layers</i>	66
4.4 <i>Substrate materials</i>	68
4.5 <i>Manufacturing concept</i>	70
4.5.1 <i>Mount design</i>	72
4.5.2 <i>Reflective metallization</i>	75
5 Optimization of the thermo-mechanical properties of deformable unimorph mirrors	77
5.1 <i>Analytical modelling</i>	79
5.1.1 <i>Thermally-induced changes: homogeneous loading</i>	79
5.1.2 <i>Piezoelectric stroke</i>	83
5.2 <i>Finite element analysis</i>	91
5.2.1 <i>Piezoelectric stroke</i>	92

5.2.2	Dynamic multilayer characteristics	93
5.2.3	Thermally-induced changes: homogeneous loading	102
5.2.4	Examination and selection of mirror mount material	107
5.2.5	Thermally-induced changes: inhomogeneous loading	110
5.3	<i>Summary of modelling results</i>	114
5.4	<i>Construction guidelines for temperature loading of deformable mirrors</i>	115
5.4.1	Homogeneous loading	115
5.4.2	Inhomogeneous loading	118
6	Experimental verification of the deformable unimorph mirror design	123
6.1	<i>Deformable mirror assembly</i>	123
6.2	<i>Mirror manufacturing</i>	126
6.3	<i>Experimental set-up</i>	130
6.3.1	Adaptive optical measurement set-up: homogeneous loading	130
6.3.2	Adaptive optical measurement set-up: inhomogeneous loading	132
6.3.3	Additional characterization methods	133
6.4	<i>Mirror characterization</i>	134
6.4.1	Initial mirror shape	134
6.4.2	Piezoelectric stroke	135
6.4.3	Thermally-induced changes: homogeneous loading	141
6.4.4	Thermally-induced changes: inhomogeneous loading	147
6.4.5	Thermally-induced changes: compound loading	150
6.4.6	Comparison with simulated values	153
6.5	<i>Application: Compensation of static wavefront aberrations</i>	154
7	Summary and discussion of the results	157
	Thesen zur Disputation	I
	Appendix	III
	List of figures	VIII
	References	XV

List of Acronyms/Abbreviations

Abbreviation	Explanation	unit
47/53	$(\text{Pb}_{0.94}\text{Sr}_{0.06})(\text{Ti}_{0.47}\text{Zr}_{0.53})\text{O}_3$	
48/52	$\text{Pb}(\text{Ti}_{0.48}\text{Zr}_{0.52})\text{O}_3$	
53/47	cf. 47/53	
A	Amplitude	W
A	Aging rate constant	1
a	Relative thickness	1
AIF	Actuator influence function	1
Al_2O_3	Alumina	
AO	Adaptive optical	
BK10	Schott optical glass N-BK10	
BPP	Beam parameter product	mm x rad
c	Relative stiffness	1
c	Elastic stiffness	N/m^2
CCD	Charge-coupled Device	
CE7	Si70Al30	
CMOS	Complementary Metal Oxide Semiconductor	
CLPT	Classical laminated plate theory	
C_N	Zernike coefficient	
CVD	Chemical vapour deposition	
CTE	Coefficient of thermal expansion	1/K
C_{th}	Thermal capacity	J/K
Cu	Copper	
cw	Continuous wave	
D	Dielectric displacement	C/m^2
DM	Piezoelectric deformable unimorph mirror	
DoD	Drop-on-demand	
d_{ii}	Piezoelectric charge constant	C/N
E	Young's modulus	Pa
E_c	Coercive field strength	V/m^2
E_{field}	Electric field	V/m^2
E_i	Electric field strength	V/m^2
FEM	Finite element method	
G_{ij}	Shear modulus	N/m^2
h_{max}	Maximum penetration depth	m
h_p	Thickness of the piezoelectric layer	m

HVA	High voltage amplifier	
i	Degree of Zernike term	1
I(r)	Intensity distribution (depending on distance r)	W/m ²
IKTS	Fraunhofer Institute for Ceramic Technologies and Systems	
LGEF	Laboratoire de Génie Electrique et Ferroélectricité	
LTCC	Low temperature cofired ceramic	
LTS	Laser triangulation sensor	
m	Azimuthal order	1
M ²	Beam quality factor	1
MEMS	Micro-electro-mechanical-systems	
MMDM	Micromachined membrane deformable mirror	
ML	Multilayer	
N	Radial order	1
n _i	Normalization factor corresponding to degree of Zernike term	1
P	Porosity	1
P	Polarization	C/m ²
P _i	Induced polarization	C/m ²
p _i	Pyro electric coefficient	C/m ² K
PIC 151	Lead titanate zirconate materials from Pi Ceramic GmbH	
PIC 255	Lead titanate zirconate materials from Pi Ceramic GmbH	
PMN	Lead-magnesium-niobate	
PMN:PT	cf. PMN	
PMN:BA	cf. PMN	
P _r	Remnant polarization	C/m ²
P _s	Spontaneous polarization	C/m ²
P-V	Peak to valley	m
PVD	Physical vapour deposition	
PZ 5100	Piezoceramic thick film based on (PbZr _{1-x} Ti _x O ₃ - PZT)	
PZT	Lead zirconate titanate (Pb[Zr _x Ti _{1-x}]O ₃ 0≤x≤1)	
PZT-5H	Lead titanate zirconate material from Morgan Electro Ceramics	
PZT-PMN	Lead zirconate titanate - lead-magnesium-niobate	
Q	Quality factor	1
r	Distance to the propagation axis	m

R_a	Surface roughness	m
r_i	Radius of the piezoelectric layer	m
r_s	Radius of the substrate	m
rms	Root mean square	m
s	Elastic compliance	m^2/N
S	Strain	1
SiC	Silicon carbide	
Sonox P505,	Lead titanate zirconate materials from CeramTec	
Sonox P51	Lead titanate zirconate materials from CeramTec	
Sonox P53	Lead titanate zirconate materials from CeramTec	
SPDT	Single point diamond turning	
S_x	Stress in x-direction	Pa
S_y	Stress in y-direction	Pa
T	Mechanical tension	Pa
TF	Thick film	
t	Time	s
t_0	Starting time	s
t_p	Layer thickness (of the piezoelectric TF)	m
t_s	Substrates thickness	m
T_s	Sintering temperature	$^{\circ}C$
ULE [®]	Ultra Low Expansion material	
WFS	Shack Hartmann wave front sensor	
W_{in}	Internal energy density	J/m^2
Y_{it}	Indentation modulus	GPa
Z_i	Zernike polynomial	
α	Coefficient of thermal expansion (CTE)	1/K
δ	deflection	m
ϵ	relative permittivity	$C/(Vm)$
κ	Thermal conductivity	$W/(Km)$
ν	Poisson's ratio	1
ϑ	Temperature	$^{\circ}C$
ϑ_C	Curie temperature	$^{\circ}C$
\varnothing	diameter	m
φ	divergence	
λ	wavelength	m
ς	pupil radius normalized coordinate	m
ρ	density	g/cm^3

ρ_0	theoretical density	g/cm^3
σ	entropy	
σ^2	variance of wavefront	$\text{m}^2 (\lambda^2)$
ω_0	beam radius at its narrowest point	m
φ	Azimuthal angle	

1 Introduction

Laser is the acronym for light amplification by stimulated emission of radiation. It describes the physical process of light amplification but is now generally recognised as a device that delivers (laser) radiation. Laser in the industrial practice of material machining is meanwhile an important, and no longer imagine living without technology. The laser is a modern beam tool that is used for cutting, welding, drilling, marking and ablation. Laser based surface modification (hardening and coating) also is standard.

In laser machining, the laser is focussed onto the workpiece that absorbs the electromagnetic energy on its surface. The impact of the laser radiation depends on the mechanism of energy absorption, and thus on its exposure time and power density. The power density (power per unit area) increases with decreasing spot size. Depending on the power density, different processes and material changes are induced. The absorbed power density evokes a temperature increase around the laser spot in the workpiece. Low power densities increase the temperature of the machined material below its melting point. A hardening of the workpieces surface is achieved. The further increase of power density induces temperatures in the exposed area greater than or equal to the melting temperature. This material melt is used for heat-conduction welding. If the absorbed energy induces evaporation temperatures in the exposed area, a capillary with a diameter in the range of the laser spot is generated and thus, the material can be cut. Laser drilling is possible if the power density achieves values between 10^7 W/cm² and 10^8 W/cm² generating plasma that is ejected due to pressure differences between ambient and drill location. Highest power densities of 10^{20} W/cm² are generated for laser-matter-interaction experiments. These highest power densities are accomplished by focussing especially developed high power lasers to small spot sizes.

The efficient application of laser machining is attributed to the efficient generation and to the efficient coupling of energy into the machined material which is characterized by the specific material absorption. The material absorption relies on the wavelength, polarization and angle of incidence of the

incoming beam. The most outstanding property of the laser is the spatial and temporal high precision energy input into the workpiece which causes a minimized heat-affected zone.

Laser machining is contact free and force free. Complex part geometries can be machined by applying a 3D tool head. Therefore, application of laser in material machining requires the inclusion of the mechanical equipment (machine technology) e.g., optical, mechanical and structural components to work as a machine tool. Furthermore, the laser beam needs to be guided from the location of generation to the work zone by mirrors, lenses and optical fibres. Additionally, focussing the laser must be accomplished by lenses or mirrors.

A high power laser beam interacts not only with the workpiece but also with the optical components of the machine tool. This results in a negative impact on the laser beam quality, leading to lower power densities applied to the workpiece. The absorption of laser power in the optical components causes an increase in temperature and thus a corresponding gradient in the optical components. This temperature increase induces shape variations in the optical components, thereby changing their optical characteristics. Further, the temperature increase changes the refractive index of the transmissive optical components due to its temperature dependence. Both effects result in unwanted optical path length differences over the optical aperture. Thermally-generated optical phase length differences degrade the phase front and the beam quality. These unwanted laser-power-induced changes cause the focus position to shift. In addition, the spot size of the laser beam is increased. This phenomenon is referred as thermal lensing¹.

Thermal lensing can be reduced by an active optical component in the laser chain that introduces an opposed optical path length difference. Such correcting optical components are for example deformable mirrors. Their surface can be deformed in order to compensate for path length differences.

The challenge of deformable mirror applications in high-power laser systems arises due to the laser-induced deformations of their surface. The mirror surface absorbs a fraction of the laser radiation, and the mirror temperature increases depending on the optical coating and the heat dissipation capability of the

substrate used. Thermal lensing establishes in the deformable mirror itself, restricting its working range. Therefore, very few types of mirrors are capable of high-power beam shaping.

Unimorph mirrors that consist of a mirror substrate with a piezoelectric disk bonded to the substrate's rear surface have successfully been used as active mirrors. A dielectric coating is applied on the mirror substrate either before or after the bonding of the piezoelectric disk. The minimization of the differences in thermal expansion of the substrate and the piezoelectric disk in turn minimizes the bimetal effect of the active mirror. The bimetal effect converts a temperature change into an undesired mechanical displacement. This construction is referred to as athermal. The suppression of the bimetal effect is only possible if less heat needs to be dissipated because the frequently used thermally adapted substrates (e.g. BK10 or PZT) suffer from low thermal conductivity.

Another construction method is to select a substrate material that dissipates the absorbed radiation; on doing so, temperature gradient and peak temperature in the mirror substrate decreases, and consequently, so does the mirror's surface deformation. If the thermal conductivity of the substrate is too low, the resulting heat cannot be dissipated and thermal lensing develops. One conventional solution involves increasing the optical aperture in order to decrease the power density of the laser beam. A lower power density reduces the temperature increase at the mirror. Therefore, the requirements for optical coating and heat dissipation are reduced. A low mirror temperature change decreases the contribution of material instabilities (due to thermal expansion and thus reflected by the coefficient of thermal expansion) of the piezoelectric material to the deformation. Nevertheless, this approach is not always favourable, as the manufacturing labour input strongly depends on the mirror's diameter. The larger the mirror diameter the more difficult is the mirror polishing process and the bonding of the piezoelectric disk. Further, the associated decrease of the first natural frequency due to this approach can limit the application.

This work addresses the development of deformable mirrors for the application in high power laser chains. Special emphasis is put on the thermo-mechanical design of the deformable mirror and the development of a manufacturing

regime based on batch-fabrication. The objective of the thermo-mechanical design considerations is the optimization of the deformable mirror architecture, to minimize laser-induced deformations of the mirror surface. The high power reliability of the uncooled architecture shall be achieved through a multi-material design. In addition, the mirror performance is demonstrated with a large compensation range of wavefront aberrations at a bandwidth of more than 1 kHz.

This thesis is divided into six chapters. After the introduction and the physical technical fundamentals, the current state-of-the-art technology in deformable mirrors is discussed and the scope of the thesis is defined. The chapter screen-printed piezoelectric deformable unimorph mirrors examines piezoelectricity as the actuating material for deformable mirror, and the screen printed layer material characteristics are reviewed.

A manufacturing concept almost entirely based on batch-fabrication techniques is developed. Special emphasis is put on the mirror mount concept. Chapter 0 reviews the existing analytical models for piezoelectric actuation and homogeneous thermal loading. Beginning with these models, an optimization is performed with regard to the required large piezoelectric range and low thermally-induced deflection. Further, I introduce the *zero deflection* multilayer concept in the setting up of a deformable mirror. The range of the validity of the analytical *zero deflection* approach is determined by the finite element method (FEM). In addition, I show the influence of the material inhomogeneity, copper-layer thickness, and membrane boundary conditions on thermally-induced deflection. The applicability of the optimized multilayer (ML) design to inhomogeneous loading is the special focus of this chapter. Inhomogeneous loading is induced by laser beams. The simulations of the loading are used to evaluate the influence of different mount materials and copper-layer thicknesses for small laser-induced membrane deformations. The chapter also puts special emphasis on the modelling of dynamic behaviour of the mirror membranes. The work investigates the influence of the substrate's copper-layer thickness, its initial curvature, and residual stresses in the mirror membrane on the resonance frequency. The chapter concludes with the formulation of construction

guidelines for homogeneous and inhomogeneous temperature loadings. The *Experimental verification of the deformable unimorph mirror* is performed in the 0th chapter of the present thesis. After reviewing the different characterization set-ups, the obtained results are presented. The results show a large piezoelectric stroke of the deformable mirror along with low thermally-induced deflection. A new compensation regime for high laser loads (compound loading) is developed and tested. The last chapter summarizes and discusses the results.

2 Physical technical fundamentals

Laser for material machining are characterized by their average power and beam quality. The beam quality of a laser beam is specified by the beam parameter product (BPP), being the product of beams divergence φ and the radius ω_0 at its most narrow point (beam waist).

$$\text{BPP} = \varphi * \omega_0 = M^2 * \frac{\lambda}{\pi} \quad (1)$$

M^2 is referred to as the beam quality factor and λ is the wavelength^{2,3}. In theoretically case of ideal beam quality $M^2 = 1$. The beam is diffraction-limited. A decrease of the beam quality increases M^2 . A diffraction limited beam with $M^2 = 1$ equals a single mode laser possessing a Gaussian shaped intensity distribution (beam profile). Such single mode laser beams have excellent focus abilities leading to smallest possible spot sizes.

The power density is the quotient of average laser power and the beams cross-sectional area. In laser machining, the beam is focussed into a small spot generating large power density. In case of not reducing the beam quality due to aberrations introduced by the optical components, the beam profile will remain its Gaussian shape.

Wavefronts define surfaces of constant optical path length from a certain point source. "Rays and wavefronts are always orthogonal to one another"⁵. A point source emits a spherical wavefront whose radius changes with distance to its source and becomes a flat wavefront if the source is moved to infinity. In this case, the rays are parallel forming a collimated beam. These kinds of wavefronts are ideal constructions that serve as reference wavefronts against which other real wavefronts can be compared.

Real laser systems and especially high-power laser systems emit with $M^2 > 1$. They exhibit aberrations that are deviations from the reference wavefronts (cf. Figure 1(a)). The aberrations in high power laser systems are mostly thermally generated and referred to as thermal lensing. Here, a fraction of the laser power is absorbed and converted into heat. The heat needs to be dissipated as

otherwise the temperature increases which should be suppressed as this is a possible source of aberration due to:

- Deformation of optical components such as lenses and mirrors due to their thermal expansion and hence change of their optical properties.
- Temperature dependency of the refractive index of transmissive optical components. Inhomogeneous heating of circular lenses by laser load establishes a radial temperature profile and hence a radial gradient of the refractive index across aperture. This is disturbing not only in lenses but also in laser crystals where also non-radial temperature profiles establish.
- Deformation of laser crystals by thermal expansion and thermal stress.
- Thermally-induced birefringence in optical components.
- Temperature dependency of the thermal conductivity in optical and mechanical components.

A laser induced temperature increase of several Kelvins (< 10 K) in the lens centre can already result in strong thermal lensing. Typical time constants are several seconds. A characteristic is that thermal lensing scales with the absorbed power in the laser system and therefore needs an active compensation for the aberrations.

Active compensation for the aberrations or a specific variation of the optical path can be generated by changes in the refractive index or geometrical path length variations. The change in refractive index can be created by birefringence in electro-optical materials, e.g., liquid crystals. Liquid crystals can provide large aperture and high resolution; however, energy loss and light scatter due to their discrete structure limit their range of application. Furthermore, they have a limited thermal range because of the strong temperature dependence of the material used. Liquid crystals based light modulators are not within the scope of this study as they offer low stroke, low switching rates, and no handling of high laser power⁴.

The second alternative relies on geometrical path length variations. Such variations can be introduced by deforming a mirror surface. The surface of the

active mirror used for this purpose is adapted in such a way, that the deformed mirror offers the same degree of optical phase difference that is present in the laser beam, but with half the amplitude as the beam is reflected and the deformable mirror imposed optical path length differences double. Longer optical paths lengths are assigned to precursory parts of the wavefront by the deformable mirror, thereby balancing wavefronts phase differences (cf. Figure 1(b)).

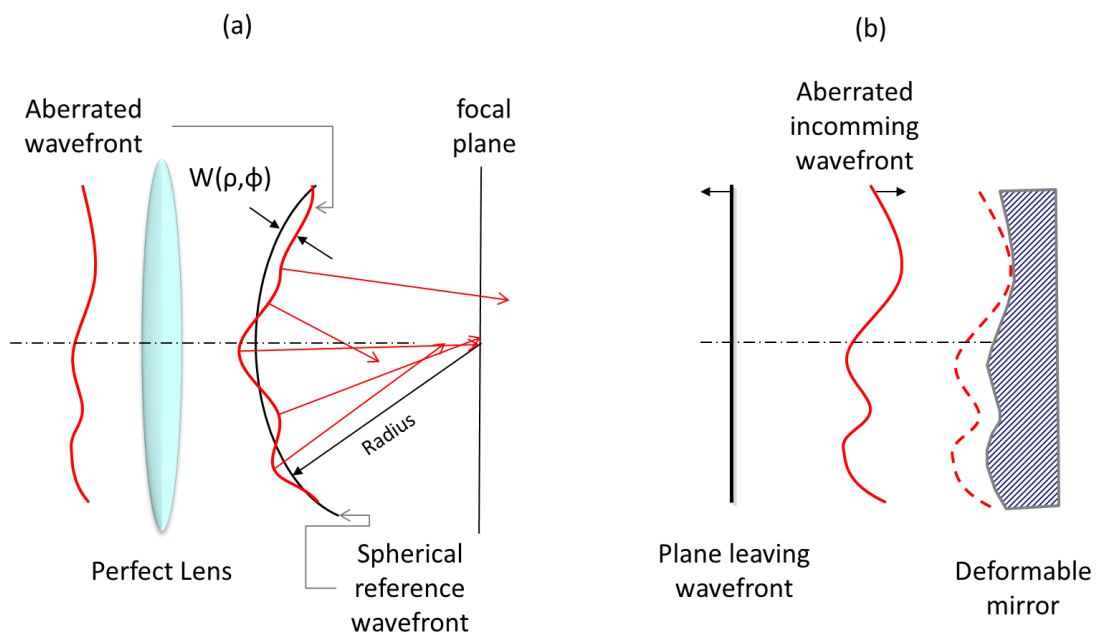


Figure 1 (a) Wavefront aberration $W(\rho, \phi)$, (b) Compensation for wavefront aberration by variation of the optical path length by a deformable mirror.

In order to correct the wavefront using a deformable mirror, the present aberrations have to be well-known. However, the phase of a single photon cannot be directly measured as there is no possibility to interact with the beam of light to determine the instantaneous direction of its electric field vector. We can only detect the intensity of light, and not its amplitude or phase^{5,6}. Direct and indirect wavefront sensors are available as standard measurement sensors. Direct measurements explicitly determine the phase, for e.g., through interference with a reference wavefront. Indirect measurements translate information related to the phase, for e.g., local wavefront tilt, into signals. "Wavefront sensors estimate the overall shape of the wavefront from a finite number of discrete measurements"⁵ at uniform spatial intervals. Within these

spatial intervals (subapertures) the wavefront is assumed to be flat and thus exhibiting a constant wavefront tilt. The local wavefront tilt/slope of the subaperture is determined by the tangent to the wavefront at the centre of subaperture. The orthogonal in this point pierces the focal plane. The distance between the focus of the reference wavefront and the aberrated wavefront at the focal plane is called the transverse ray aberration. The potential of a sensor to measure the transverse ray aberration is its ability to measure the slope of the wavefront within a subaperture. Sensors that measure small transverse ray aberration very precise are referred to as sensors with high sensitivity. In contrast, sensors that measure very large transverse ray aberration are referred to as sensors with a large dynamic range.

The requirements for phase sensing depend on the type of application. The determination of thermally-induced changes demands for moderate dynamic range, high sensitivity and moderate measurement rates of a few Hz. Optical testing refers to the determination of the optical surface of optical components, e.g., lenses or (deformable) mirrors. Optical testing of deformable mirrors needs a high spatial resolution and a large dynamic range since deformable mirrors offer large stroke and a large number of actuators between several tens and hundred. Optical testing usually refers to moderate measurement rates (in the order of a few Hz). On the other hand, sensors used for the compensation for atmospheric aberrations need to have a large dynamic range, high measurement rate (several hundreds of Hz⁷) and real-time processing. The measurement results need to be insensitive to intensity fluctuations of the radiation to be monitored.

A convenient method for optical testing and aberration measurements is the use of Shack-Hartmann wavefront sensors (WFS). The sensor employs a lens array in front of a detector (cf. Figure 2). The lens array discretises/divides the aperture of the beam into small sub-apertures and focuses the light of each sub-aperture onto a detector array (e.g., CCD- or CMOS -camera) that senses the position of the focal spot. A reference wavefront provides the focal spot reference positions (the pitch of the lens array corresponds to the focal spot). The sensor measures the shift in the focal spot between reference positions and aberrated wavefront

and thus the slope of each sub-aperture of the aberrated wavefront. The wavefront can be reconstructed from these slope measurements.

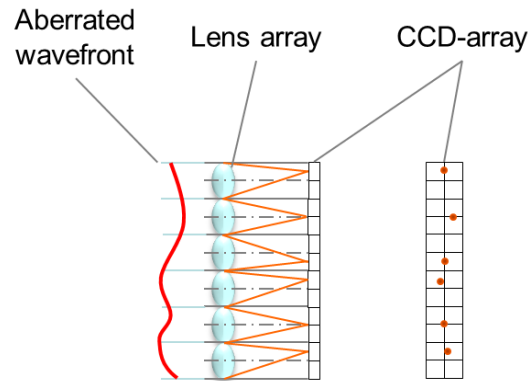


Figure 2 The lens array focuses discrete parts of the aberrated wavefront onto a CCD array with 4 pixel underneath every lens.

The aberrated wavefront is compared to the reference wavefront. The centre of curvature of the reference wavefront coincides with the ideal image point (cf. Figure 1(a)). The optical path difference between aberrated wavefront and reference wavefront is measured along the radius of the spherical surface. The mathematical description of this optical path difference is frequently done by sets of polynomials. This is very useful as each polynomial can describe a specific aberration. Each polynomial is weighted by its coefficient according to its influence on the wavefront.

Polynomial description of aberrations is typically done by Zernike polynomials⁸. Zernike polynomials are sets of orthogonal polynomials that are defined in a continuous fashion over the interior of a unit circle. This work uses sets of Zernike polynomials defined in polar coordinates describing the optical path difference $W(\zeta, \varphi)$ by the sum over the product of i -Zernike polynomials $Z_i(\zeta, \varphi)$ and their coefficients c_i :⁸:

$$W(\zeta, \varphi) = \sum_{i=0}^n c_i Z_i(\zeta, \varphi) \quad (2)$$

In which ζ is the pupil radius normalized coordinate ($0 \leq \zeta \leq 1$) and φ is the azimuthal angle with $0 \leq \varphi \leq 2\pi$. The coefficients c_i are linearly independent due to their orthogonality. **Fehler! Verweisquelle konnte nicht gefunden werden.**

shows the Zernike polynomials and their designation based on ISO 10110-5⁹. Figure 3 depicts the Zernike polynomials and their designation up to term 15.

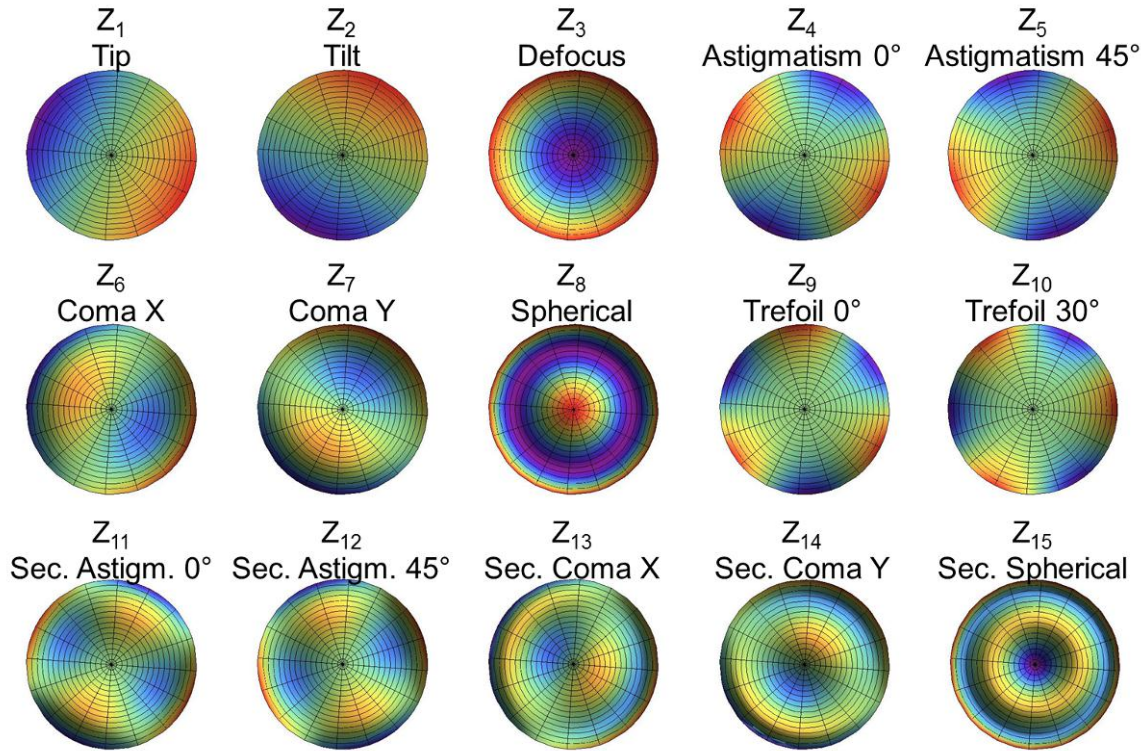


Figure 3 Zernike Polynomials Z1 to Z15.

In literature, different definitions of Zernike coefficients exist¹⁰ e.g. of Noll¹¹, and Born and Wolf¹² that differ from their normalization factor. This work uses the definition according to ¹³ as shown in the table in A1 that can be normalized by the division with their normalisation factor n_i (cf. table in A1) as described in ¹³. Therewith, the root-mean-square (rms) value of the aberrated wavefront can be calculated as follows:

$$rms = \sqrt{\sum_{i=1}^{\infty} \frac{c_i^2}{n_i}} \quad (3)$$

Piston, Tip and Tilt are typically not included to calculate the rms-value as they do not influence the beam focussing characteristics. In case of compensation for thermal lensing, the rms-value is minimized by the activation of the deformable mirror. It is also possible to calculate rms-values for a discrete quantity of Zernike coefficients. This is advantageous if the performance of active optical

elements is evaluated. Deformable mirrors for example are characterized by its potential of setting specified Zernike polynomials. In this case, the rms-value for $i = 1 \rightarrow \infty$ is calculated excluding the desired Zernike coefficient.

The intensity distribution of the focus can be calculated using a Fourier transform of the Gaussian laser beam. In case of a flat or spherical wavefront, it is transformed into a Gaussian intensity distribution. In contrast, the focussed intensity distribution changes and the peak intensity decrease for aberrated wavefronts. The Strehl ratio S , also called the normalized intensity is the ratio between the maximum focussed intensity of an aberrated beam and the maximum focussed intensity of a reference wavefront. The derivation of the formula and its approximation is found in several works^{14,15,23}. For small aberrations, corresponding to rms phase aberrations of up to $\lambda/14$ (Maréchal's expression), the focal plane is displaced to its Gaussian focus. The Strehl ratio can be approximated by:

$$S = e^{-\left(\frac{2\pi}{\lambda}\right)^2 * rms^2} \quad (4)$$

The Strehl ratio reduces to unity, $S = 1$ for diffraction limited optical systems. Systems with any aberration ($rms > 0$) have a Strehl ratio less than 1. A rule of thumb for a good image quality is that the phase aberrations remain below⁷ $\lambda/10$ leading to a Strehl ratio of $S = 0.6$. This shows the impact of any small aberrations on the ability of being focused can be summarized in a number.

3 Deformable mirror architectures

Mirrors that can selectively deform their surface are also referred to as deformable mirrors. Such phase-correction mirrors are classified into segmented (zonal) and continuous mirrors¹⁶ (cf. Figure 4). In the segmented mirror, the mirror substrate is segmented into minor parts that can be assembled as the mirror surface. In contrast, the mirror surface is continuous in the case of the latter classification. Both types of phase-correction mirrors can be further classified by the actuation that is used in them. The actuation can act either along or against the mirror substrate. A hybrid architecture mirror combines both types. Different types of deformable mirrors have been developed in parallel, and each of these types has its individual characteristics. The following section discusses the state-of-the-art of active optical elements by their optical classification. One chapter is devoted to MEMS mirrors and all their possible optical classifications.

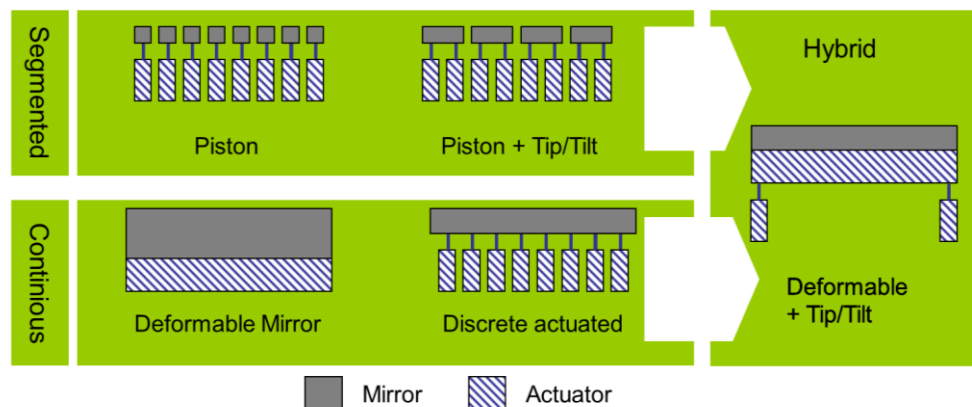


Figure 4 Optical classification of active optical elements.

3.1 Segmented mirrors

Segmented correction mirrors comprise a number of small mirror segments that can be moved by means of either a piston or piston plus tip/tilt movement system (cf. Figure 4). They are placed closely side-by-side while assembling the mirror surface. The movement of the individual mirrors discretely deforms the mirror surface.

The first practical realization of a piston plus tip/tilt mirror was done by Gebhardt and Kendall in 1973¹⁷ for phase-shaping applications. They built a 20-segment mirror with differential micrometres screw underneath. Each segment is composed of a rectangular (5.15 cm × 8.35 cm) fused silica plate with additional metallization, and the segment is supported by an Invar frame. This mirror is used in applications involving phase correction of thermal blooming, and they can increase the intensity of reflected light by a factor of 1.8.

Segmented mirrors are also under investigation for use in astronomical observations. Hardy¹⁸ was the first to implement segmented mirrors for astronomical use. Sandler and Hulburd¹⁹ introduced a deformable mirror with 512 rectangular segments, and each segment had a tubular piezoelectric actuator underneath. The tubular actuator offers a piston plus tip/tilt movement mechanism via the patterning of its exterior electrode. The actuator is divided into three electrically isolated domains, with each domain covering most of a 120° sector that extends along the length of the tube. The advantages of this design approach include the ease of fabrication and coating of the small single segments and the assembling of the mirror from working modules comprising 4 × 4 or 14 × 14 segments. Every working module is placed into a casing and adjusted via screw adjusters.

The application of this mirror facilitates atmospheric turbulence compensation for white light and the $n\lambda$ -mode for a single wave length. Another study by Acton reports the design and construction of a mirror with 19 segments and 57 actuators²⁰. Three piezoelectric stacks are glued to the mirror segments. Each segment is hexagonal and measures 2.8 cm across the hexagonal width. The mirror surface over all segments has a measurement of 0.1λ peak-to-valley (P-V), and hence, the surface is optically flat. The entire set-up is contained within an Invar frame for thermal stabilization. The piezoelectric actuators can easily be replaced, and the drift and nonlinearities are compensated by strain gauges. This mirror system has been used for solar imaging, and it has led to substantial improvements in the quality of the acquired image; a maximal resolution of 0.33 arcsec for visible wavelengths has been achieved under (1-3)-arcsec seeing conditions.

Nowadays, segmented mirrors are almost solely used as primary mirrors in (extremely) large optical telescopes. The European Southern Observatory^{21,22} has recently developed a scaled-down 61-segment active segmented mirror fabricated using Zerodur with an aluminum coating. The side-to-side width of each actuator is 17 mm (cf. Figure 5). The mirror serves for testing the alignment and phasing of the segments, and every segment has piezoelectric actuators with a piston, tip and tilt movement mechanism underneath. The range of segment displacement is more than 15 μm with a precision better than 2 nm. The gap between the segments is between 80 μm and 150 μm , and the surface roughness of each segment is 15 nm rms. A mirror of the European Extremely Large Telescope (astronomical telescope) has been designed for a diameter of 42 m, and 984 hexagonal elements that have equal displacement and surface quality as the scaled down 61-segment mirror system. Other segmented mirrors have already been in successful operation for many years in astronomical telescopes, e.g., the primary mirror of the KECK telescope.

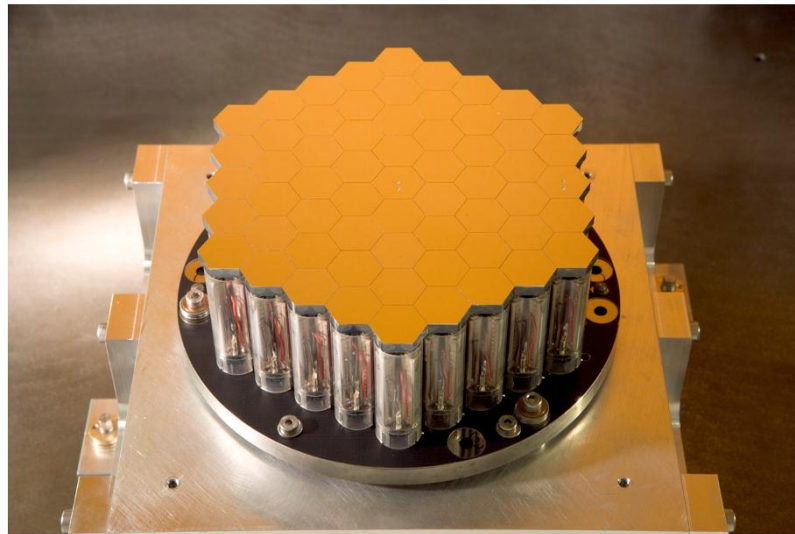


Figure 5 Active segmented mirror composed of sixty-one hexagonal segments. Each hexagonal mirror can be controlled via a piston, tip and tilt mechanism. Credit: Picture and text taken from the ESO website.

Segmented mirrors inherently feature a gap between adjacent segments. The gaps need to be small as they can impact the overall performance of the mirror. The exposed gap area needs to be less than 2 % of the total mirror surface area to ensure tolerable energy loss and energy diffraction from the central lobe of the

diffraction pattern. When a broadband source is shaped, the mirror segments have to be absolutely phased, since modula- 2π steps would seriously degrade optical performance²³. The step response of the segments can be as fast as 100 μs depending on the driver, actuator characteristics, and the segment mounting. Segmented mirrors are assembled from hundreds of segments with hundreds of actuators and associated parts. Large mirrors can be assembled in this manner; however, the manufacturing and assembly process is complicated and expensive.

3.2 Mirrors with discrete actuators

The increase in generated laser power requires correction devices that have a high (spatial) resolution and are able to withstand high power densities. Mirrors with continuous surfaces and discrete actuators can fulfill these requirements. The first deformable mirrors with discrete actuators were based on piezoelectric stack actuators. They were developed in 1979 due to the need for low-voltage and moderate stroke requirements ($>1 \mu\text{m}$) for compensation in infrared and high-energy systems. In 1990, Ealey et al.²⁴ designed a mirror with 37 actuators arranged hexagonally over a circular 16.5-cm aperture. The device operated under a 300-Hz bandwidth with 16- μm stroke at a supply voltage of 3 kV. The surface quality of the mirror was 223 nm P-V. The mirror showed better performance in terms of sensitivity to movement when compared with monolithic deformable mirrors used during its time; however, the surface quality was not satisfactory and the supply voltages were considered as too high. The next development step featured a low-voltage electrodisplacive mirror with a supply voltage of 150 V and a stroke of 5 μm through a lead-magnesium-niobate (PMN:PT) actuator material. In this case, the standard mirror had 241 actuators that could be scaled up to 2000 actuators, and the mirror was qualified for space operation. Further developments in the actuator material (PMN:BA) increased the sensitivity of movement of the system by a factor of two. In general, developments in actuator technology have resulted in response times faster than 300 μs together with a repeatability rate better than 99 % due to negligible hysteresis. The electrodisplacive mirror was fabricated using Ultra-

Low Expansion (ULE®) material and had a surface quality better 32 nm. The innovations in this mirror system were driven by the need for a higher number of actuators and the consequent need for reducing the cost per actuator. In 1984, Itek introduced the concept of cooled deformable mirrors. In such a system, the mirror faceplate includes a silicon-multiport pin-fin heat exchanger with actuators connected²⁵. The coolant enters and exits the silicon through the actuators, and thus, the coolant flow distances are limited. Itek has built a mirror with 250 actuators arranged in a square zonal array with a 20-cm cooled aperture. Mirrors with discrete piezoelectric stack actuators are nowadays made commercially available by OKOtech⁵⁵, AOA Xinetics²⁶, and CILAS³⁹.

In 2008, Hamelinck et al.²⁷ introduced a mirror with electromagnetic actuators that deformed a thin continuous membrane. In this system, the actuators can deform the membrane via push-and-pull movements; each actuator has ± 10 stroke, nanometer resolution, and heat dissipation of the order of only a few milliwatts. The prototype system has 427 actuators with a pitch of 6 mm (cf. Figure 6). The actuators are connected via rods that are affixed by means of a small glue droplet to the membrane. The 6-inch membrane is composed of 100- μm thick Pyrex®, and it can be flattened to 28 nm rms by 10 % of the available actuator stroke. The resonance frequency is larger than 1 kHz, and the control bandwidth is larger than 200 Hz. The large actuator pitch and the large mirror size are preferable for astronomical systems and not laser (machining) applications.

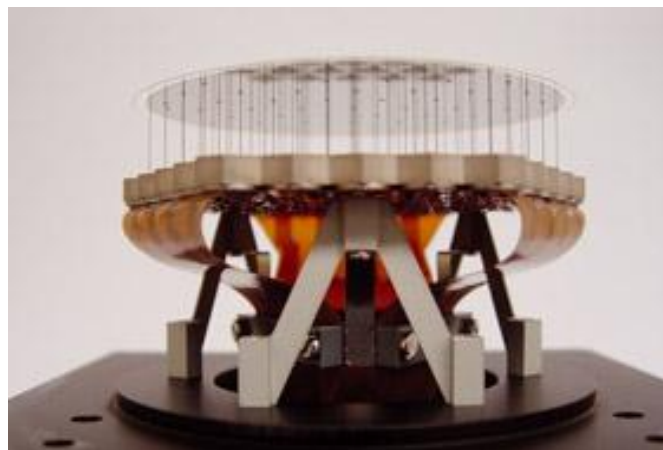


Figure 6 Prototype of Hamelinck's mirror system with 61 actuators in one of its assembly steps. Credit: Picture and text by Roger Hamelinck.

The company Alpao²⁸ has used electromagnetic voice-coil actuators to deform mirror membranes. In such a system, solenoids are placed underneath a set of magnets that are attached to the membrane²⁹. The advantages of this technology include high stroke ($>25\ \mu\text{m}$), displacement, and the facility of using a large number of actuators (52–241). Further, the forces exerted by the actuators are directly proportional to the currents (linearity errors are less than 3%). The mirror surface is controlled typically to a limit of less than 10 rms nm in closed-loop mode. The bandwidth of the mirror is $> 500\ \text{Hz}$ or $> 750\ \text{Hz}$ depending on the mirror model.

Deformable mirrors with discrete actuators can provide good mirror-surface quality and a high stroke. However, their drawbacks include the low heat dissipation of the passively cooled assemblies and the difficulties involved in replacing the actuators.

3.3 Deformable mirrors

In 1974, Feinleib et al.³⁰ reported the first implementation of the monolithic construction of a piezoelectric deformable unimorph mirror (DM). The DM set-up consists of a piezoelectric block (with a thickness of 1.5 cm and a diameter of 4 cm in the original design) and a bonded glass substrate with a reflecting surface on the front. The addressing electrodes are positioned between the glass substrate and the piezoelectric block while the common electrode is affixed to the rear surface of the piezoelectric block. In currently developed DM set-ups, the positions of the common and addressing electrodes have been interchanged (cf. Figure 7). The application of an electric field between the common and addressing electrodes forces the piezoelectric material to expand along the thickness (poling) direction and to contract along the lateral direction as the piezoelectric material is poled along the thickness direction. Because the piezoelectric block and the glass substrate are joined together, the mirror surface changes its shape. This effect is similar to the bending of a bi-metallic strip under temperature change. This design is referred to as the unimorph set-up as only one layer is active (cf. Figure 7).

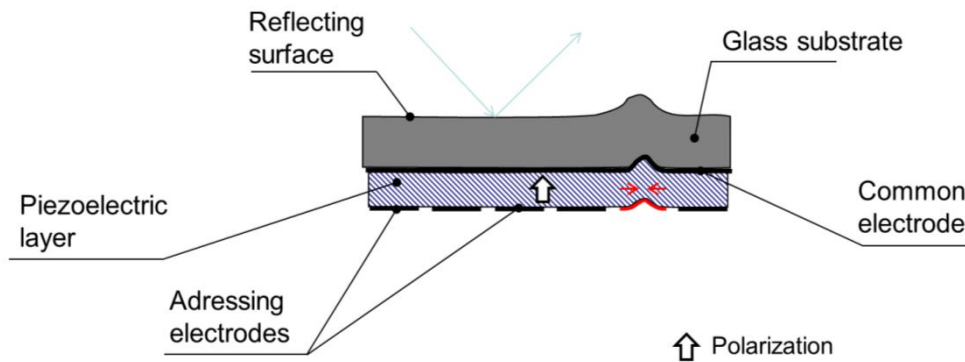


Figure 7 Cross-section of a unimorph deformable mirror. One segmented electrode is activated (shown in red). The activation causes the piezoelectric material between activated electrode and ground electrode to contract.

Primmerman and Fouche³¹ showed the first experimental evidence of the feasibility of compensating for cw convection-dominated thermal blooming by using a deformable (unimorph) mirror in 1976. They increased the intensity of the laser beam with an emitting power of 2 W by a factor of 1.76. The mirror was set-up from a monolithic disk (\varnothing 3.8 cm) of piezoelectric crystal and a metalized glass disk. The DM had 57 electrodes and required a driving voltage of ± 1.5 kV to achieve a stroke of ± 0.5 μm . The desired shape of the mirror surface and the required addressing electrodes were calculated in advance. The voltages of the addressing electrodes were accordingly to the desired mirror deformation varied during the experiments. Steinhaus and Lipson³² proposed a deformable mirror with a piezoelectric disk glued onto a glass plate. This mirror system was used for the correction of atmospheric turbulence aberrations. In this system, the glass substrate and the piezoelectric plate have identical thicknesses (1.5 mm) and diameters (5 cm). The common electrode is positioned between the substrate and the piezoelectric disk and the rear surface of the piezoelectric disk is patterned with the addressing electrodes. The resulting mirror system showed a dynamic response that was flat up to 550 Hz. The DM deformed by 1.5 μm when all 12 electrodes were set at 200 V. The study indicated that the change in voltage across one electrode affects the surface at all points on the mirror. This effect guarantees a smooth surface under all circumstances. However, the primary issue is the polishing of the glass mirror to optical flatness.

Schwartz et al.³³ investigated the applicability of wavefront correction by means of a deformable unimorph mirror in conjunction with a curvature sensor. Their study discusses the limits of wavefront correction, and further shows the dependency of the limits on mirror boundary conditions and the discreteness of the addressing electrodes. The unimorph mirror is composed of a layer of piezoelectric material and a substrate layer (e.g., glass or silicon). Further, the authors examine a set-up with two oppositely poled piezoelectric layers that are bonded together, thereby making the system more sensitive to movement. This bimorph set-up requires at least one piezoelectric layer that can be polished to optical quality. The second piezoelectric layer can be composed of smaller elements, thereby facilitating manufacturing of large mirrors. The mirror has an athermal design because the two oppositely poled piezoelectric layers offer identical thermal expansion and bonding layer and metallization are small, thereby no thermally-induced deflection occurs (in theory). The mirror is simply-supported at the rim. In 2007, Sinquin et al.³⁴ compared unimorph and bimorph large aperture DMs for laser applications. The paper presents the unimorph approach improving the polished surface quality from 7 nm rms residual defects of the wavefront for bimorph set-up to 3.4 nm rms for unimorph set-up. They point out that bimorph architectures suffer in contrast to unimorph architectures from print through effects that lower the residual wavefront quality through inner electrodes and thicknesses discontinues. These high spatial frequency surface effects lead to an energy modulation of the laser

In 1996, Safronov³⁵ presented a report on deformable mirrors obtained from experimental and industrial samples. The study indicates that “small” adaptive optics that feature a small number of actuators are most effective in compensating for large-scale phase distortions. Such systems are of simpler design, cost-effective, and only slightly less effective compared to “large” adaptive optics that feature a large number of actuators. During the time of this study, the existing mirrors were mainly experimental optical devices, and only a few mirrors were available as industrial samples.

Kudryashov et al.³⁶ have discussed the use of the unimorph deformable mirror for atmospheric adaptive optics applications based on theoretical and

experimental results of the response functions of the unimorph mirror surface and its description by Zernike polynomials. Subsequently, they have estimated the efficiency of correcting atmospheric turbulence (by means of the Kolmogorov spectrum) with a DM by varying the number of actuators and their shape. Experimental and theoretical response functions of the mirror could “*verify the possibility of efficient application of bimorph correctors to compensate for phase distortions caused by atmospheric turbulence*”³⁶. In 1998, Dainty and Kudryashov provided proof of compensation for laboratory-generated aberrations by a bimorph mirror³⁷. They set up a glass water cell to induce turbulence/aberrations and a photo diode to measure the Strehl ratio. A deformable mirror with nine addressing electrodes optimized the focus intensity of the aberrated beam by a factor of two. This DM uses two piezoelectric disks glued to a glass substrate. One disk accounts for defocus correction with one addressing electrode while the other eight addressing electrodes on the second piezoelectric disk account for the correction of higher-order waveform aberrations including defocus, astigmatism, spherical aberration, and coma. In this DM system, instead of the generally used O-ring support, a glass tube clamps the mirror at its centre. Further, their study investigates thermally-induced changes to the mirror surface. As a result, the focus changes by $0.38 \mu\text{m}/^\circ\text{C}$.

Rukosuev³⁸ introduced the first commercially available adaptive optical (AO) closed-loop system for compensating for the aberrations occurring in a laser beam during the transmission of the beam from the radiation generation to the laser machined material. Their AO system is based on a bimorph mirror similar to the one described in ³⁷, a Shack Hartmann wave front sensor and a control unit. The focused spot size of the laser was reduced by a factor of three, and real-time correction was achieved at a frame rate of 25 Hz. The DM comprises a copper substrate with cooling channels present between soldered copper disks. The cooled mirror was tested under CO₂-laser radiation with a power density of $2.5 \text{ kW}/\text{cm}^2$. The company Cilas³⁹ manufactures commercially available DMs. Their DM systems include bimorph and unimorph architectures. Unimorph architecture is used mainly in high-power lasers while bimorph architecture is used for atmospheric turbulence correction in astronomical telescopes. Both

architectures can use additional dielectric coatings. Other deformable mirrors are commercially manufactured by TURN Ltd.⁴⁰ and Active Optics NightN Ltd⁴¹. Both companies produce bimorph mirrors and unimorph mirrors with piezoelectric disks glued onto various substrates (optical fused silica, glass, copper, and silicon).

Very few studies have focused on DMs with screen-printed actuator layers^{42,43}. Rodrigues et al.⁴³ have proposed DMs based on the use of silicon-wafer substrates and screen-printed piezoelectric thick film. In their design, the 700- μm -thick silicon wafer has a diameter of 150 mm with 91 hexagonal actuators screen-printed on the rear surface of the mirror. These actuators are screen-printed to a thickness of 80 μm , and they are sandwiched between screen-printed gold electrodes with thickness of 14 μm each (cf. Figure 8(a) and (b)).

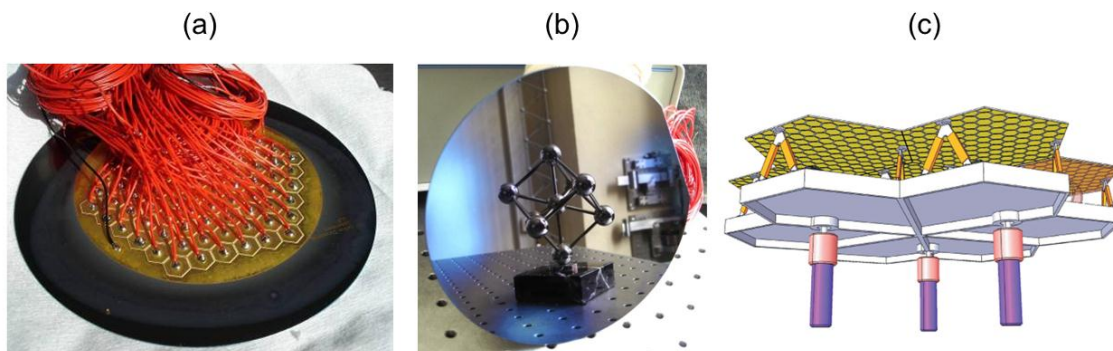


Figure 8 Silicon wafer (\varnothing 150 mm, thickness = 700 μm) with 91 screen printed piezoelectric actuators and an active optical aperture of 65 mm; (a) Soldered wires, (b) Mirror surface, and (c) modular mirror comprising silicon wafer with screen-printed thick film⁴⁴.

The mirror is supported by two rubber O-rings with diameter of 100 mm. The mirror aperture is 65 mm. The maximum operating voltage is 140 V at which the defocus P-V value is 5 μm . In addition, the above study lists the measurements of further Zernike polynomials (e.g., tetrafoil with a P-V of 2.8 μm). In the study, the initial deformation of the mirror surface occurred during the course of the manufacturing process. Therefore, the authors could not implement their mirror design in an AO system. No measurements on the thermal behaviour of the system are available.

Deformable mirrors show great potential for laser and imaging applications. Their primary advantage is that the continuous faceplate over the entire aperture

offers high optical image stability. This architecture features a high stroke and large bandwidth of operation. A reduced number of actuators are required for this system when compared with those with segmented mirrors or discrete actuators. Very few studies have examined the thermally-induced changes in such systems.

Patent research

This section includes only the patents relevant to DMs. The first basic patent dates back to 1975⁴⁵, and it describes a unimorph architecture with a piezoelectric wafer³⁰. The piezoelectric wafer is sandwiched between two metallic layers with one thin metallic layer acting as the ground electrode. The other metallization layer is segmented, thereby enabling a controlled and continuous surface deformation. The piezoelectric wafer can also be segmented. The phase modulator is used for distortion correction. The first bimorph architecture was patented by G. Michelet⁴⁶ in 1981. An increase in sensitivity is achieved through the use of ML piezoelectric material bonded to a mirror and a base plate⁴⁷. The number of piezoelectric layers can be as large as 16. The stacked layers are oppositely poled and the electrodes are positioned alternately. The like electrodes are connected electrically. In this system, increased stacking of the piezoelectric layers leads to decrease in the supply voltage. The ML architecture had also been patented by Safronov in 1997⁴⁸ ; however, this system uses elastic sealant filled into the cavity of the housing that covers the rear surface of the mirror. This reduces labor costs as the elastic sealing damps the pressure of the polishing tool. The elastic sealing also increases mirror strength and reliability as it damps external impacts and vibrations. Further, the sealing protects the piezoelectric actuators from direct damage. Besides elastic sealing, the patent also claims the use of a cooling liquid to fill the cavity.

Möller⁴⁹ fabricated a DM in which the thicknesses of the passive and active layers varied over the mirror aperture. This invention particularly relies on technological processes such as spin-coating and molding/casting. The patent for heat-dissipating layers in DMs is claimed by Griffith in 2006⁵⁰. The patented heat spreader distributes the thermal energy evenly across the mirror and to the mirror holder. The dissipating layer (0.2–0.5 mm thick) needs to have high

thermal conductivity and a linear coefficient of thermal expansion (CTE) similar to that of the active material. Diamond has been identified as the heat spreader material, while silicon carbide (SiC) has been used as the substrate material. The use of SiC as a substrate material allows the implementation of an annular support that extends downward into an annulus (cavity). Diamond can be grown directly onto this annular support. PocoFoam™ is suggested as the thermally conductive and compliant filler in the cavity. Preumont⁵¹ patented a DM using a tip/tilt mounting mechanism with flexible electrical connections and a damping layer at the rear surface of the mirror. The mirror is composed of materials with different thermo-elastic properties, and this provides the required initial curvature of the faceplate without actuation. The arrayed active layers are preferably applied simultaneously by screen-printing and not discretely jointed/glued.

3.4 Modular / hybrid mirror architecture

Hybrid mirrors are a combination of deformable and segmented mirrors, and they offer the advantages of both principles—a smooth surface and large deformation paired with an assembly of large mirrors from many modules that are moderately priced. Hybrid mirrors based on this approach are mainly used in astronomical telescopes and certain laser-shaping applications.

Griffith⁵² discusses the use of structural support for unimorph mirrors from underneath instead of the edge (as in the case of the O-ring support). Each addressing electrode has its own compliant pillar, thereby resulting in a localized zonal response. A dual-stage actuated mirror with different structural configurations has been proposed. Therewith, a deformable unimorph mirror is supported from underneath by a second unimorph mirror. Both unimorph mirrors are supported by compliant pillars. The second lower unimorph mirror can also be a stack actuator. Therewith, this dual-stage actuated mirror offers a simplified tweeter (high density) and woofer (high dynamic) approach. A flexi-circuit is used for electrical contacting, thereby resulting in a thin (<1 mm) sandwich with plenty of construction options. Rodrigues^{43,53} has discussed the possibility of the hybrid approach based on screen-printed piezoelectric

unimorph mirrors. These DMs have hexagonal-shaped silicon substrate with hexagonal screen-printed actuators. The DMs are modularly assembled and supported by a three-point active kinematic mount to ensure the alignment of the piston, tip, and tilt of the single modules. The combination of many such identical modules simplifies the control of curvature for a large number of actuators (cf. Figure 8(c)).

3.5 MEMS mirrors

Micro-electro-mechanical-systems (MEMS) refer to the technology of very small electricity-operated devices in the μm -range. They are (mainly) based on silicon that has a high optical polish and a plane surface; further, silicon can easily be produced by means of batch production. MEMS mirrors are considered as special types of mirrors based on their technological characteristics although they can also be classified as either continuous or segmented mirrors (cf. Figure 4).

Vdovin⁵⁴ demonstrated the first membrane deformable mirror that had 37 electrodes, and it was first fabricated by means of bulk micromachining in 1995. The micromachined membrane-deformable mirror (MMDM) consists of a thin mirror membrane that is mounted at a distance range of 20 μm to 100 μm away from the actuator structure. The actuator structure is mounted directly over a chip carrier or a printed electronics board, and it has a patterned aluminium metallization structure. The deformable membrane is deformed through the application of an electrostatic field between the actuator structure and the membrane. The initial study proposed the design of a mirror with a 0.5- μm -thick silicon nitride membrane with a 10.5 mm \times 10.5 mm square aperture. The membrane is coated with a 200-nm reflective aluminium layer. The reflecting surface is initially plane with a deviation of approximately 633 nm (rms). These mirrors have a total stroke of 9.4 μm , and an individual stroke of 0.5 μm for the 37 actuators. This mirror has been in production since 1997; in addition, standard silicon nitride-based mirrors with thicker polysilicon membranes are also available. These mirrors feature higher reliability and snap-on protection covers. The optical quality is better than 400 nm rms across the aperture with a 1-kHz

response. The stroke of the 15-mm mirror is 25 μm (at 400 V), and the metal-dielectric coatings can handle power levels of up to 600 W cw⁵⁵. This corresponds to power densities of 330 W/cm²; however, power densities of 2 kW/cm² have been reported⁵⁶.

Bonora⁵⁷ recently introduced a membrane mirror (37 electrodes) with a thin, aluminium-coated nitrocellulose membrane (5- μm -thickness) with an initial flatness of less than 60 nm (rms). The maximum stroke at the centre is 10 μm at 230 V. In a later study, Bonora⁵⁸ increased the spatial resolution and performance of the system for the correction of optical aberrations through the additional application of transparent electrodes on the top surface of the membrane. This facility of having electrodes on both sides of the membrane allows it to be shifted both upwards and downwards. This mirror has successfully been used in commercially available AO systems. This standard mirror system includes drive electronics with 32 actuators, an aperture of 11 mm, and a stroke of 10 μm (NT83-985)⁵⁹.

In 1999, Bifano et al.⁶⁰ investigated three different types of mirror systems based on a parallel plate capacitor with a 5- μm air gap that was fabricated using surface micromachining. The mirror systems had identical electrostatic actuator structures; however, their mechanical coupling mechanisms to the mirrors varied. The study investigated continuous mirrors, segmented mirrors, and segmented mirrors with tip/tilt motion, and the feasibility of these designs was demonstrated. Bifano et al. demonstrated the performance of a continuous mirror with a 2- μm stroke and 10-nm repeatability at 200 V, and no hysteresis or drift was observed. The active mirror area of this system is 7 mm \times 7 mm, and it includes 400 active elements. The surface maps of the mirror system show that the actuator pattern has a print through to the mirror layer that results in a waffle pattern with a P-V value of 50 nm. The mirror layer also has holes that are required to release the sacrificial layers in the machining process. This type of mirror is used in two commercially available products, the Multi-DM and the Kilo-DM. The Multi-DM has 140 actuators with a stroke ranging between 1.5 μm and 5.5 μm and an aperture between 3.3 and 4.95 mm. The Kilo-DM has 1020 actuators with a 9.3-mm aperture and 1.5- μm stroke. Both mirrors offer a surface

finish of better 20 nm rms. The thickness of the mirror membrane determines the available stroke, interactor coupling (generally between 25% and 40%), and response time (between 20 μ s and 50 μ s)⁶¹. Interactor coupling indicates the actuator influence on its surrounding membranes that are not directly activated by the actuator. These mirrors are applied in commercial adaptive optics kits⁶² with a Shack-Hartman WFS, control software, and mounting hardware.

Electrostatic actuated mirrors with a parallel-plate capacitor set-up have an air gap that limits the mirror's stroke due to "snap through" beyond one third of the gap. Various alternatives have been suggested in order to overcome this drawback, e.g., building lever structures that magnify the motion⁶³ or the use of curved electrostatic actuators⁶⁴. The last-mentioned system uses surface-micromachining to create the actuator arrays and flip chips to bond the mirror arrays to the top surface of the actuators (cf. Figure 9). The mirror segments are hexagonal, and they have a fill factor of 98.6% (with a 6–7- μ m gap between adjacent elements). The actuator platform lifts the mirror segment automatically through engineered residual stresses in the three supporting bimorph flexures.

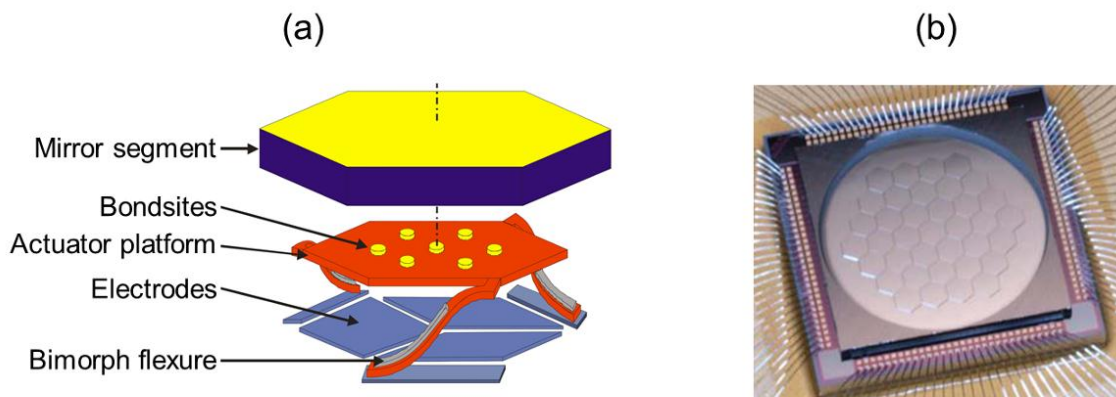


Figure 9 (a) Diagram of a single mirror segment. Engineered stress in the bimorph flexure lifts the mirror segment. The three electrodes enable piston plus tip/tilt movement. (b) Scanning electron microscopy image of the Iris AO 37-segment deformable mirror. Credit: Pictures taken from ⁶⁴.

The residual stresses are engineered via a film of high stress material on a polycrystalline silicon suspension. The three underlying electrode ignite the piston plus tip/tilt movement of the mirror segments. Mirrors with 37 (PTT111-5 and PTT111-8) and 163 (PTT489-5 and PTT489-8) segments and apertures of

3.5 mm and 7. mm, respectively, have been reported. Their stroke is between 5 μm and 8 μm , and a maximum tilt angle of ± 8 mrad at a maximum voltage of < 200 V can be achieved. Due to the electrostatic principle, the hysteresis is below 0.1%. The optical surface error is < 30 nm rms, and the mirror is capable of handling powers up to 100 W/cm². These mirrors have been made commercially available by Iris AO, Inc.⁶⁵ and Laser 2000 GmbH⁶⁶.

In research labs, MEMS mirrors utilizing continuous face sheets with up to 4096 elements have been fabricated for the purposes of high-contrast imaging⁶⁷, and their performance has been successfully demonstrated. MEMS mirrors are micromachined devices, and therefore, they can be efficiently fabricated in large quantities. These mirrors have high spatial resolution and limited stroke. Since the dimensions of the devices make them small and flat, their corresponding masses are also low, and their first resonance frequency is high. Their drawbacks include the gap between adjacent segments and the etching holes⁶⁸ on the membranes; these result in energy loss with a grating/edge diffraction effect. Further, the system is subject to heating. Architectures that have no gaps and etching holes result in very thin mirror membranes that dissipate very little heat. In the case of (dielectric) breakdown, the faulty actuators are not individually replaceable.

3.6 Discussion of the state of the art solutions

Chapters 2.1 to 2.5 analyse the various available deformable mirror devices from research and industry. Table 1 shows a list of selected commercially available devices. I have only selected devices with continuous mirror surface and an aperture between 15 mm and 85 mm to ensure their comparability.

Three actuating principles are available for deformable mirrors—electrostatic, electromagnetic, and piezoelectric. Mirrors actuated by piezoelectric stack actuators are not considered in the list as the use of stack actuators makes the manufacturing efforts high and the devices expensive.

Table 1 Commercial deformable mirror solutions.

Model	Distributor	Actuator	Aperture	Individual stroke	Damage threshold	Mass production compatibility	Available coatings	Remarks
15 mm 37ch OKO MM/DM	Flexible OKO optical	Electrostatic; 37; membrane deformable mirror	15 mm	0.5 μm	(2-0.33) kW/cm ²	yes	Metal, dielectric, metal- dielectric with a couple of dielectric layers	Very thin substrate: SiN - 0.5 μm , PolySilicone about 10 μm
Hi-Speed DM277-15	Alpao	Electromagnetic (277)	24.5 mm	<u>3 μm</u>	n.a. (manufactural claim no use it with high pulse energy)	yes	different metallic materials available (Ag, Al, Au).	Operating temperature: 10°C - 35 °C; Mirrors working at -40°C available
AT 26	Turn Ltd.	Piezoelectric layer (20)	66 mm	9 μm	n.a.	No, manually wiring	Multilayer dielectric, others by customer order	
Tiny mirrors	Active Optics NightN Ltd.	Piezoelectric layer (10)	12-30 mm	n.a.	20J/cm ² for Glass, 3J/cm ² for TiS	No, manually wiring	protected Al, Ag, metal- dielectric coating, multilayer dielectric coating on customer demand	
DM30	Active Optics NightN Ltd.	Piezoelectric layer (<11)	30 mm	< 0.7 μm	20J/cm ² for Glass, 3J/cm ² for TiS	No, manually wiring	protected Al, Ag, metal- dielectric coating, multilayer dielectric coating on customer demand	
Mono 31	CLIAS	Piezoelectric layer (31)	85 mm	n.a.	2J/cm ² @ 600ps; 6J/cm ² @ 10ns; 300J/cm ² @ 10ms	n.a.	metal + dielectric layers	Operating temperature: 20°C - 25 °C;

Electrostatic mirrors with continuous and segmented mirror surface are available for commercial use. A commonly used mirror is the 15-mm, 37-channel OKO MMDM with segmented electrodes underneath the mirror membrane. The application of an electric field results in a downward bending of the membrane, and thus, the mirror has a large interactor coupling as the activation of one actuator heavily influences the mirror membranes surrounding. The mirror membrane is deformed by electrostatic forces that increase hyperbolically with the approximation between two plane electrodes. Therefore, large stroke capabilities and low driving fields in thin mirror membranes result in low restoring forces. Mirror membranes with thicknesses between 0.5 μm and 10 μm result in low membrane-heat-spreading capabilities, and consequently, the demand for excellent high-power coatings has increased. In addition, a pull-in effect acts on the membrane after one-third of the electrode distance (maximum stroke) has been traversed. This drawback has been overcome in the PTT111-8 and NT83-985 mirror systems; however, these are not listed in Table 1 as their apertures are only 3.5 mm and 11 mm, respectively⁶⁵. Restoring forces that can be used to avoid the pull-in effect and to reduce the interactor coupling can be delivered by bimorph flexures underneath the segmented apertures. This can also be achieved by deposit electrodes on both sides of the membrane.

An electromagnetically driven mirror features electromagnetic actuators underneath the mirror membrane that push and pull the membrane. In such systems, the deformed membranes are fairly thin ($< 50 \mu\text{m}$). The hi-speed DM277-15 mirror has outstanding actuating capabilities; however, it has no specified damage threshold. Consequently, it is not suitable for high-pulse energy applications. The manufacturing of these electrostatic and electromagnetic mirrors is very straightforward as developers use batch-fabrication processes.

Piezoelectrically activated DMs have a piezoelectric disk bonded onto the mirror substrate. Piezoelectric actuators inherently include piezoelectric hysteresis, creep and relaxation. Consequently that reduces the mirror performance in terms of ease of application and control loops are required to address these issues. Despite these issues, the simple set-up of these mirror systems and their

radiation stability even under high-power conditions (due to the continuous surface and well-established coating technologies) has made them popular for use in AO systems.

In contrast to electrostatic and electromagnet mirrors, piezoelectrically actuated mirrors are rarely batch-fabricated. The state-of-the-art piezoelectric DM devices are mainly handcrafted, with an active layer adhesively bonded on miscellaneous substrates. Moreover, the electrical wiring is very elaborate as each discrete actuator is (manually) contacted.

Figure 10 depicts four typical electrical conducting (wiring) configurations for addressing electrodes. Each configuration is shown on one-fourth of a piezoelectric mirror's rear surface. The addressing electrodes affixed at the mirror's rear are hexagonally shaped. The structuring of the addressing electrodes can be obtained using mechanical shadow masks, advanced lithographical processes and etching, and by laser structuring. In particular, the latter two technologies result in an excellent resolution with sub-micrometer structure size; hence, they are frequently used. The mechanical shadow masks are relatively thicker than the structure size. Thus, patterning using mechanical shadow masks leads to unwanted metallization merging and the need for a mechanical mask mount to address this problem.

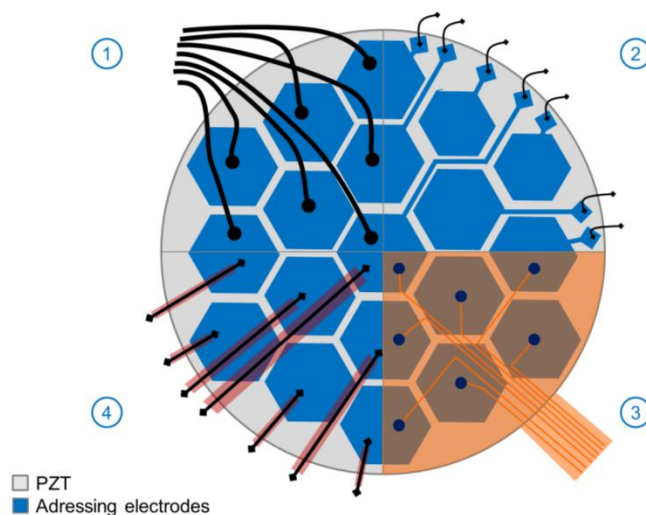


Figure 10 Addressing electrodes with four configurations of electrical wiring. Each configuration covers one-fourth of a piezoelectric mirror's rear surface. (1) Glued/soldered wires, (2) drawing-out of the electrodes, (3) flexible copper-clad laminates, and (4) 3D-structuring by lithographic processes or screen printing.

The wiring of the addressing electrodes is an aspect which demands careful consideration. Typical techniques for wiring include soldering or gluing of thin wires onto the addressing electrodes (cf. Figure 10 (1)). Wire soldering and wire gluing can lead to deformation of the mirror membrane, which can be caused by thermal activation of the bonding layer between substrate and piezoelectric layer during soldering, or shrinkage of wire glue drops. The wires also need to be strain-relieved and wire-weighting-induced mirror deformation needs to be reduced. Wire bonding is an alternative to soldering and gluing. However, the process does not allow for interconnection distances of more than 10 mm; the distance between the central addressing electrode and piezoelectric layer's rim can be more than 10 mm. One solution is the drawing-out of the electrodes (cf. Figure 10(2)) to the piezoelectric layer's rim. The wire joints are outside the mirror aperture in this case. However, a primary disadvantage is the dead space between two addressing electrodes or between the electrical wiring and addressing electrodes. This dead space is determined by the dielectric strength of air (2 kV/mm) and the supply voltage. The integration of electrical wiring into the addressing electrodes layout reduces the active area of the addressing electrodes, and it increases the total dead space between the addressing electrodes. Another possibility is the wiring via flexible copper clad laminates (cf. Figure 10(3)). The thin laminates (approximately 100 μm thick) are composed of a polyimide (Kapton®) substrate and a single (or double)-sided copper cladding⁶⁹. The copper clad laminate has bores that are filled with fillers such as conductive epoxy or small solder droplets. The copper cladding has structured conducting lines, and it offers the possibility of integration with an electrical connector. This reduces the effects of wire-weighting-induced mirror deformation. However, a primary difficulty is the increase of number of addressing electrodes that consequently increase the labour input of the single interconnections.

From the technological point of view, the 3D-structuring of electrical wiring is pleasing (cf. Figure 10(4)). Photoresist can be used not only for the structuring of the addressing electrodes but also for depositing an insulation layer between the addressing electrodes and the electrical conductor. Further, it can be used for the

subsequent deposition of the conducting line (cf. red in Figure 10(4)). In this approach, the gaps between the patterned piezoelectric layers and the height differences between the piezoelectric layer and substrate can be bridged. Other methods of structured deposition include screen-printing or ink-jet printing processes. In particular, screen printing and lithographic structuring are mass-production compatible, and the labour costs do not vary with the shape, pitch, and number of addressing electrodes.

Another factor to be discussed is the thermal design of the DMs; this issue becomes more important in the light of the anticipated increase in laser power and the need for beam-shaping. The high-power compatible deformable mirrors apply either highly thermally conductive elements as substrate material (e.g., copper), thermally adapted (athermal) materials, or a combination of both⁵¹. The resulting material selection in this manner ensures that the thermally-induced deflection is small compared to the piezoelectric stroke. The approach attempts to match the coefficient of thermal expansion (CTE) of the substrate and active layers. The use of this material selection criterion is limited as the material characteristics of piezoelectric materials vary with the production run. The general counter measure to address this issue is the manufacturing of several mirrors that are characterized and subsequently selected according to their intended application purposes. Another widespread approach is the integration of cooling channels, thereby increasing the thermal dissipation of the mirror substrates. The miniaturization of cooling channels has a physical limit, as the coolant flow decreases strongly with decreasing flow cross-section. The cooling channels are distributed over the aperture, and their distribution results in a non-homogeneous temperature profile over the aperture. These abovementioned approaches require high substrate thickness, and relatively thick and/or expensive cooling channels; consequently, this decreases the performance of the mirror with respect to high deflection and low interactor coupling. A further increase in laser power requires new thermal compensation techniques in which the DMs performance is not affected by temperature changes or gradients in the mirror assembly. The review of the state-of-the-art and this discussion shows that deformable mirrors exhibit good characteristics such as low interactor

coupling, large stroke and simple set-up, but especially the thermo-mechanical design and manufacturing regime requires a revision.

In general, very few mirrors have successfully been applied in industrial and research applications. Most devices are used in academic institutions for study purposes or for high-power beam shaping applications. This is mainly due to the prohibitive cost of the active optical elements and their complexity of integration into adaptive optical systems. Moreover, their successful implementation relies on the design and practical set-up of AO systems. Active optical elements, sensor elements, and monitoring cameras have to be positioned in conjugated planes to effectively compensate for aberrations which demands for highly skilled staff. High-power closed-loop AO systems are not easily available, and the wider market lacks knowledge about the possibilities of AO systems⁷⁰. Another drawback is the lack of a plug-and-play standard for AO devices; this leads to increased integration efforts. These days, (almost) all large optical inventory distributors (Thorlabs, Edmund Optics, Laser 2000 GmbH) and AO companies (Imagine Optics, CILAS, Turn, ActiveN) feature complete AO systems; However, proprietary hardware and software for the devices makes it difficult for them to function interchangeably or in a combined manner. These factors restrict new applications and markets.

3.7 Objectives of this thesis

The primary objective of this thesis is the development of mainly batch-fabricated non-cooled deformable unimorph mirrors for high homogeneous temperature loads and high inhomogeneous laser loads. The active layer of the DM is a piezoelectric actuator that acts laterally on the mirror membrane. To achieve this objective, I use a multi-material approach. The multi-material approach integrates certain layers with thermo-mechanical parameters that differ from the substrate and the active layer into the mirror set-up. The secondary objective of this thesis is the development of a manufacturing regime that consists mainly of batch-fabrication and reduced manual processes. Special attention is paid to the simplification of mirror contacting and electrical wiring can also be achieved by this approach.

A new manufacturing regime for the deformable mirror is developed in this thesis. It is based on LTCC substrates and screen-printed actuator structures. The screen-printed layer material characteristics and their characterization methods are theoretically analysed. Subsequently, the density and indentation modulus of the sample screen-printed patterns are measured. The stiffness matrix components of the piezoelectric layer are deduced. The mount design of the screen-printed piezoelectric deformable mirror is subsequently developed.

A detailed thermo-mechanical analysis is carried out to optimize the multi-material layer structure. The thickness and diameter of the piezoelectric layer are optimized to enable large piezoelectric stroke. Thermal lensing of the deformable unimorph mirrors is suppressed or compensated by the thermo-mechanical structure exclusive of the piezoelectric stroke application. The thickness of the reflective copper layer with respect to the boundary conditions is theoretically investigated in order to generate thermally favourable behaviour of the deformable mirror under different loading conditions. The thermo-mechanical performance of the DM is demonstrated. Further, the measurements of the mirror response under homogeneous loading and inhomogeneous (laser) loading conditions are presented. Compound loading is theoretically and experimentally introduced to compensate for thermal lensing of the deformable unimorph mirrors. In addition, I experimentally show the compensation of static wavefront aberrations by using the developed deformable mirror. However, an optimization of the piezoelectric actuator pattern and the development of a dielectric layer with respect to special applications, e.g., compensation for thermal lensing, atmospheric aberrations, etc., are not within the scope of this thesis.

4 Screen-printed piezoelectric deformable unimorph mirrors

This chapter describes the investigations of the actuating layer material and its application regime. The chapter begins with an introduction to piezoelectricity and its mathematical description. A subsequent section reviews the different application methods of piezoelectric materials and the selection of the screen-printing technology as a suitable method. The screen-printed layer characteristics are discussed in section 4.3, and subsequently, the choice of substrate selection is addressed. The chapter concludes with the presentation of the mirror concept and its manufacturing regime.

4.1 Piezoelectricity

Piezoelectricity is the linear interaction caused by the coupling between the mechanical and electrical states of certain materials. Several studies have analysed this phenomenon^{71,72,73,74}. This thesis is based on the explanations by Ruschmeyer⁷⁵. The mechanical loading of a piezoelectric material causes a corresponding electrical loading, thereby resulting in an electric field (direct piezoelectric effect). This is a reversible process; materials exhibiting this direct piezoelectric effect also exhibit the reverse piezoelectric effect. The reverse piezoelectric effect describes the application of an electric voltage that leads to a change in the materials shape.

This effect occurs only in crystalline materials with no centre of symmetry. The mechanical loading separates the positive and negative centre of charge in each unit cell, thereby resulting in charge accumulation at the outer faces. This effect is linear and directional. Charges induced by tension have a sign opposite to those induced by compression. Moreover, the effect is reciprocal; the application of an electric field results in elastic tension in the crystal, thereby inducing expansion or contraction depending on the polarity of the field.

The existence of a positive and negative centre of charge in each unit cell makes the cell an electrical dipole. Dipoles have opposing negatively and positively charged ends. Dipoles affect each other by building areas of uniform orientation

called Weiss domains. Macroscopic bodies are composed of statistically distributed domains showing no polarization or piezoelectric effects. Therefore, polycrystalline materials require polarization to be used as piezoelectric materials. The application of an electric field results in an expansion of the body along this axis of application with a corresponding perpendicular contraction (cf. Figure 11).

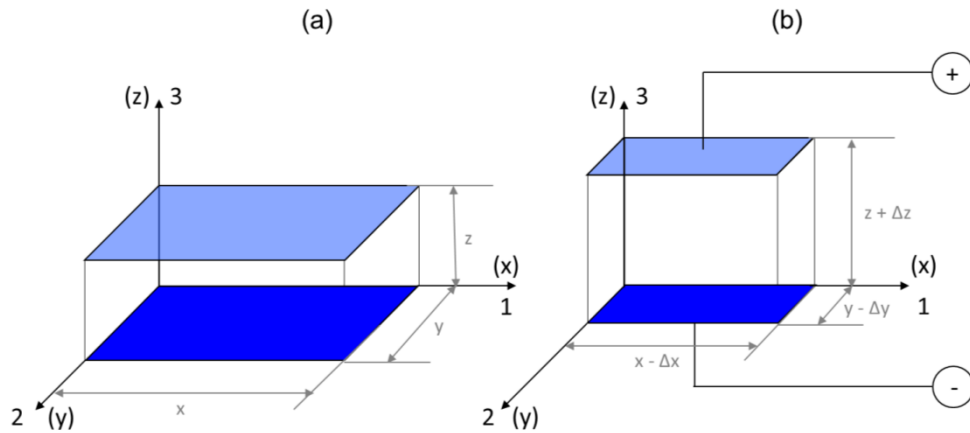


Figure 11 Piezoelectric sample with definition of the axes. Reverse piezoelectric effect: application of an electric field results in an expansion in the direction of the field and contraction perpendicular to the field axis.

The reverse piezoelectric effect (and hence, the change in polarization) can be activated by small or large signals. Small signals imply small activation amplitudes of the electric field. A large field-induced change in shape requires large electric fields (large signals). Large-signal activation of piezoelectric actuators results in a larger stroke along with nonlinearities; these are discussed in the next section.

4.1.1 Large-signal activation

A piezoelectric material undergoes an electric-field-induced change in polarization. In the case of a non-polarized sample, the polarization proceeds along the initial polarization curve shown in Figure 12(a) (the line of the initial polarization curve is dashed in the figure). An increase in polarization leads to the movement and switching of the domain walls until all domains are aligned along the same direction. A further increase in electric field strength does not lead to an enhanced polarization (point 1); the polarization is saturated.

Decreasing the electric field strength reduces the polarization until the remnant polarization P_R value is retained in the absence of an electric field (point 2). The application and further increase in opposing electric field strength leads to further polarization decrease until it changes the direction and it turns negative (point 3) for the coercive field strength E_c . A further increase in the opposing field leads to repolarization; however the polarization increases to a maximum along the negative direction (opposite direction). The polarization decreases with the electric field strength until it saturates as all domains switch to point in the opposite direction (point 4). A decrease of the opposing field until its absence, and again an increase of electric field changes the polarization to point 5 and point 1. The electric-field-induced polarization curve forms a hysteresis loop that is characteristic for every material.

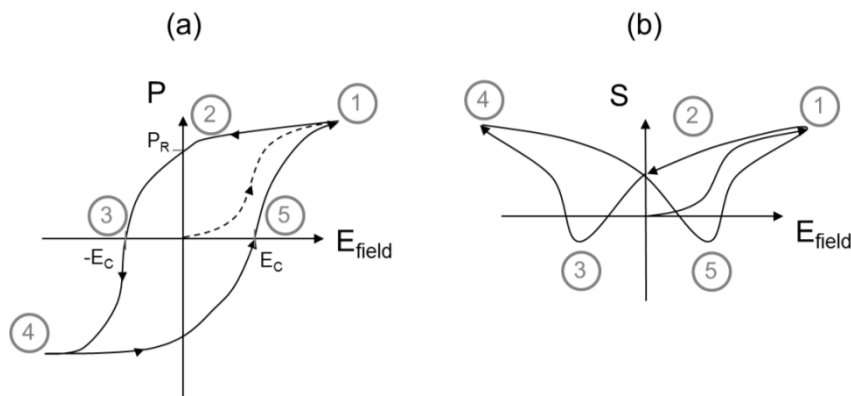


Figure 12 Polarization: (a) electric field curve and (b) strain-electric field curve.

Figure 12(b) shows the large-signal-induced strain in a piezoelectric element forming a butterfly loop. From a zero field, the crystal strain is assumed to be zero. When the field strength increases, the strain (expansion) correspondingly increases in the direction of spontaneous polarization. The sample volume is maintained constant, thereby resulting in a contraction perpendicular to the electric field (cf. Figure 11). The expansion along the electric field increases until it saturates (point 1). When the electric field is decreased, the strain decreases and the crystal contracts until point 2. Further decrease leads to the building of an opposing field, that strengths is increased until the strain becomes zero (point 3). At point 3, the direction of the polarization changes because of the strong opposed field. The polarization curve is anti-parallel to the spontaneous

polarization, and thereafter parallel to the opposed field. The strain becomes positive again as the field strength and polarization are parallel. Further increase of the opposed field leads to an increase in strain and a corresponding expansion of the crystal until it saturates (point 4). A subsequent change of electric field into positive leads again to a switching of the domains to the direction of the spontaneous polarization at point 5.

As shown, a non-polarized sample needs to be polarized by poling. Poling orients the spontaneous polarization by an external electric field and generates the remnant polarization. In the poling process, a large electric field ($>E_c$) is applied for a certain duration and at a certain (elevated) temperature regime. Afterwards, deformation, mechanical stress, and mechanical tension reside within the domains (also in the absence of an electric field). It is to be noted that poling conditions are material-specific.

Besides the hysteresis and butterfly loops, other large-field induced nonlinearities and time variable effects exist. These are listed as follows:

- Aging is the change in material properties with time. It describes the tendency of the piezoelectric material to change back to its original spontaneously polarized state prior to poling, e.g., relaxation because of domain reorientation over time. Aging is time-dependent; it is very rapid immediately after poling (at t_0), and aging slows down gradually a few days after poling. This phenomenon can be logarithmically expressed as follows:

$$d(t) = d(t_0) + A \log\left(\frac{t}{t_0}\right) \quad (5)$$

Here, A denotes the “aging rate” constant that is specific to the composition, the microstructure, and the processing history of the material. As a rule of thumb, the aging of piezoelectric ceramic is around 1 % per decade (year), and the effect is neglectable for piezoelectric actuators as their polarization is regularly oriented with a large-signal.

- Relaxation is a time-dependent change in strain (overtravel) due to change in the electric field strength. It occurs a few minutes or seconds after loading, and it results either in a time-dependent increase in strain

under a constant field or a time-dependent decrease in strain with short-circuiting of electrodes and under no load. Actuators used for positioning purposes are affected by this characteristic.

- The mechanical hysteresis curve of a piezoelectric bending actuator is shown in Figure 13. A positive electric field is applied, cycled twice and the deflection of the bending actuator is sampled. The distance between the rising and falling curves of the deflection is called the hysteresis width. The hysteresis width of the curve expresses the electrical losses that are dissipated as mechanical work and heat. Mechanical hysteresis signifies the dependency of the deflection (elongation) of the activated material on its previous (history of) applied electric field. The electrical field induced deflection also depends on the velocity (rate) of the change of the electric field. Another point is that time-dependent relaxation also affects the hysteresis. Hysteresis and relaxation have a superposition. Here, relaxation is suppressed as the cycle time is small when compared with the relaxation time. The hysteresis width increases with the duration of the hysteresis run. Thus, the use of the piezoelectric material as an actuator requires position control.

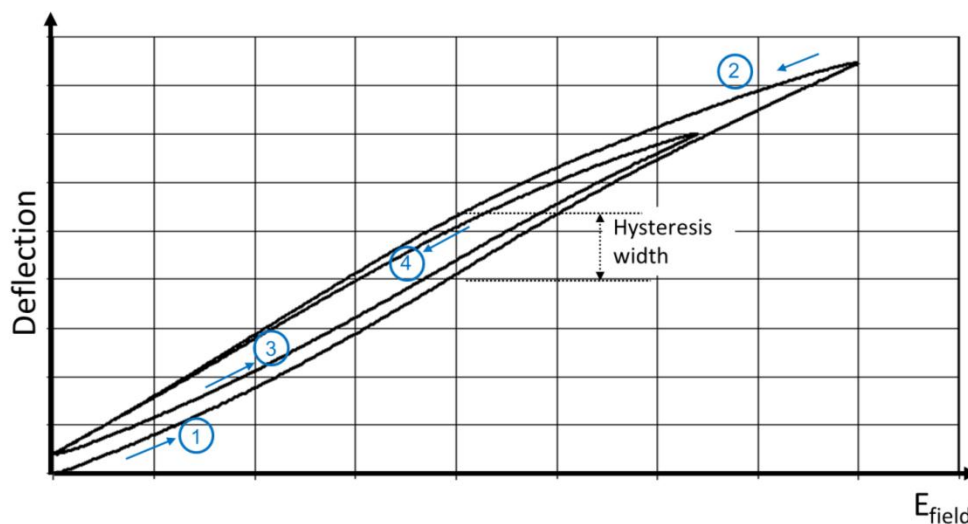


Figure 13 Mechanical hysteresis: hysteresis width is the difference between the rising and falling curves.

4.1.2 Temperature effects

Pyroelectricity is defined as the reversible change in polarization, ΔP , with temperature, $\Delta \theta$. Consequently, pyroelectricity is formation of charge in the piezoelectric material^{71,76}

$$\Delta P = p_i \Delta \theta \quad (6)$$

Here, p_i denotes the pyroelectric coefficient. The sample dimensions are maintained constant. The spontaneous polarization of the material depends on the temperature of the material. In contrast, the inverse effect is referred to as the electrocaloric effect, and a reversible temperature change is observed in the material under an applied electric field.

Secondary pyroelectricity is the generation of electrical charge due to thermal stress and dilatation caused by inhomogeneous heating⁷¹. Other theories define secondary pyroelectricity as an additional contribution to primary pyroelectricity that can be observed when the sample dimensions are allowed to relax during temperature change.

Piezoelectric materials do not exhibit polarization for a temperatures above the Curie temperature, θ_C , as the crystal lattice with an absent centre of symmetry changes to a symmetric lattice. This fact defines their maximum working temperature as $(0.5 - 0.75)\theta_C$. Temperature changes also affect piezoelectric properties such as charge constant and coupling factor. Material properties such as the coefficient of thermal expansion and material stiffness are also affected. Very little data is available with respect to piezoelectric materials. The chapter titled *Evaluation of screen-printed material characteristics* reviews the material properties of applied piezoelectric, ceramic, and metallization layers.

4.1.3 Mathematical description of piezoelectricity: piezoelectric equations

A piezoelectric material deforms to minimize its total energy. The internal energy density, W_{in} , is composed of its thermal, electrostatic, and mechanical energy densities.

Its total differential is:

$$dW_{in} = \mathcal{G}d\sigma + E_i dD_i + T_\lambda dS_\lambda \quad (7)$$

In the equation, entropy σ , dielectric displacement D_i , and strain S are independent variables while temperature, electric field strength E_i , and mechanical tension T are dependent variables. Temperature and entropy are scalar quantities. Electric field strength and dielectric displacement are vectors, and they are defined with reference to a set of axes. Mechanical tension and strain are defined as tensors, and they are expressed as a 3×3 matrix. Three coordinates are used to express the normal stresses and six coordinates the shear stresses. With regard to the reference condition $\Delta \mathcal{G} = 0$, $E_{j0} = 0$, $T_{\mu 0} = 0$, the definition of the Gibbs energy provides the linear coupled equations^{77,78}:

$$D_i = p_i^T \Delta \mathcal{G} + \varepsilon_{i,j}^{\mathcal{G},T} E_j + d_{i,\mu}^{\mathcal{G}} T_\mu \quad (8)$$

$$S_\lambda = \alpha \lambda^E \Delta \mathcal{G} + d_{j,\lambda}^{\mathcal{G}} E_j + s_{\lambda,\mu}^{\mathcal{G},E} T_\mu \quad (9)$$

Values that remain constant during the derivation are indicated by superscripts. The superscript T indicates a zero or constant stress field and the superscript E indicates a zero or constant electric field. For the isothermal case $\Delta \mathcal{G} = 0$, the behaviour of dielectric materials under an electric field vector $\{E_{field}\}$ is expressed by the simplified matrix equations for the direct and reverse piezoelectric effect, respectively, as below:

$$\{D\} = [\varepsilon^T] \{E_{field}\} + [d] \{T\} \quad (10)$$

$$\{S\} = [d] \{E_{field}\} + [s^E] \{T\} \quad (11)$$

The dielectric displacement vector $\{D\}$ is composed of the dielectric shift $[\varepsilon^T] \{E_{field}\}$ and a mechanical loading vector $\{T\}$ applied on the piezoelectric coefficient matrix $[d]$. The permittivity matrix $[\varepsilon]$, or the relative dielectric matrix is a measure of the polarizability of the material. The permittivity is dependent on the electric field, thereby resulting in a nonlinear behaviour (of the large-signal). The second equation above expresses the strain vector $\{S\}$ that is developed in a piezoelectric element when the electric field vector $\{E_{field}\}$ acts on

the piezoelectric coefficient matrix [d] of a piezoelectric material and when a mechanical loading {T} is applied on a body with the compliance matrix [s].

In general, the elastic, dielectric, and piezoelectric constants of piezoelectric materials are directional as the materials are polarized in one direction; thus, they are anisotropic. In the matrix equations below, the material constants are twice subscripted with reference to a set of axes as depict in Figure 11; the numeral 3 indicates the direction of positive polarization, and 1 and 2 indicate the perpendicular axes. The properties along plane 1 and 2 are isotropic. The indices 4, 5, and 6 refer to shear stress along axes 1, 2, and 3, respectively.

The subscripts have two indices; the first index depends on the direction of the material constant and the second index depends on the direction of the applied loading (electric field, mechanical tension, or strain). Hooke's law provides the relationship between strain and stress via the elastic stiffness [c] and Young's modulus [E]:

$$\{T\} = [c]\{S\} = [E]\{S\} \quad (12)$$

Piezoelectric materials that are used for actuating applications are often lead zirconate titanate ($\text{Pb}[\text{Zr}_x\text{Ti}_{1-x}]\text{O}_3$ $0 \leq x \leq 1$) based materials. Such PZT materials *"have the same matrix elements as piezoelectric crystals that belong to hexagonal class 6 mm symmetry, for which the same coefficients as those for the 4-mm non-oriented polycrystalline material poled in the third direction are needed"*⁹⁴. This results in five independent elastic compliance constants [s], three independent piezoelectric charge constants and two dielectric constants (Voigt notation) that are related by the following expressions:

$$\begin{bmatrix} S_1 \\ S_2 \\ S_3 \\ S_4 \\ S_5 \\ S_6 \end{bmatrix} = \begin{bmatrix} s_{11}^E & s_{12}^E & s_{13}^E \\ s_{12}^E & s_{11}^E & s_{13}^E \\ s_{13}^E & s_{13}^E & s_{33}^E \\ & & & s_{44}^E \\ & & & & s_{44}^E \\ & & & & & 2(s_{11}^E - s_{12}^E) \end{bmatrix} \begin{bmatrix} T_1 \\ T_2 \\ T_3 \\ T_4 \\ T_5 \\ T_6 \end{bmatrix} + \begin{bmatrix} d_{31} \\ d_{31} \\ d_{33} \\ d_{15} \\ d_{15} \\ d_{15} \end{bmatrix} \begin{Bmatrix} E_1 \\ E_2 \\ E_3 \end{Bmatrix} \quad (13)$$

$$\begin{bmatrix} D_1 \\ D_2 \\ D_3 \end{bmatrix} = \begin{bmatrix} & & & d_{15} \\ & & & d_{15} \\ d_{31} & d_{31} & d_{33} & \end{bmatrix} \begin{Bmatrix} T_1 \\ T_2 \\ T_3 \\ T_4 \\ T_5 \\ T_6 \end{Bmatrix} + \begin{bmatrix} \varepsilon_{11} & & \\ & \varepsilon_{11} & \\ & & \varepsilon_{11} \end{bmatrix} \begin{Bmatrix} E_1 \\ E_2 \\ E_3 \end{Bmatrix} \quad (14)$$

The elastic compliance matrix in Eq. (13) can further be assigned with the Poisson's ratio ν and Young's modulus and shear modulus G_{ij} as follows:

$$[s] = \begin{bmatrix} \frac{1}{E_1} & \frac{-\nu_{12}}{E_2} & \frac{-\nu_{13}}{E_3} & & & \\ \frac{-\nu_{21}}{E_2} & \frac{1}{E_2} & \frac{-\nu_{23}}{E_3} & & & \\ \frac{-\nu_{13}}{E_3} & \frac{-\nu_{23}}{E_3} & \frac{1}{E_3} & & & \\ & & & \frac{1}{G_{12}} & & \\ & & & & \frac{1}{G_{12}} & \\ & & & & & \frac{1}{G_{13}} \end{bmatrix} \quad (15)$$

Piezoelectric elements are at times modelled with isotropic materials due to the lack of elastic material properties. This is also true for the case of analytical modelling of certain components such as piezoelectric benders or piezoelectric unimorph membranes. For isotropic materials, the matrix can be further reduced to only two parameters—Young's modulus E and the Poisson's ratio ν .

$$E_1 = E_2 = E_3 = E \quad (16)$$

$$\nu_{13} = \nu_{12} = \nu_{23} = \nu \quad (17)$$

$$[s] = \frac{1}{E} \begin{bmatrix} 1 & -\nu & -\nu & & & \\ -\nu & 1 & -\nu & & & \\ -\nu & -\nu & 1 & & & \\ & & & 2(1+\nu) & & \\ & & & & 2(1+\nu) & \\ & & & & & 2(1+\nu) \end{bmatrix} \quad (18)$$

4.2 Layer deposition

Piezoelectric actuators can be deposited on mirror substrates by means of several techniques including the jointing of piezoelectric disks and several direct application techniques of thick film layers. These include modified sol-gel, doctor-blade, ink-jet, and screen printing methods. Thin film techniques have also been proposed, but they are not suitable for manufacturing multi-material deformable unimorph mirrors. This is explored fully in the simulations section.

4.2.1 Jointing of piezoelectric disks

Jointing of piezoelectric disks is the assembly of sintered and cut piezoelectric plates with a mirror substrate. The commercially available plates are cut to shape using a wafer saw, a laser or by means of ultrasonic milling. Subsequently, they are assembled manually or via assembling robots. This is a very widespread technique; however, with decreasing disk dimensions and disk thicknesses, the labour input and costs increase significantly. Further, the adhesive jointing between the substrate and piezoelectric layer can become complicated under extremely low outgassing or temperature application.

4.2.2 Direct thick film application

Direct thick film application techniques provide excellent adhesion between the substrate and the active layer as the thick films are sintered directly with the substrate. A primary issue is the sintering of piezoelectric film, substrate, and metallization due to the thermal mismatch of different materials and the lateral clamping of the applied layers. Another challenge can arise due to chemical reactions with the substrate material and lead-oxide (PbO)-loss in the piezoelectric layer. The development of low sintering material systems minimizes these risks.

Direct application by sol-gel coating is the deposition of suitable materials in form of a mixture of suspended precursor materials⁷⁹. Piezoelectric layers are fabricated through piezo-ceramic powder that is present in a metal organic precursor. The material is applied via spin-coating or dip-coating covering the whole area on the substrate and subsequently structured by etching processes⁸⁰.

Another technique is the application of piezoelectric films by tape casting. Slurry composed of low-sintering piezoelectric powder and organic additives are applied onto a metalized substrate surface by doctor blade. Thick films can be obtained by multiple coating. Several layers of piezoelectric material are deposited on the metalized substrate and then laminated and sintered at elevated temperatures. Subsequently, the piezoelectric films are laser-structured⁸⁶.

These direct application techniques require an additional structuring step. Techniques that feature inherent structuring are ink-jet printing and screen printing. The ink-jet technology deposits slurry with ultrafine piezoelectric particles onto a surface by means of a high-speed jet stream. The nozzle moves over the surface, thereby directly writing the actuator or met-allization layouts. Functional materials are deposited using drop-on-demand (DoD) systems, thereby optimizing the use of costly materials and enabling fine line-widths. The slurry is dried on the substrate at elevated temperatures. Schroth proved the actuation capability of ink-jet-printed piezoelectric layers in his study in 1997⁸¹. Subsequent investigations of different PZT suspensions suitable for DoD and continuous printing have since been carried out^{82,83}. The major advantage of ink-jet technology is its sub-nanoliter voxel resolution; however, the method is not suitable for deposition of thick films as the drop volume is very small. Typical film thicknesses are around 10 μm and below. The deposition of thick films with thicknesses of around 100 μm would be possible with this technology, but the process would be time consuming, impractical, and costly. For ink-jet printing, no single complete technology solution that can be used for the deformable unimorph mirror system is currently available.

4.2.3 Screen printing

Screen printing is a widespread technique in the manufacturing of thick film hybrid microelectrical systems. The material to be deposited by screen printing is referred to as ink or paste^{84,79}. A screen is positioned over the substrate and a squeegee blade is passed over it. The squeegee blade forces the paste through the screen openings onto the substrate. The deposited material is subsequently dried

to remove the volatile solvent components. Next, it is fired to burn away the organic binder, and the material is sintered. The sintering involves chemical reactions that form the final film, thereby providing substrate adhesion and ensuring film density. This technique is suitable for mass production as it can be used to fabricate large, accurate patterns of material with well-defined dimensions at high repeatability rates. Further, it is possible to screen-print different actuator mirror layouts onto one substrate. The selected process parameters define the achieved accuracy and layer thicknesses. The minimum feature sizes of the screen-printing process are line widths of $<80\ \mu\text{m}$ in the field of electronics and $<30\ \mu\text{m}$ in electrical circuits with a web width of $<30\ \mu\text{m}$ ⁸⁵. Layer thicknesses between $10\ \mu\text{m}$ and $300\ \mu\text{m}$ can be achieved via screen printing. Printing of thick film conductors, resistors, dielectrics, and inductors on different substrates is a standard process. The development of piezoelectric pastes with high actuating capability has been the focus of several research groups for the past 20 years^{86,87,88,89,91} since Baudry provided working proof of the principle in 1987⁹⁰. He screen-printed piezoelectric paste onto alumina substrates for use as a loud speaker. Recent commercially available substrates include silicon, fused silica, metal, and different ceramics such as Al_2O_3 , LTCC, AlN , and ZrO . An additive printing process achieves fired piezoelectric film thicknesses between 20 and $150\ \mu\text{m}$ ⁹¹ and ceramic substrates with thicknesses down to $150\ \mu\text{m}$ have been processed.

The characteristics of the screen-printing process in combination with the availability of piezoelectric pastes with high actuating capabilities have made screen-printing techniques popular for use in the fabrication process of deformable mirror systems. The DMs in this study use the screen-printed piezoceramic thick film PZ 5100 that has a lead zirconate titanate base ($\text{PbZr}_{1-x}\text{Ti}_x\text{O}_3$ or PZT). These films are low sintering pastes obtained through addition of a low sintering eutectic oxide and a borosilicate glass to a PZT-PMN powder. PZT thick film actuator structures are basically prepared using the following procedure (S. Gebhardt, personal communication, December 1, 2011):

1. Screen printing and sintering of bottom electrode at $T_s = 850\text{ }^\circ\text{C}/0.17\text{ h}$.
2. Multiple screen printing (3–5 times according to designated film thickness) of PZT thick film. Sintering at $T_s = 900\text{ }^\circ\text{C}/2\text{ h}$.
3. Repetition of multiple screen printing (3–5 times according to designated film thickness) of PZT thick film. Sintering at $T_s = 900\text{ }^\circ\text{C}/2\text{ h}$.
4. Multiple screen printing and sintering (at least two times) of isolation layers at $T_s = 850\text{ }^\circ\text{C}/0.17\text{ h}$.
5. Screen printing and sintering of top electrode at $T_s = 850\text{ }^\circ\text{C}/0.17\text{ h}$.

4.3 Evaluation of screen-printed material characteristics

The effective material parameters of screen-printed devices depend not only on the starting material composition but also on the application regime, sintering conditions, the compatibility of the film with the sandwiching electrodes, and the substrate material. Moreover, there is little available data on the screen-printed piezoelectric thick film PZ 5100 and screen-printed metallization layers of bottom and top electrode with respect to the material parameters. Therefore, a primary challenge is the population of the piezoelectric equations with reliable data. The thick film layers are too small and brittle to use the standard ANSI/IEEE methods^{92,72}. For the accurate prediction of actuator capability, the complete set of piezoelectric, mechanical, and electrical characteristics are needed as the usability of simulation models increases with increasing material data.

Standard literature provides a few details on the determination of the material parameters of screen-printed thick films; Zarnik et al.^{93,94} have studied the numerical modelling of piezoelectric actuators and measured the mechanical and piezoelectric material parameters by nanoindentation and standard resonance methods. Standard resonance measurements are not suitable for thick films as the standard measurement geometries cannot be manufactured. The nanoindentation and standard resonance measurements achieve identical results in the case of piezoelectric bulk material. The effects of mechanical loading of the piezoelectric ceramic caused by the diamond during nanoindentation do not result in a significant electrical charge (direct piezoelectric effect), or stiffness

modification of the piezoelectric thick film. This suggests nanoindentation as an appropriate technique for evaluating the compliance of piezoceramic thick films. Zarnik et al.⁹⁴ printed PZT paste (53/47) onto Al₂O₃ substrates fired to a thickness of 38–45 μm. They prepared cantilever test samples, and they used a nanoindentation method and an adapted substrate-flexure method for the determination of the Young's modulus and of the piezoelectric coefficient d_{31} , respectively. The Young's modulus was measured at the surface of the film after the upper electrode was carefully rubbed after poling. The Poisson's ratio was obtained from the bulk material, and it was used to calculate the Young's modulus from the indentation module. The authors defined this modulus as the elastic stiffness along polarization c_{33}^D since there was no electrical load. They used the piezoelectric bulk material ratios to calculate s_{33}^E from c_{33}^D , and the other stiffness parameters. The piezoelectric transverse coefficient $e_{31,f}$ was determined by stretching the cantilever and measuring the generated electric charge. The work also includes a parametric numerical study showing the insensitivity of the cantilever stroke to variations in d_{33} and d_{51} that can only roughly be estimated. The measured Young's modulus along the thickness/poling direction of the piezoelectric film is reduced by 50 % in comparison to the bulk material with the same composition⁹⁴. Additionally, the measured Young's modulus shows a high standard deviation. This is most probably caused by the high porosity of the film. The authors also confirmed the influence of the substrate material on the film, and they showed⁹³ that the compliance of the piezoelectric thick film on LTCC is nearly doubled for Al₂O₃. The population of the FEM models with the measured and approximated material parameter results in good agreement between the experimental measurements and numerical simulations for static and dynamic deflection.

Walter et al. carried out a comparative study determining the Young's modulus of two different screen-printed piezoelectric thick films on Al₂O₃ measured by three different mechanical characterization tests^{95,96}. They tested hard and soft piezoelectric thick films using dynamic, quasi-static, and nanoindentation tests. The soft-PZT paste was deposited by the Fraunhofer IKTS and the hard-PZT paste was deposited by LGEF in Lyon. The measured porosity was 5% and 50%

for the soft-PZT film and the hard-PZT film, respectively. Again, the porosity in this case causes the Young's modulus to decrease when compared with that of the bulk ceramic. The authors estimated a Poisson's ratio of $\nu = 0.3$ for the substrate and piezoelectric layer and the density of the bottom electrode as 19.3 g/cm^3 . The effects of the porosity of the metallization layer caused by the screen-printing process are not taken into account. The authors provide no values for the density of the piezoelectric layer. The results for the measured Young's modulus of the soft-PZT film were: $E_{\text{dynamic}} = 51.5 \pm 9 \text{ GPa}$, $E_{\text{static}} = 52.8 \pm 8 \text{ GPa}$, $E_{\text{nano}} = 66 \pm 22 \text{ GPa}$. The authors also measured $d_{31} = -120 \pm 5 \text{ pC/N}$ by detecting the free deflection of the sample cantilever using the formulae derived by Smits⁹⁷. Consequently, they applied an electric field and measured the cantilever deflection with and without mechanical loading. Sivanandana⁹⁸ uses a similar approach in evaluating the transverse piezoelectric property e_{31}^* of a screen-printed piezoelectric thick film on alumina by measuring the piezoelectric deflection of PZT/alumina unimorphs (L = cantilever length, h = substrates thickness):

$$e_{31}^* = \frac{d_{31}}{s_{11, \text{film}}^E} \cong \frac{h_{\text{substrate}}^2}{3s_{11, \text{substrate}} L^2} \frac{\delta}{V} \quad (19)$$

Torah et al.⁹⁹ investigated the clamping effect of piezoelectric thick films screen-printed onto a substrate. They conducted a theoretical formulation of the clamping effect, and they confirmed the decrease in the measured d_{33} due to the device being fixed onto the substrate and therefore, due to the clamping of the piezoelectric device. Simon et al.¹⁰⁰ compared piezoelectric thick film characteristics with bulk ceramics, and they explained the differences with respect to the residual porosity of the films and the lateral clamping of the substrate. The effect of the residual porosity on density and permittivity can be reduced by applying uniaxial pressure on the film during manufacturing. The lateral clamping effect of screen printed thick films is higher for material with large coupling factor and large piezoelectric coefficient (d_{31}).

Banno¹⁰¹ theoretically investigated the relationship between porosity and change in material properties by a homogeneous distribution of the pores and a random

shape-orientation. Zeng et al.¹⁰² investigated the influence of porosity and pore shape on the properties of porous PZT 95/5 ceramics. They experimentally showed the decrease in the piezoelectric coefficient (d_{33}), dielectric constant (ϵ_{33}), and remnant polarization (P_r) with increase in porosity. Moreover, spherical porous PZT ceramics exhibit better material properties than ceramics with irregular pores, e.g., they exhibit a higher Young's modulus due to lower microstress. The application of the developed formulae is restricted by the limited knowledge of bulk material characteristics.

4.3.1 Experimental investigation of screen-printed layer characteristics

Designed sample structures are subsequently fabricated by IKTS, Dresden. They were obtained to measure the material characteristics of the screen-printed actuator layers on different substrates (cf. Figure 14). Different cantilever and circular patterns on LTCC and Al_2O_3 were screen-printed. The substrate wafers were laser-cut for singularization of the single sample structures. The PZT thick films have a thickness of $t_p = 100 \mu\text{m}$ and the thickness of the substrates is $t_s = 250 \mu\text{m}$ for Al_2O_3 . All structures were poled at room temperature for two minutes at 2 kV/mm.

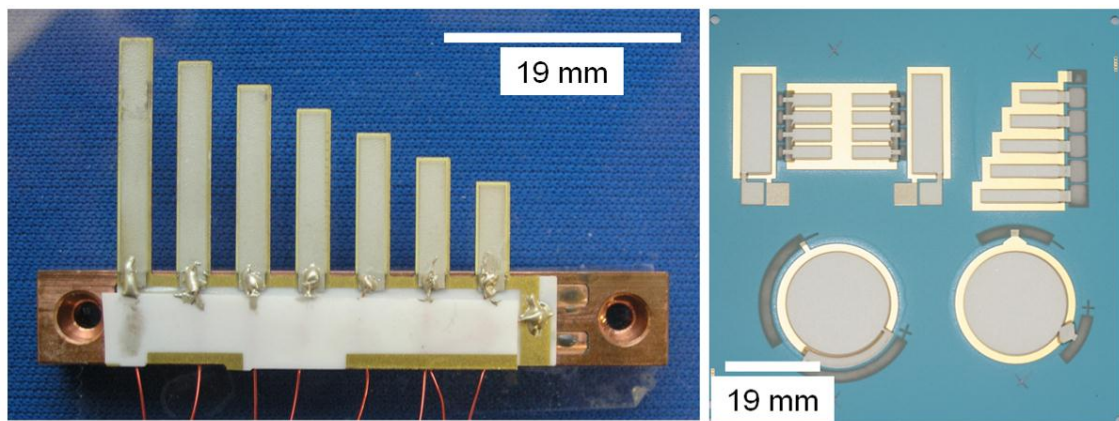


Figure 14 Screen-printed sample structures: (a) singularized piezoelectric cantilever with different cantilever lengths on Al_2O_3 substrate and (b) different screen-printed cantilever and circular membrane structures on LTCC before singularization.

I obtained microscopic images of the surface's top view and cross-sectional view (cf. Figure 15) for two sample cantilevers in order to investigate the layer thickness of the piezoelectric thick films, the metallization thick film, and the

substrates. The microscopic images are obtained on polished surfaces with a magnification of 20 (cf. Figure 16). The microscopic measurements reveal a thickness of $206.9 \mu\text{m} \pm 5.0 \mu\text{m}$ for the LTCC substrate. The bottom metallization thickness is $6.7 \mu\text{m} \pm 0.7 \mu\text{m}$ and $7.7 \mu\text{m} \pm 1.5 \mu\text{m}$ for LTCC and Al_2O_3 , respectively.

Measurements of the density for screen-printed thick films were also carried out with these sample structures. The screen-printed thick films were relieved from the substrate by using hydrofluoric acid, and subsequently rinsed with deionized water and dried. Hydrofluoric acid etches not only the gold thick film but also the PZT thick film. This is why the residence time is generally kept as short as possible.

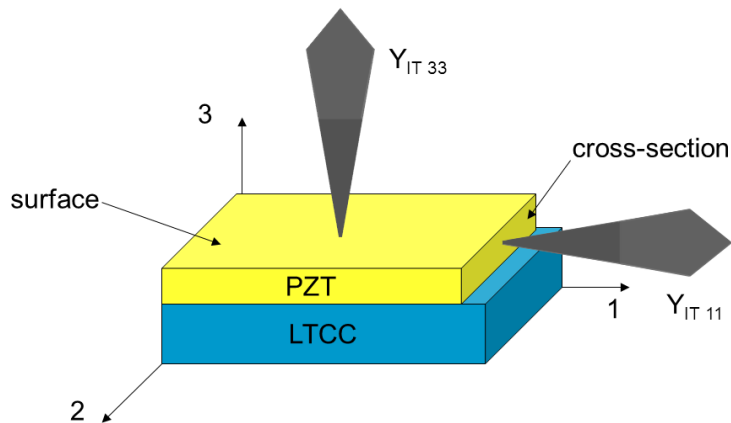


Figure 15 Schematic of the screen-printed sample structures: surface and cross-section.

In addition, the PZT thick film is cut and polished, thereby cancelling the variation in dimensions and the zone of influence of hydrofluoric acid. The substrates were also cut and polished while the metallization layer was recovered only from the substrate and cleaned, as its small thickness ($\leq 10 \mu\text{m}$) could not be polished. The substrate and metal films were measured for thickness and lateral dimensions with a gauge and microscope, respectively. The weight of the different samples was measured using a high-precision balance, and the density was calculated by using the weighing and cubature method.

The measurement by the weighing and cubature method provided a density of 3.2 g/cm^3 for the LTCC (DP 951) substrate. The manufacturer-specified value was 3.1 g/cm^3 , and this difference corresponds to a deviation of less than 3% between

the specification and the measurement. Therefore, the validity and applicability of this measurement method was confirmed.

Metallization layer

The measured density ρ of the thick film gold electrode on LTCC was 14.8 g/cm³, while the theoretical density ρ_0 of gold was 19.3 g/cm³. This corresponds to a porosity P of 23.3% and a decrease in Young's modulus from 78 GPa to 48.5 GPa by using the following expressions:

$$P = 1 - \frac{\rho}{\rho_0} \quad (20)$$

$$Y_{film} = Y_{Bulk} (1 - P^{2/3}) \quad (21)$$

This linearized model¹⁰³ does not consider the effect of morphology and pore geometry. The effective shape factor of the particles is assumed as unity. The change in Poisson's ratio is evaluated by:

$$\nu_{film} = \nu_{Bulk} (1 - P^{2/3}) \quad (22)$$

This evaluation leads to a decrease from 0.42 to 0.26 for the Poisson's ratio. The calculated porosity values need to be carefully considered as the hydrofluoric acid etches not only the gold but also other components in the gold layer and not necessarily in the same ratio as they occur. Another important point to consider is the small physical dimensions of the samples, particularly in thickness. Density measurement values can also be obtained by Archimedes' principle and a pycnometer. The problem in this case is again the release of the sintered thick film from the substrate. The screen-printed metallization layers are very thin, and their impact of porosity-induced changes to the Young's modulus, Poisson's ratio, and density on the deflection and resonance behaviour can be neglected. The bulk values of the coefficient of thermal expansion (CTE) are valid for screen-printed layers as this property does not depend on porosity¹⁰⁴. The influence of porosity on heat capacity is not specified for screen-printed thick films. The thermal conductivity of screen-printed metallization layers have been specified at $\kappa = 70 \text{ Wm}^{-1}\text{K}^{-1}$ and $\kappa = 130 \text{ Wm}^{-1}\text{K}^{-1}$ for Au¹⁰⁵- and Au/Pt¹⁰⁶-films. The

thermo-mechanical properties of the screen-printed gold layer are summarized at the end of this chapter in Table 9.

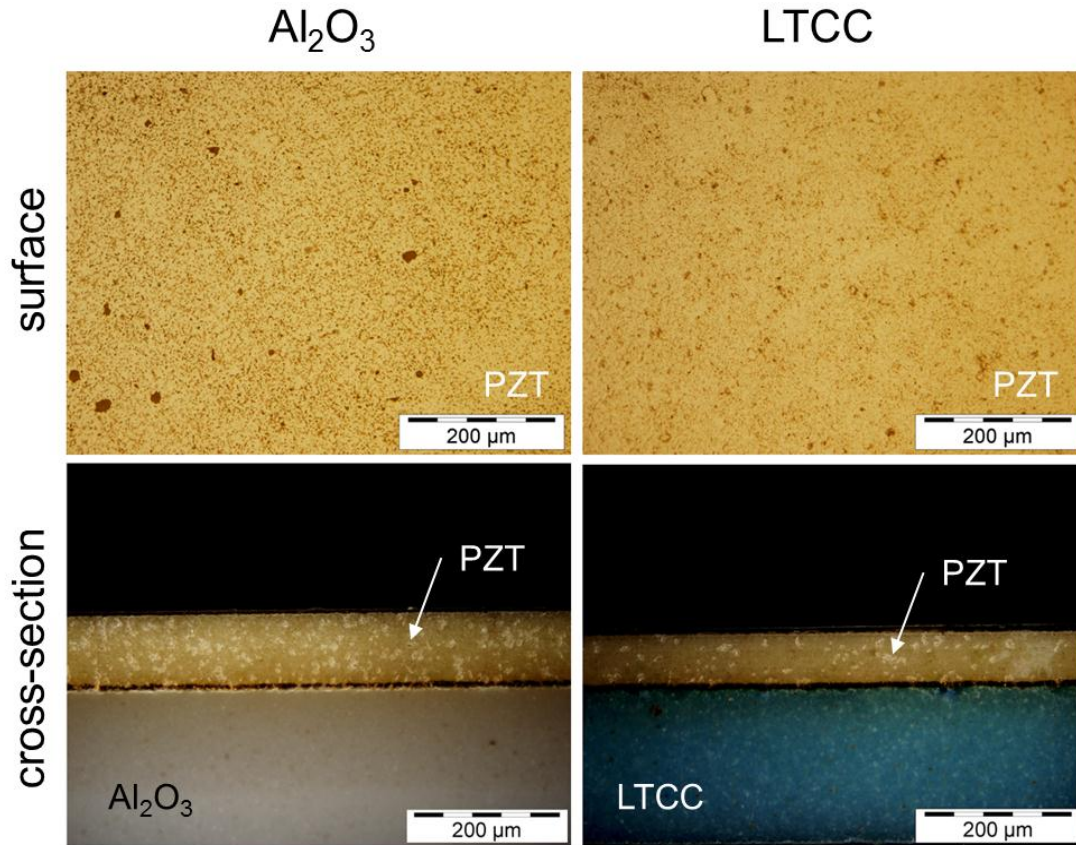


Figure 16 Microscopic images of polished piezoelectric thick film samples on Al_2O_3 and LTCC substrates.

PZ 5100 layer

Figure 17 shows the schematic of the evaluation of the material characteristics of screen-printed piezoelectric thick films using the measurements of the film density and indentation modulus along surface Y_{it33} and cross-section Y_{it11} . The density and the ratio of the indentation modulus are compared with bulk data in order to identify the corresponding bulk material characteristics.

The Young's moduli E_{11} and E_{33} are calculated by nanoindentation measurements and by an educated guess of the Poisson's ratio. The Young's moduli values are compared with the stiffness parameter of different piezoelectric bulk and glass materials. Therefore, the crystal symmetry of the piezoelectric thick film material is assumed to be identical to that of the bulk material⁹⁴. The full stiffness matrix

is calculated by taking the same value for the ratio between elastic stiffness components c_{ij}^D ($i, j = 1, \dots, 6$) components for both the thick films and the bulk. The ratio d_{31}/d_{33} of the bulk material is calculated, and it is used to determine d_{31} from the measured thick film's d_{33} value from the literature data. The measurement data of the electrical properties of the screen-printed thick film and the piezoelectric bulk material are available from the literature, and they are used to obtain the complete piezoelectric thick film material characteristics.

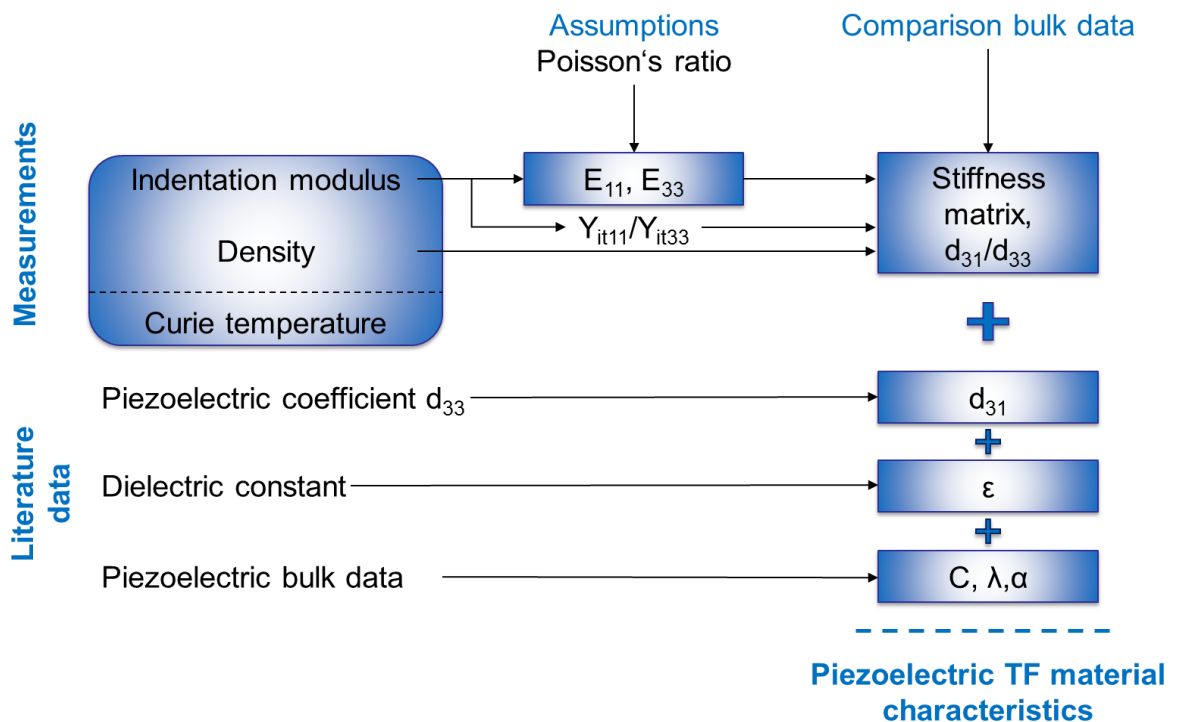


Figure 17 Schematic of the evaluation of the material characteristics of piezoelectric thick films based on measurements and comparison with piezoelectric bulk data.

The density of the piezoelectric layer is measured by the weighing and cubature method. The measurements reveal a PZ 5100 layer density of 5.94 g/cm^3 and 6.16 g/cm^3 for screen-printed piezoelectric layers on Al_2O_3 and LTCC substrates, respectively. Measurements of the closed porosity of screen-printed PZT showed a value of $8.5 \text{ vol. } \%^{107}$ for alumina substrates; this value amounts to a corresponding theoretical density ρ_0 of 6.49 g/cm^3 for the PZ 5100 layer on Al_2O_3 using equation (20). The expected values for the theoretical density ρ_0 are approximately 7.60 g/cm^3 (S. Gebhardt, personal communication, December 1,

2011) and are considerably higher than the measured values. The density measurements of the PZ 5100 layer as obtained by the weighing and cubature method suffer from dimensional uncertainties as the post-measurement samples show pitting in the polished PZ 5100 layer (cf. Figure 16). As in the case of the metallization layer, the release of the layer by hydrofluoric acid can also lead to lower measured densities. The sample volume also is small; however, this can lead to a lower measured density of the thick film. Further, material variations composition is also conceivable.

Measurements of the indentation modulus of the screen-printed thick film PZ 5100 on LTCC and Al₂O₃ substrates are obtained using the MTS NanoIndenter G200 with a diamond Berkovich tip. The samples are prepared, and they are measured for cross-section polish and surface polish (cf. Figure 15). The Berkovich indenter tip is forced onto the piezoelectric material and the resulting load-deflection curve is used to calculate the indentation modulus Y_{it} based on DIN EN ISO 14577 standards. The indentation modulus is related to the Young's modulus E as follows:

$$E = \frac{Y_{it}}{1 - \nu^2} \quad (23)$$

A reliable measurement set-up needs special requirements. The maximum penetration depth needs to be less than the piezoelectric layer thickness ($h_{\max} < 0.1 t_p$) and greater than the surface roughness R_a ($h_{\max} > 20R_a$). The film must be sufficiently thick to overcome the influence of the substrate's stiffness. The measurements show a penetration depth smaller than 5 μm and thus less than 5% of the substrate's thickness. The influence of the substrate stiffness on the measurement results can be neglected. The distance between the rim of the specimen and indentation needs to be at least 5 times the indentation diameter. The test is repeated 10–20 times for different loads of 25 mN, 50 mN, and 75 mN along the cross-section. The results are shown for Al₂O₃ (Table 2) and LTCC (Table 3).

As seen from the tables, both thick films show decreasing Y_{IT11} values and decreasing deviation with increasing probe load. The average Y_{IT11} values are 74.8 GPa and 79.9 GPa for Al₂O₃ and LTCC, respectively. The graphical

representation shows that the confidence region overlaps for both materials (cf. Figure 18). The indentation modulus measured for a force of 75 mN is used for further calculations. The Young's modulus is calculated for Poisson's ratios of $\nu = 0.2$ and $\nu = 0.3$, thereby leading to values between 70 GPa and 74 GPa for LTCC, and between 64 GPa and 68 GPa for Al_2O_3 .

Table 2 Measured indentation modulus of screen printed PZT thick film on Al_2O_3 substrate in cross-section¹⁰⁸.

Indentation force [mN]	25	50	75
No. of measurements	20	10	20
Indentation modulus Y_{IT} [GPa]	$79.4 \pm 15,9$	74.4 ± 11.5	70.6 ± 5.9
Young's modulus E_{11} [GPa], $\nu=0.2$	$76.2 \pm 14,5$	71.4 ± 11.0	67.8 ± 5.7
Young's modulus E_{11} [GPa] $\nu=0.3$	72.2 ± 13.7	67.0 ± 10.4	64.3 ± 5.4

Table 3 Measured indentation modulus of screen printed PZT thick film on LTCC substrate in cross-section¹⁰⁸.

Indentation force [mN],	25	50	75
No. of measurements	20	10	20
Indentation modulus Y_{IT} [GPa]	81.4 ± 17.8	81.6 ± 13.5	76.7 ± 8.2
Young's modulus E_{11} [GPa], $\nu=0.2$	78.2 ± 17.1	78.3 ± 13.0	73.6 ± 7.9
Young's modulus E_{11} [GPa], $\nu=0.3$	74.1 ± 16.2	74.2 ± 12.3	69.8 ± 7.5

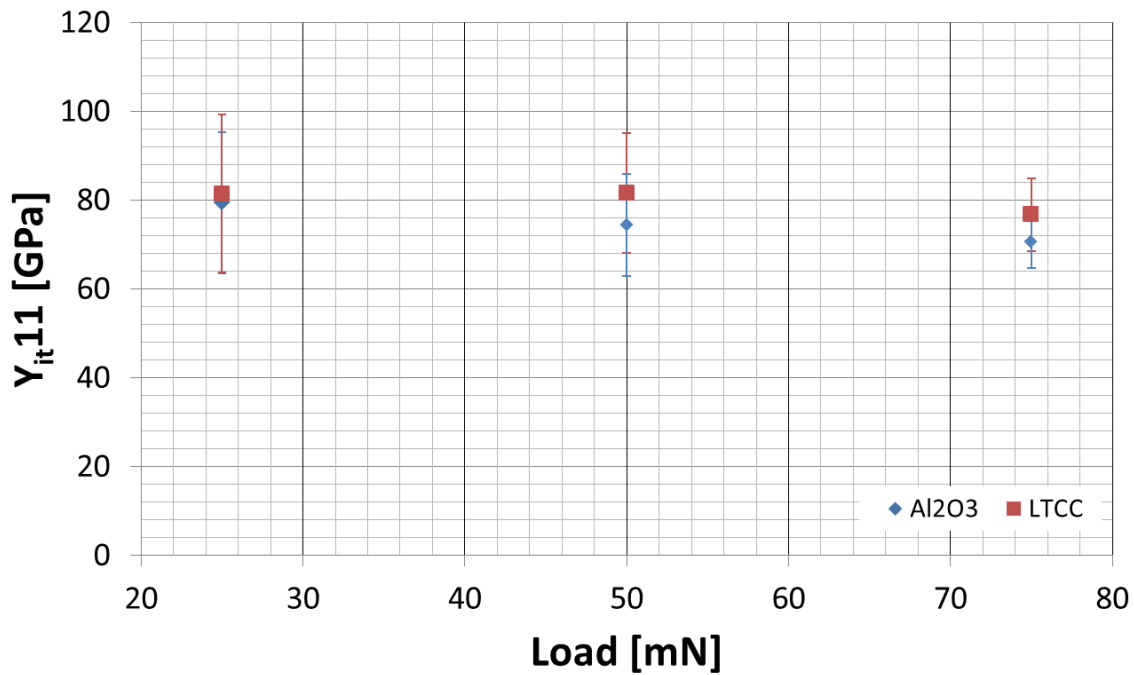


Figure 18 Measured indentation modulus in cross-section.

The indentation modulus on the surface of the piezoelectric material is measured over 10 trials with a loading of 250 mN for both substrates (cf. Table 4 and Table 5). The surface is again polished for reduction in surface roughness and its effects on measurement deviation. The measurements for each substrate were carried out separately for two different Poisson's ratios of $\nu = 0.2$ and $\nu = 0.3$.

Table 4 Measured indentation modulus for surface of screen-printed PZT thick film on Al₂O₃ substrate¹⁰⁸.

Indentation force [mN]	250	250
Number	10	10
Indentation modulus Y_{IT} [GPa]	66.0 ± 10.8	62.9 ± 11.1
Poisson's ratio ν	0.2	0.3
Young's modulus E_{33} [GPa]	63.4 ± 10.4	57.2 ± 10.1

Table 5 Measured indentation modulus for surface of screen-printed PZT thick film on LTCC substrate ¹⁰⁸.

Indentation force [mN]	250	250
Number	10	10
Indentation modulus Y_{IT} [GPa]	62.1 ± 2.7	60.9 ± 4.8
Poisson's ratio ν	0.2	0.3
Young's modulus E_{33} [GPa]	59.6 ± 2.6	55.5 ± 4.4

The measurements reveal that the indentation modulus varies slightly between the two measurements of the same material but the different Poisson's ratios; however, the calculated deviation permits a comparison. A comparison between the measurements along the cross-section and on the surface reveals a higher stiffness in cross-section.

The screen-printed thick film is composed of lead zirconate titanate ($PbZr_{1-x}Ti_xO_3$ - PZT), and Bi_2O_3/ZnO and a borosilicate glass are added in order to reduce the original sintering temperature from $T_s = 1200$ °C down to 950 °C¹⁰⁹. If the quantity of the additives are small and homogeneously distributed and thus not modifying the mechanical properties one can calculate the modifications in compliance (and piezoelectric coefficients) due to the grade of borosilicate glass and porosity by the following equations^{101,110}:

$$s_{11_film} = \frac{s_{11_bulk}}{(1 - P^{2/3})} \quad (24)$$

$$s_{33_film} = \frac{s_{33_bulk}}{(1 - P^{2/3})} \quad (25)$$

$$s_{12_film}^E = -s_{11_film}^E g_{film} \quad (26)$$

No data about the actual material composition or borosilicate content of the piezoelectric thick films were available. Therefore, I attempted an identification of the corresponding piezoelectric bulk material by comparison of the material characteristics. I compared the density, c_{11} , c_{33} , and the ratio Y_{11}/Y_{33} of different piezoelectric bulk materials with the measured values of the screen-printed piezoelectric material. The piezoelectric bulk materials include two different lead

titanate zirconate compositions⁷¹ $\text{Pb}(\text{Ti}_{0.48}\text{Zr}_{0.52})\text{O}_3$ (abbreviated form 48/52) and $(\text{Pb}_{0.94}\text{Sr}_{0.06})(\text{Ti}_{0.47}\text{Zr}_{0.53})\text{O}_3$ (abbreviated form 47/53) and lead titanate zirconate materials from Pi Ceramic GmbH (PIC 255, PIC 151). The complete material data for PIC 151 and PIC 255 are shown in the appendix A2 and A3, respectively. The materials from CeramTec (Sonox P505, P51, P53)^{111,112} and Morgan Electro Ceramics (PZT-5H)¹¹³ as well as borosilicate glass also are used for comparison.

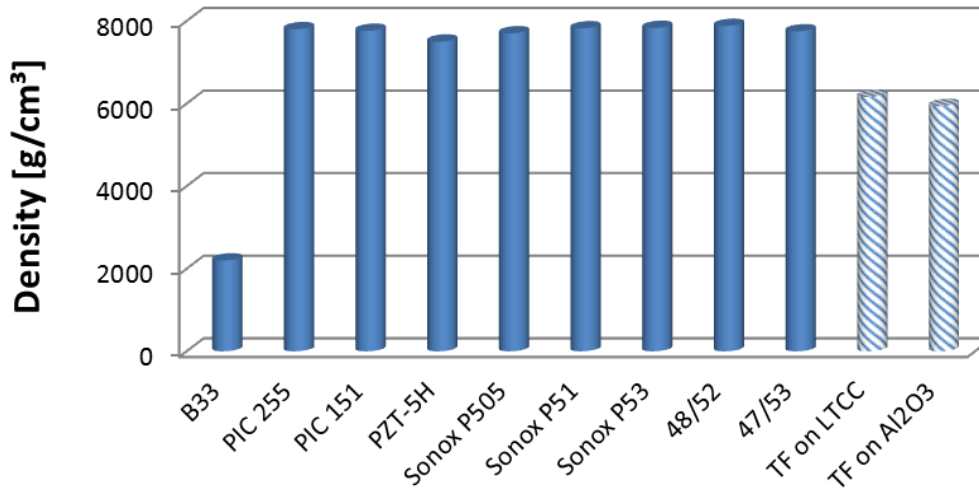


Figure 19 Identification of suitable material by comparison of measured data of PZT thick film (TF) with available material.

The comparison of the density reveals that all the piezoelectric bulk materials have a higher density than the screen-printed layer and the borosilicate glass (cf. Figure 19). In agreement with the rule of mixture, the density decreases with increasing borosilicate glass or porosity content.

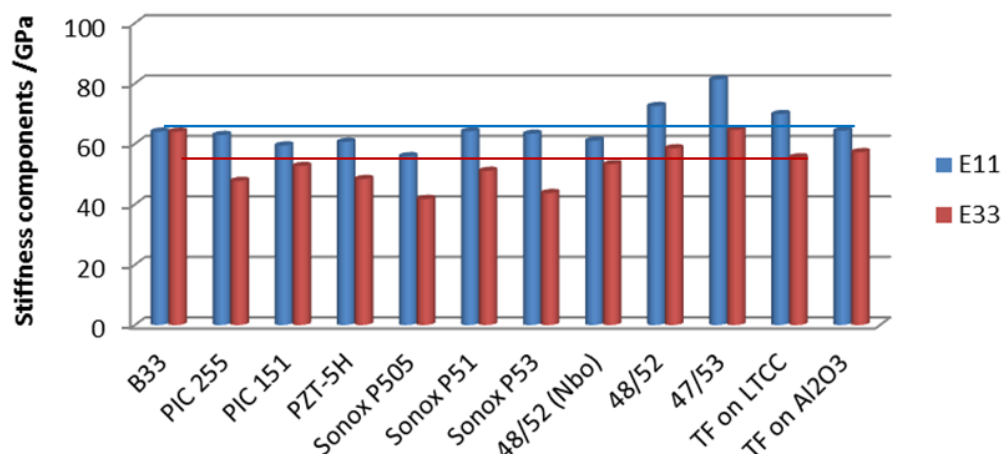


Figure 20 Comparison of measured stiffness of PZT thick films (TF) with material characteristics of bulk materials. Poisson's ratio is assumed to be 0.3.

The second criterion is that the measured stiffness of the screen-printed film ($E_{11film}=C_{11film}$ and $E_{33film}=C_{33film}$) needs to be smaller than that of the bulk material. Figure 20 depicts the comparison results. The criterion $E_{bulk} > E_{film}$ limits the selection to 48/52 and 47/53 as all other bulk values show small stiffness values. The third criterion relies on the ratio of the stiffness components (cf. Figure 21). The ratio of the indentation modulus for the cross-section to surface is equal to the cross-section to surface ratio of the films Young's modulus (at a constant Poisson's ratio). The same cross-section to surface ratio applies to the Young's modulus of the bulk material:

$$\frac{Y_{IT33}}{Y_{IT11}} = \frac{E_{33film}}{E_{11film}} \cong \frac{E_{33bulk}}{E_{11bulk}} \quad (27)$$

For the determination of the ratio of the stiffness components (stiffness ratio), the indentation moduli obtained with 75 mN and 250 mN are chosen. The Young's moduli are calculated with Poisson's ratio of $\nu = 0.3$ from the indentation moduli, and values of 55.5 GPa and 69.8 GPa are obtained for E_{33} and E_{11} , respectively, for LTCC substrates. The values for Al_2O_3 substrates are 57.2 GPa and 64.3 GPa for E_{33} and E_{11} , respectively. The stiffness ratio of the piezoelectric thick film for LTCC is 0.80. The material characteristics of 47/53 and 48/52 have stiffness ratios of 0.79 and 0.81, respectively. I chose 47/53 as bulk material in order to calculate the missing stiffness and elastic compliance constants of PZ 5100 thick film as it showed good agreement with the calculated results above (99.8 %). The stiffness ratio for the piezoelectric thick film on Al_2O_3 coincides only by 89.2% with that of 47/53. This is caused by the small measured surface indentation modulus and its large standard deviation.

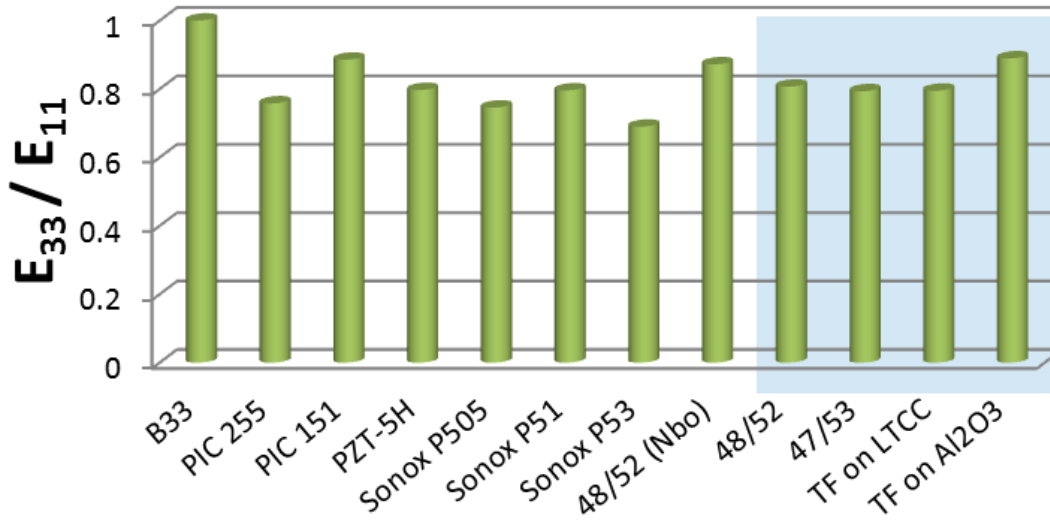


Figure 21 Comparison of calculated stiffness ratio.

Again, the full stiffness matrix is calculated by taking the same ratio between c_{ij}^D ($i, j = 1, \dots, 6$) of the stiffness matrix constants for the thick film and the bulk.

I assume that the piezoelectric thick film's have the same Poisson's ratio as the bulk material 47/53 of 0.329 and 0.34 for $-v_{12}$ and $-v_{13}$ respectively and calculate s_{12} and s_{13} using equation (26) and the bulk Poisson's ratio. The calculated ratio of S_{11_Bulk}/S_{11_Film} and S_{33_Bulk}/S_{33_Film} are 0.859 and 0.860 on LTCC substrate. The ratio S_{12_Bulk}/S_{12_Film} and S_{13_Bulk}/S_{13_Film} are also 0.859 and 0.860 on LTCC substrates. The ratio for the calculation of the missing material stiffness constants S_{44_Film} and S_{66_Film} are assumed to be 0.86 (mean value). The same routine is applied for the determination of the missing material parameter for screen-printed thick films on Al_2O_3 . The ratio for the determination of S_{44_Film} and S_{66_Film} on Al_2O_3 is 0.87. Therefore, the compliance components for the thick film on LTCC and Al_2O_3 are:

Table 6 Compliance components for screen-printed thick films and bulk material.

Parameter	TF on LTCC	TF on Al ₂ O ₃	(Pb _{0.94} Sr _{0.06})(Ti _{0.47} Zr _{0.53})O ₃
S ₁₁	1.43×10^{-11}	1.56×10^{-11}	1.23×10^{-11}
S ₃₃	1.80×10^{-11}	1.75×10^{-11}	1.55×10^{-11}
S ₁₂	-4.72×10^{-12}	-5.12×10^{-12}	-4.05×10^{-12}
S ₁₃	-6.17×10^{-12}	-5.99×10^{-12}	-5.31×10^{-12}
S ₄₄ = S ₅₅	4.53×10^{-11}	4.40×10^{-11}	3.90×10^{-11}
S ₆₆	3.80×10^{-11}	3.69×10^{-11}	3.27×10^{-11}

Table 7 Stiffness components for screen-printed thick films and bulk material.

Parameter	TF on LTCC	TF on Al ₂ O ₃	(Pb _{0.94} Sr _{0.06})(Ti _{0.47} Zr _{0.53})O ₃
E ₁₁	6.98 × 10 ¹⁰	6.43 × 10 ¹⁰	8.13 × 10 ¹⁰
E ₃₃	5.55 × 10 ¹⁰	5.72 × 10 ¹⁰	6.45 × 10 ¹⁰
ν ₁₂	0.329		
ν ₁₃	0.34		
G ₁₂	2.63 × 10 ¹⁰	2.71 × 10 ¹⁰	3.06 × 10 ¹⁰
G ₁₃	2.21 × 10 ¹⁰	2.27 × 10 ¹⁰	2.56 × 10 ¹⁰

These evaluations of the compliance and stiffness components of the screen-printed materials include assumptions and approximation. It is suggested to verify the values with a larger number of samples.

The ratio d_{31}/d_{33} of the bulk material 47/53 is -0.426. The specified film values of d_{33} are 180 pC/N and 210 pC/N for LTCC and Al₂O₃, respectively¹¹⁴. The application of the bulk ratio $-0.426 = (d_{31}/d_{33})$ leads to d_{31} values of -76 pC/N and -89 pC/N for LTCC and Al₂O₃ substrates, respectively. Another rule of thumb approximation is given by $d_{31} = -0.33d_{33}$, and this calculation leads to lower d_{31} values of -70 pC/N and -60 pC/N for Al₂O₃ and LTCC, respectively. Measurements of the dielectric constant and dielectric loss are also available for different substrate materials¹¹⁴; these are shown in Table 8.

Table 8 Electrical properties of screen printed piezoelectric thick film PZ5100 (active area = 400 mm²) on LTCC and Al₂O₃ substrate materials¹¹⁴.

Property	PZT on Al ₂ O ₃ (99.6 %)	PZT on LTCC (DP 951)
Dielectric constant ($\epsilon_{33}^T/\epsilon_0$)	1900	1500
Dielectric loss (tan δ)	0.038	0.033
Piezoelectric coefficient: d_{33} [pC/N]	210	180
Piezoelectric coefficient: d_{31} [pC/N]	-89 (calculated) -70 (approx.)	-76 (calculated) -60 (approx.)
Remnant polarization : Pr@50 Hz [μ C/cm ²]	16	10
Coercive field: E _{C@50 Hz} [kV/cm]	15	13
Internal resistance R _{is} at 30 kV/cm after 30 s [Ω]	2 × 10 ¹¹	

As in the case of the data for the mechanical parameters of piezoelectric thick films, very little data are available regarding their thermo-mechanical characteristics such as thermal conductivity, thermal expansion, and heat capacity. Literature data¹¹⁵ from commercially available piezoelectric elements (Pi Ceramic GmbH) are assumed to be a good approximation; the values of $350 \text{ Jkg}^{-1}\text{K}^{-1}$, $1.1 \text{ Wm}^{-1}\text{K}^{-1}$, and $(4-8) \times 10^{-6}\text{K}^{-1}$ are assumed for heat capacity, thermal conductivity, and CTE (perpendicular to polarization, hot-wired), respectively.

4.3.2 Stress effects on screen-printed layers

The formation of stress in screen-printed piezoelectric devices can be attributed to the following reasons: (i) shrinkage and constrained densification during sintering of screen-printed metallization layers and piezoelectric layers, (ii) polarization of piezoelectric layers, (iii) CTE mismatch of substrate and screen-printed layers (e.g., piezoelectric layer and metallization layer), (iv) application of substrate coatings, and (v) shrinkage of the substrate membrane during sintering (e.g., LTCC substrate).

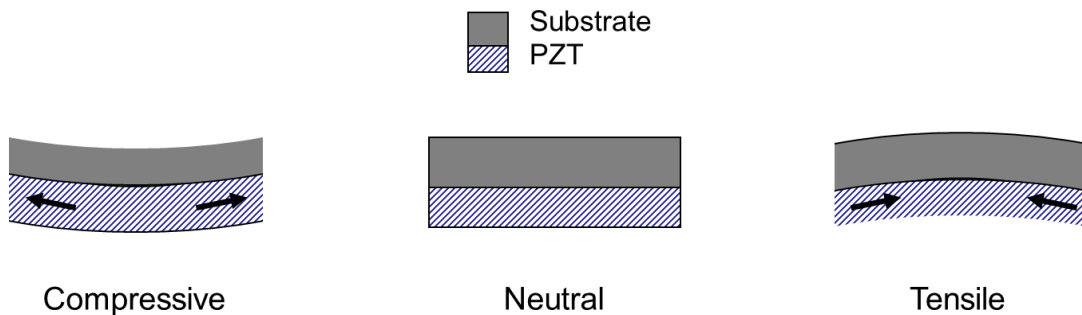


Figure 22: Definition of the stress level in the piezoelectric layer

The stress-forming causes either tensile or compressive stresses in different layers. Figure 22 shows deformation of a bilayer by compressive and tensile stress in the piezoelectric layer. Shrinkage and polarization of the piezoelectric layer induce tensile stress in the piezoelectric layer as the plane-layer contraction is suppressed by the substrate (clamping effect). High-temperature sintering processes of screen-printed layers and their subsequent cooling to room temperature induce residual stress due to CTE mismatches of the piezoelectric

and structural layers. Consequently, the membrane bends (as shown in the figure), and number of layers and the material characteristics influence the magnitude and direction of the bending.

Several studies have examined the effects of manufacturing-generated stresses on piezoelectric stroke, electromechanical properties of the piezoelectric films, resonance frequency, and sensitivity of multilayer structures. An increase in piezoelectric stroke induced by stress is caused either during the manufacturing processes^{116,117}, by externally applied mechanical stress¹¹⁹ or by thermal loading¹¹⁸. Piezoelectric benders with manufactured tensile pre-stress¹¹⁶ show increased d_{31} values, and thus increased piezoelectric deflection. The increase in d_{31} is attributed to a change in the initial domain configuration (and thus the electromechanical properties) under a suitable stress state.

Externally applied mechanical strains ($-T_3$) induce elastic stresses and piezoelectric polarization in the piezoelectric material. The piezoelectric polarization creates an internal electric field in the material that acts against the mechanical deformation. This is the reason for the strain asymmetry of piezoelectric elements between tensile loading and compressive loading and the complex electrical boundary conditions in piezoelectric benders⁷⁴. Externally applied stresses in piezoelectric benders result in internal loading and complex stress levels. In particular, dynamic stresses in piezoelectric benders may be fairly large, and even greater than static stresses⁷⁴. Finite element simulations have the potential to account for all these effects; however, this strongly depends on the availability of material data for all the layers. The lack of availability of such data leads to the use of linear finite element simulations and piezoelectric equations. Linear finite element simulations (neglecting nonlinear material behavior) appear to be sufficient for initial estimations of piezoelectric stress levels. Piezoelectric equations use the elastic coefficients of the piezoelectric layer that are defined for a constant electric field. In reality, the piezoelectric coefficients of the piezoelectric equations (cf. sec. 4.1.3) depend on the applied loading conditions, loading direction, loading rate, and frequency⁷⁴. The changes in the piezoelectric parameters by temperature are also not taken into account. These simplifications are driven by the lack of material data; however, they are

valid for the assumptions of small linear and non-linear changes of the material data over certain temperature ranges.

The stress state is also of particular importance for piezoelectric transducers as it affects resonance frequency and sensitivity. It is shown that frequency deviations mainly originate due to membrane bowing while stiffness variations influence the quality factors of vibrations for membrane bowing in the range of the total membrane thickness of sol-gel-derived thin film multilayer structures¹¹⁹. Other studies¹²⁰ have confirmed a significant increase in the resonance frequency and decrease in piezoelectric stroke caused by (uniform in-plane) stress. In this case, the stress-induced membrane bowing is only 20% of the membrane's total thickness. The resonance frequency also depends on the applied electric field¹²¹, and it decreases with an applied electric field. This change in resonance frequency is attributed to nonlinear elastic coefficients (stiffness variations) of the piezoelectric layer. In addition, a decrease in the mechanical quality factors has also been shown, and this attributed to increase in the air-damping effect as well as actuator internal friction.

4.4 Substrate materials

The screen-printing of PZ 5100 allows for the application of piezoelectric and metallization layers on different materials such as alumina, silicon, and LTCC. In the following section, the available substrates are investigated for their suitability in DM applications.

Aluminum oxide

Al_2O_3 is a very hard material with a high Young's modulus (>350 GPa) and a density of approximately 3.9 g/cm³. This leads to very stiff mirror geometries with a high first resonance frequency and an excellent strength; however, the resulting piezoelectric stroke is less. Its heat spreading capability is moderate ($\sim 30 \text{ Wm}^{-1}\text{K}^{-1}$). The material is inexpensive and offers a good adhesion for printed layers and good hermeticity (moisture is not able to seep in and reduce quality of prints during firing). The thermal expansion of Al_2O_3 (between $5.4 \times 10^{-6} \text{ K}^{-1}$ and $5.8 \times 10^{-6} \text{ K}^{-1}$) matches that of the piezoelectric PZ 5100 thick film.

Silicon

Silicon is widely used as mirror substrate material. It exhibits a good surface quality for thin substrate dimensions. Further, silicon has low density, high heat conductivity ($\sim 150 \text{ Wm}^{-1}\text{K}^{-1}$), and good mechanical strength. Silicon allows exact dimensional control with micromachining technologies. The CTE is very small ($2.6 \times 10^{-6} \text{ K}^{-1}$), and it does not overlap with that of the piezoelectric thick film. One drawback is lead diffusion from the piezoelectric thick film layers into the silicon during firing. The lead diffusion results in thick films with lower piezoelectric properties when compared to those with alumina substrates. Investigations have shown that the large manufacturing-imposed deformation of the screen-printed mirrors cannot be negated by polishing⁵³.

Low temperature co-fired ceramic (LTCC)

LTCC is used to fabricate ceramic multilayer circuit boards. The substrate material comprises glass ceramic layers that are cofired (fired simultaneously) at low temperatures (below 1000°C). The manufacturing process consists of the stacking of a preferably even number of green foil layers that undergo sintering and are subsequently fired. The ceramic layers have the ability to allow embedding of passive components (inductors, capacitors, resistors, and dielectrics). Therefore, the layered substrate enables the integration of sensors into a monolithic device. The layer can also be structured by integration of cavities and cooling channels into the substrate. The 3D-structuring can be used to integrate packaging, mounting, or alignment structures. LTCC is used in radio frequency and high frequency applications, general purpose packaging, and optoelectronic and automotive modules. The technology is also used to construct microsystems (fuel cells, drug delivery mechanisms, biological parameter monitoring, etc.)^{122,79}. LTCC has mechanical properties similar to those of silicon. Moreover, it has a higher CTE that is compatible with the piezoelectric layer. Its thermal conductivity is lower than that of silicon. The LTCC sinter process causes material shrinkage. However, the LTCC surface cannot be polished to optical quality, and it requires some thick film metallization than can be processed to optical quality. The overall deformation of the surface is large (in

the order of tens of μm) at a specified diameter of 50 mm. Its heat conductivity is low ($3 \text{ Wm}^{-1}\text{K}^{-1}$).

The deformable mirror used in this study is based on LTCC. This is motivated by its great potential of integration of mechanical cavities for cooling channels and mounting aids due its 3D-structural capabilities. Another important fact is the possibility of the integration of screen-printed, flat metallization and sensor elements into the multi-layered mirror membrane. The integration of flat metallization and cooling channels enables thermal balancing and better heat dissipation, respectively. The integration of sensor elements such as strain gauges and temperature sensors can facilitate better mirror deformation control.

4.5 Manufacturing concept

The proposed uniform deformable mirror is optically classified as a unimorph deformable mirror. Its manufacturing is based on processes adapted from microtechnology that allows device miniaturization and batch fabrication. The miniaturization occurs in the fabrication of thin mirror substrates with large mirror diameters and optical apertures. Thin substrates of $\sim 200 \mu\text{m}$ are layered with functional thick films by batch fabrication. The utilization of thick and thin film deposition techniques allows for the design of more degrees of freedom in structural and thermal aspects.

The DM is based on LTCC substrates with screen-printed piezoelectric and structural thick-film layers. The structural degrees of freedom are the 3D-structuring capability of the LTCC substrate and the screen-printing of the structural and functional layers. The 3-D structuring capability of the LTCC substrate is used to integrate the mirror membrane into a rigid LTCC mount. In particular, the screen-printing process allows a large structural degree of freedom. This fabrication process enables batch fabrication of the actuating layers and thus reduces the costs of fabricating the actuator layouts. The piezoelectric layer is sintered and joined to the substrate, thereby creating a strong interface with a high-temperature working range and potentially low outgassing. Metallization layers can be deposited on the front and rear surfaces

of the substrate; in addition, they can be integrated into the substrate. The layered mirror set-up allows for the development of an ML design. The ML design is based on multiple layers with different material properties and layer thicknesses that are accurately adjusted by the substrate's manufacturing and thick film deposition processes. Therefore, ML design allows for a new thermo-mechanical design approach, thereby controlling thermal lensing on deformable mirrors. The proposed mirror concept is the combination of a practical mirror design with up-to-date fabrication processes that enable the design of more degrees of freedom along with batch fabrication.

The developed manufacturing flow of the DM is shown in Figure 23. The substrate material is a multi-layered LTCC that is fabricated by laminating single green sheets. These green sheets are composed of a flexible raw material that consists of a mixture of glass, ceramic, and organic additives. The single sheets are laminated together to form a stack before being sintered to a monolithic substrate at about 850 °C. The mirror membrane is reinforced by additional outer LTCC layers. The reinforcements serve as integrated mounting aid structures, thereby simplifying handling and mounting as they absorb mechanical stresses. The manufacturing of the substrate is the first of the six steps necessary to complete the DM (cf. Figure 23 (2)-(6)).

In the second step, the thick film actuator structure is applied onto the rear surface of the substrate. By using the screen-printing process, different DM actuator layouts can be printed onto one substrate (in one batch). In the third manufacturing step, the mirrors are singularized. The singularized mirrors are affixed to the mirror mount in the fourth step. The mirror substrate is mounted before the application of the thick-film metallization and finishing. Subsequently, copper metallization of the front surface is carried out. The LTCC substrate is fixed by its reinforcements onto the mounting. Therefore, the copper metallization is electroplated onto the LTCC substrate and onto the mount to ensure a rigid joint and optimum heat dissipation of the mirror. In the sixth step, the mirror surface is finished by means of single point diamond turning (SPDT) of the copper thick film; this results in excellent mirror surface quality and high reflectivity. The reflective surface may subsequently be coated.

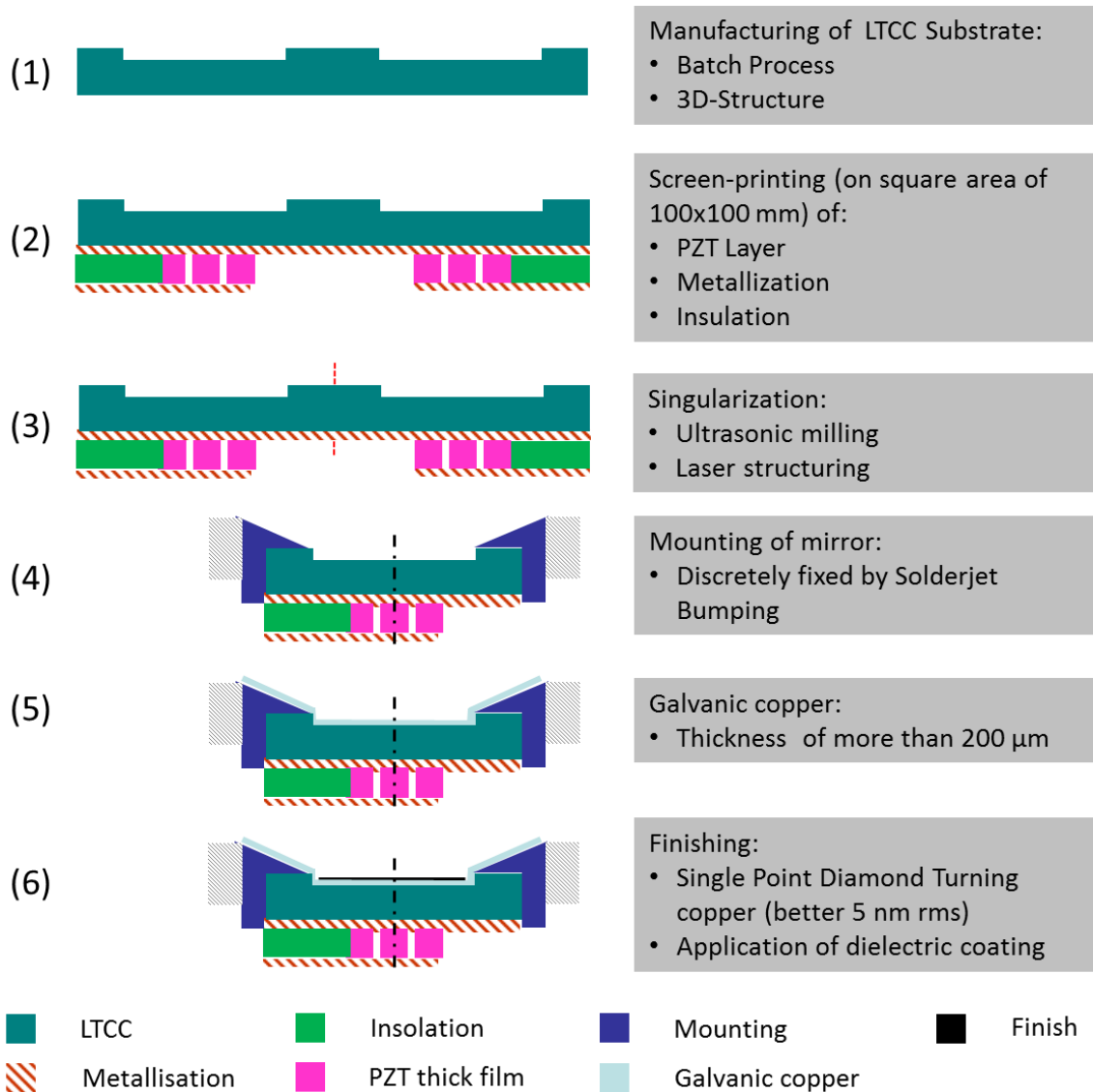


Figure 23 The mirror manufacturing concept is comprised from six steps. Schematic shows the cross-section of a mirror membrane.

4.5.1 Mount design

The mounting of most deformable mirrors is crucial since it heavily affects the stroke and the resonance frequency of the mirror. The practical realization of the mounting is difficult as the mechanical (mounting) stress can easily be induced in the mirror membrane, thereby affecting mirror deflection and resonance behaviour also.

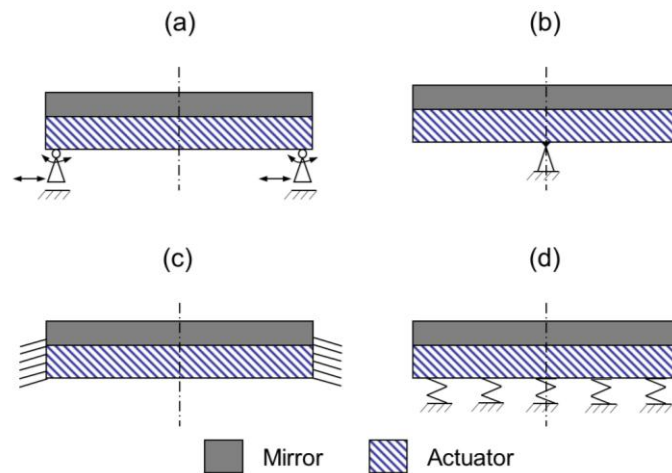


Figure 24 Mirror mounting options: (a) loose mounting, (b) central clamping, (c) fixed mounting, and (d) discrete compliant membrane support.

Figure 24 shows the typical deformable mirror mounting options: (a) loose mounting, (b) central clamping, (c) fixed mounting, and (d) discrete compliant membrane support. Loose mounting describes a membrane support that permits translation and rotation of the membrane's rim. Central clamping only clamps the membrane's centre, and this enables free translation and rotation of the membrane's rim. Fixed mounting relies on the clamping of the membrane's rim translational and rotational motion. Discrete compliant membrane support allows free movement of the membrane.

Loose mounting and central clamping enable the highest piezoelectric stroke. Loose mounting is practically realized by the use of the following: (i) flexible rubber O-rings^{123,124,125,126}, (ii) flexures^{127,128}, and (iii) elastic support ring¹⁵³. In contrast, very few mirror systems are found to use central clamping³⁷. Central clamping provides excellent heat dissipation as the maximum temperature occurs at the membrane's centre, and consequently, the heat can be removed via the central clamp. A disadvantage is that the clamping prevents the active piezoelectric deformation of the membrane centre by actuators. Discrete compliant membrane supports enable piezoelectric stroke comparable with that of loose mounting along with a higher resonance frequency. This can only be achieved if the compliant membrane support is particularly soft and can be deformed by the piezoelectrically generated force. The resonance behaviour is

determined by the patterning of the compliant support structures. Practical realizations of this type of support are discussed in ¹⁶⁵, and the techniques of mounting include the use of discretely deposited bumps ^{129,52}, springs or flexures. The heat-dissipation properties depend on the compliant material; soft, highly conductive materials are ideal. In addition, providing for a short distance between the baseplate underneath the compliant material and the mirror membrane can also assist in better heat dissipation. Fixed mounting offers reliable and rigid clamping combined with reduced deflection. Fixed mounting allows for a two-dimensional contact between the LTCC and the mount; this is advantageous for heat dissipation. For the abovementioned reasons, the study uses fixed mounting as the choice for mounting the deformable mirror.

Fixed mounting can be practically realized by clamping, gluing, or soldering. It is popularly used in cooled unimorph deformable mirrors. The substrate is joined to the level surface of the mounting by retaining rings¹³⁰, flange-type retainers, screws, or springs on the mirror's rear surface. The (mount and mirror) interfaces need to be levelled as their unevenness induces contact stress and mount-induced moments in the substrate. Experiments have shown that the number of screws used for rear screw clamping affects the resonant behaviour of the free membrane. In addition, soft pads¹³⁰ or gap pad¹³¹ may be required to overcome the unevenness of the mounting surfaces. The use of gap pads has not been considered promising as they have a low thermal conductivity. A rim mount realized using adhesive bonding is an obvious choice as it is a very simple and inexpensive technique. However, this technique has drawbacks that include low thermal conductivity of the adhesive, shrinkage, long-term instability and eventual outgassing. For these reasons, I chose Solderjet Bumping^{132, 133} as the technology for fixing the mount. In Solderjet Bumping, the mating parts are joined by a solder bump that is filled into a conical joining geometry. This conical joining geometry has a central bore that is used to solder the mount and mirror substrate. Thus, the substrate and mount are form-locked and tightly connected. Another advantage is the good thermal conductivity of the solder. I chose 24 mechanical fixing joints to guarantee reliable mounting conditions and good thermal conductivity (cf. Figure 25).

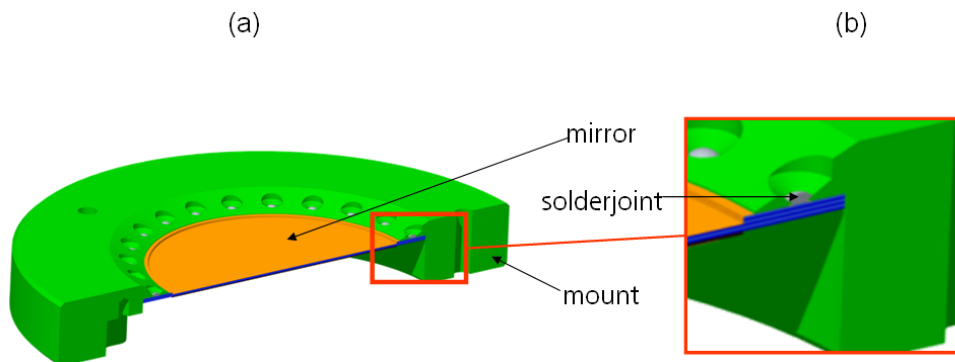


Figure 25 Mirror design concept. (a): cross section of mounted mirror membrane; (b): detail with mounting aid structures, mount and solder filled conical bores.

4.5.2 Reflective metallization

The choice of a glass ceramic substrate material requires a metallization layer acting as the reflective optical surface. I decided on copper as the reflective surface due to its excellent thermal conductivity. Thus, in the fourth step, a thin metallization layer (titanium/copper) is sputtered onto the front surface of the ceramic substrate. Subsequently, I electroplated copper onto the substrate. This is a very robust process, and copper-layer thicknesses of up to 150 μm can be achieved for a run time of 7 hours. The copper is also electroplated onto the mount (Figure 25), thereby increasing the heat spreading capability of the thin layer.

However, the surface of the copper metallization has no optical quality, and it needs additional finishing. The finishing process is done by SPDT, which is a reliable surface-flattening technique that makes use of a (monocrystalline) diamond tool, and by precision machining. The diamond tool can provide a fine finish to non-ferrous metals, and it is capable of producing mirrors with surface roughness in the nanometric range and micrometric form accuracy. Rotational symmetric shapes such as spheres, aspheres, and off-axis aspheres are standard-use in mirror systems. This process is used to flatten the electroplated copper surface and create a mirror surface with optical quality^{134,135}. The mirror mounting process is carried out before the application of the reflective thick film layers and the SPDT process. This is advantageous in that the mounting does not induce stress in the machined mirror membrane.

The copper metallization is not athermal to the substrate and piezoelectric layer. Therefore, thermal simulation optimizes the copper-layer thickness in order to enable self-balancing of the thermally-induced deflection due to homogeneous loading and high-laser load capability. Table 9 shows the thermo-mechanical properties of the screen-printed metallization layer, LTCC substrate (DuPont 951), and the galvanic copper layer. The properties of the galvanic layer are assumed to be independent of the application regime.

Table 9 Mechanical properties of screen printed thick film layers.

Material	ρ [g/cm ³]	E [GPa]	ν	σ_{\max} [MPa]	α [10 ⁻⁶ K ⁻¹]	κ (@23°C) [Wm ⁻¹ K ⁻¹]	C [Jkg ⁻¹ K ⁻¹]	Remark
Au TF	14.8	46 (2)	0.26 (2)	52	14.2	70	160	² calcul.
DP 951	3.1	120 (150)	0.24	320	5.8	3	989	
Cu	8.9	117	0.35	69-365	16.7	391	385	Bulk mat.

5 Optimization of the thermo-mechanical properties of deformable unimorph mirrors

Objective of this chapter is the theoretical investigation and optimization of the thermo-mechanical properties of deformable unimorph mirrors by analytical modelling and finite element modelling (FEM). The optimization is performed with respect to the interaction of piezoelectric stroke, homogeneous thermal loading and laser loading. Based on the manufacturing process, a mechanical model of the circular multilayer mirror membrane is set-up (Figure 26).

The substrate of the deformable mirror is set-up using an even number of LTCC substrate layers. The design uses two 100- μm -thick layers (DuPont PT), thereby leading to a substrate thickness of 200 μm . The actuating layer is a screen-printed piezoelectric thick film located between two sandwiching electrodes. The electrode material is screen-printed gold, and the two sandwiching electrodes have a thickness of 10 μm each. The investigations of the properties of screen-printed materials in chapter 4.3.1 are used in this chapter. The substrate's front surface consists of a copper thick film that's thickness needs to be defined during the optimization. The diameter and thickness of the piezoelectric thick film shall also be determined. The boundary condition as well of the impact of the membrane mount and mount material shall also be defined.

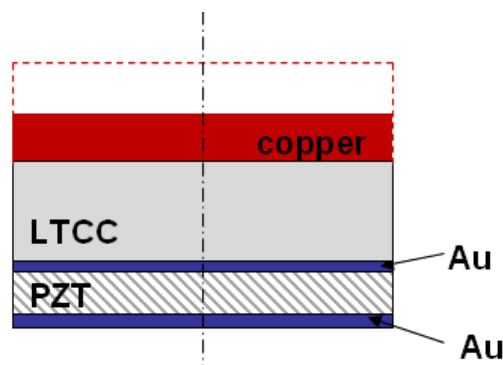


Figure 26 Model of a circular multilayer mirror membrane.

The chapter on simulations is divided into two sections—analytical modelling and modelling by finite element methods. The analytical modelling is used to evaluate the thermally-induced changes in the multilayer under homogeneous thermal loading and the static deflection of the piezoelectric layer. The thermal

considerations define the optimum copper-layer thickness in order to minimize the thermally-induced deflection of the multi-material membrane upon homogeneous thermal loading. Subsequently it discusses the effect of boundary conditions and layer discontinuity under thermal loading.

The static piezoelectric considerations analyse the actuation potential of different piezoelectric layer set-ups dependent on the number of piezoelectric layer. The influences of relative thickness and relative stiffness for a piezoelectrically actuated multi-layer with clamped edge are also investigated. Based on these investigations, the optimum piezoelectric layer thickness and its diameter are defined in the next step. The investigations of the static piezoelectric considerations are finished with the determination of the number of piezoelectric actuators, based on a review of theoretical investigations.

Extensive FEM simulations are used to evaluate the static and dynamic properties of the membrane for piezoelectric activation and the multi-layer response upon different thermal loading. The piezoelectric total stroke of the multi-layer membrane is simulated subject to copper-layer thickness variations. The results are compared with the static piezoelectric considerations. The influence of the material model (isotropic vs. orthotropic) is also investigated. The dynamic properties of the multi-layer are evaluated subject to stiffness variations of the piezoelectric layer, copper thickness, initial curvature of the membrane, and residual stress of the membrane. These investigations are intended to verify the impact of manufacturing related variations such as piezoelectric thick film properties, variations from the anticipated copper-layer thickness or stress induced multi-layer deformations on the dynamic behaviour.

The thermally-induced changes in the membrane are also evaluated. I begin with the homogeneous loading of the multi-material, thereby showing the comparability between the analytical and FEM models that result in the *zero deflection* configuration. Subsequently, I integrate the structural inhomogeneity of the piezoelectric layer and the two boundary conditions (simply supported and fixed rim). After defining the boundary conditions, I examine the suitability of the mirror mount material under homogeneous and inhomogeneous loading conditions.

5.1 Analytical modelling

5.1.1 Thermally-induced changes: homogeneous loading

The classical beam-and-plates theory is frequently used to calculate and optimize two-layer structures^{136,137}; however, it cannot be used in ML set-ups. Very few studies have focused on the determination of thermally-induced stresses and deflection in thick-film ML systems¹³⁸. Hsueh¹³⁹ derived a closed-form solution for thermal stresses in elastic ML systems. It is based on the classical beam-bending theory, and it is suitable for plane geometries via the replacement of the Young's modulus with the biaxial modulus $E/(1 - \nu)$. The general solution describes the strain distribution in the system by decomposing the total strain into a uniform strain component and a bending strain component. The curvature r^{-1} is given as follows:

$$\frac{1}{r} = \frac{2 \left[E_s (c - \alpha_s \Delta T) t_s^2 - \sum_{i=1}^n E_i t_i (c - \alpha_i \Delta T) (2h_{i-1} + t_i) \right]}{E_s t_s^2 (2t_s + 3t_b) + \sum_{i=1}^n E_i t_i [6h_{i-1}^2 + 6h_{i-1} t_i + 2t_i^2 - 3t_b (2h_{i-1} + t_i)]} \quad (28)$$

with

$$c = \frac{(E_s t_s \alpha_s + \sum_{i=1}^n E_i t_i \alpha_i) \Delta T}{E_s t_s + \sum_{i=1}^n E_i t_i} \quad (29)$$

and

$$t_b = \frac{(-E_s t_s^2 + \sum_{i=1}^n E_i t_i (2h_{i-1} + t_i))}{2(E_s t_s + \sum_{i=1}^n E_i t_i)} \quad (30)$$

Here, c denotes the uniform strain component, t_b the position of the bending axis, and t_x the layer thickness. The subscript s denotes the substrate layer and subscript i denotes the layer number for the film, and it ranges from 1 to 4 in the actual simulation. Layer 1 is the layer in direct contact with the substrate. The CTE of each layer is denoted by α_x , and ΔT denotes the temperature load. The formulae serve to calculate the effects of the thickness of the copper metallization

on the deflection for temperature loads of 10 K and 30 K. Copper is used as the substrate layer (subscript s for equations (28)-(30)), and its layer thickness ranges from zero to 100 μm . The thermal expansion of the piezoelectric thick film is varied between (4, 6 and 8) $\times 10^{-6}/\text{K}$. The complete set of material parameters and the layer numbers are given in the following Table 10:

Table 10 Mechanical properties used in the analytic simulation.

Layer		Young's modulus	Poisson's ratio	Thickness	CTE
Copper	5	117 GPa	0.35	-Variable-	$16.7 \times 10^{-6} \text{ K}^{-1}$
LTCC ¹⁴⁰	1	120 GPa	0.24	200 μm	$5.8 \times 10^{-6} \text{ K}^{-1}$
Au	2	48.5 GPa	0.3	10 μm	$14.3 \times 10^{-6} \text{ K}^{-1}$
PZT	3	67 GPa	0.3	100 μm	-Variable-
Au	4	48.5 GPa	0.3	10 μm	$14.3 \times 10^{-6} \text{ K}^{-1}$

The left hand section of Figure 27 shows the calculated curvature for three different piezoelectric CTEs and homogeneous temperature loading between zero and 30 K. The curvature is positive in absence of copper ($t_s=0$), and the values decrease with increasing copper-layer thickness (t_s). At maximum copper-layer thickness, all the calculated curvatures are negative. The magnitude of the curvature increases for increasing temperature loads. Interestingly, for all three CTEs of the piezoelectric thick films, there exists a copper-layer thickness that induces no thermal deflection over the entire temperature range. The *zero deflection* copper-layer thicknesses are 11.9 μm , 18.4 μm , and 24.4 μm for (4, 6 and 8) $\times 10^{-6} \text{ K}^{-1}$, respectively. Figure 27 (right hand section) depicts the deflection of the membrane for temperature loads of 10 K and 30 K. The deflection δ is calculated as the following:

$$\delta = \frac{\phi^2}{8} \frac{1}{r} \quad (31)$$

Here, ϕ denotes the diameter of the membrane ($\phi = 50 \text{ mm}$). It can be observed that for increasing CTE values of the piezoelectric thick film, the slope of the deflection decreases. The material set-up becomes more insensitive to variations in the copper-layer thickness. From the simulations, it can be inferred that there

exists a copper-layer thickness value for which the thermally-induced strains in the single layers of the multilayer system balance each other, thereby inducing no deflection in the ML system. This type of ML system is referred to as a *zero deflection* configuration.

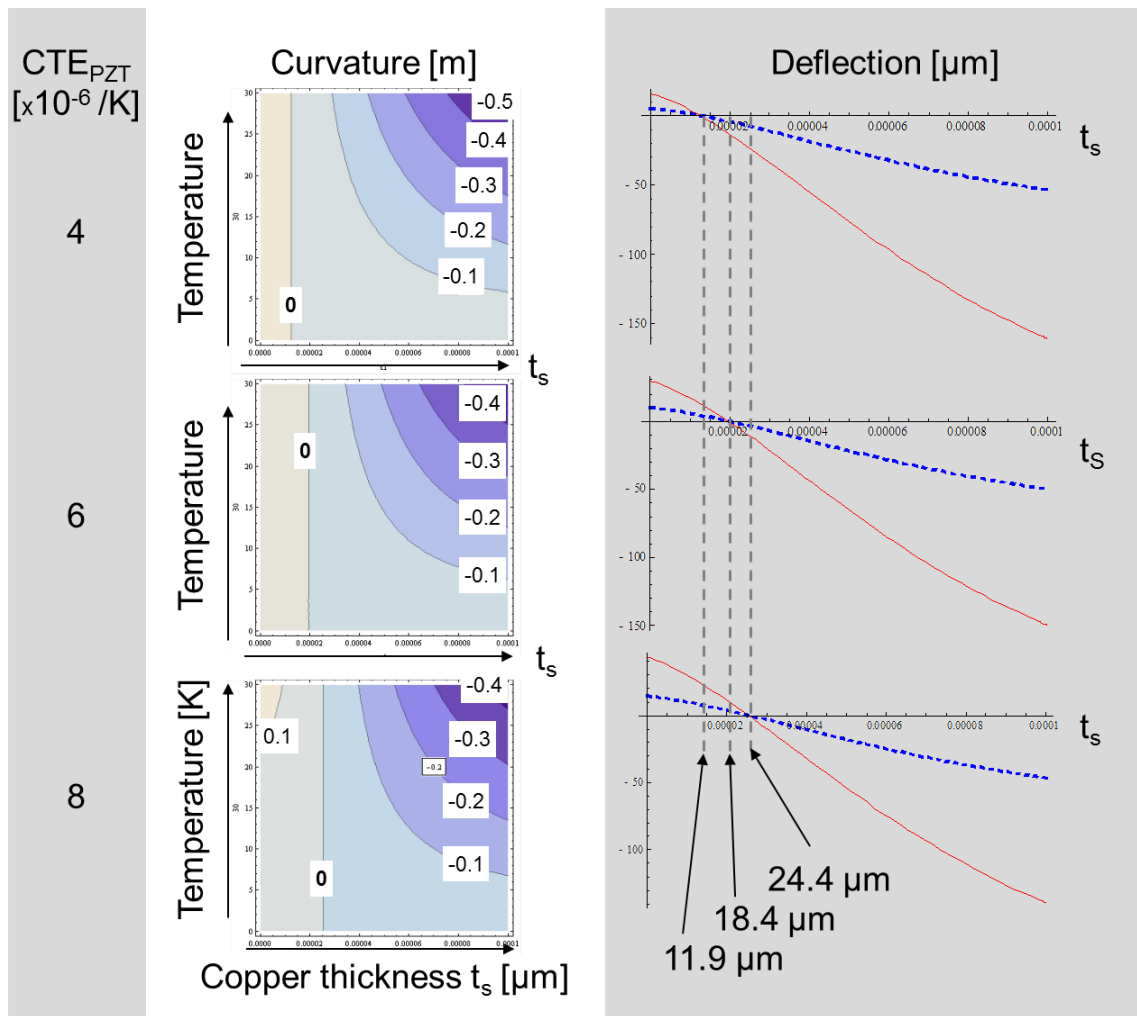


Figure 27 Thermally-induced curvature and deflection for copper-layer thicknesses t_s between 0 μm and 100 μm at a thermal loading of up to 30 K. The CTE of the piezoelectric material varies from 4 to 8 $\times 10^{-6}\text{K}^{-1}$. Left: Curvature. Right: Deflection for 10 K (blue, dashed) and 30 K (red line) loads. The *zero deflection* copper-layer thickness is insensitive to the temperature load.

However, the confidence of these simulations are limited as the copper layer, that serves as substrate layer is very thin compared the (sum) of the remaining layers, thereby leading to possible deviations in the calculation of the optimum copper-layer thickness. Further, this model is not suitable for very large

temperature loads as the material parameters are treated as constants (and not temperature-dependent as under actual conditions), and the model assumes that the radii of the piezoelectric and metallization layers equal that of the substrate layer. The clamped boundary conditions are also not considered while calculating the deflection. These limitations are overcome by finite element simulations.

Effects of boundary conditions and layer discontinuity

The effects of thermal self-balancing for different boundary conditions and (structural) layer discontinuities can be studied using a two-way membrane electro-thermal actuator (bimetal). It comprises two materials—silicon dioxide and aluminium as the substrate and top surface material, respectively, with different CTEs¹⁴¹. The deflection magnitude and direction are affected by the top-layer patterning and the boundary conditions (clamped rim and simply-supported rim) as qualitatively shown in Figure 28.

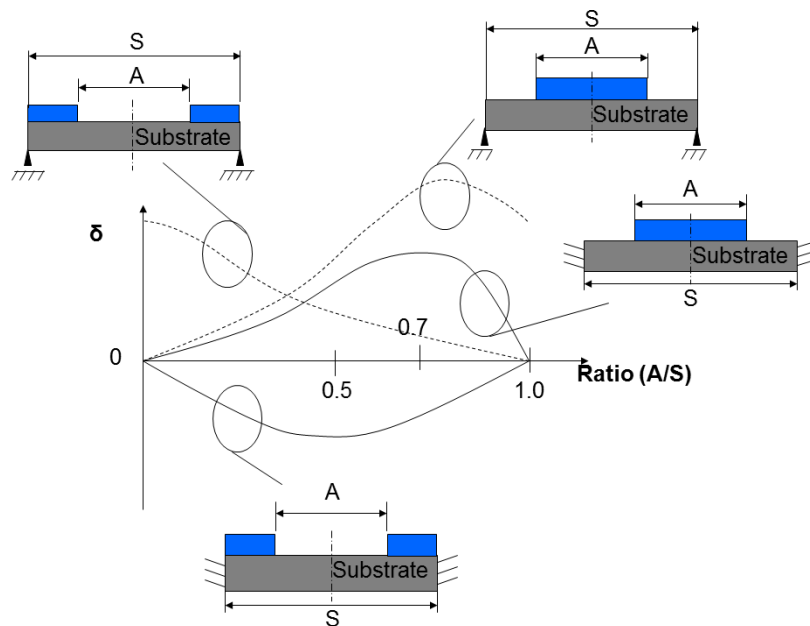


Figure 28 Deflection of a circular plate. Two cases are examined: circular and annular top layer (blue) with simply-supported and fixed-rim boundary conditions. Ratio A/S is the coverage ratio of the substrate.

Two top layer patterns are studied—a central top layer and an annular top layer. The deflection depending on the coverage ratio A/S between the length (diameter) of top layer and that of the substrate is shown in Figure 28. It can be

observed that the direction of the deflection depends on the patterning of the top layer and the boundary conditions. For a clamped rim membrane, the deflection is positive for a circular top layer and negative for an annular top layer. This proves that, depending on the position along the radius, the top layer contributes to either positive deflection or negative deflection. This effect (of possible self-balancing) can be explained as follows: the top layer has a larger CTE than that of the substrate. Heating leads to the expansion of both layers; however, the top layer expands more. The central top layer expands, and this leads to an upward convex shape, and the uncovered substrate assumes a downward concave shape. The annular top layer deforms in a convex downward bow as the covered rim is fixed. The tailoring of the upward and downward deflections via the thickness along the diameter of the active layer is very interesting in terms of thermal compensation as such tailoring would allow the bending effects to balance themselves out. The screen-printed mirror set-up consists of five layers of (mostly) different materials, thereby providing a multi-material assembly. An application of this effect is the tailoring of thermal deflection through the patterning of large (expansion) layers. The patterning may also be used to introduce thickness variations (inhomogeneities) in one layer in a multilayer system. Figure 28 depicts also a decreased deflection in the case of clamped boundary condition compared to simply supported BC.

Here, the active top layer is discussed as a thermally activated layer, but the induced deflection can also be activated by a piezoelectric layer. A tailoring of the coverage ratio A/S also gives the chance to increase the piezoelectric induced deflection compared to the full coverage of a fixed-rim membrane.

5.1.2 Piezoelectric stroke

A first, extensive mathematical description of piezoelectric bimorphs consisting of two piezoelectric plates has been made by Kokorowski¹⁴². Li et al.¹⁴³ developed a theory describing piezoelectric stroke and resonance behaviour of a piezoelectric unimorph disk. The bonding and metallization layers between the active layer and the passive substrate are neglected. Li et al. assumed a perfect bonding under simply-supported conditions at the rim. Another model¹⁴⁴

proposes the integration of three layers (a substrate layer, piezoelectric layer, and a bonding layer) into a simply-supported membrane. The model allows for the analysis of the effects of the bonding layer between the substrate and piezoelectric layer. Further, the effects of the dimensional variations in the piezoelectric layer can be examined via this model. Mo et al.¹⁴⁵ have investigated the stroke of a circular piezoelectric membrane for different boundary conditions, thicknesses and radii of piezoelectric and substrate layers; however, their study does not consider the integration of electrode layers. In contrast to previous approaches¹⁴²⁻¹⁴⁴, Pfeifer¹⁴⁶ developed working equations for the stroke of a circular membrane with a clamped rim, but he has assumed equal radii for the substrate and piezoelectric layers. The author introduces the relative thickness a and relative stiffness c as follows:

$$a = \frac{t_s}{t_p} \quad (32)$$

$$c = \frac{E_s}{E_p} \quad (33)$$

The free deflection (stroke) is calculated as follows:

$$\delta = \frac{3}{4} d_{31} E_{field} \left(\frac{\phi}{2}\right)^2 \frac{1}{t_p} \frac{4ac(1+a)}{4ac(1+a)^2 + (1-ca^2)^2} \quad (34)$$

The indices s and p denote the substrate and piezoelectric layers, and ϕ denotes the diameter of the disk. Ellis¹⁴⁷ investigated the integration of additional active piezoelectric layers in order to increase the piezoelectric-induced stroke. He studied the actuation potential of four different active layer set-ups—unimorph, bimorph, cooperative bimorph, and symmetric bimorph (Figure 29)—under clamped edge conditions. The bimorph set-up comprises two piezoelectric layers that are inversely poled¹ whereas the cooperative bimorph has equally poled

¹ The bimorph set-up has also been referred to as two piezoelectric plates without a passive mirror layer.

piezoelectric layers that act along the same direction. The thickness of the piezoelectric layer is doubled at constant voltage. The symmetric bimorph has two inversely-poled piezoelectric layers and a second substrate layer on the rear surface, and this may potentially be advantageous for various temperature loadings. The use of a five-layer set-up explores the benefits of a piezoelectric multilayer.

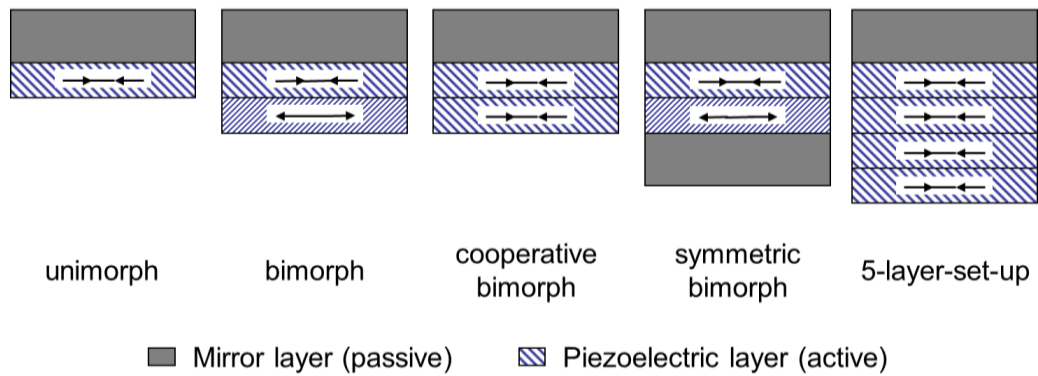


Figure 29 Active layer mirror set-ups.

The curvature for each of the designs is given as follows:

Unimorph:

$$\frac{1}{r} = \left(\frac{d_{31}E}{t_s} \right) \left(\frac{6ca(1+a)}{1+c^2a^4+2ca(2+3a+2a^2)} \right) \quad (35)$$

Cooperative bimorph:

$$\frac{1}{r} = \left(\frac{d_{31}E}{t_s} \right) \left(\frac{12ca(2+a)}{16+c^2a^4+8ca(4+3a+a^2)} \right) \quad (36)$$

Bimorph:

$$\frac{1}{r} = \left(\frac{d_{31}E}{t_s} \right) \left(\frac{12(2+ac)}{16+c^2a^4+8ca(4+3a+a^2)} \right) \quad (37)$$

Symmetric bimorph:

$$\frac{1}{r} = \left(\frac{d_{31}E}{t_s} \right) \left(\frac{3}{2+2ca(3+3a+a^2)} \right) \quad (38)$$

The results for the unimorph and bimorph systems are in accordance with those obtained by Ning et al.¹⁴⁸, and they calculate also the response functions of a **5-layer bimorph** as follows:

$$\frac{1}{r} = \left(\frac{d_{31}E}{t_s}\right) \left(\frac{24ca(4+a)}{256 + a^4c^2 + 16ca(16 + 6a + a^2)}\right) \quad (39)$$

The response functions for the different layer set-ups are evaluated for the simplified deformable mirror design. The relative stiffness value of $c = 1.8$ is calculated by using the ratio ELTCC/EPZT (cf. Table 10). The variation in the thickness of the copper layer changes the Young's modulus of the substrate is not taken into account.

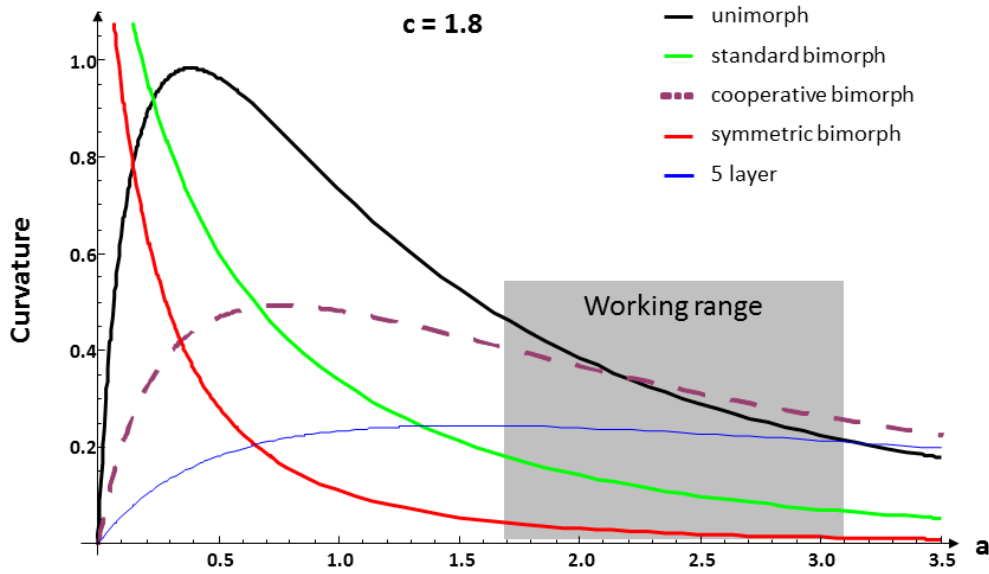


Figure 30 Comparison of different piezoelectric layer set-ups. Highest stroke is induced by unimorph and cooperative set-ups within the working range.

The design concept suggests a preferred LTCC substrate thickness of 200 μm and an additional copper-layer thickness around 50 μm , thereby leading to a total substrate thickness of 250 μm . The thickness of the piezoelectric thick film is between 80 and 150 μm . This corresponds to a working range between 3.1 and 1.7 for the thickness ratio a . The curvatures of the different active layer set-ups are plotted in Figure 30 without considering the coefficient $(d_{31}E/t_s)$ as it remains stable for all set-ups.

The simulations show that the unimorph set-up exhibits the largest curvature potential for the lower limit of the working range of the thickness ratio. The stroke potentials of the unimorph, cooperative bimorph, and the 5-layer bimorph are very similar in the working range. The unimorph set-up can be manufactured through state-of-the-art screen-printing processes. The cooperative bimorph and the 5-layer bimorph set-ups would require multiple printing of piezoelectric and metallization layers. The latter process is more complicated and thus more expensive. Therefore, I selected the unimorph set-up for the study.

In the next step, the copper-layer thickness and the dimensions of the piezoelectric layer and sandwiching electrodes require to be optimized. Deshpande et al. have developed "*an analytical model and working equations for static deflections of a circular multi-layered diaphragm-type piezoelectric actuator*"¹⁴⁹. They present an analytical model based on the classical laminated-plate theory (CLPT) for the stroke of multi-layered circular piezoelectric membranes. The equations are solved in a closed form, and they are valid for multi-layered set-ups with different radii of the substrate and the piezoelectric layers. The operating voltage is applied to the piezoelectric layer, and the membrane is clamped with a fixed rim. The model is derived using the CLPT, wherein a multi-layered heterogeneous plate structure is reduced to a kinematically-equivalent single layer, and it involves the following assumptions^{149,150}:

- Layers are perfectly bonded to each other
- Materials of each layer are linearly elastic and transverse isotropic
- Each layer has uniform thickness
- Strains and strokes are small
- Plane stress conditions apply
- Transverse shear on the top and bottom surfaces of the laminate are zero
- Piezoelectric material is assumed to be polycrystalline film poled along the z-axis
- In-plane strains and in-plane piezoelectric coefficients of the piezoelectric film are isotropic and $d_{31} = d_{32}$, respectively

This model is used to examine the influence of increasing copper-layer thickness on the maximum achievable stroke and the optimum diameter ratio between active layer and substrate layers.

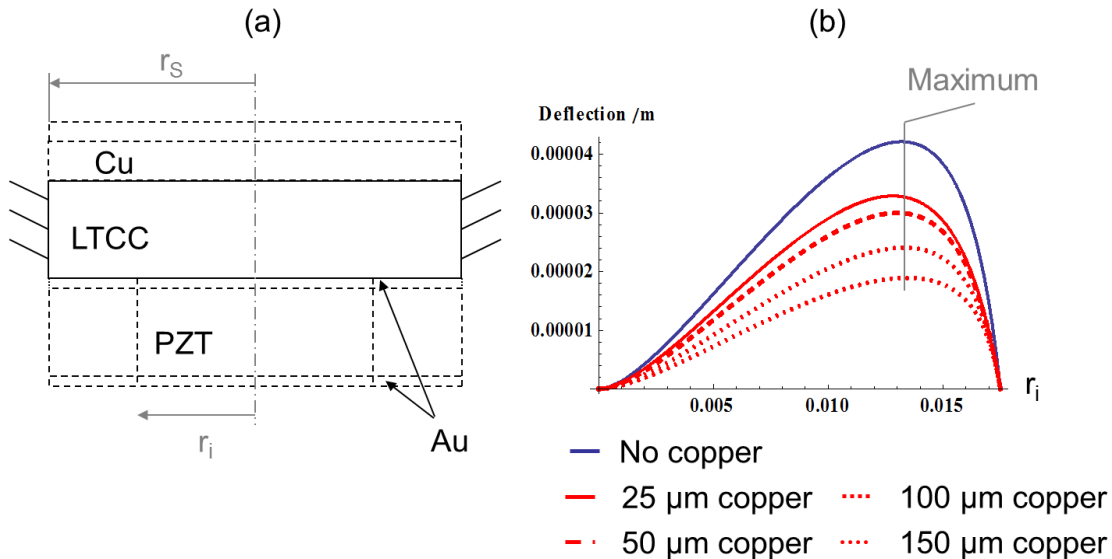


Figure 31 Optimization of piezoelectric layer diameter for different copper-layer thicknesses.
 (a) Model and (b) simulated deflection of the membrane centre for different copper-layer thicknesses.

The simulation results are shown in Figure 31, wherein Figure 31 (a) depicts the simulation model and Figure 31 (b) depicts the simulation results. The results provide the stroke value at the centre of the mirror membrane. The substrate's radius is 17.5 mm, and the other material characteristics and dimensions are obtained from Table 9 and Table 10.

First, I carried out a reference simulation without copper metallization (blue) in which I varied the radius (r_i) of the piezoelectric and the top gold-metallization layers. The simulations showed a maximum achievable stroke of 41.8 μm at $r_i = 13.2$ mm, thereby corresponding to a ratio $r_i/r_a = 0.75$. Subsequently, I simulated the influence of the copper metallization on the achievable stroke and the optimum ratio r_i/r_a . An increase in the copper-layer thickness to 150 μm results in a corresponding decrease in achievable stroke. The ratio of r_i/r_a at maximum stroke remains stable. This leads to the following conclusion: A thin copper layer is preferred for high stroke and the ratio r_i/r_a is constant at 0.75 for the evaluated copper-layer thicknesses. Therefore, the radius of the piezoelectric

layer should be fixed at 13.2 mm. The results also show insensitivity to deviations from the optimum ratio r_i/r_a as the stroke decreases by only a very small magnitude. The effect of the copper-layer thickness on the stroke is depicted in Figure 32. The stroke decreases from 41.8 μm without copper metallization to 23.8 μm and 18.7 μm with 100 μm and 150 μm copper, respectively.

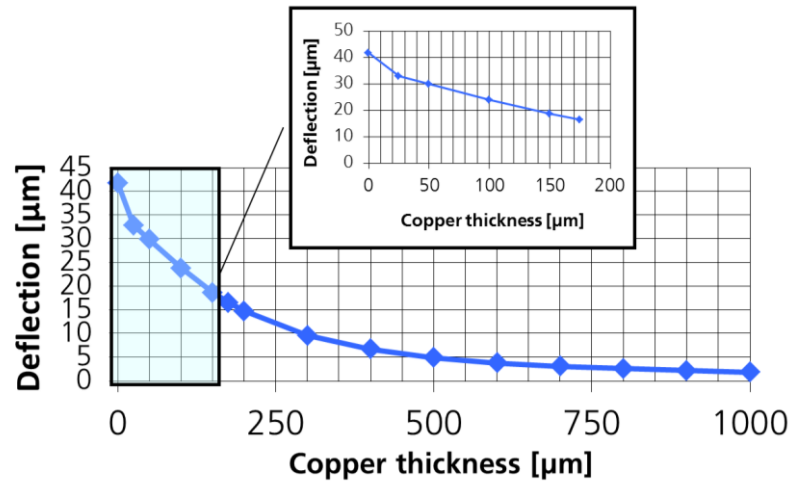


Figure 32 Influence of the copper-layer thickness on the piezoelectric stroke.

Piezoelectric actuator pattern

The optimum design of deformable mirrors relies not on maximum achievable stroke if all actuators are activated. Here, additional boundary conditions apply; such as the potential of cancelation of optical aberrations or the optimum shape and number of the actuating patterns.

The pattern of the addressing electrodes of the piezoelectric actuator influences the mirror potential of setting desired surfaces. Besides the optimization of the total stroke (described in the previous section), the ratios of mirror diameter to the aperture and piezoelectric diameter to the aperture also require optimization. The present case of a membrane mirror with clamped edge has also been analyzed in the literature¹⁵¹. The simulations reveal ratios of 1.8 and 1.2 for mirror diameter to aperture and piezoelectric diameter to aperture, respectively. The results are valid for 37 hexagonal or segmented ring actuator structures.

Therefore, a mirror diameter of 35 mm gives a mirror aperture of 19.4 mm and a piezoelectric diameter 23.3 mm. These optimization results, based on turbulence-induced phase distortions, are very close to the calculated diameter of 26.4 mm of the piezoelectric element in the previous section. The authors¹⁵¹ also show that the actuator pattern does not significantly influence the potential to cancel turbulence-induced phase distortions as long as they homogeneously cover the effective piezoelectric area.

Vdovin et al.¹⁵² have calculated the number of actuators to be placed within and external to the mirror aperture for an effective correction of Zernike modes. They employ the Poisson's equation describing the stroke of a unimorph mirror with a free edge. For a high-quality correction of low-order Zernike terms up to the degree $i = 24$ ($N=4$; cf. A1), a total of at least 15 actuators are needed. The total number of actuators is given as follows:

$$Total _ Actuator \geq (N^2 + 3N + 2) / 2 \quad (40)$$

The number of actuators placed external to the mirror aperture is given as follows:

$$Extern _ Actuator \geq 2N + 1 = \underline{\underline{9}} \quad (41)$$

Verpoort and Wittrock carried out extensive finite element simulations to determine the optimum actuator pattern¹⁵³. They simulated 11 different actuator patterns by calculating the amplitude for Zernike terms (up to 90 terms) and the purity of the desired Zernike modes for a said laser aperture. The authors varied the shape of the actuator pattern and the diameter of the mirror; however, the ratio of the piezoelectric layer diameter to the substrate diameter was maintained constant. Their investigation shows an increase in Zernike amplitude and purity if actuators are placed external the mirror aperture. Consequently, the substrate diameter increases. The ratio of the laser aperture to the substrate diameter for ideal mirror set-ups is 0.4–0.5. In contrast to the proposed mirror concept, the simulations incorporate the free boundary conditions that are similar to the boundary conditions of the simply-supported rim.

5.2 Finite element analysis

The first part of the section on simulations deals with analytical investigations. These investigations are adequate for the optimization of material dimensions; however, they are also limited due to the assumptions of their base approaches. A more realistic description is possible with the finite element method that allows for (i) complex geometries of patterned piezoelectric patches with piezoelectric passive regions, (ii) the incorporation of residual stresses from manufacturing or thermal loading, and (iii) non-linear material behaviour. Finite element analysis (FEM) methods consist of three major steps. The set-up of the mechanical model including the material databases (pre-processing) is the first step. The second step is the application of loads and boundary conditions and the solving of the resulting partial equations (solution). The post-processing step involves the analysis of the simulation results. *“In order to solve the differential equations, the continuous system is discretized into a mesh of elements. Each element is defined by at least 2 nodes. The differential equations are solved at every node and the field values between the nodes are calculated by a polynomial interpolation”*¹⁵⁴. More detailed descriptions can be found in ^{154,155,156}.

The (subject) matter of this section is a detailed analysis of piezoelectric stroke, and the thermal, and dynamic mirror characteristics. I obtain the finite element modelling of the dynamic and static performances of the deformable mirror membrane as a function of the copper-layer thickness. The second part of this section investigates the influence of residual stress and initial curvature of the membrane on the resonance behaviour of the membrane. A further set of simulations models the thermally-induced bowing of the mirror membrane and the thermally-induced frequency shift due to homogeneous temperature loading under different mechanical boundary conditions. The simulations define the optimum copper-layer thickness according to the mechanical model and its boundary conditions. This section is followed by a section that examines the choice of the mirror mount material. The last subsection on simulations evaluates the laser-induced membrane bowing (inhomogeneous loading). This section also verifies the transferability of mirror design strategy from homogeneous loading to inhomogeneous loading. The dynamic performance of the DM needs to be

investigated with the objective of obtaining a first natural frequency larger than 1 kHz.

For these simulations, two different FEM software are used—CoventorWare™ and ANSYS Multiphysics 11.0. CoventoreWare™ 2010 is design software that enables efficient MEMS modeling. The mirror model is meshed with *Extruded bricks* (parabolic) that use the Pave, QMorph algorithm, and a mesh element size of 750 μm and 100 μm along the lateral and thickness directions, respectively. The full model is configured and solved by the MemMech solver. The ANSYS program uses the element type Plane 223 for all elements and materials¹⁵⁶. The element's degree of freedom is set to structural-thermal with a weak (load vector) coupling and axisymmetric element behaviour (et, 1, plane 223, 11, 1, 1). CoventorWare™ is used to analyse the static and dynamic mirror characteristics whereas ANSYS is employed for dynamic and thermodynamic investigations. The substrate's diameter is 17.5 mm, and the piezoelectric and gold metallization diameters are 12.5 mm. The other mechanical dimensions are obtained from Table 7.

5.2.1 Piezoelectric stroke

The static stroke is simulated while the LTCC membrane is clamped at its circumference. An electric potential (field) is applied to the top and bottom surfaces of the piezoelectric layer. The electric potential of the upper electrode is set to 200 V and while that of the bottom electrode is 0 V. The effects of the copper-layer thickness on the free stroke of the mirror membrane are investigated. The thickness of the copper layer is varied between 10 μm and 400 μm in 10- μm steps. I investigate the influence of two different sets of piezoelectric material parameters—the complete set of stiffness components of the material matrix (cf. Table 8) and the simplified piezoelectric material parameters from

Table 10. The results of the CoventorWare™-based simulations are compared with the closed-form solution¹⁴⁹ that uses the simplified piezoelectric parameters. The material data of the other materials are given in Table 9 and Table 10.

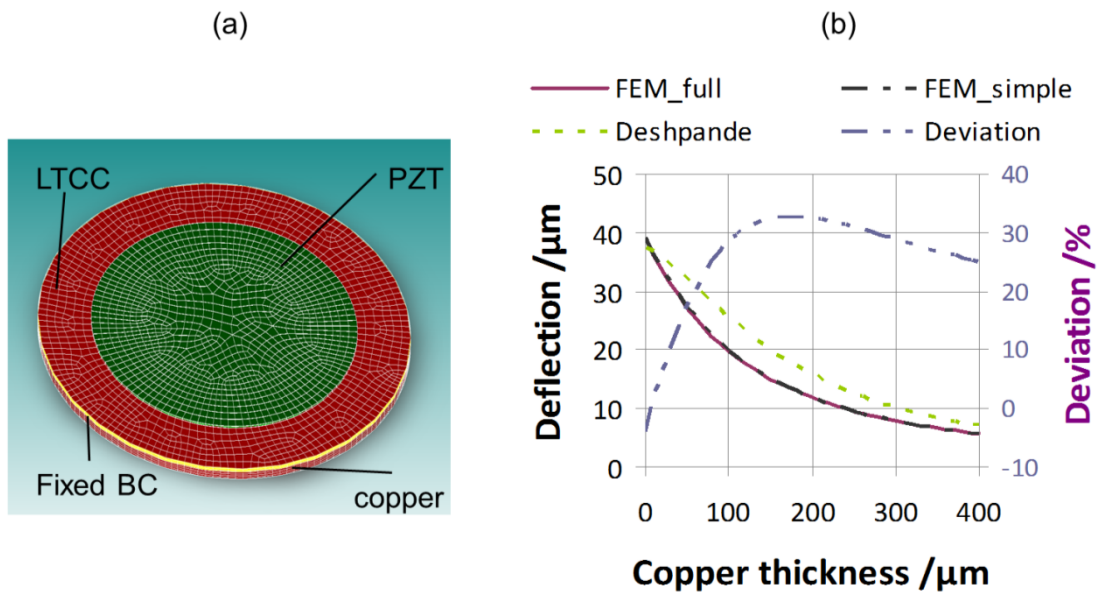


Figure 33 (a) 3D model using CoventorWare™. The fixed boundary condition is highlighted (yellow). (b) Simulation results of both finite element method and closed-form solutions. The deviation between both methods increases with increasing copper-layer thickness.

The piezoelectrically induced stroke is plotted against the copper-layer thickness (cf. Figure 33 (b)). The FEM-based simulations and those by Deshpande (cf. 5.1.2) show a decrease in stroke with increasing copper-layer thickness. The simulations show that, regardless of the material parameter data used (simplified or complete), the material parameters do not affect the stroke. Material parameters obtained with a simplified database based on isotropic materials provide similar simulation results to those obtained with from a model of Perovskite crystalline structures (whose complete material parameters are available) poled along the z-direction. The comparison between analytical and FEM modelling reveals good agreement for copper-layer thicknesses below 80 μm ; larger thickness values lead to a deviation of 20% and above. Therefore, the influence of copper-layer thickness on the stroke can only be modelled with finite element modelling.

5.2.2 Dynamic multilayer characteristics

The five factors that influence the resonance behaviour of the membrane are identified. These factors include stiffness variations in material layers, substrate thickness, residual membrane stress (cf. 4.3.2), the initial membrane shape, and

temperature changes. ANSYS FEM simulations can be used to validate the impact of these factors on the membrane resonance behaviour. The analysis type is modal, and it uses the Block Lanczos calculation method.

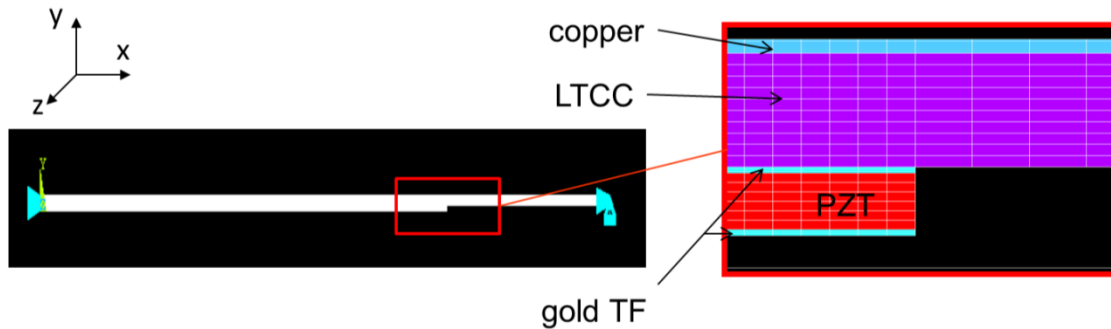


Figure 34 ANSYS model of the piezoelectric membrane. Boundary conditions suppress the membrane movement at its rim. The membranes centre can freely move along the y-direction.

Figure 34 shows the axisymmetric model of the mirror membrane. The dynamic properties are evaluated with the movement of the model's centre being suppressed along the x-direction. The movement of the membrane's rim is suppressed along the x- and y-directions. The model is map-meshed.

Stiffness and copper-layer thickness variations

Stiffness variations in the utilized materials are induced by the manufacturing process or material composition variations, and they lead to statistically distributed material values. For example, the Young's modulus of the LTCC material DuPont 951 is specified as between 120 GPa^{140, 157} and 152 GPa¹⁵⁸ by the manufacturer. The measured stiffness parameter of the screen-printed piezoelectric layers can change by up to $\pm 20\%$. The material values of commercial piezoelectric ceramics are also statistically distributed (cf. A2, A3). Therefore, the next set of simulations is used to investigate the influence of stiffness variations in the piezoelectric material, depending on the copper thickness. The first mechanical resonance frequency is calculated for copper-layer thicknesses between 0 μm and 300 μm , and 10 μm and 400 μm for the material data sets 2 and 1, respectively (cf. Table 11).

The data sets are (nearly) identical for LTCC, copper, and Au; however, the stiffness components of the piezoelectric thick film differ. Set 1 is obtained from the identification of the layer characteristics (cf. Table 7). Set 2 uses a reduction of

7%–8 % in the stiffness components for E_{11} , G_{12} , and G_{13} when compared to those of set 1.

Table 11 Material parameters: sets 1 and 2 of simulation data.

Parameter		set 1	set 2
PZT	E_{11}	6.98×10^{10}	6.43×10^{10}
	E_{33}	5.55×10^{10}	5.72×10^{10}
	ν_{12}	0.329	
	ν_{13}	0.34	
	G_{12}	2.63×10^{10}	2.71×10^{10}
	G_{13}	2.21×10^{10}	2.27×10^{10}
	density	6160	
	C_{th}	350	
LTCC	E_{11}	12.0×10^{10}	
	Poisson's ratio	0.24	
	density	3100	
	CTE	5.8×10^{-6}	
	C_{th}	989	
Copper	E_{11}	11.7×10^{10}	
	Poisson's ratio	0.35	
	density	8940	
	CTE	16.7	
	C_{th}	385	
Au	E_{11}	48.5×10^9	46.0×10^9
	Poisson's ratio	0.26	
	density	14800	
	CTE	14.2×10^{-6}	
	C_{th}	160	
Software		CoventorWare™	Ansys

Figure 35 shows the plot of the calculated resonance frequencies and measurement data of a screen-printed membrane with electroplated copper. Both simulations show an increase in the first resonance frequency value with increasing copper-layer thickness. The comparison of the measurement data without the use of copper, and with 50- μm and 220- μm copper-layer thicknesses shows good mutual agreement.

The deviation between simulation with set 2 and experiment is only in the range of -20 Hz to 60 Hz. The decrease in stiffness parameter can be explained by statistical distribution of the material coefficients. Therefore, future thermodynamic investigations rely on set 2. The simulated resonance frequency for the case without copper metallization serves as the reference system for subsequent FEM simulations. The simulated resonance frequency of the reference system is 1592.3 Hz.

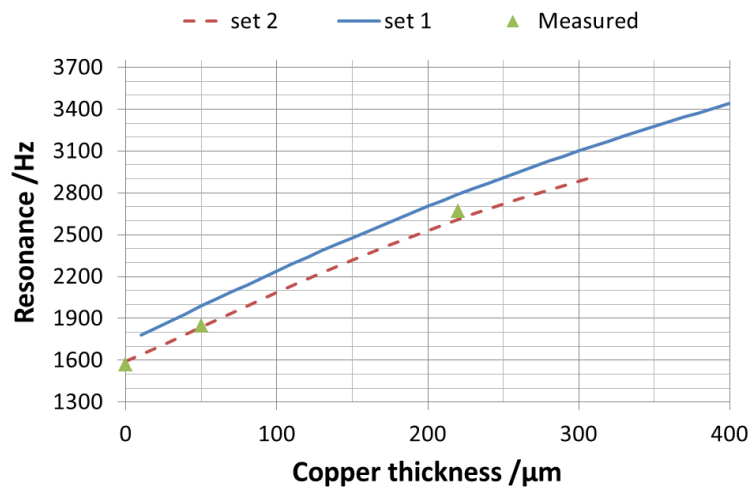


Figure 35 Resonance frequency as a function of the copper-layer thickness for two different sets of piezoelectric material properties.

Initial curvature of the membrane

Stress in the piezoelectric layer can cause membrane bowing. Therefore, the shape of the stressed membrane differs from the membrane in the plane form. Plane stress in the piezoelectric layer induces a spherical membrane bowing. The membrane is concavely or convexly curved with a bow in the range of (or even larger than) the membrane thickness (cf. Figure 36(a)). For instance, measurements of screen-printed mirror substrates show an initial curvature of 2.5 m with a bow of $\sim 50 \mu\text{m}$. Simulations are carried out to investigate the influence of membrane bowing on its resonance behaviour. The focus of this simulation is to investigate whether the direction or magnitude of the curvature determines a resonance frequency shift. The analysis is divided into two steps—prestress in the membrane that generates the initial membrane curvature and the

subsequent calculation of its resonance frequency. The prestress can be applied by a force or by a constrained displacement of the membrane centre. In this investigation, the prestress is applied by a surface load (pressure) on the surface of the top electrode and the induced bow is calculated (cf. Figure 36 (a)). In the second step, the geometry of the model is updated to the deformed configuration with the generated displacements of the prestress (*UPGEOM*); however, the prestress effects are not included (*PSTRES, off*). Subsequently, the modal analysis is performed.

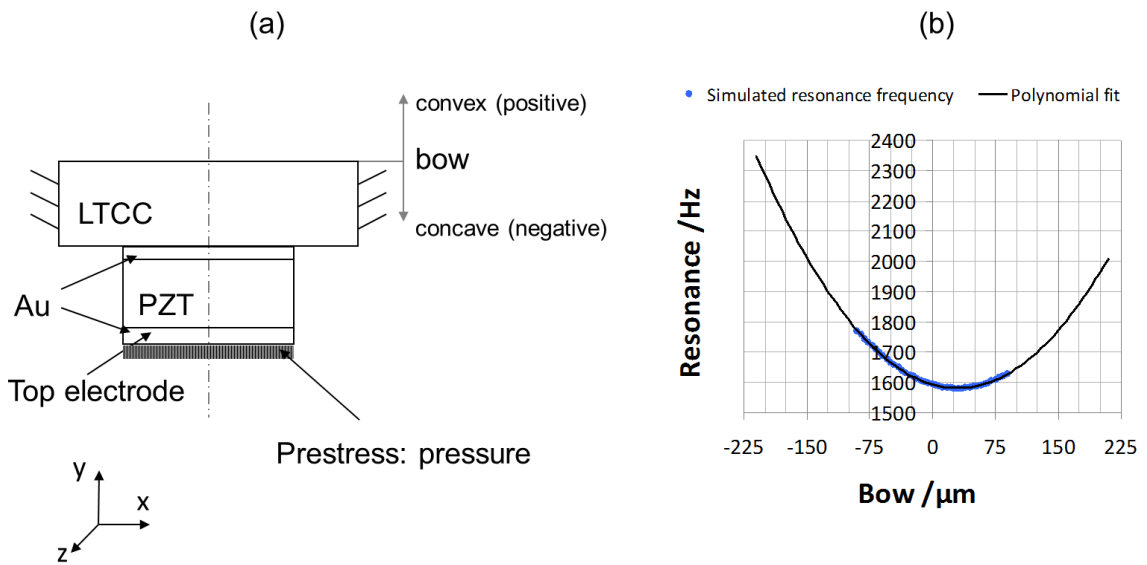


Figure 36 (a) Mechanical model with fixed rim and applied prestress on the top electrode, (b) Modeled change in resonance frequency by initial curvature of the membrane.

The results show a steep increase in the first resonance frequency for negative (concave) bowing (cf. Figure 36 (b)). Positive bowing leads to a small decrease of 15 Hz at a 25-μm membrane deflection (minimum). Further deflection results in an increase in the first resonance frequency. The relative change of first resonance frequency is up to 10 % for membrane curvature variations (bowing) up to -40 % of the substrate thickness. Bowing up to +40 % of the substrate thickness results in less than 2 % relative change of first resonance frequency. A polynomial fit ($\text{resonance} = 0.0133 \times \text{bow}^2 - 0.8095 \times \text{bow} + 1592.3$) approximates the change in the first resonance frequency, thereby leading to an increase of ~30 % and ~20 % in the resonance frequency for bowing of -100% and +100%, respectively, of the substrate's thicknesses. Bowing in the range of the substrate

thickness induces a strong modification of the first resonance frequency, in agreement with the observations for thin films^{119,120}.

The simulations provide evidence that an initial membrane curvature between 0 μm and +50 μm for the available screen-printed membranes does not induce strong modification of the first resonance frequency. The observed deviation of the first resonance frequency between measurement and simulation (deviation of about -20 Hz) can be explained by the convex membrane shape variation.

Residual stress in the membrane

Residual stresses in the membrane are caused by different mechanisms, and they are very difficult to predict and control (cf. sec. 4.2.39). Therefore, simulations serve to investigate the influence of residual manufacturing-imposed stresses on the membrane deflection and resonance frequency. A prestressed modal analysis is carried out for different compressive and tensile prestress levels in the piezoelectric layer. The stress level range from -100 MPa to +100 MPa. Positive values indicate tensile stresses, and they arise due to shrinkage and polarization of the piezoelectric layer. The mirror membrane bends upwards in this case (positive bow, cf. Figure 36 (a)). In contrast, compressive stress bends the membrane downwards. As in the previous simulation, the copper layer is not modelled, and fixed boundary conditions are applied to the membrane's rim. The simulation is divided into two steps. In the first step a large-deflection static analysis (*NLGEOM, ON*) with prestress effects is performed (*PSTRES, on*). The initial state of the piezoelectric layer is defined by the *INISTATE* command. The stress levels are applied only in x and z by assuming a plane stress condition in the entire piezoelectric layer (*INISTATE, DEFINE,,,,, S_x, S_z*). No stress occurs in *S_y* as the layer can shrink along its thickness direction. The solution of the loading reveals stress-induced membrane bowing. The membrane bowing (*UPCOORD, 1, on*) and the stresses (*PSTRES, on*) are imported to the subsequent modal analysis.

The simulations reveal a different stress-induced membrane deflection for tensile and compressive loading (cf. Figure 37). A tensile stress of 100 MPa results in 164 μm of membrane deflection, while a compressive stress of -100 MPa results in a membrane deflection of -300 μm .

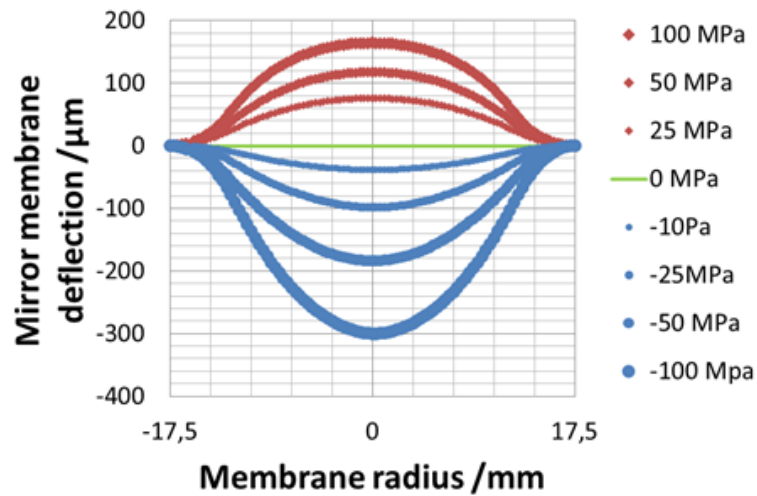


Figure 37 Membrane deflection for different tensile and compressive stress levels.

Both tensile and compressive stress level magnitudes ≥ 10 MPa induce an increase in the first natural frequency (cf. Figure 38). The compressive stresses increase the first natural frequency by a larger value than that by tensile stresses. The analysis of low stress level of ≤ 10 MPa reveals a small decrease of 3.11 Hz in the first resonance frequency for 1 MPa of tensile stress (cf. Figure 38(b)). No stress-induced decrease in the first natural frequency is observed for compressive stress. The stress-induced shape variations in the membrane are large, and they are in the range of the membrane thickness.

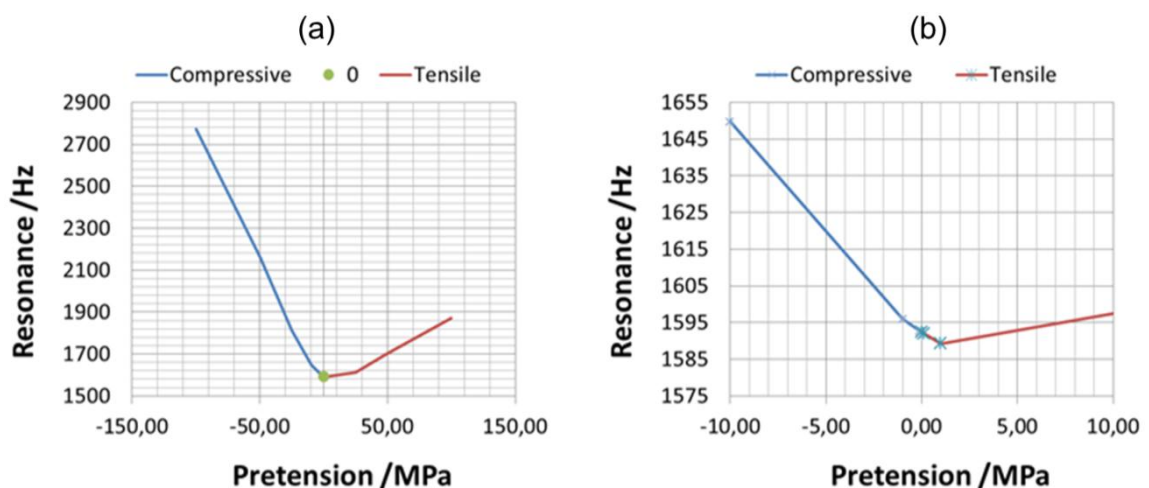


Figure 38 (a) Stress-induced resonance shift for stress levels between -100 MPa and +100 MPa, (b) Resonance shift for low stress levels.

In order to examine if these changes are attributed to the stress level in the membrane or to the induced shape variations in the membrane, the variations are compared with the simulation results of the *initial curvature of the membrane*. The comparison with the polynomial fit reveals an excellent agreement for P-V deflections between $-100\ \mu\text{m}$ and $75\ \mu\text{m}$; this indicates the dominance of the shape variations (cf. Figure 39). Therefore, the minimum first natural frequency is expected for a $25\text{-}\mu\text{m}$ P-V deflection as in the case of the initial curvature of the membrane. Increasing stresses lead to deviations from the polynomial fit of the initial shape-variation-induced frequency shift. These variations can either be attributed to the stress level in the membrane or to deviations from the polynomial fit for large deflections. However, this discussion is not considered relevant to the content of this work.

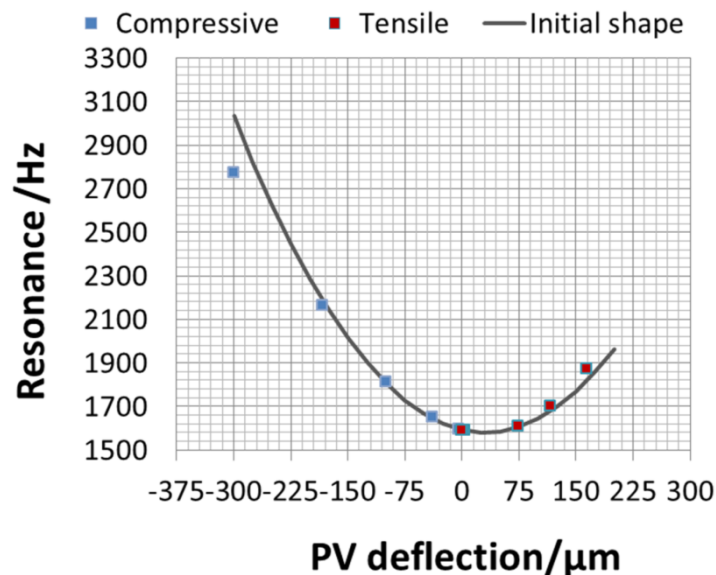


Figure 39 Comparison of the induced frequency shift depending on the membrane deflection.

However, a question arises to the reason for the different magnitudes of the stress-induced deformations. The simulations do not consider material non-linearity; however, they reveal non-linear membrane behaviour depending on the load direction. This is surprising as Hooke's law shows a linear relationship between strain and stress via the Young's modulus, and it is independent of the load direction. In order to understand this effect, the case for 50-MPa tensile and compressive prestresses are illustrated in Figure 40 (arrows signify dilatation).

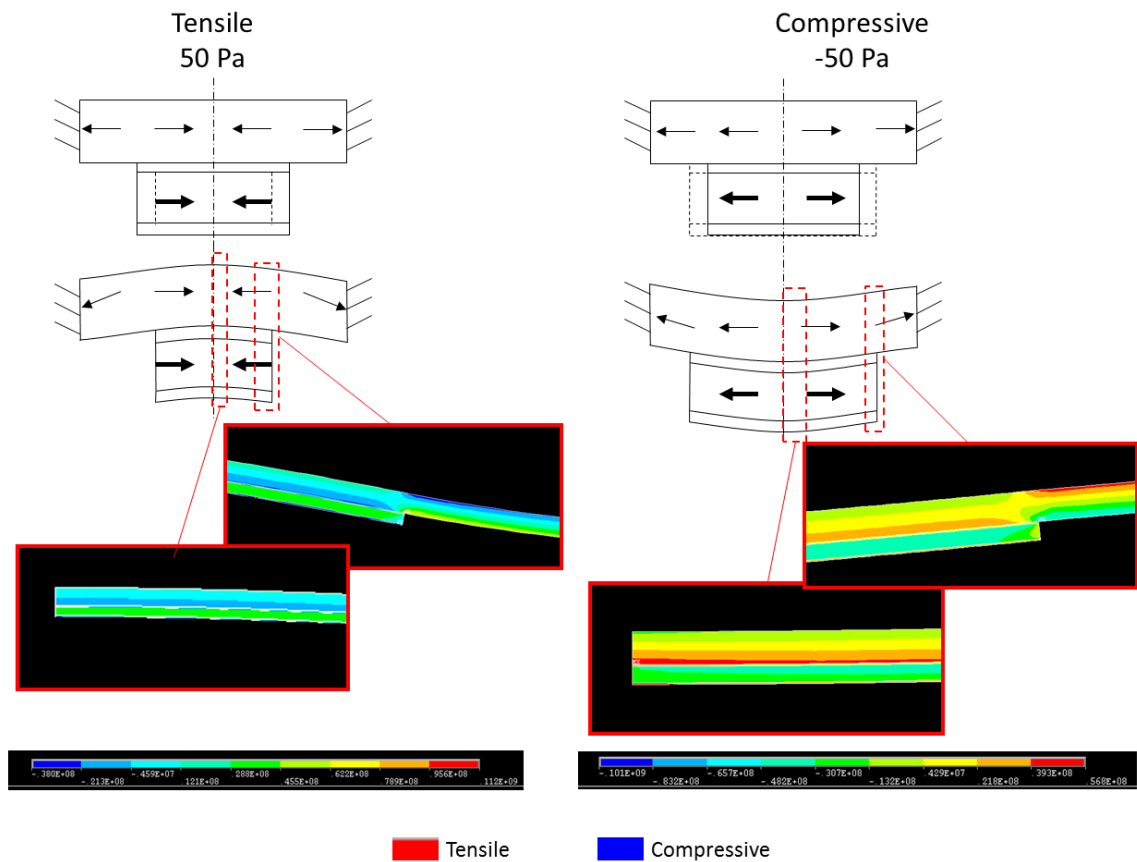


Figure 40 Comparison of dilatation and stress S_x for tensile and compressive pre-tension of the piezoelectric membrane. The arrows represent the forces in the mirror membrane.

Tensile stress in the piezoelectric layer contracts this layer and the central part of the membrane. The tensile prestress induces an upward bending of the membrane that is inhibited by the clamping at its rim (this constraint on the rim counteracts the piezoelectric layer contraction). In the case of compressive prestress, the membrane is dilated by the stress in the piezoelectric layer. Hence, the membrane bends downwards. The dilatation arrows indicate a lower restoring force when compared with that for tensile prestress. Thus, the compressive stress-induced bowing is larger compared with that for tensile prestress. Figure 40 also shows the stress along the x-direction (S_x) corresponding to radial stress in the axisymmetric set-up. Tensile prestress induces the largest stress level in the discontinuity between the membrane and the piezoelectric layer. In the case of compressive stress, the largest value of S_x occurs at the membrane centre. The S_x values range from -38 MPa to 112 MPa for tensile

prestress and from -101 MPa to 56.8 MPa for compressive prestress. The membrane induced-stress magnitudes are comparable in both cases.

The piezoelectric layer shows reverse trends due to opposite loadings. The meshed elements at the piezoelectric layer centre and outer rim show the maximum stress values, and these elements and values are deselected to eliminate (rough) discretization influences and artefacts (stress concentration at geometric discontinuities). After the deselection of the peak stress values, the piezoelectric layer shows S_x values between -20.7 MPa and -43.4 MPa for compressive loading and between 22.7 MPa and 43.7 MPa for tensile loading. These reverse values gain in importance due to the complex strain asymmetry between tensile and compressive mechanical loading in piezoelectric elements. In case of perpendicular polarized PZT, higher strain occurs for tensile loading when compared with that for compressive loading. These effects cannot be modelled due to the lack of material data.

5.2.3 Thermally-induced changes: homogeneous loading

The analytical simulations confirm the scenario of an ML set-up with a defined copper-layer thickness causing no bowing by temperature change. This *zero deflection* ML set-up shall now be confirmed by FEM (ANSYS). The first simulation step calculates the thermally-induced bowing for a large-deflection (*NLGEOM, ON*) static analysis of an ML membrane. Temperatures of 10 K and 30 K are applied in the simulation to all the membrane nodes and the stress matrix is calculated (*Pstress, on*). The shape variation and the stress distribution of the membrane is analysed and compared with the closed-form solution. The layer thicknesses are obtained from Table 10 and the material properties from Table 7 and Table 9. The CTE of the piezoelectric thick film is set to $8 \times 10^{-6} \text{ K}^{-1}$ and the copper-layer thickness is variable. The ML design is shown in Figure 41(a). The membrane has a radius of 12.5 mm (radius of the piezoelectric thick film). The centre of the axisymmetric membrane is fixed and the thermally-induced deflection due to homogeneous loading is calculated for 10 K and 30 K for copper-layer thicknesses up to 200 μm . The maximum membrane

deformation along the membrane radius at the top of the LTCC layer gives the thermally-induced deflection.

The P-V membrane deformation remains stable for large copper-layer thicknesses between 100 μm and 200 μm for both loading cases (cf. Figure 41 (b)). The values are negative as the membrane deflects downwards. Lower copper-layer thicknesses decrease the magnitude of the membrane deformation steadily until no deformation is introduced. A further decrease in copper-layer thickness and the absence of a copper layer lead to an increase in deflection; the membrane bends upwards. The membrane deflection along the membrane radius for copper-layer thicknesses between 10 μm and 18 μm for the 30-K loading is also shown (cf. Figure 41 (c)). Low copper-layer thicknesses of 10 μm and 12 μm lead to a concave membrane and copper-layer thicknesses of 16 μm and 18 μm lead to convex membrane deformation. A copper-layer thickness of 14 μm leads to zero thermally-induced deflection. The thermally-generated strains are self-balancing at this *zero deflection* ML configuration.

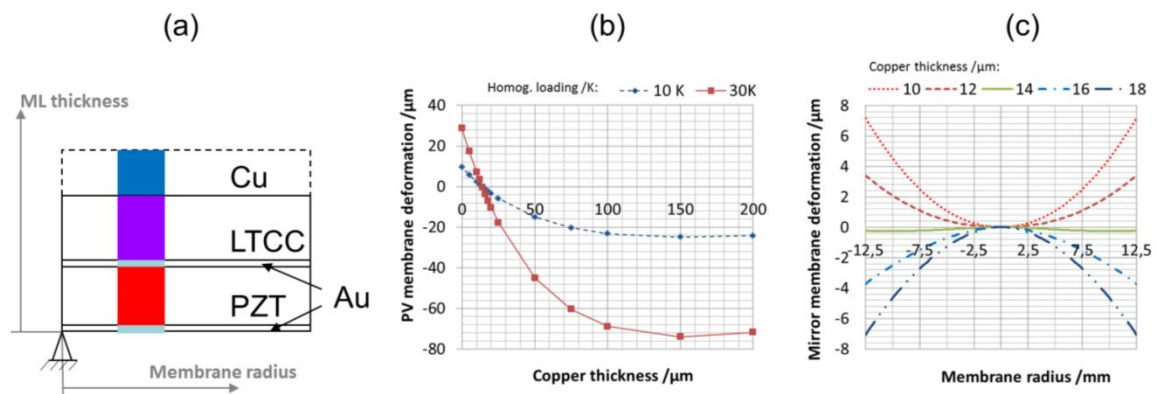


Figure 41 (a) Mechanical model and boundary conditions, (b) P-V membrane deformation for copper-layer thicknesses up to 200 μm at 10-K and 30-K homogeneous loadings. (c) Mirror membrane deformation along membrane radius. Zero deflection multilayer set-up requires 14 μm of copper-layer thickness.

A comparison between the analytical method and FEM reveals a qualitative conformity about the existence of a *zero deflection* copper-layer thickness. The *zero deflection* copper-layer thickness of 14 μm is smaller than the analytically evaluated thickness of 19 μm . The calculated membrane deformations also differ. The analytical results are almost double the FEM results. This is due to the analytical calculation of the deflection by assuming a circular membrane shape

and the utilization of the equation for the circle. Figure 41(c) depicts that the membrane deflection is not fitted well by a circle. Nevertheless, the qualitative membrane deformation over the copper-layer thickness (cf. Figure 41(b)) is comparable with the analytical results for the deflection in Figure 27. The next set of investigations evaluates the comparability of the stress in each layer.

The stress in each layer is calculated and mapped on a path at a distance of half the membrane radius along the ML thickness. Temperature loads lead to layer dilatation that depends on the CTE of each layer. Variations in CTE (and thus a dilatation mismatch) lead to layer stresses. Stress discontinuities occur at the interfaces as the values of the elastic moduli and CTE change (differ). The ML expands along the membrane radius, and each layer undergoes tensile or compressive stresses.

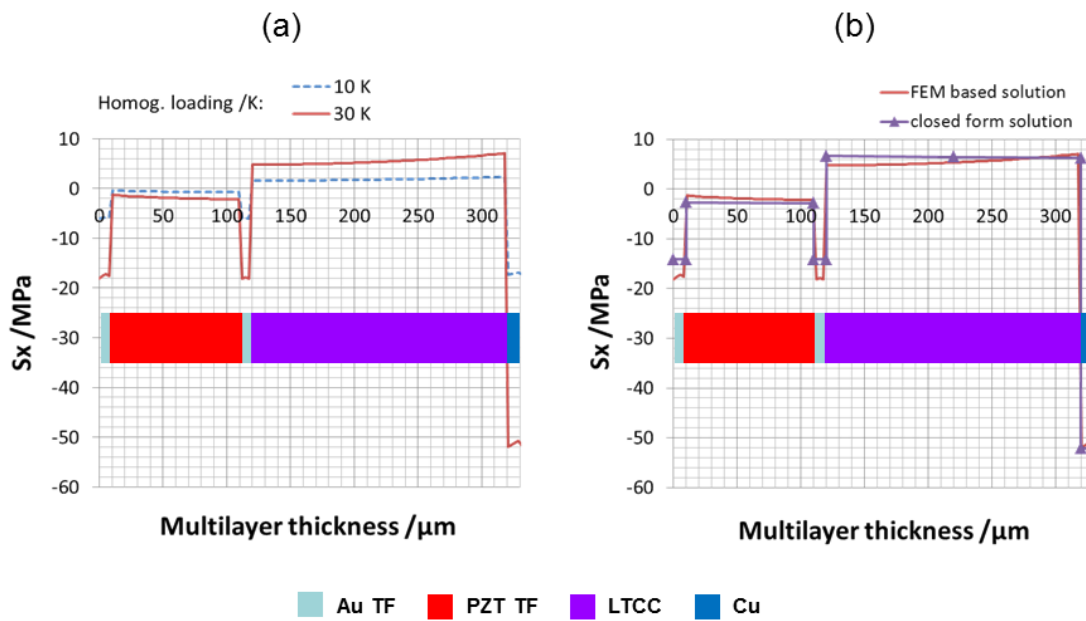


Figure 42 (a) S_x calculated by FEM for temperatures of 10 K and 30 K. Positive values indicate tensile stress and negative values indicate compressive stress. (b) Comparison between FEM and closed-form solution reveal good agreement of the results.

Analysis of the stress level (S_x) reveals compressive stresses in the metallic layer and small tensile stresses in the ceramic layer (cf. Figure 42 (a)). The compressive stresses originate due to the large CTE of the metallic layers, and the expansion inhibition is due to the CTE of the ceramic layer. The magnitudes of S_x increase with temperature loading as the suppressed thermal strains increase. The fatigue

strength² of the ceramic layers decreases with increasing tensile stresses. The manufacturer-specified LTCC tensile strength of 320 MPa¹⁴⁰ is not critical compared with the occurring stress level. The tensile strengths of the gold thick film and copper are 52 MPa and between 69–365 MPa, respectively. Both tensile strengths are not reached during the above thermal loadings.

The zero-deflection FEM results for a temperature of 30 K are compared with the ML closed-form solutions of stress distribution from studies ¹³⁶ and ¹³⁹ (cf. Figure 42 (b)). The stress distributions are in excellent agreement, and this proves the applicability of the force and moment balances based on the analytical model. The large expansion of copper is balanced by those of the gold thick film and the piezoelectric layer.

Effects of boundary conditions and piezoelectric layer discontinuity

The mirror design features a smaller diameter of the piezoelectric layer with sandwiching electrodes when compared with the diameters of the LTCC substrate and the copper thick film. The *zero-deflection* ML approach is applied next to the piezoelectrically-optimized DM design. The simulations validate the thermally-induced deflection and change in resonance behaviour at a homogeneous temperature loading of 30 K with change in the copper-layer thicknesses and piezoelectric layer discontinuity. Two boundary conditions are investigated—a fixed mirror membrane rim and a simply-supported membrane (cf. Figure 43). The mechanical equivalents of these conditions are mirror mounts with extremely small CTE values that prevent the expansion of the membrane and mirror mounts that allow a thermally-induced deflection identical to that of the unmounted mirror membrane and permit rim rotation. The thickness of the copper metallization is varied between 0 μm and 200 μm while calculating the thermally-induced deflection. The simulations also investigate the influence of piezoelectric CTE variations of (4, 6 and 8) $\times 10^{-6} \text{ K}^{-1}$ on the thermally-induced deflection. The large-deflection static analysis is followed by modal analysis. The

² Stress that can be applied to the material, without causing fatigue failure.

coordinates of the nodes are modified based on the thermal loading (*UPCOORD*, 1, *On*). The prestress effects are activated (*PSTRESS*, *On*) in the simulation and the modes are extracted using the Block Lanczos method. The modal analysis is executed for a fixed mirror membrane rim.

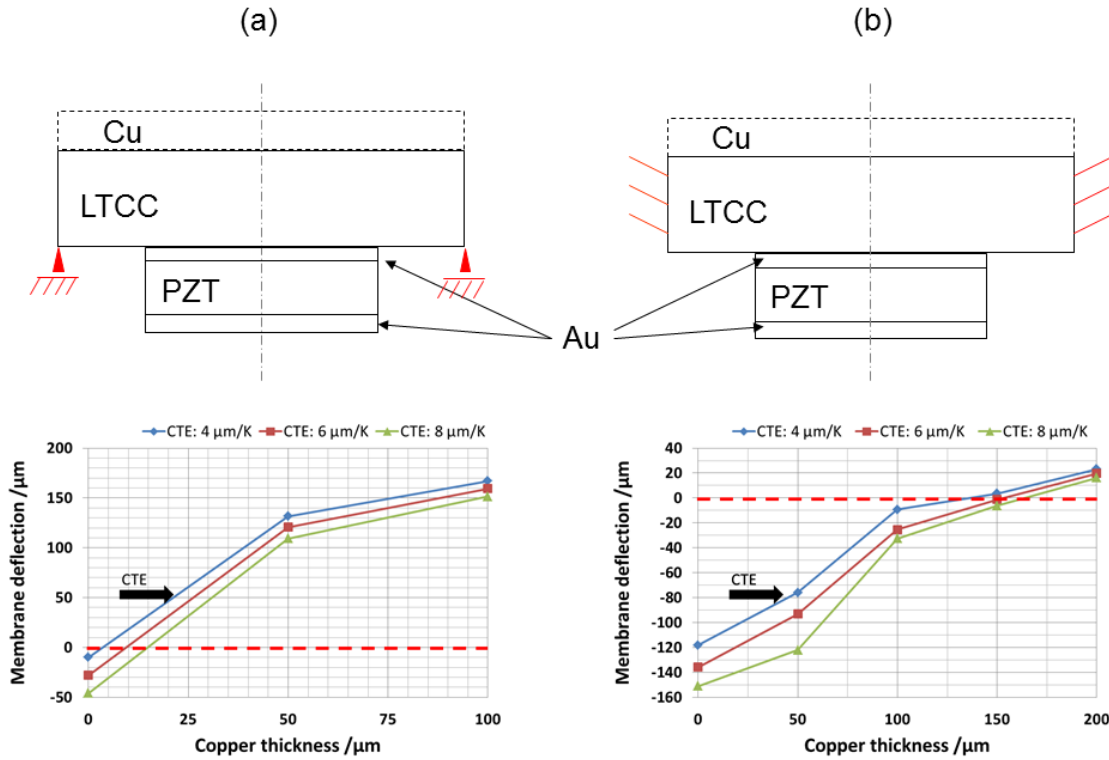


Figure 43 ML membrane's centre deflection for CTE values of (4, 6 and 8) $\times 10^{-6} \text{K}^{-1}$ for (a) simply-supported mirror membrane and (b) fixed rim boundary conditions.

Figure 43 depicts the model and the constraints of thermal analysis for both boundary conditions. The thermally-induced P-V membrane variations for different copper-layer thicknesses and CTEs of the piezoelectric layer are shown below each model. The simply-supported membrane (cf. Figure 43 (a)) shows an increase in thermally-induced deflection with increasing copper-layer thickness. The absence of a copper layer leads to a negative thermally-induced deflection. The *zero deflection* copper-layer thickness for the simply-supported membrane is between 5 μm and 20 μm depending on the piezoelectric layer's CTE. The *zero deflection* copper-layer thickness increases with the piezoelectric layer's CTE. The subsequent modal analysis (not shown) reveals a natural frequency shift that is

directly attributed to the membrane deflection, and thus, this shift is minimized at the *zero deflection* copper-layer thickness.

The fixed boundary condition (cf. Figure 43 (b)) reveals a large negative membrane deflection in the absence of a copper layer. The membrane deflection magnitude decreases with the copper-layer thickness, and no thermally-induced deflection occurs for a copper-layer thickness of around 150 μm . A further increase in the copper-layer thickness leads to a (positive) increase in the membrane deflection. The zero-deflection copper-layer thickness increases with the piezoelectric CTE value. The simulations show a copper-layer thickness between 130 μm and 170 μm for zero deflection, depending on the piezoelectric CTE value. In a manner similar to the case of the simply supported edge, a thermally-induced change in the mirror membrane shape results in a change in the resonance behaviour. The stress distribution at 150 μm copper-layer thickness under fixed boundary conditions does not induce a change in the resonance behaviour. The stress stiffening results in no significant change in the resonance behaviour.

The simulations assume simplified boundary conditions; this is not true for the real mirror mount as here a combination of both simplified boundary conditions apply. Nevertheless, the simulations provide the copper-layer thickness value for both boundary conditions with minimized membrane deflection. The application of the DM in high-power laser results in the requirement of excellent heat handling properties and thus the choice of the fixed rim over the simply-supported rim, as the heat dissipation potential increases with the copper-layer thickness. The next set of simulations investigates realistic boundary conditions through the simulation of the mirror assembly with a mirror membrane and mount, and the simulations assist in the choice of the mirror mount material.

5.2.4 Examination and selection of mirror mount material

The mount material needs to meet various requirements. The material needs to be solderable and exhibit high thermal conductivity and standard machining properties along with ease of integration into the optical set-up. The possibility of cooling systems within the mount also needs to be considered. Preferably, the

mount must not introduce additional membrane deformation due to temperature changes.

Solderability is achieved by the provision of a wetting surface through thin-film coating processes (e.g., PVD³ and CVD⁴) or thick-film coating processes. Metals with high thermal conductivity are suitable for mount material. In this section, I identify metals that prevent deformation in the thick film metalized mirror membrane due to temperature changes.

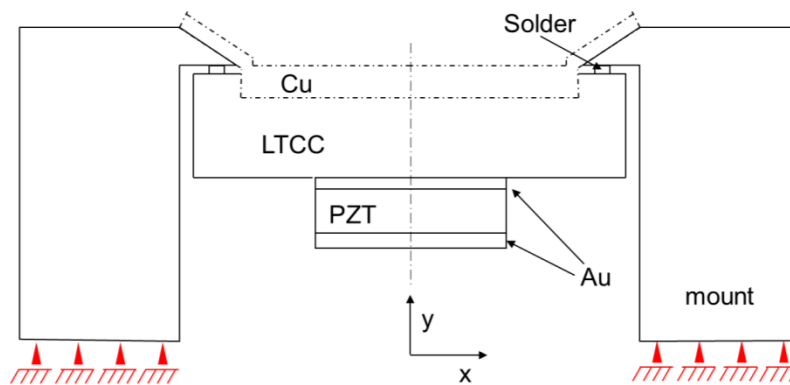


Figure 44 Simulation model with mount and boundary conditions (figure not drawn to scale).

Therefore, I simulate the assembly consisting of an LTCC mirror substrate, a PZT layer and sandwiching electrodes, solder, and a copper layer grown onto both the LTCC membrane and the metallic mount. The mirror substrate is soldered using 24 conical joining geometries that are equally spaced in a metallic mount with a diameter of 40 mm. The conical joining geometries have bores of 1 mm diameter, and they are placed onto the membrane mounting aid and filled with solder bumps. The developed axisymmetric simulation model simulates a 1-mm-wide and 10- μm -thick solder layer (Sn3Ag0.5Cu) between the mount and mirror substrate. The conical joining geometries are not modelled. The movement of the centre of the model (mirror membrane) is suppressed along the x-direction, and the mount's bottom area of support is allowed to radially expand. Figure 44 shows the cross-section of the model for a simplified representation.

³ Physical vapour deposition

⁴ Chemical vapour deposition

I followed the procedure described in section 5.2.3 for thermal loading. The membrane deformation at the membrane centre is detected for copper-layer thicknesses of 150 μm , 200 μm , and 225 μm for different mount materials. The following mount materials are investigated: aluminium (Al), Invar[®] (Fe65Ni35), Kovar[®] (Fe-Ni-Co alloy), copper (Cu), W85Cu15 (WCu) and CE7 (Si70Al30). Aluminium is chosen because of its application in mechanical engineering and its inexpensiveness. Copper has good thermal conductivity. The CTE of Invar is very low. The materials W85Cu15, Kovar[®], and CE7 are considered because they have CTEs similar to that of LTCC. The mount materials exhibit CTEs between $1.7 \times 10^{-6} \text{ K}^{-1}$ and $23.8 \times 10^{-6} \text{ K}^{-1}$.

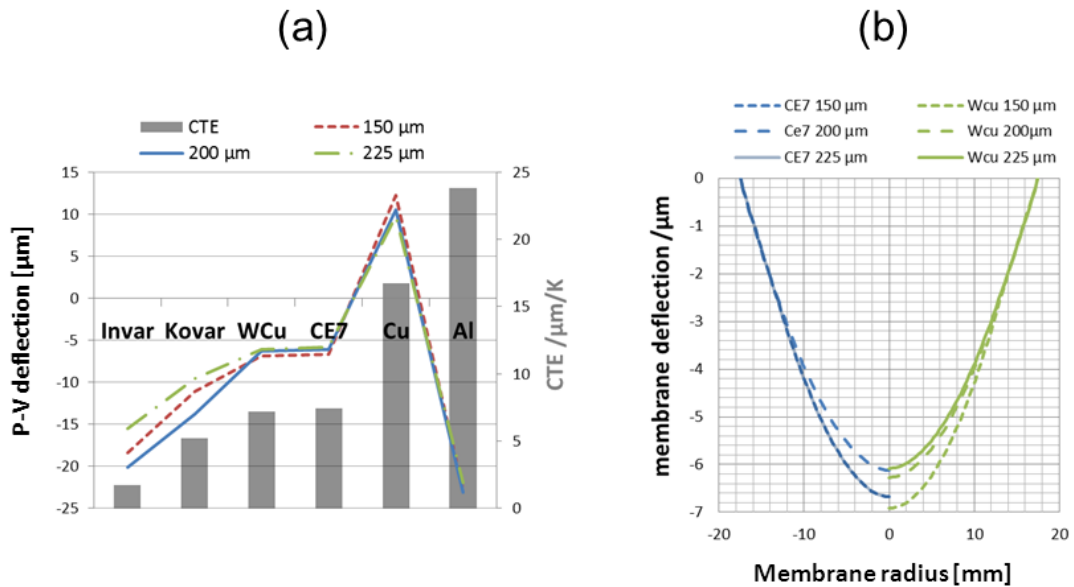


Figure 45 (a) Thermally-induced P-V mirror deformation for different mount materials. (b) Comparative representation of the simulation results of membrane deformation for CE7 and WCu.

The results of the P-V membrane deflections show considerable dependence on the mount material (Figure 45 (a)). In particular, aluminium (CTE = $23.8 \times 10^{-6} \text{ K}^{-1}$) and invar (CTE = $1.7 \times 10^{-6} \text{ K}^{-1}$) cause large membrane deformations due to their strong CTE mismatch when compared to the CTE of the LTCC substrate. The insensitivity of the membrane deflection with copper-layer thickness variations increases with the CTE values of the mounts. Kovar[®] has a CTE ($5.8 \times 10^{-6} \text{ K}^{-1}$) that is compatible with that of LTCC; however, it causes large P-V membrane deflections between -10 μm and -15 μm . Further, Kovar[®] also shows

a considerable dependence on the copper-layer thickness. A copper (CTE = $16.7 \times 10^{-6} \text{ K}^{-1}$) mount matches the CTE of the thick copper metallization; however, it shows a membrane deflection between $22 \mu\text{m}$ and $23 \mu\text{m}$.

The materials W85Cu15 and CE7 exhibit CTEs of $7.2 \times 10^{-6} \text{ K}^{-1}$ and $7.4 \times 10^{-6} \text{ K}^{-1}$, respectively, and they show the lowest deflection and dependence on copper-layer thickness variations. The comparative representation of W85Cu15 and CE7 show larger dependence on copper-layer thickness variations for W85Cu15 than that for CE7 in terms of the membrane deflection (cf. Figure 45 (b)). The CE7 material shows the same thermally-induced deflection ($0.2 \mu\text{mK}^{-1}$) for thicknesses of $225 \mu\text{m}$ and $150 \mu\text{m}$. In contrast, for W85Cu15, the deflection decreases with increasing copper-layer thickness. This behaviour could be explained by the larger Young's modulus of W85Cu15 when compared with that of CE7.

The boundary conditions of the assembly's membrane differ from the simplified boundary conditions (simply supported and fixed rim). The assembly's membrane rim cannot freely rotate; it is fixed by the solder joints and the copper. This is the reason for the large value of the copper-layer thickness at which the deformation of the mirror membrane is zero. The simulation results also indicate the availability of a *zero deflection* mount material with a CTE between $9 \times 10^{-6} \text{ K}^{-1}$ and $11 \times 10^{-6} \text{ K}^{-1}$ for which there is no P-V membrane deformation. These mount materials include CE9 (AlSi60), W72Cu28, and CE11 (AlSi50).

5.2.5 Thermally-induced changes: inhomogeneous loading

The inhomogeneous loading of a DM is caused by laser beams that show an intensity distribution that varies with the distance r to the propagation axis. Beams that are mostly used in laser can be considered as Gaussian beams. Gaussian beams have transverse electric fields and an intensity distribution $I(r)$ that is well-approximated by the following Gaussian function:

$$I(r) = I_o \left(\frac{\omega_o}{\omega_r} \right)^2 \exp\left(\frac{-2x^2}{r^2}\right) = A * \exp\left(\frac{-2x^2}{r^2}\right) \quad (42)$$

The Gaussian-shaped intensity distribution implies a non-homogeneous absorption, and it induces a non-homogeneous temperature distribution in the

mirror membrane. Therefore, inhomogeneous loading differs from homogeneous temperature loading by environmental temperature increase, and it needs to be simulated. The thermally-induced changes by inhomogeneous loading are evaluated by simulations that implement a Gaussian-shaped heat flux. The heat flux is applied to the copper surface (line) of the mirror with a beam radius r of 1 cm (corresponding to a correctable laser beam with a diameter of 2 cm). The movement of the centre of the axisymmetric model is suppressed along the x -direction, and the mount's bottom area of support is allowed to move radially. The temperature at the mounts bottom area is maintained constant. Figure 46 shows the Gaussian heat flux and the model's cross-section (instead of the axisymmetric simulation model). The temperature change is evaluated at three points that are also marked in the figure. Point 1 is located on the copper surface and at the mirror centre, and Point 2 is located on the radius of the piezoelectric layer and at the mirror centre. Point 3 is on the radius of the solder joint on the surface of the deposited copper. This point would be a practical measurement point for a hand-held thermocouple unit that can monitor the temperature changes in the mirror assembly.

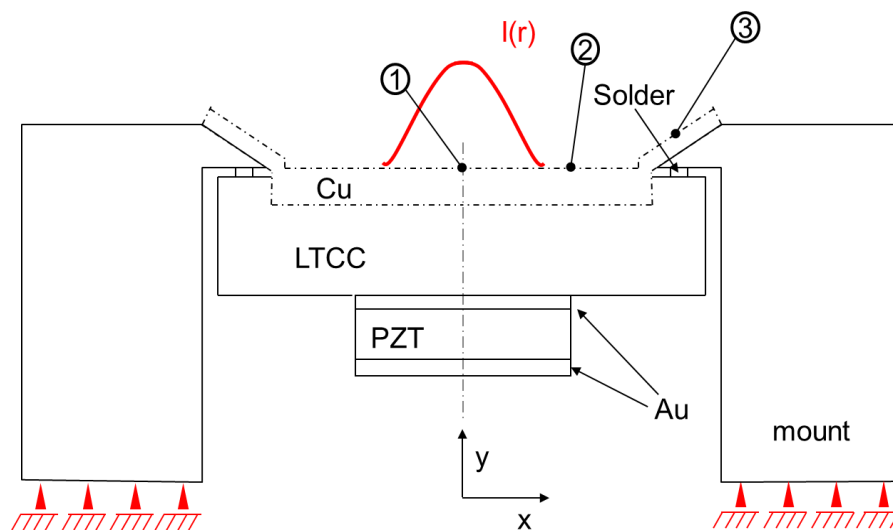


Figure 46 Simulation model of inhomogeneous loading with measurement points 1-3 (not drawn to scale).

Next, I investigate the impact of mount materials and copper-layer thickness on the inhomogeneously generated thermal changes. The mount materials are CE7,

CE11, and W85Cu15 and their properties are to be found in A4. The investigated copper-layer thicknesses are 100 μm , 150 μm , 200 μm , and 225 μm . The term A in equation (42) is scaled down until the heat flow is 1 W for every value of the copper-layer thickness. Surface convection effects are not taken into account as the maximum temperature increase is below 10 K.

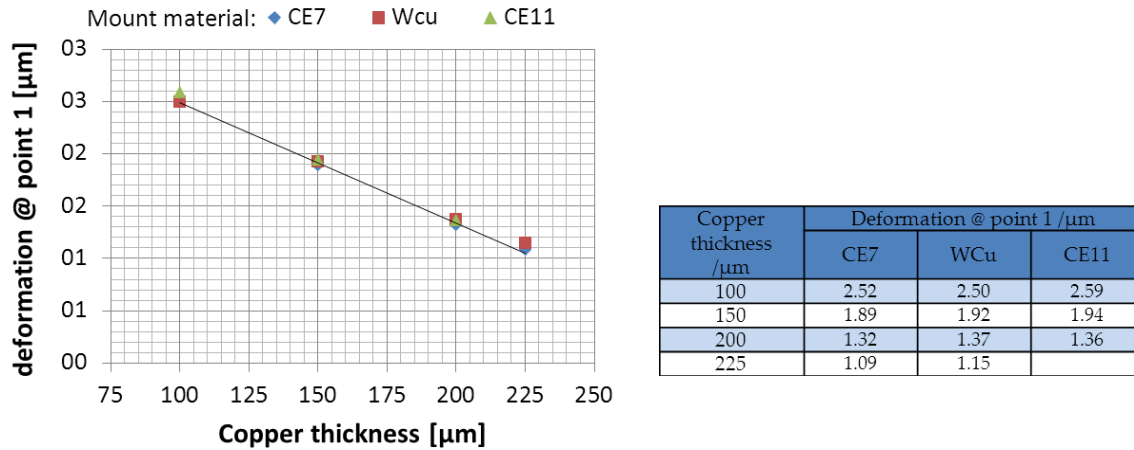


Figure 47 Induced deformation at measurement point 1 for different mount materials.

I evaluate the static and the transient membrane deformation, and the temperature increase at the characteristic points 1, 2, and 3 of the mirror assembly. Figure 47 depicts the heat-flux-induced deformation at measurement point 1. The deformation decreases (linearly) with the copper-layer thickness values from 2.5 $\mu\text{m}/\text{W}$ to 1.3 $\mu\text{m}/\text{W}$ for 100 μm and 200 μm , respectively. Thus, one can deduce the insensitivity of the mount material on the laser-induced deformation. Therefore, the following transient analysis of the simulation results is made solely for the CE7 mount material.

The transient behaviour of deformation and temperature at point 1 begins with a steep increase in the deformation until the curve flattens out (Figure 48). The simulated deformation and temperature increase are fitted by the following exponential curve:

$$T(t) = T_{\max} (1 - \exp^{-\frac{t}{\tau}}) \quad (43)$$

The time constants τ are different for deformation and temperature. The deformation time constants range between 1.91 s and 0.37 s for copper-layer thicknesses of 100 μm and 225 μm . The temperature time constants are larger,

and they vary between 1.85 s and 1.37 s. Both, deformation and time constants decrease with increasing copper thickness.

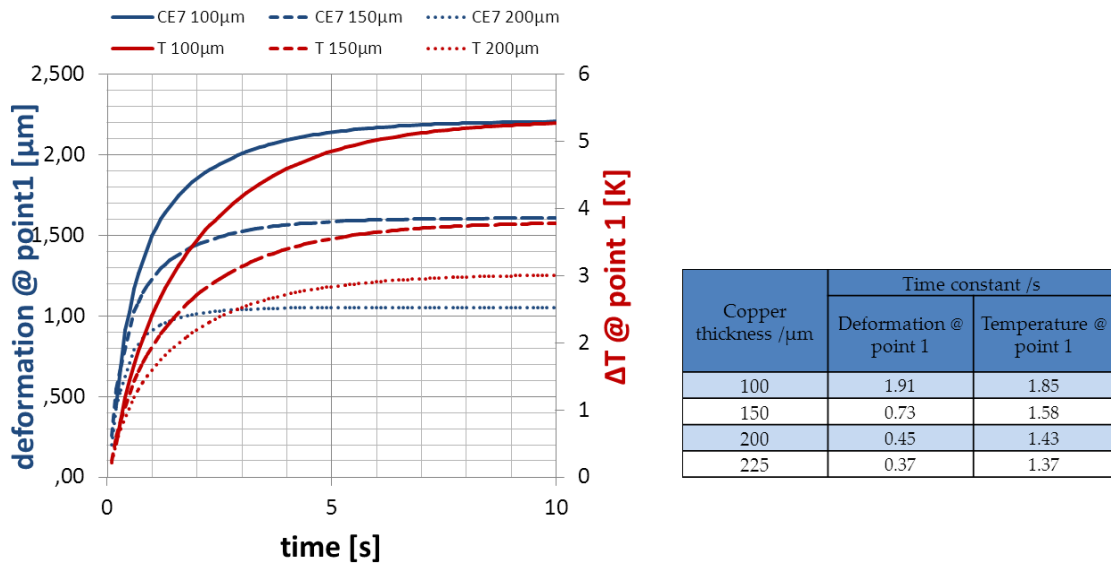


Figure 48 Laser-load-induced deformation and temperature change at measurement point 1 for different mount materials.

The temperature increases at measurement point 1 are 5.3 K, 3.8 K, and 3.0 K for 100 μm , 150 μm and 200 μm , respectively (cf. Figure 49). These temperature changes are moderate; they are not critical for depolarization of the piezoelectric element to occur. The laser-induced temperature changes at measurement points 2 and 3 are also of note (cf. Figure 49). The simulations reveal a temperature decrease with mirror radius and copper-layer thickness. Measurement point 2 only shows a temperature increase between 1.3 K and 1.9 K for 200 μm and 100 μm , respectively. The temperature increase at the mirror mount is very small, and it is between 0.8 K and 1.0 K for 200 μm and 100 μm , respectively. These changes are in the range of the measurement resolution temperature monitoring devices such as hand-held thermocouple units. The maximum temperature increase occurs at the mirror centre as the highest flux (laser intensity) is centered here as the absorbed power is dissipated mainly by the copper layer. The thermal conductivity of the mount material plays a subordinate role in heat dissipation.

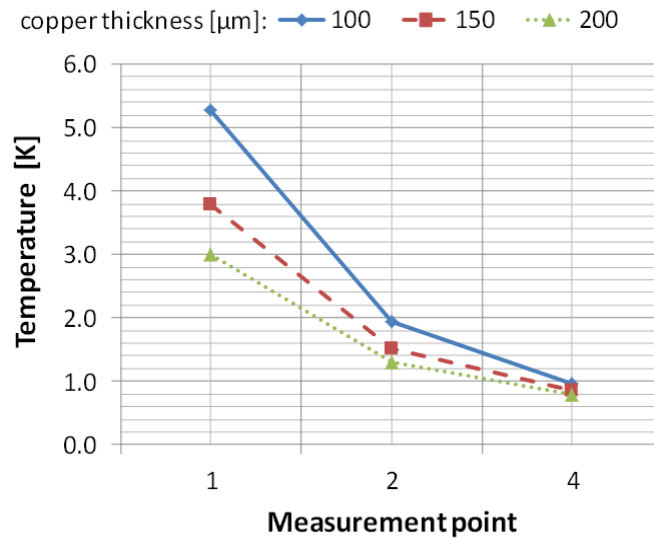


Figure 49 Simulated temperature increase on measurement points 1-3.

5.3 Summary of modelling results

The modelling results obtained in chapters 5.1 and chapter 5.2 are summarized in this section. The piezoelectric stroke decreases with increasing copper-layer thickness. Copper-layer thicknesses below 200 μm are preferred for a large piezoelectric stroke. A further increase leads to a very small total stroke. This is crucial as the piezoelectric layer will be further patterned into at least 15 segments to compensate for aberrations other than defocus.

The dynamic investigations show an increase in the resonance frequency with increasing copper-layer thickness. Further, a stiff piezoelectric layer increases the resonance. The influence of the curvature of a piezoelectric membrane is investigated in the next step. I show that the changes in resonance depend on the membrane's bowing direction. Convex bowing of up to 40% induces a relative change of less than 2% in the resonance frequency. Concave bowing of the same magnitude induces stronger relative changes of up to 10%. Bowing can be induced by residual stresses in the membrane. I show that the stress-induced bowing depends on the type of stress. A similar magnitude of tensile stress in piezoelectric thick films induces lower deflection than that by compressive stresses. The changes in the resonance frequency are not attributed to the stress magnitude, but to the shape variations and particularly the direction of

curvature for the present ML model. These results are important if the resonance is critical. Minor tensile stresses in the piezoelectric layer deform the membrane by a very small margin, and they induce only a weak resonance shift. Therefore, these stresses could compensate for the tensile stress in the copper layer or other metallization layers on the LTCC substrate.

The FEM simulation of the thermally-induced changes reveals the existence of a *zero deflection* copper-layer thickness due to which there is no bowing by temperature change for two different mirror membrane boundary conditions—simply-supported and fixed rim. The *zero deflection* copper-layer thickness is around 10 μm and 150 μm for the simply-supported and fixed rim conditions, respectively. The application of a metallic mount and technical mount geometries reveals an insensitive *zero deflection* copper-layer thickness between 150 μm and 225 μm for W85Cu15 and CE7. The thermally-induced changes by inhomogeneous loading using laser also reveal a preferred copper-layer thickness between 150 μm and 225 μm to ensure heat removal. The temperature increase at the centre is inversely influenced by the copper-layer thickness.

5.4 Construction guidelines for temperature loading of deformable mirrors

The results of the abovementioned simulations are elaborated into construction guidelines for homogeneous and inhomogeneous temperature loading of deformable mirrors.

5.4.1 Homogeneous loading

Homogeneous temperature loading of deformable mirrors is caused by environmental conditions during storage or working. An ambient temperature increase during storage can cause reversible or irreversible membrane shape variations. Reversible membrane shape variations include temperature-induced bowing of the substrate. They become irreversible if the thermally-generated bow and stress is too large and the layers delaminate from the membrane or the membrane irreversibly breaks. Other reasons include changes in material properties or thermally-induced shrinkage. Thermally-induced shrinkage such

as that due to post curing of adhesives in the mirror assembly can induce permanent membrane shape variations. An ambient temperature increase during operation (and thus the membrane bowing) changes the active mirror properties. An originally flat mirror can subsequently focus or defocus light. An active levelling by the piezoelectric actuators decreases the mirror's operating range, and therefore, a primary objective of deformable-mirror developers is to minimize the changes in the mirror membrane by homogeneous temperature loading.

By default, the CTE mismatches between the layers are minimized, thereby leading to an athermal design (cf. Figure 51). Practical realizations of such designs result in glued PZT disks on BK 10 or Pyrex substrates^{147,159}. Another practical realization exclusively uses piezoelectric disks glued together and polished to optical quality³³. An alternative athermal approach is the application of a piezoelectric layer on metal. Suitable metals are include titanium, AlSi70, W80Cu20, Mo80Cu20, and W85Cu15 with corresponding thermal conductivities of $7.6 \text{ Wm}^{-1}\text{K}^{-1}$, $120 \text{ Wm}^{-1}\text{K}^{-1}$, $248 \text{ Wm}^{-1}\text{K}^{-1}$, $165 \text{ Wm}^{-1}\text{K}^{-1}$ and $162 \text{ Wm}^{-1}\text{K}^{-1}$, respectively. These metal-based substrates are not popularly used as their manufacturing and finishing leads to increased labour costs when compared with that of glass substrates. The athermal approaches neglect the use of the metallization layer of the piezoelectric elements as well as the joining layer because they are much thinner than the piezoelectric elements in relative terms. The screen-printing process results in constraints in the substrate materials on which the piezoelectric and metallization layers are deposited. The substrate materials LTCC and Al_2O_3 are thermally well-adapted; however, the necessary structural metallization layer (front side metallization, sandwiching electrodes) are thick in relative terms. Therefore, the athermal design approach cannot be applied.

The investigations in sections 5.1.1 and 5.2.3 suggest another approach—an ML approach whereby the metallization layers are used to balance thermally-induced stresses and deflections between the substrate and the active layer. A similar ML approach uses functionally graded material (FGM)¹⁶⁰ that allows for a change in the composition and structure over volume, thereby resulting in

corresponding changes in the properties of the material. For instance, an FGM configuration can consist of thermal-resistant ceramic and fracture-resistant metal¹⁶¹. The material properties of the multi-material set-up can change gradually from one to another or stepwise in a discontinuous way, for e.g., along the thickness direction of the mirror membrane. In the case of the ML approach with stepwise change in material properties, the thickness and homogeneity of the single layer qualify the possible self-balancing. In particular, the copper layer enables the tuning of thermally-induced deflection. The simulations show the requirement of relatively thin copper layers (of 14 μm) for a simply-supported ML membrane. Such optimized ML membrane mirrors could be mounted with a discrete compliant membrane support, as described in section 4.5.1.

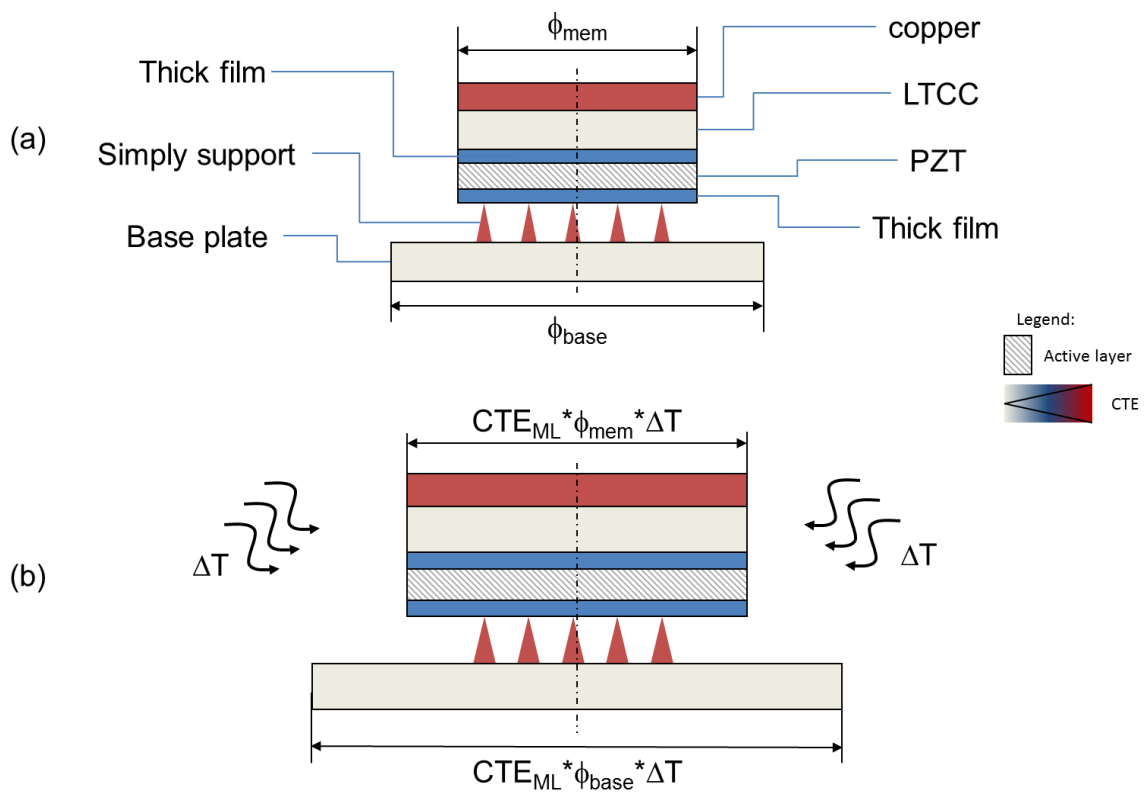


Figure 50 (a) Multilayer membrane with *zero deflection* design and simply-supported from underneath on a base plate. (b) The assembly is homogeneously loaded (heated) and the ML expands laterally ($\text{CTE}_{\text{ML}} = \text{CTE}_{\text{base}}$). The radial expansion of the mount (base plate) is equal to the radial expansion of the ML. The thermally-induced deflection is zero.

The simple support must not introduce mirror deformation during mounting, storage, and operation. This is ensured by spot-bonding (compliant pillar) and a base plate that matches the thermally-induced lateral expansion of the ML (cf. Figure 50). A limiting aspect of the discrete-supported ML membrane is the thin copper layer of the designed ML (cf. 5.2.3). Electroplated copper cannot be machined to optical quality for a layer thickness of 14 μm . The implementation of the mirror mount and the structural inhomogeneity of the piezoelectric layer plus its sandwiching metallization layers change the zero deflection thickness (cf. 5.2.4). The lowest theoretical mirror membrane deformation of a fixed, mounted ML mirror membrane is $-0.2 \mu\text{m}/\text{K}$. This value is achieved in the case of a CE7 mount with 200- μm copper-layer thicknesses.

5.4.2 Inhomogeneous loading

Inhomogeneous loading by a laser load changes the mirror requirements as a fraction of the laser load is absorbed. The usage of an athermal design approach would be possible in this scenario as a temperature increase in the mirror assembly would not lead to a bimetal effect. Nevertheless, a large temperature increase is a serious drawback that can lead to device failure; simulations show a radial temperature decrease from the mirror centre in case of a Gaussian laser load. Mirrors that can withstand high (laser) power preferably have a (dielectric) coating to decrease the power absorption. A high mirror temperature increase in the range of tens of Kelvins can lead to coating delamination and destruction. The stress distribution caused by the radial temperature profile can also lead to substrate delamination and breakage. The interface between the substrate and the active layer (adhesive joint) might post-cure, thereby inducing permanent mirror deformation or delamination. Another aspect is the temperature-dependent thermo-mechanical material properties of the single layers, and thus, the discarding of the athermal approach. Moreover, the piezoelectric properties are temperature-dependent, and depolarization of the screen-printed layer would lead to a mirror fall out. The laser-power-generated heat has to be dissipated and removed. The contemporary solution is the usage of a high heat

dissipation substrate, e.g., copper, that is bonded with the active (piezoelectric) layer (cf. Figure 51).

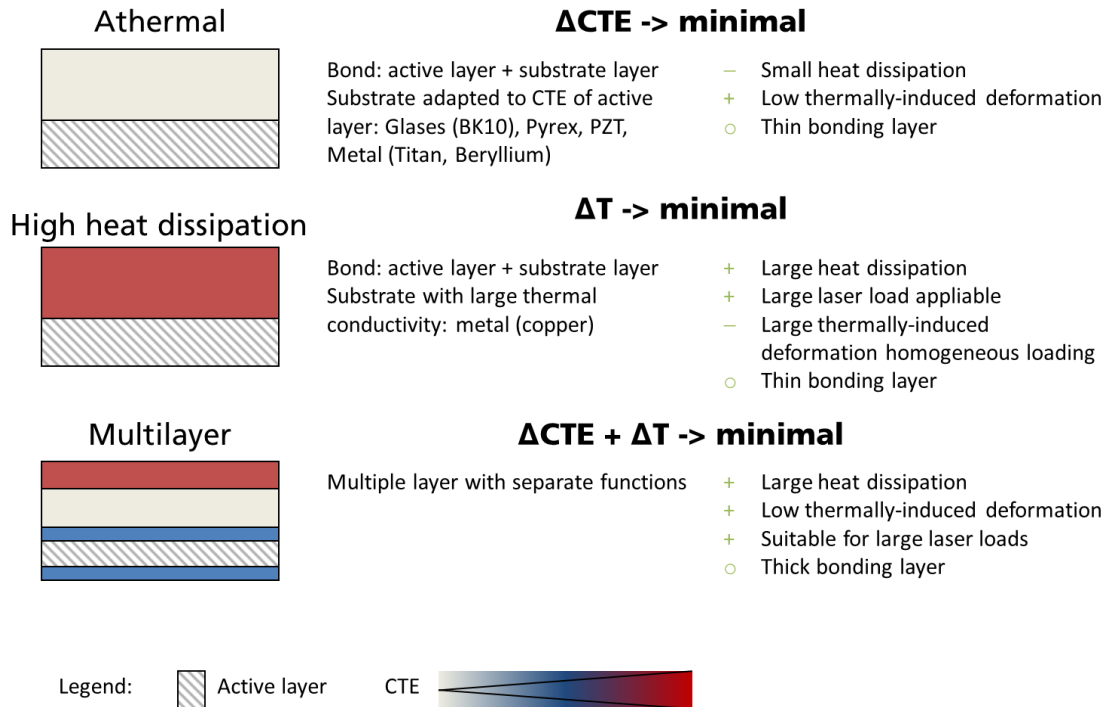


Figure 51 Thermo-mechanical design approaches for deformable mirrors.

The goal is to minimize the temperature difference in the mirror and between the mirror and the environment. The large heat dissipation and the low occurring mirror temperature gradient minimize the mirror deformation. However, the drawbacks persist in the form of (i) adhesive interface technology and (ii) the bi-metal effect. The bimetal effect can be reduced by the application of thermally adapted metals with good heat dissipation properties. W80Cu20, Mo80Cu20, and W85Cu15 are viable options.

A new promising construction enables the multilayer concept through the application of multiple layers with separate functions (cf. Figure 51). The reflective layer is a heat-spreading layer with a large CTE. Therefore, the rear surface of the mirror substrate is also equipped with layers that exhibit a large CTE. The thermally-generated strains are balanced and the bimetal effect is suppressed. The heat-spreading capability of the copper layer is $0.4 \text{ kWm}^{-1}\text{K}^{-1}$ and only a few materials such as silver, diamond, and graphite show higher

values. The use of a silver electrolyte (e.g., Atotec Ag 0-56) is a possible alternative to copper; it has properties similar to copper. In contrast, diamond and graphite are sophisticated materials that are more expensive. Nevertheless, a thin-layer CVD diamond⁵ on precision-tuned or polished mirror surfaces would also be an alternative. Thick diamond layers are not suitable as their high Young's modulus would decrease the piezoelectric stroke. Graphite exhibits interesting thermo-mechanical properties; however, its use suffers from its limited availability.

Another possibility of the multilayer approach is the pre-compensation of laser-generated mirror deformation either by manufacturing-imposed mirror deformation or homogeneous-thermal-loading-imposed mirror deformation. The tailoring of the thickness of the large CTE front surface layer leads to the tailoring of the thermally-induced deflection by homogeneous loading. The homogeneous loading of the optimized design results in a thermally-induced deflection with a rate of $-0.2 \mu\text{m}/^\circ\text{C}$, while a laser loading causes a deflection with a rate of $1.3 \mu\text{m}/\text{W}$. A 40 K temperature increase of the mirror assembly results in $-8 \mu\text{m}$ P-V membrane deformation that can compensate for an absorbed power of 6 W ($1.3 \mu\text{m}/\text{W} \times 6 \text{ W} = 7.8 \mu\text{m}$). This novel approach of specific loading is defined as compound loading and shall be reviewed as part of this work.

The theoretical investigation in case of compound loading show that the application of a mirror coating with a reflectivity of 99 % (1 % absorption) would lead to a laser load of 600 W compensated by a temperature increase of 40 K. A further increase of the reflectivity by a dielectric coating (reflectivity 99.9 %; 1 % absorption), leads to a possible laser load of 6 kW. The proposed mirror design is suitable to practically realize the pre-compensation of laser generated mirror deformations.

⁵ prepared by Microwave Plasma, e.g., Fa. Diamond Materials GmbH.

A variation of this approach is the application of a temperature gradient to the mirror membrane. The membrane is thermally loaded only at its rim. The resulting heat is transferred by conduction to the membrane's centre and surface where it radiates outward. A radial temperature profile is established and this bends the membrane downwards and compensates for the laser-induced membrane deformation. A similar idea has been proposed for thermal lensing in transmissive optics; either the transmissive optic element itself¹⁶² or a fused silica compensation plate¹⁶³ in front of the optic element is heated by a heating ring. A temperature gradient is established, and this changes the optical path in the heated element radially to the optical axis. Thus, the design compensates for the thermal lensing in optical elements.

6 Experimental verification of the deformable unimorph mirror design

This chapter reports on the manufacturing and characterization of a deformable mirror. The initial two sections introduce the deformable mirror assembly that is set-up based on the optimization in chapter 0. Thus, the realized mirror manufacturing regime and the experimental set-up is presented in 6.2 and 6.3, respectively. Chapter 6.4 reports on the characterization results—initial surface shape (cf. 6.4.1), piezoelectric stroke (cf. 6.4.2), and thermally-induced deflection. Special emphasis is put on the evaluation of the mirror response upon different thermal loading conditions (cf. 6.4.3 - 6.4.5). The results are compared in 6.4.6 with the expected values from the simulations. The last chapter gives a proof for compensation for large static wavefront aberrations.

6.1 Deformable mirror assembly

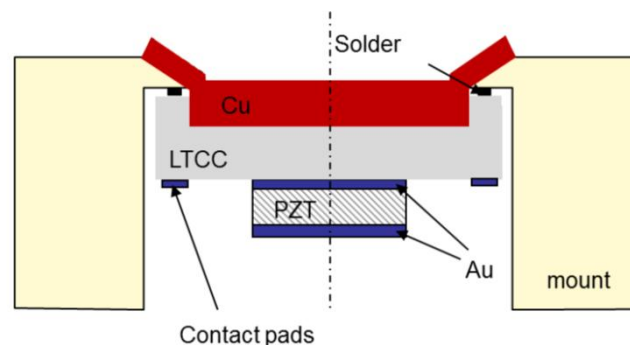


Figure 52 Cross-sectional view of the deformable mirror assembly.

Figure 52 shows the cross-sectional view of the designed DM assembly. LTCC is chosen as the substrate material. Its thickness is set to $200\ \mu\text{m}$; this value is the smallest possible LTCC thickness due to inherent sinter shrinkage and polarization of the piezoelectric layer. The thickness of the piezoelectric layer is $100\ \mu\text{m}$ that is driven by a maximum electric field of $2\ \text{kV/mm}$. Moreover, this thickness optimizes the electro-mechanical-layer properties; thus, the actuating potential is also optimized. The substrate's diameter is set to $34\ \text{mm}$ under fixed rim boundary conditions. The copper-layer thickness is set to $200\ \mu\text{m}$. This gives

a relative thickness of $a = 4$, and it results due to a trade-off between a low value of thermally-induced deflection for copper-layer thicknesses between $150\ \mu\text{m}$ and $200\ \mu\text{m}$ and a high piezoelectric stroke with thermally favourable copper-layer thicknesses.

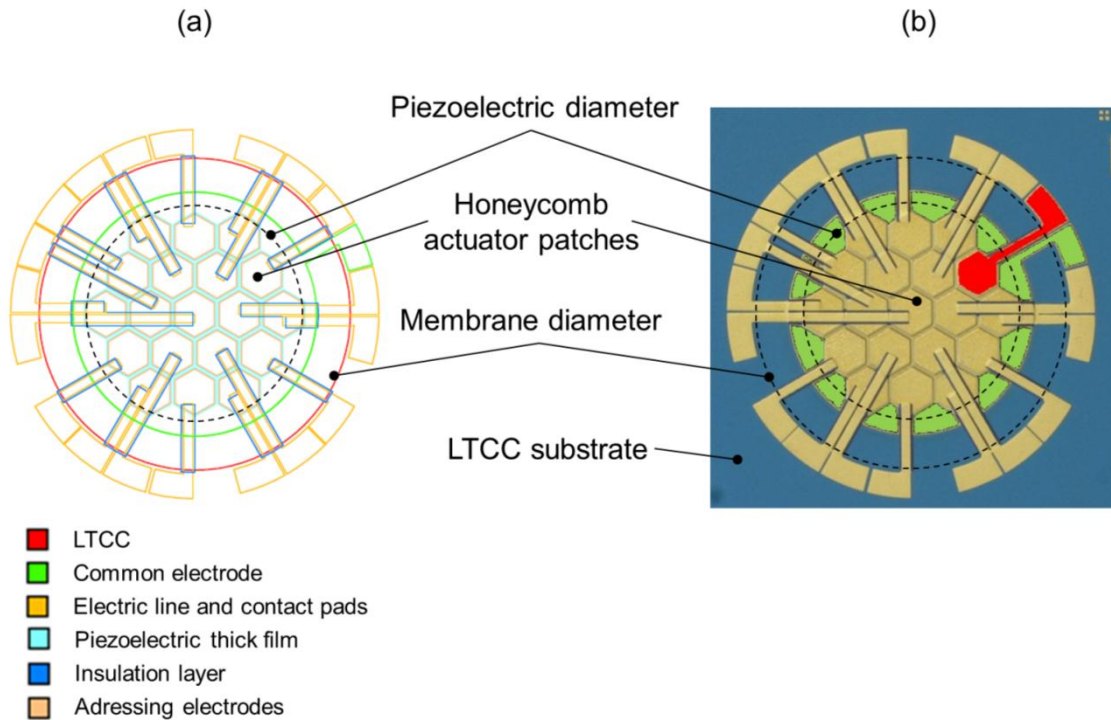


Figure 53 Comparison between (a) mesh design and (b) screen-printed sample mirror.

The total number of actuators is set to 19; nine actuators are designed to be placed external to the mirror aperture. Each actuator has a hexagonal (honeycomb) shape. Figure 53 shows the comparison of (a) the designed mesh layout with (b) the screen-printed actuator layout of the unimorph mirror. The 19 manufactured actuators each have an area of $17.1\ \text{mm}^2$. Due to each actuators shape, an inner and outer diameter of the piezoelectric pattern exist. The outer diameter is $24.7\ \text{mm}$ while the inner diameter is $21.2\ \text{mm}$. The area within the inner diameter is completely covered with PZT thick film while the area between inner and outer diameter is partially covered with the piezoelectric layer. This is due to the choice of the honeycomb pattern; the pattern cannot completely cover an entire circle. The averaged piezoelectric diameter is $23\ \text{mm}$. The piezoelectric stroke is maximized by the diameter ratio of the passive LTCC membrane to the active piezoelectric layer; this value is 0.75 (see page 88). Another analytical

optimization gives the value of 0.67 for an exact reproduction of the Zernike modes. The ratio of the manufactured sample is 0.66 with an averaged piezoelectric diameter of 23 mm and a manufactured substrate diameter of 34.7 mm. The calculated optimum aperture diameter ratios are 19.3 and 19.1 for $\varnothing_{\text{Substrate}}/\varnothing_{\text{Aperture}}$ and $\varnothing_{\text{PZT}}/\varnothing_{\text{Aperture}}$, respectively. The optimum mirror aperture needs to be experimentally defined. The designed parameters and the manufactured parameters of the developed DM are summarized in Table 12.

Table 12 Design parameters of the deformable mirror.

Design parameter	Value	Motivation	
Thickness _{LTCC}	200 μm	Smaller values are preferred for large piezoelectric stroke, Smallest possible LTCC thickness value is chosen due to shrinkage and polarization of piezoelectric layer	
Thickness _{Piezo}	100 μm	$E_{\text{field}} = 2\text{kV/mm}$, supply voltage = 200 V	
Thickness _{Copper}	200 μm	LTCC deformation in course of the manufacturing process \rightarrow tens of μm , Negative thermally-induced deflection due to homogeneous loading and large heat dissipation for inhomogeneous loading	
Relative thickness _a	2.6	Ratio of piezoelectric active to inactive layer thicknesses	
Total number of actuators	19	As per Equations (40) and (41), with a minimum of 15 actuators, 9 of which are placed externally	
Ratio $A/S = \varnothing_{\text{PZT}} / \varnothing_{\text{Substrate}}$		Design: 0.75 (p. 67)	Sample: 0.66 (calculated)
		$\varnothing_{\text{Substrate}} = 34.0 \text{ mm}^{(152)}$ $\varnothing_{\text{PZT}} = 25.5 \text{ mm}$	$\varnothing_{\text{Substrate}} = 34.7 \text{ mm}$ $\varnothing_{\text{PZT}} = 21.2 - 24.7 \text{ mm}$
		Design: 0.67	
		$\varnothing_{\text{Substrate}} = 34.0 \text{ mm}$ $\varnothing_{\text{PZT}} = 22.7 \text{ mm}$	
Ratio $\varnothing_{\text{Substrate}} / \varnothing_{\text{Aperture}}$	1.8	Design	Sample
		$\varnothing_{\text{Substrate}} = 34.0 \text{ mm}$ $\varnothing_{\text{Aperture}} = 18.9 \text{ mm}$	$\varnothing_{\text{Substrate}} = 34.7 \text{ mm}$ $\varnothing_{\text{Aperture}} = 19.3 \text{ mm (calculated)}$
Ratio $\varnothing_{\text{PZT}} / \varnothing_{\text{Aperture}}$	1.2		Sample
			$\varnothing_{\text{PZT}} = 23 \text{ mm (averaged)}$ $\varnothing_{\text{Aperture}} = 19.1 \text{ mm (calculated)}$

The LTCC has a mounting aid with a thickness of 600 μm on which the electric wirings and contact pads are screen-printed. The outer mirror diameter is 43 mm to that the metallic mount is adapted by its inner diameter of 44 mm. The mount material consists of CE7 that is machined by ultrasonic milling. The mount has 24 conical bores that are evenly distributed on a mount diameter of 40 mm. The bores have a smallest diameter of 0.7 mm at the front and a groove (1 mm \times 0.1 mm) at the rear. The conical bores and the groove (partly) are filled with tin-silver-copper (Sn3Ag0.5Cu) solder.

6.2 Mirror manufacturing

The mirror manufacturing regime is described in section 4.5. This section provides the details of the manufacturing steps for mounting, electroplating, and finishing of the mirror.

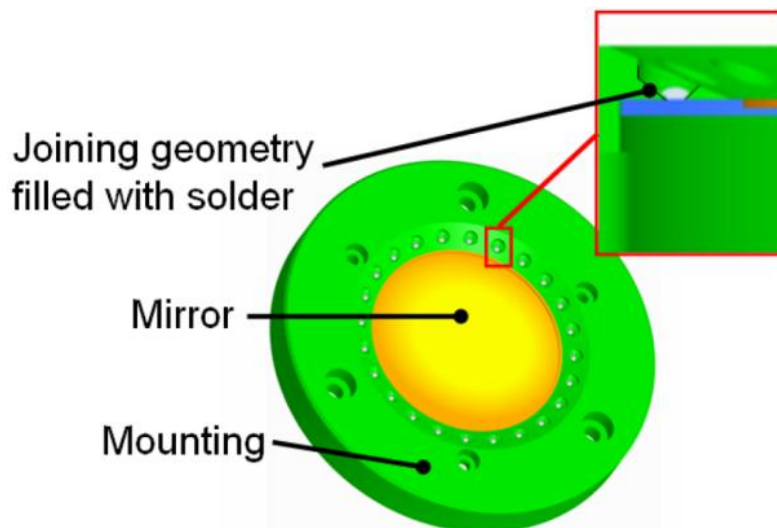


Figure 54 Design of the mounting and attached mirror including a detailed view of the conical joining geometry that allows the solder to form a joint between the mirror and the mount.

The screen-printed mirror membrane is soldered by means of the Solderjet Bumping process to the mount. This laser-based soldering process is flux-free, and it provides liquid solder droplets of tin-silver-copper (Sn3Ag0.5Cu). The solder droplets are jetted onto the mating parts, and they subsequently solidify. The diameter of the solder spheres is 760 μm , with each solder sphere providing 230 nL of solder alloy per droplet. Both the mating parts, i.e., the mount and mirror need to be wetted and fixed simultaneously. This is realized by the

provision of wetting surfaces and special joining geometries. The wetting surfaces on the CE7 mount and on the LTCC mirror substrate (mounting aids) consist of TiPtAu⁶ and TiCu, respectively, and both surfaces are applied by PVD. The thin TiCu layer on the LTCC substrate is used for both soldering and the subsequent copper plating. The mount (cf. Figure 54) has 24 conical-shaped joining geometries in which the liquid solder is deposited. The solidification of the liquid solder droplets and their inherent phase transformation ensures a material closure between the metallization and the solder, and a form closure is ensured by means of the joining geometries. In addition, the solder's thermal conductivity of $56 \text{ Wm}^{-1}\text{K}^{-1}$ guarantees thermal contacting between the mount and the mirror.

The copper wetting surface of the LTCC mirror is prepared for soldering by a one-minute etching process using 30% hydrochloric acid. This is followed by thorough rinsing with de-ionized water and isopropanol and finalized by a drying process under a nitrogen atmosphere. The wetting metallization on the mounts does not need special treatment. In the study, the process of soldering was divided in four runs; three bumps were delivered in the two first runs, six bumps in the third run, and twelve bumps in the last run. The bumps of the first run are placed at an angle of 120 degrees around the centre of the mirror, and the bumps of the second run are placed diametrically opposite those of the first run. The next six bumps are placed evenly between the solidified joints; each bump is placed with one (empty) joining geometry in between. The last run fills the empty joining geometries. The application of the solder droplets was accomplished using 20-ms laser pulses from a Nd:YAG laser system with an equivalent pulse energy of 3.2 J at a free-flight distance of 1.5 mm from the solder spheres. An visual inspection of the solder joints confirmed proper wetting at the cone-shaped holes of the mounts.

⁶ The titanium layer is used as the adhesion promoter, the platinum layer as diffusion barrier, and gold is the finish layer; this results in a total thickness of approximately 500 nm.

The electroplating of the copper layer is carried out after the mounting of the deformable mirror. This low-temperature process is based on the SurTec® 865 electrolyte. The electrolyte produces mirror-bright, ductile and low-stressed copper layers¹⁶⁴. The mirror's TiCu metallization on its front surface is contacted via the electrically-conductive soldered CE7 mount. The screen-printed rear surface of the mirror is hot-wired and masked. In this manner, the copper is plated onto the mirror's and (partly) the mount's front surface. It is also plated onto the solder joints.

The screen-printed membrane is inherently curved, and it is caused by the LTCC manufacturing and the shrinkage and polarization of the screen-printed layers. The copper layer is electroplated onto the warped (curved) membrane, and it needs to be machined to optical quality. The galvanic copper is grown onto the curved membrane, thereby acquiring the surface topography of the LTCC membrane. The SPDT process is adapted to cut the copper while retaining the membrane's inherent curvature. The process simply flattens the deviation from its curvature radius. Thus, a constant copper-layer thickness over the entire mirror membrane is achieved. This manufacturing step is challenging as the turning tool pushes the mirror membrane away during machining. The mirror membrane is strengthened during machining to address this issue (cf. Figure 55). Liquid adhesive layers are applied and cured on the rear surface of the mirror membrane. This process is repeated several times, thereby increasing the original LTCC membrane thickness many times over. A surface profilometer detects the changes induced by the membrane strengthening. The tool path for the objective curvature is calculated with respect to the membrane curvature induced by membrane strengthening. The SPDT process is performed and the machined membrane curvature is measured. Depending on the measured membrane curvature at this stage, a second SPDT process may be applied. The dissipation of the cured adhesive provides the desired membrane curvature. The mirror shape remains stable after machining as no additional stress is induced in the mirror membrane through the mounting process.

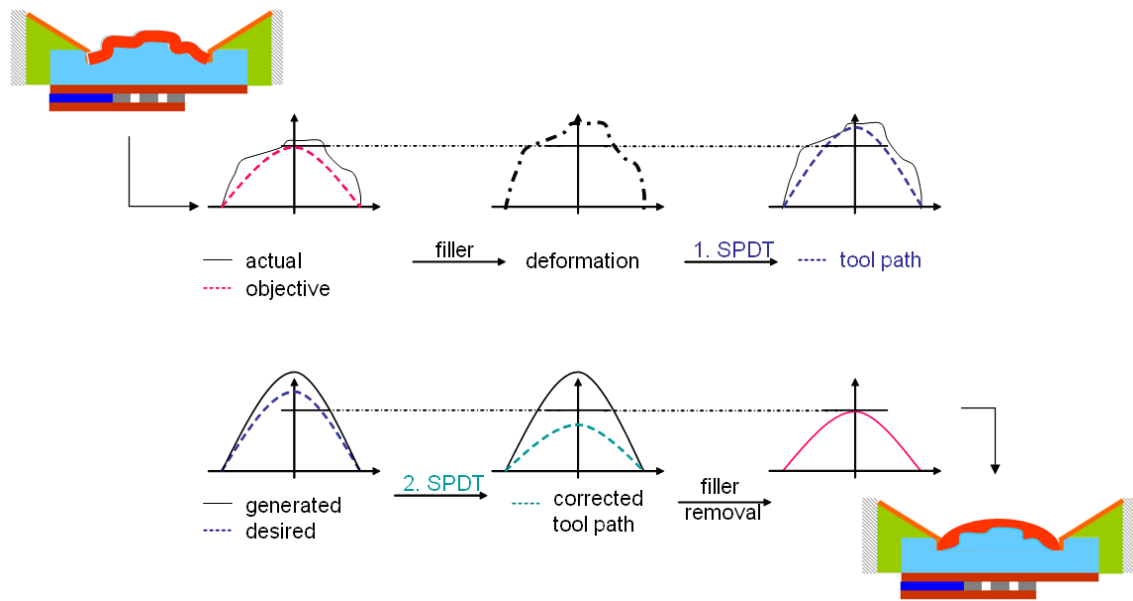


Figure 55 Single point diamond turning (SPDT) tool path generation. Dashed lines indicate the design tool path and solid lines indicate the membrane shape. The tool path is generated with respect to the filler-induced deformation and the mechanical load of the SPDT tool.

In the study, the measurement of the inherent membrane curvature was difficult as the P-V membrane-shape was in the range of $50\ \mu\text{m}$ on the front surface and more than $250\ \mu\text{m}$ on the screen-printed rear surface (diffuse reflection also needs to be considered for the measurement). Two measurement procedures were successfully applied—automated surface scanning with a laser triangulation sensor (cf. section 6.3.3) and fringe projection. The measurements revealed an upward bend with a radius between 1.5 m and 2.5 m in the membrane. The objective tool path radius was 2.5 m.

The machined mirror in its mount needs to be attached to housing with cooling and heating properties. Therefore, the mirror mount is attached to a back plate onto which a Peltier element and heat sink are fixed (cf. Figure 56). It is to be noted that the mounted mirror substrate and the back plate need to be thermally very well-adapted. The back plate is mounted on the housing by hinges. This link permits free radial expansion of the mount and the back plate. The heat dissipation between the housing and back plate is also very low. The joint between the heat sink, Peltier element, and back plate is thermally well-conducting and mechanically radially decoupled. This set-up ensures good

thermal connection between the mirror membrane and Peltier element. A weak mechanical coupling arises between mirror and the housing as well as between the mirror and the Peltier element (heat sink).

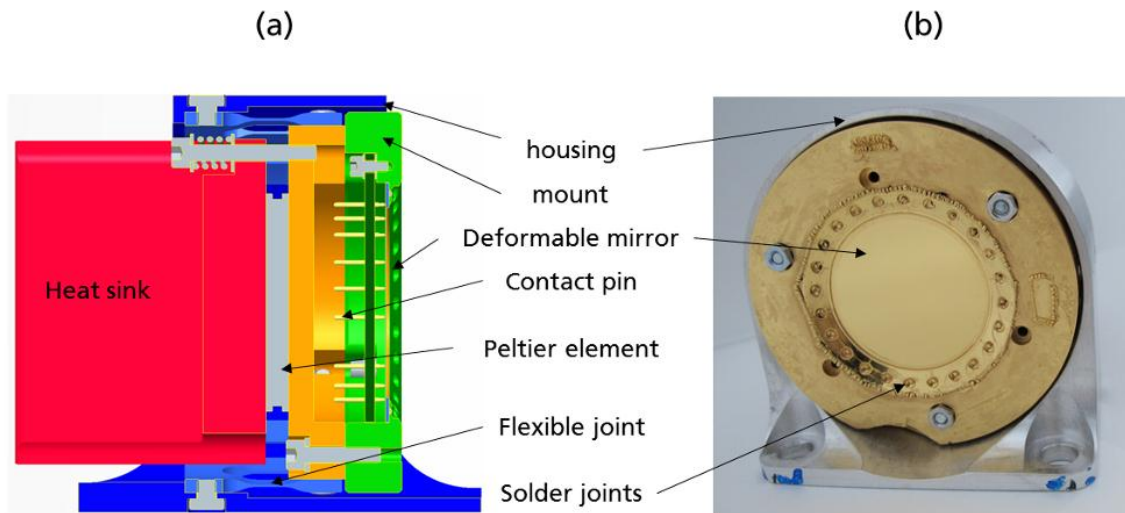


Figure 56 (a) Cross-sectional view of the deformable mirror mount with integrated Peltier element for thermal control of the mirror. (b) Image of the mounted mirror with applied gold coating.

6.3 Experimental set-up

The experimental set-up introduces the utilized characterization methods. It starts with the adaptive optical measurement set-up that measured the mirror response upon piezoelectric activation, homogeneous loading, inhomogeneous loading and compound loading. Characterization methods for the investigation of the static and dynamic mirror properties are also introduced.

6.3.1 Adaptive optical measurement set-up: homogeneous loading

The adaptive optical measurement set-up (cf. Figure 57) consists of a collimated laser diode (LD) emitting laser radiation at 535 nm. The laser beam is expanded to 25.7 mm and reflected by the deformable mirror. A beam splitter cube (BSC) directs the beam to a WFS and a second beam expander (BE 2) compresses the beam to the WFS aperture. The WFS (SHSLAB-HR-130-FW; Optocraft GmbH) has a dynamic range of 420 μm , a repeatability of 2.1 nm to 3.175 nm, and a measurement accuracy of 50 nm. The measurement plane of the WFS is

conjugated to the DM plane, thereby ensuring absolute wavefront measurement. The data from the WFS are analysed using SHSWorks software (Optocraft GmbH), and they are subsequently processed with LabVIEW (National Instruments). The LabVIEW also samples the measurement of the mirror temperature and controls voltages of the piezoelectric actuators and the power of the Peltier element.

The PC-based digital analogue converter (24-ch, 8-Bit PCI DAC card, OKOtech) generates analogue low-voltage signals. Subsequently, the signals are amplified to high voltages (HVA 40-ch, OKOtech) that activate the piezoelectric actuators. The Peltier element is controlled by a laboratory power supply unit (PSU, EA-PS 3016-20B, Elektro-Automatik), and it works in a LabVIEW-generated closed loop with a temperature sensor (digital thermometer HH506-RA, Omega) that is placed very close to the mirror membrane at one of the solder joints on the mount. The evaluation of the mirror response and the mirror temperature are carried out simultaneously. More details of the LabVIEW-based automated measurement and control system can be found in¹⁶⁵.

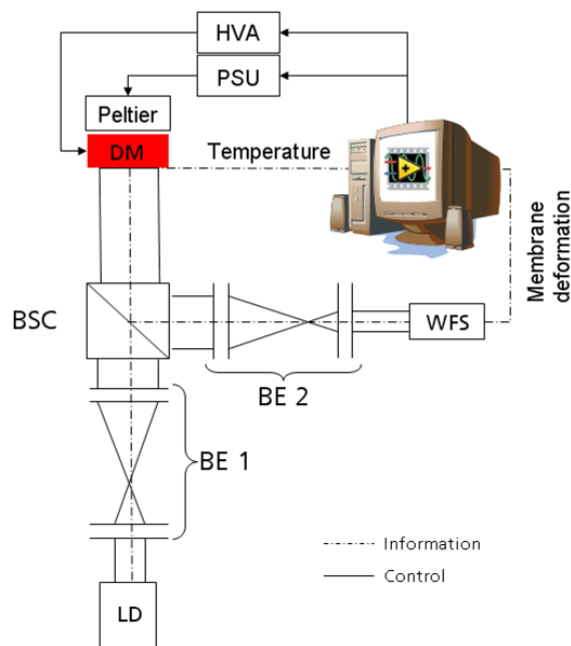


Figure 57 Adaptive optical measurement and control set-up: The collimated beam of a laser diode (LD) is expanded by a beam expander (BE 1), and it is incident on the deformable mirror. The DM reflects the light that passes through a beam splitter cube (BSC). A second beam expander (BE 2) adapts the light diameter to the aperture of the wavefront sensor (WFS).

6.3.2 Adaptive optical measurement set-up: inhomogeneous loading

The adaptive optical monitoring set-up as reported in section 6.3 is additionally equipped with a high-power laser path. The high-power laser beam loads the mirror and the mirror absorbs a fraction of the reflected power. The consequent changes in the mirror surface are analysed (cf. Figure 58).

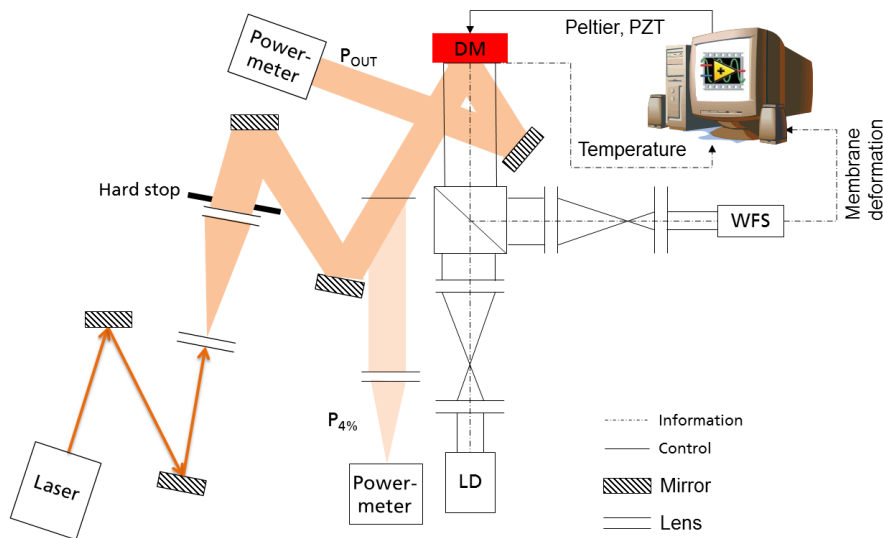


Figure 58 Experimental set-up for inhomogeneous and compound loading. High power laser beam is expanded to 20 mm whereat the hard stop ensures the beam diameter. Peltier element and piezoelectric actuators (PZT) are hot-wired during inhomogeneous loading and controlled during compound loading.

The high-power laser beam with a diameter of $5.0 \text{ mm} \pm 0.7 \text{ mm}$ is expanded to 20 mm by a beam expander and shaped by a hard stop that provides the necessary beam diameter. The expanded beam is incident on the DM at a small angle with reference to the normal to the mirror surface. Thus, the diameter remains constant and it is not elliptically deformed. The power of the reflected beam is measured by a power meter. Moreover, 4% of the incoming light to the DM can be detected. Thus, one can calculate the absorption of the mirror metallization (zero transmission and scattering). The gold coating of the DM provides absorption of 2% and a reflectivity of 98% at the emitted high-power laser wavelength. The high-power laser (JenLas® fiber cw 400) emits radiation at $1070 \text{ nm} \pm 10 \text{ nm}$, and it has an output power up to 400 W. The laser can be operated in the continuous-wave (cw) mode or modulated at a 100-kHz

repetition rate. The M^2 value is better than 1.1 and its polarization is random. The high-power laser is used with an isolator. The inhomogeneous loading of the DM is performed in three stages by varying the duty cycle. The duty cycle is maintained constant at 5%, 50%, and 100 %, and the laser power is varied. The piezoelectric elements of the DM are hot-wired and the Peltier element is only used for the compound loading.

6.3.3 Additional characterization methods

- The FLX-2320 (KLA Tencor) thin film stress measurement system is used to measure the mirror surface with and without homogeneous loading. A laser samples the mirror surface that reflects the light while an array of photodiodes detects the light. The measurements are line scans, and therefore, multiple repeats are required to obtain an impression of the 3D-surface. The measurement system also features a hot plate that is used to evaluate the thermally-induced deviation in the membrane shape. These measurements verify the adaptive optical measurements.
- A laser triangulation sensor (LTS, Keyence LK-G 10) measures the total mirror stroke and the mirror hysteresis. A one-point sensor that is mounted on an automated translation stage is used to position the sensor in the membrane centre.
- A single -channel vibrometer (Polytec OFV-511) measures the dynamic membrane behaviour. A sinusoidal electrical voltage with an amplitude of 2 V and an offset of 2 V drives the piezoelectric actuators. The frequency of the sinusoidal voltage is varied between 50 Hz and 3 kHz while measuring the deflection of the membrane centre.
- A scanning vibrometer (Polytec PSV 400) is used to evaluate the quasi-static behaviour of the mirror membrane. A sinusoidal electrical voltage (100 Hz) is applied to all actuators with an amplitude of 100 V and an offset of 100 V. The voltage varies between 0 V and 200 V. This measurement regime enables the detection of the static response of the mirror under moderate measurement durations.

6.4 Mirror characterization

Measurements of the initial mirror shape show the feasibility of using the developed SPDT process. The piezoelectric-induced membrane shape variation validates the mirror usability for wavefront shaping, and the thermally-induced membrane deflection shows the feasibility of the mirror's use under homogeneous temperature loading. These measurements validate the ML approach (simulation), and allow a comparison of the state-of-the-art solutions.

6.4.1 Initial mirror shape

The desired optical membrane shape is spherical; this is caused by the spherical-shaped screen-printed membrane. The SPDT-machined mirror shape is detected by two different measurement methods—the adaptive optical set-up and the Tencor FLX-2320 (both measurements are obtained taken with hot-wired piezoelectric actuators). The Tencor FLX-2320 measurements are repeated four times for an incident angle of 45° , and they show membrane radii of 2.502 m, 2.503 m, 2.500 m, and 2.497 m (c.f. Figure 59 (a)). The Shack-Hartman WFS measurements reveal a P-V value of $32 \mu\text{m}$ measured on a mirror aperture of 25.7 mm; the dominant aberration at this shape is defocus (cf. Figure 59 (b)). This results in a mirror radius of 2.6 m as determined by SHSWorks. The measured deviation from the intended spherical shape is $1.4 \mu\text{m}$ upon neglecting the Zernike polynomials piston, tip/tilt, and defocus (cf. Figure 59 (c)).

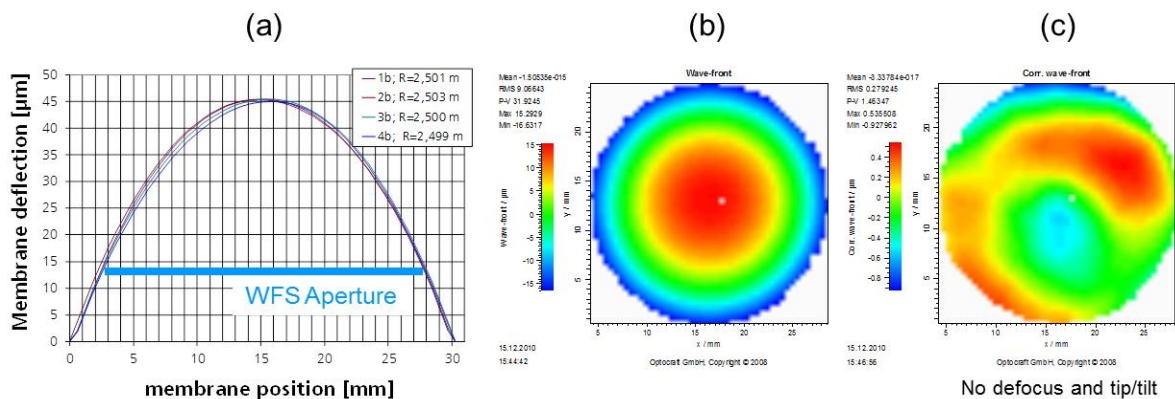


Figure 59 Initial mirror membrane shape: (a) Tencor FLX-2320 measurements reveal a radius of approximately 2.5 m. The WFS aperture of the adaptive optical set-up is also shown. (b) Measurement of the AO set-up. (c) Mirror shape without piston, tip, tilt, and defocus.

A portion of the piezoelectric stroke needs to be utilized to actively level the deviation from spherical shape. However, the small deviation of $1.4 \mu\text{m}$ of the SPDT-machined mirror membrane from defocus shows the high quality of SPDT machining. Thus, the results show the successful deployment of SPDT as a simple initial defocus of the mirror membrane can easily be pre-compensated by the optical system. Another option would be the reapplication of the SPDT to compensate for the deviation from defocus. Therefore, the measured membrane deviation would be used to generate the SPDT tool path.

The investigations in section 5.1.2 show a theoretical increase in the Zernike amplitude and purity if actuators are placed outside the mirror aperture. The piezoelectric actuator pattern has a diameter of 25 mm. Therefore, the mirror aperture to efficiently adapt Zernike polynomials needs to be further experimentally evaluated by evaluation of the piezoelectric stroke.

6.4.2 Piezoelectric stroke

This section investigates the working range of the piezoelectric actuators by their actuator influence function (AIF). An obvious result of the investigation is the active balancing (active levelling) of the deviation from the desired curved mirror membrane (cf. Figure 59 (c)) and the active setting of mirror shapes, e.g., the practical realization of Zernike polynomials by the superposition of the stroke of the single piezoelectric actuators.

The AIF is the mirror's response to the activation of one actuator; therefore, the AIF of each actuator needs to be measured. The individual stroke of the 19 single actuator pads characterizes the mirror potential to actively shape wavefronts. The AO set-up and the scanning vibrometer are used to evaluate the AIF on the mirror membrane. Each actuator is activated stepwise using a electric field of 2 kV/mm by the HVA, and the corresponding membrane deformation and P-V values are measured and calculated by the WFS. The results are validated by the scanning vibrometer. The WFS measurements for each of the 19 actuators are shown in Figure 60. All actuators are successfully activated. Measurements show a peaked AIF as a result of the (relatively) thin substrate.

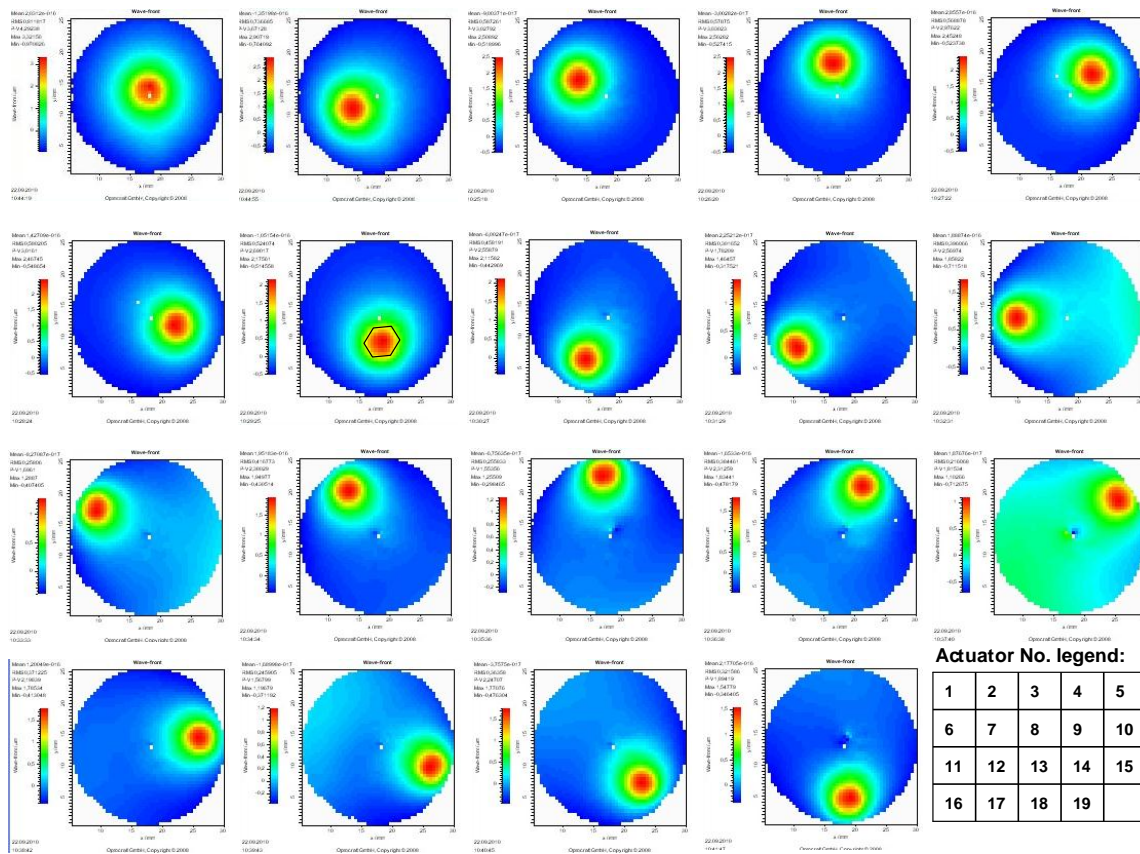


Figure 60 Measured actuator influence function for machined screen printed DM.

The results of the P-V mirror deformation by both the vibrometer and wavefront measurements are shown in Figure 61. The diagram depicts the P-V values of the AIFs for all 19 actuators, and it reveals an excellent agreement between the different measurement set-ups. This proves that the measurement plane of the WFS is conjugated to the DM plane in the AO set-up. The mean value of deviation is only $-0.01 \mu\text{m}$ with a standard deviation of $0.09 \mu\text{m}$. The deviation between both measurement set-ups originates from the non-triggered WFS measurements that involve slightly varying times between piezoelectric activation and image grabbing; this is due to the influence of piezoelectric relaxation. The position of the actuators on the active pattern is also shown. The largest deflection is due to the actuator at the centre of the mirror/actuation pad. The individual stroke decreases with radial distance from the mirror centre. The outer actuators 19, 17, 15, 13, 11, and 9 show the smallest stroke values that range

between 1.5 μm and 2 μm . The maximum stroke ranges between 2.6 μm and 3.6 μm , and it is generated by the inner actuators (1–7).

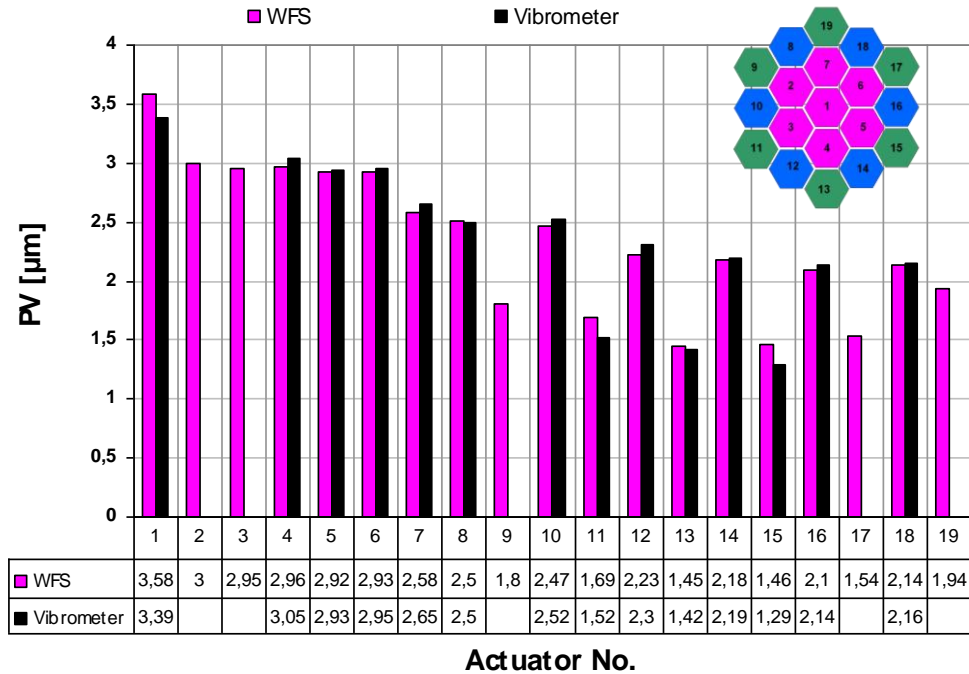

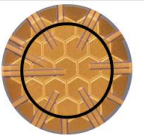
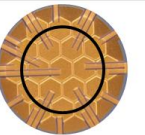
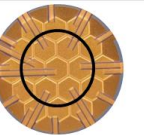
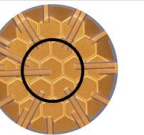
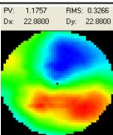
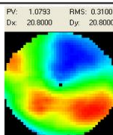
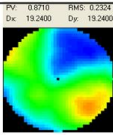
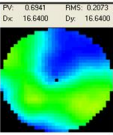
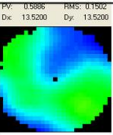
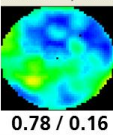
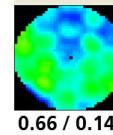
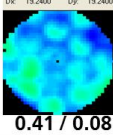
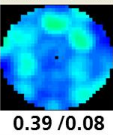
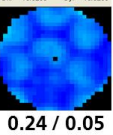


Figure 61 Graphical representation of the calculated P-V values of the AIFs measured by WFS and vibrometer. The comparison reveals good agreement between the two measurement set-ups. P-V values decrease with radial distance from the mirror centre. Some actuators have not been measured by the scanning vibrometer.

Active levelling

The next set of experiments analyses the potential of the 19 piezoelectric actuators to actively level the mirror membrane (neglecting defocus) for different mirror apertures of 15.3 mm, 18 mm, 20.8 mm, 22.5 mm, and 24.5 mm. The manufacturing instructions preset the voltage range of the piezoelectric actuators from 0 V to 200 V. Therefore, the piezoelectric actuators are set manually to voltage levels of 100 V \pm 20 V to minimize the P-V and rms deviation. This small active levelling working range leaves a large working range for the setting of desired mirror shapes. SHSWorks is used to calculate the P-V and rms deviation (neglecting the defocus term). The investigated mirror apertures are positioned centrally aligned to the actuator patch. The centre of the measurement aperture is maintained after the maximum measurement aperture is aligned to the actuator patches. Now, the actuators are manually activated in a manner such

that the P-V and rms deviation are minimized. The optimum voltage distribution is detected at the maximum measurement aperture, and it is applied to all other apertures. Figure 62 depicts the actuator design with the measurement apertures, and a comparison between the uncompensated and actively levelled mirror membrane with its corresponding P-V and rms values. The investigations show that both P-V and rms deviation increase with mirror aperture. The active levelling of the mirror shape halves the uncompensated deviations. The smallest deviation of 245 nm and 46 nm for P-V and rms, respectively, occurs for a diameter of 15.3 mm. A print through of the single actuators is recognizable. A new optimized actuator design would increase the number of actuators to more evenly and accurately shape the mirror membrane. This would also minimize the print through and the dead space between adjoining actuators.

Design					
Aperture [mm]	24.5	22.5	20.8	18	15.3
Uncompensated PV/rms * [μm]	PV: 1.1757 RMS: 0.3256 Dc: 22.9800 Dy: 22.9800  1.78 / 0.33	PV: 1.0793 RMS: 0.3100 Dc: 20.8000 Dy: 20.8000  1.08 / 0.31	PV: 0.8710 RMS: 0.2324 Dc: 19.2400 Dy: 19.2400  0.87 / 0.23	PV: 0.6561 RMS: 0.2093 Dc: 16.6400 Dy: 16.6400  0.69 / 0.21	PV: 0.5886 RMS: 0.1502 Dc: 13.5200 Dy: 13.5200  0.59 / 0.15
Compensated PV/rms [μm]	PV: 0.7779 RMS: 0.1580 Dc: 22.9800 Dy: 22.9800  0.78 / 0.16	PV: 0.6717 RMS: 0.1367 Dc: 20.8000 Dy: 20.8000  0.66 / 0.14	PV: 0.4161 RMS: 0.0786 Dc: 19.2400 Dy: 19.2400  0.41 / 0.08	PV: 0.2844 RMS: 0.0769 Dc: 16.6400 Dy: 16.6400  0.39 / 0.08	PV: 0.2254 RMS: 0.0470 Dc: 13.5200 Dy: 13.5200  0.24 / 0.05

*PV and rms without defocus.

Figure 62 Image of the screen-printed actuator patterns with corresponding apertures between 15.3 mm and 24.5 mm. Comparison between uncompensated and actively levelled mirror membrane by activation of $\pm 10\%$ of the piezoelectric working range. The P-V and rms deviation of the mirror membrane without accounting for the defocus term are also shown.

Zernike Polynomials

The successful application of DMs in laser chains relies on their potential of compensate for the thermally-generated aberrations or atmospheric distortions. Aberrations and DM shapes can be described by Zernike polynomials $Z_i(\rho, \phi)$ and their coefficients c_i as described in chapter 2. In this chapter, the mirror

potential of setting Zernike Polynomials is evaluated. A 100-V offset voltage is applied to all actuators, and positive and negative Zernike polynomials are set manually by the activation of selected addressing electrodes for the different mirror apertures.

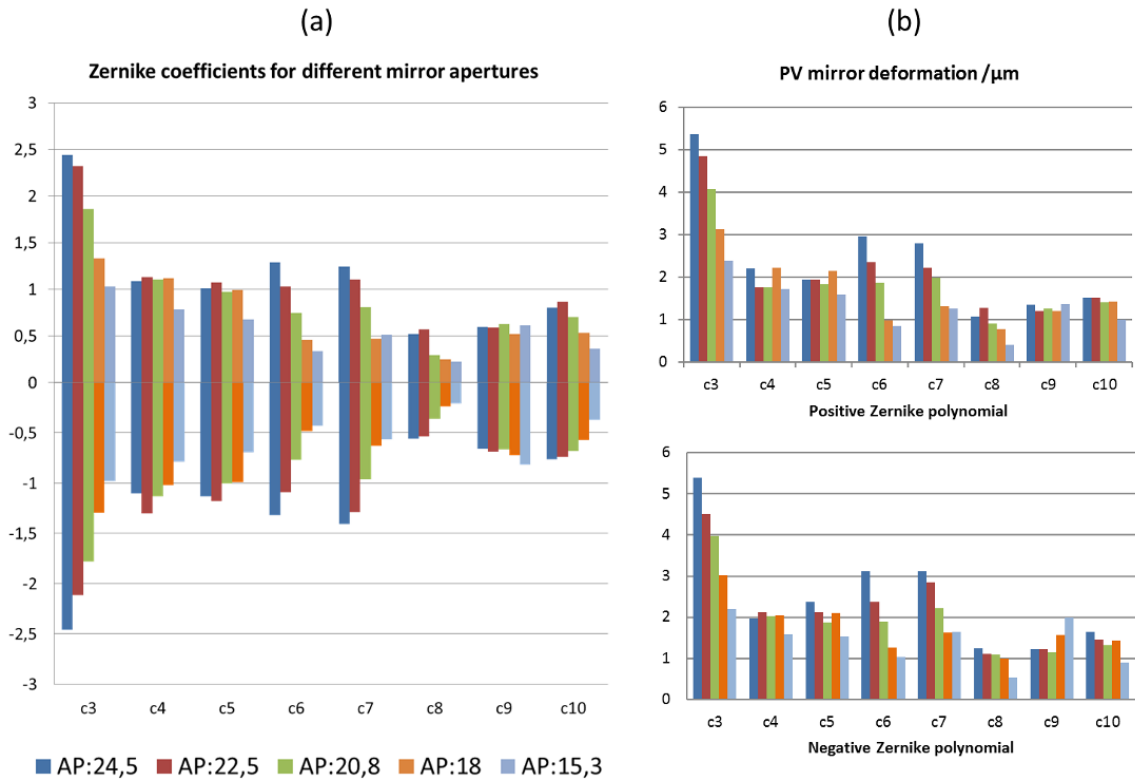


Figure 63 (a) Examples for adjustable Zernike polynomials C_3 to C_{10} . (b) P-V membrane deformation [μm] for Zernike polynomials in (a).

The results are shown in Figure 63. Figure 63 (a) shows the measured positive and negative Zernike coefficients C_3 to C_{10} for five mirror apertures. The magnitude for positive and negative coefficients is comparable. The coefficient C_3 (defocus) that pertains to defocus is the largest coefficient, and it diminishes with decreasing aperture. Astigmatism (C_4 and C_5) remains constant for apertures between 24.5 mm and 18.0 mm. The smallest aperture (15.3 mm) corresponds to the smallest coefficient values between 0.7 and 0.8. A continuous decrease for comae (C_6 and C_7) is observable with decreasing aperture. The mirror potential for the setting of the spherical aberration (C_8) is small for all mirror apertures. Only the two largest apertures show values around 0.5. The adjustability of trefoil (C_9) is constant around 0.5 for all apertures. In contrast, C_{10}

shows variability that changes with the aperture. This differing mirror property for the same type of shape is caused by the actuator pattern distribution that requires the activation of two actuators for one arm of the 120° pattern. Figure 63 (b) shows the measured P-V mirror deformation. A behaviour similar to that of the Zernike coefficients is observable: The magnitudes for the positive and negative Zernike polynomials are comparable, and defocus and comae decrease with decreasing aperture. The P-V values for all polynomials are $>1 \mu\text{m}$ (other than C_8) and the two smallest apertures of C_6 .

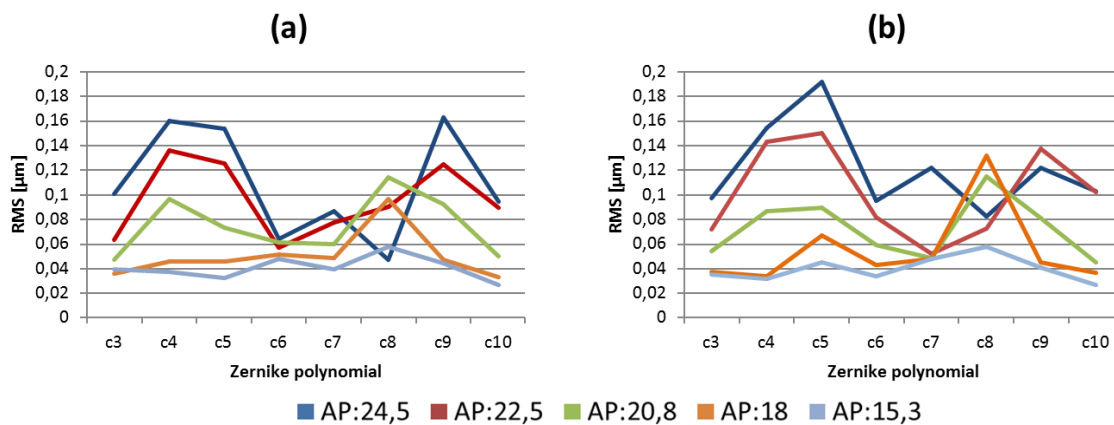


Figure 64 Rms deviation from adjusted Zernike coefficients. (a) Positive Zernike coefficients. (b) Negative Zernike coefficients.

An important criterion for the quality of the aperture setting is the minimization of the rms-value as the mean deviation from the desired Zernike polynomial to a limit below 150 nm. Figure 64 shows the calculated rms values for each polynomial. The deviation reduces with decreasing aperture. The smallest aperture of 15.3 mm results in deviations of $40 \text{ nm} \pm 10 \text{ nm}$. The deviations increase with the aperture but remain below the limit of 150 nm up to an aperture of 22.5 mm. The spherical C_8 coefficient reaches deviations below 90 nm for apertures of 24.5 mm and 22.5 mm. Minor apertures result in decreased Zernike coefficients C_8 and rms deviations above 90 nm. It is interesting to note that both comae remain constant to a limit below 100 nm. Therefore, the recommended mirror apertures are 22.5 mm and 20.8 mm as they permit a good performance trade-off between large Zernike coefficients and low residuals. The images of the pre-set and measured Zernike polynomials C_3 to C_{10} for a mirror

aperture of 22.5 mm are shown in Figure 65. For each polynomial, the positive (left) and negative (right) shapes are shown. Each desired shape is recognizable.

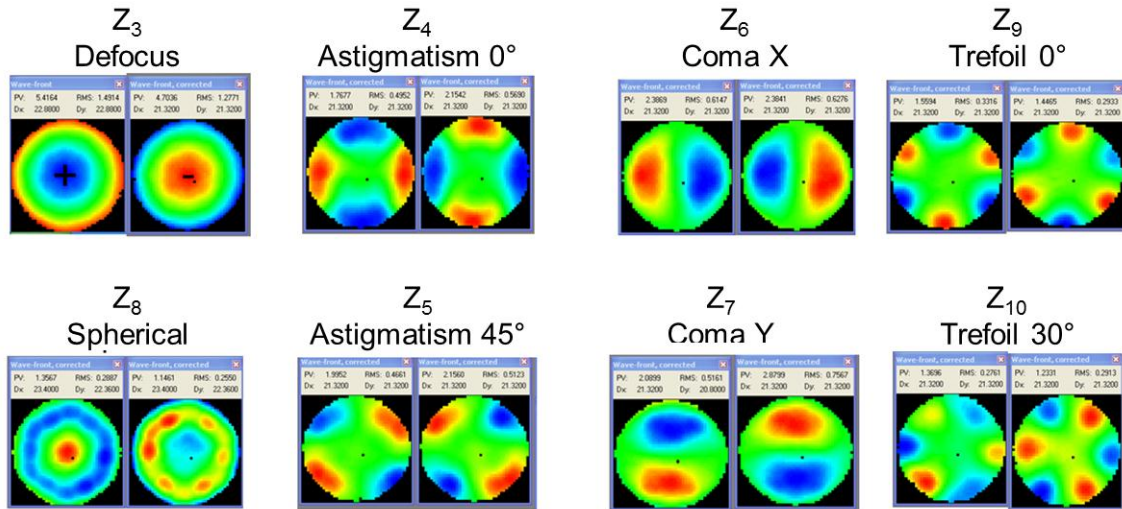


Figure 65 Examples for Zernike polynomials C₃ to C₁₀. Mirror aperture 22.5 mm and 100 V Offset applied to all actuators.

6.4.3 Thermally-induced changes: homogeneous loading

The following thermally-induced changes caused by homogeneous loading are observed: stroke, resonance behaviour, and membrane deformation. A homogeneous load applied by the Peltier element heats the deformable mirror. The Peltier element is voltage-controlled and heats the mirror from 16 °C up to 60 °C, thereby resulting in a temperature increase of up to 44 K.

Total stroke

The total stroke refers to the P-V deformation of the membrane if all actuators are activated. It is measured by the LTS for different copper metallization thicknesses upon homogeneous heating by the Peltier element. The measurements are repeated at least 15 times at every temperature, and the mean value and standard deviation of the total piezoelectric stroke are calculated and shown in Figure 66. The mounted screen-printed membrane without copper provides a total membrane stroke of $41.4 \mu\text{m} \pm 0.3 \mu\text{m}$ at room temperature. The total stroke remains stable between $41.1 \mu\text{m}$ and $43.4 \mu\text{m}$ for temperatures up to 59 °C. The mean measurement values deviate although only a small standard

deviation of each mean value is observed. The application of a 50- μm copper layer reduces the available total stroke due to the increase in membrane stiffness. At 20.9 $^{\circ}\text{C}$, the stroke is $29.4 \mu\text{m} \pm 0.3 \mu\text{m}$. The stroke increases gradually with temperature at a rate of $0.07 \mu\text{m}/^{\circ}\text{C}$. Thus, the stroke at 58.9 $^{\circ}\text{C}$ is $31.6 \mu\text{m} \pm 0.7 \mu\text{m}$. The application of a 200- μm copper layer (total) results in a stroke of $14.6 \mu\text{m} \pm 0.1 \mu\text{m}$ at 23.7 $^{\circ}\text{C}$. No change in total stroke is observed with increasing temperature. The total stroke values are between $14.6 \mu\text{m} \pm 0.1 \mu\text{m}$ and $17.0 \mu\text{m} \pm 0.1 \mu\text{m}$. After the machining of the DM, the stroke increases to $16.8 \mu\text{m} \pm 0.2 \mu\text{m}$ at 22.7 $^{\circ}\text{C}$. The stroke increases steadily at a rate of $0.1 \mu\text{m}/^{\circ}\text{C}$ until it reaches $19.6 \mu\text{m} \pm 0.7 \mu\text{m}$. The observed increase in stroke with temperature can be attributed to tensile stresses in the piezoelectric layer. This effect is observable in all cases other than that with a 200- μm copper layer. Tensile stresses in the piezoelectric layer correspond to downward bowing of the membrane.

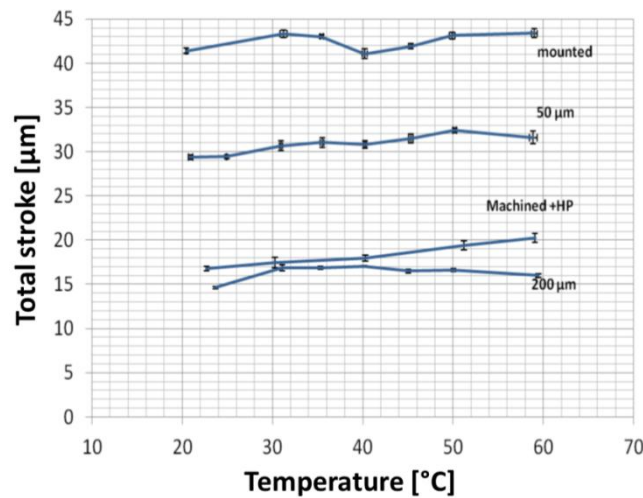


Figure 66: Total stroke of the deformable mirror for different temperatures and copper-layer thicknesses.

Resonance behaviour

The measurements of the resonance frequency are carried out using a single-channel vibrometer. The results show the first resonance peak at 1.570 kHz, 1.845 kHz, and 2.684 kHz without the use of a copper layer, with a 50- μm copper layer, and with a 200- μm copper metallization layer, respectively (cf. Figure

67 (a)). These values are each measured at $20\text{ }^{\circ}\text{C} \pm 1^{\circ}\text{C}$. The thermally-induced frequency shift is $1.12\text{ Hz}/^{\circ}\text{C}$, and $-3.42\text{ Hz}/^{\circ}\text{C}$ without copper metallization and with $200\text{-}\mu\text{m}$ copper metallization, respectively. At a $50\text{-}\mu\text{m}$ copper-layer thickness, no thermally-induced frequency shift is observable. The machining of the electroplated substrate and thus the thin-down induces a frequency decrease to 2.588 kHz at $20\text{ }^{\circ}\text{C} \pm 1^{\circ}\text{C}$. The thermally-induced frequency shift is $-3.29\text{ Hz}/^{\circ}\text{C}$ and thus comparable with the measured value at maximum copper-layer thickness.

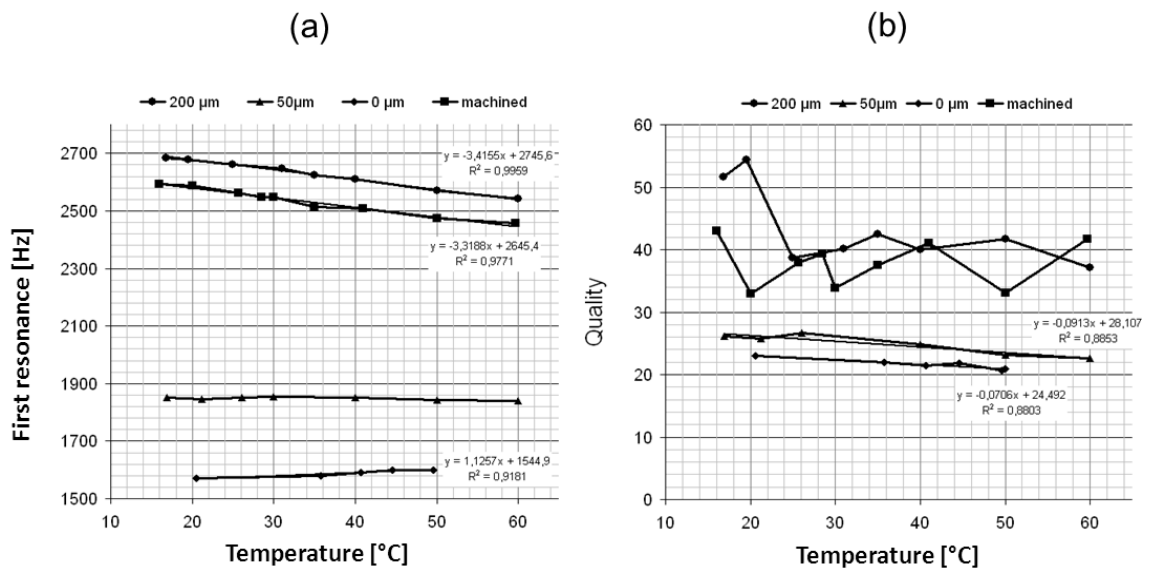


Figure 67 (a) Frequency of the first resonance, and (b) quality of resonance depending on temperature.

The quality factor Q is considered as a measure of damping of the mechanical vibration (mechanical loss) and residual stress. It is the ratio of the frequency of the first mechanical resonance to the bandwidth⁷ of the oscillation. The Q factor of the screen-printed mirror is 23 at $20\text{ }^{\circ}\text{C}$, and it decreases steadily with the temperature at a rate of -0.07 per $^{\circ}\text{C}$ to a value of 21 (cf. Figure 67(b)). The application of $50\text{ }\mu\text{m}$ of metallization increases the Q factor to 26 at $21\text{ }^{\circ}\text{C}$. The

⁷ Frequency range between the two frequencies where the amplitude of the resonance peak drops to 50%.

increase in membrane temperature again leads to a decrease in quality at a rate of -0.09 per $^{\circ}\text{C}$. The observed decrease in the Q factor with increasing temperature corresponds to a small increase in damping. Higher copper-layer thicknesses lead to large increases in the mean Q factor; the Q factor increases to 43 ± 6 and 37 ± 4 with a $200\text{-}\mu\text{m}$ copper layer and the machined copper metallization. In the study, the Q factor fluctuated over the temperature range but showed no clear tendency.

The thermally-induced changes in the first resonance are also investigated (cf. Figure 67(a)). The mounted membrane shows a small increase in resonance frequency with increasing temperature, whereas the $50\text{-}\mu\text{m}$ -thick metalized membrane shows no change in resonance behaviour. The thermally-induced frequency shift for the thick metalized membranes is steeply decreasing. Piezoelectric membranes are also used as micro resonant force gauges¹⁶⁶ that convert a temperature change into a shift in resonance frequency (or change in permittivity or capacitance). The resonance frequency is affected by perturbation of its potential (mechanical straining and changes in shape and thus stiffness) or kinetic energy (change in resonator mass and change in the density of the surrounding medium). The FEM simulations reveal that a convex membrane deformation (tensile stress in the piezoelectric layer) induces a very small change in resonance frequency. Further, the FEM simulations show that thermally induced changes correspond to shape variations. Thus, a decrease in resonance frequency is attributed to a decrease in stiffness (or mechanical stress relief) that occurs only with the use of a $200\text{-}\mu\text{m}$ copper-layer thickness. There are several reasons for this occurrence: (i) the second copper application (from $50\text{ }\mu\text{m}$ to $200\text{ }\mu\text{m}$) introduced stress that is thermally released, (ii) the thick copper metallization decreases the membrane (assembly) stiffness, or (iii) the thick copper metallization shows decreasing stiffness with increasing temperature. Apart from this occurrence, thermally-induced damping of the membrane is absent. The release in stress (reason (i)) is valid only for temperatures above $100\text{ }^{\circ}\text{C}$, and this release would lead to membrane-shape variations that were not observed. The analysis of the Young's modulus of copper reveals its decrease with increasing temperature, thereby corresponding to a stiffness decrease. The

plot of the frequency shift against the copper-layer thickness also reveals a gradual decreasing curve. This leads to the conclusion that increasing copper-layer thickness (volume fraction) causes decreases in the thermally-induced frequency shift.

The large measured thermally-induced frequency shifts show the potential use of these multilayer assemblies in micro resonant force gauges. The gauges convert temperature changes into corresponding frequency shifts with a high sensitivity of 3.3 Hz/°C. Moreover, there is the possibility of scaling the sensitivity by using electroplated copper-layer thickness, thereby enabling a sensitivity that can be adapted to the operating temperature range.

Thermally-induced deflection

The FEM simulations reveal that strong thermally-induced frequency shifts are attributed to large membrane deformations. Measurements of the thermally-induced membrane deflection are used to verify this outcome. The WFS analyses the P-V mirror-membrane deformation and the Zernike coefficients C_0 – C_{35} simultaneously for homogeneous heating; the heating is achieved due to the Peltier element integrated in the mirror mount. Measurements of the P-V membrane deformation are also made by the Tencor measurement system. Both measurements are done with short-circuiting of electrodes and the results are shown in Figure 68. The P-V of the mirror membrane increases linearly at a rate of $-0.12 \mu\text{m}/^\circ\text{C}$ between 26°C and 56°C ; this value is consistent with both measurement systems.

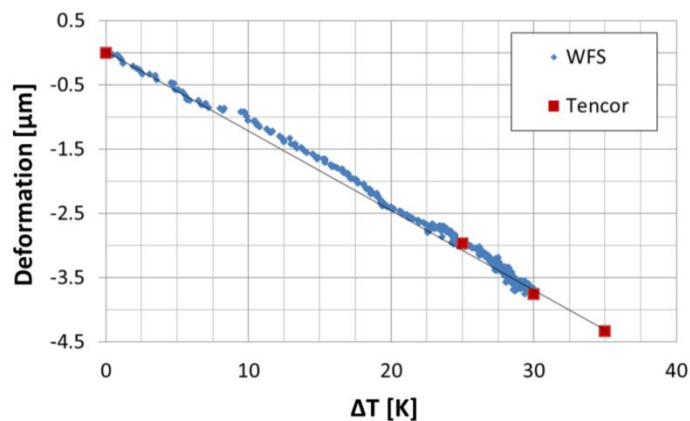


Figure 68 Temperature-induced P-V deflection of the mirror membrane. Slope of the linear fit is $-0.1 \mu\text{mK}^{-1}$.

Figure 69(b) shows the thermally-induced changes in Zernike coefficients C_1 to C_{20} for increasing temperature. The largest change occurs linearly in Zernike polynomials C_2 to C_7 ; these polynomials symbolize tip, tilt, defocus, astigmatism and comae (cf. Figure 69(a)).

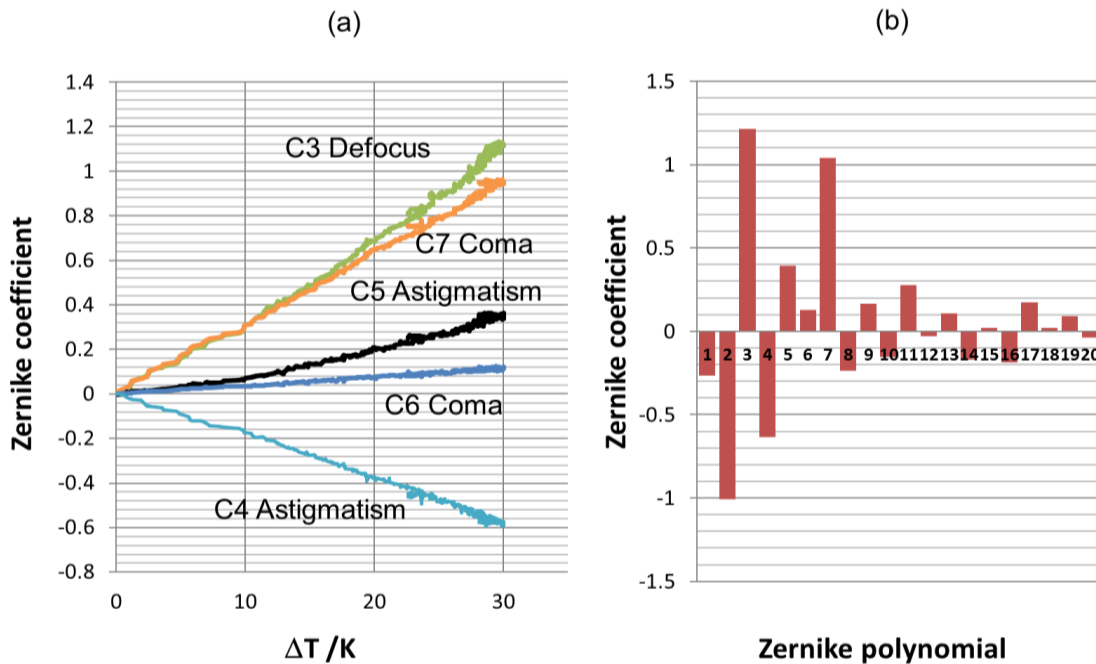


Figure 69 (a) Changes in the Zernike coefficients C_3 – C_7 for temperature differences up to 30 K. (b) Zernike coefficients C_1 – C_{20} of the mirror membrane at 35 K.

Defocus undergoes the largest change. The relatively large changes in the astigmatism and comae coefficients indicate asymmetrical deformation of the mirror membrane that may be caused by inhomogeneous layer thicknesses due to the manufacturing process. The Zernike coefficients C_8 to C_{20} are of very small magnitude and they can be neglected. The increase in C_3 corresponds to a downward bending of the membrane, thereby indicating tensile stresses in the piezoelectric thick film. The downward bending of the screen-printed mirror membrane indicates the large influence of the annular copper layer (cf. Figure 28).

Athermal design examples regarding the mirror response under homogeneous loading show similar results; thermal stability tests of unimorph deformable mirrors over a small temperature range (from 13 °C to 25 °C) show a linear membrane deformation of 0.11 $\mu\text{m}/^\circ\text{C}$ (P-V)¹⁶⁷. Other measurements reveal a

change of $0.34 \mu\text{m}/^\circ\text{C}$ due to defocus³⁷ upon homogeneous loading between 17°C and 23°C . A mirror with Pyrex substrate shows a P-V deformation of $-0.12 \mu\text{m}/^\circ\text{C}$ over a temperature range of 30°C to 45°C ¹⁴⁷. All the relevant previous studies have reported that defocus is the major component under homogeneous loading. The comparison of the ML design with the state-of-the-art athermal mirror designs reveals a comparable thermally-induced deflection.

6.4.4 Thermally-induced changes: inhomogeneous loading

Figure 70 shows the image of the optical set-up corresponding to Figure 58. The orange line indicates the path of the high-power laser beam and the thin white lines indicate the path of the monitoring beam. The free optical diameter of the monitoring system at the DM is larger than the diameter of the high-power load beam.

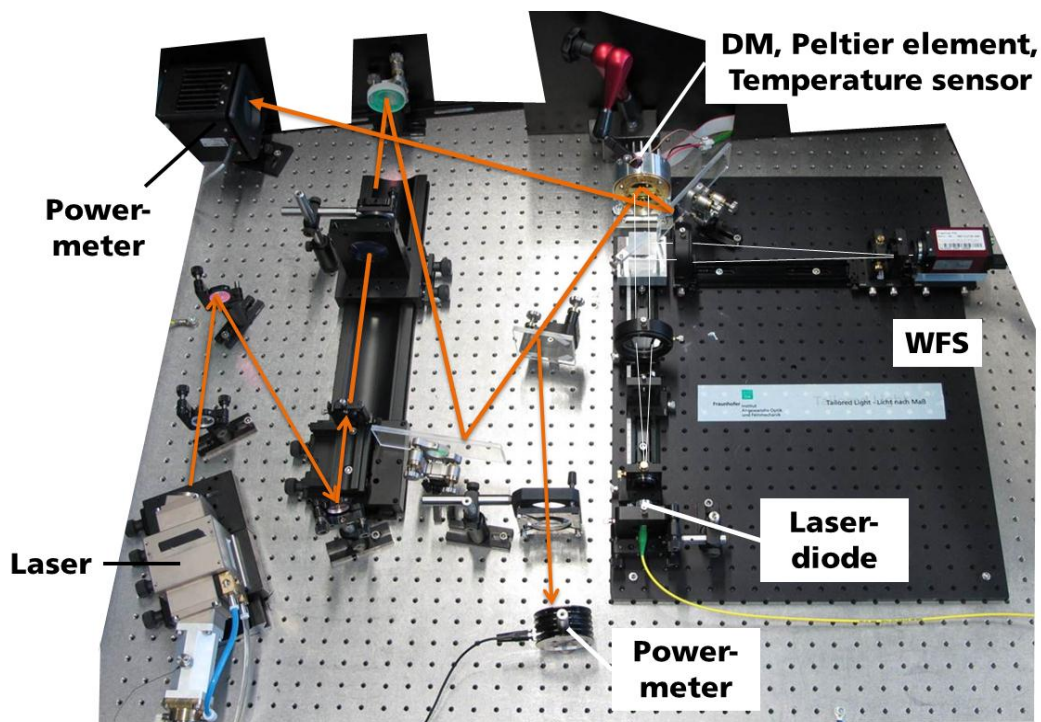


Figure 70 Image of the experimental measurement set-up for homogeneous, inhomogeneous, and compound loading of the mirror system. The red line indicates the path of the high-power laser beam and the thin white lines indicate the monitoring beam's path from the laser diode to the WFS.

The mirror membrane response to different laser loads is measured and the P-V deformation is evaluated. The first load case corresponds to a duty cycle of 5%

and an input power between 1.3 W and 11.5 W corresponding to absorption of 25 mW to 200 mW, respectively. The second load step corresponds to a duty cycle of 50% and an input power between 10.8 W and 107 W. The absorbed power values range between 220 mW and 2 W. A 100% duty cycle (under cw load) results in absorbed power values between 500 mW and 2.1 W. The results are shown in Figure 71. The use of a 5% duty cycle shows very little P-V deformation as only little power is absorbed. The P-V value decreases slightly at 25 mW of absorbed power, and it rises steadily with increasing power. The P-V deformation increases linearly with increasing values of absorbed power, and it reaches a value of 8 μm for an absorbed power of 2.1 W. The rate of the P-V membrane deformation under inhomogeneous loading is 3.4 $\mu\text{m}/\text{W}$. The mirror membrane bends upwards with increasing power absorption, thereby indicating the defocusing of a parallel beam.

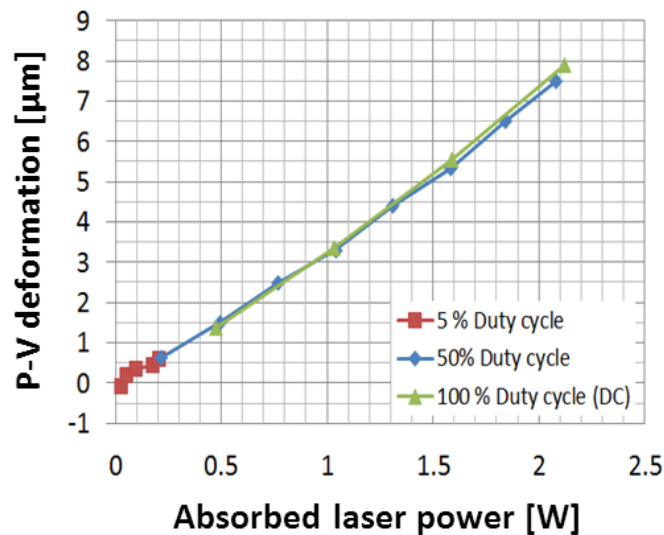


Figure 71 Plot of the absorbed power against the P-V deformation. The laser-load-induced membrane deformation is 3.4 $\mu\text{m}/\text{W}$. There is no detectable difference between the cw laser and modulated laser loads.

The settling time of the mirror response for 50% and 100% duty cycles and different laser loads is also measured. Figure 72 depicts the P-V deformation for 0.5 W, 1 W, 1.6 W, and 2 W of absorbed power for modulated (dotted) and cw (line) laser modes. The deformation exponentially increases with time. The deformation flattens out and reaches a final constant value when the mirror reaches its thermo-mechanical equilibrium. The measurements reveal a settling

time between 1.3 s and 0.9 s for the investigated absorbed power values. The settling time steadily decreases with cw laser loading, and it fluctuates in the case of pulsed-laser loading. However, a good P-V agreement is observed between the modulated and cw laser loads. Therefore, we can conclude that the mean laser power causes the mirror membrane deformation. Further, the time constant of the mirror response is larger than the time lag between two pulses.

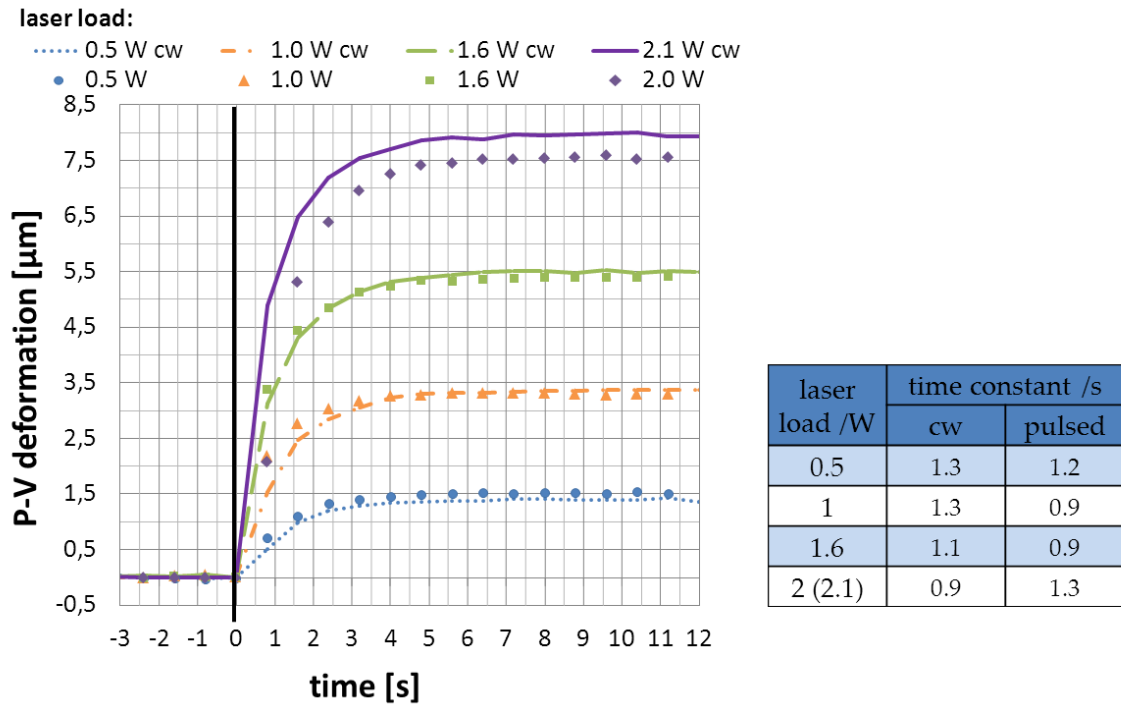


Figure 72 Transient behaviour of the mirror deformation for different cw and modulated laser loads. The table on the right summarizes the measured time constants.

The theoretical deformation time constant for 1 W of power absorption is 0.45 s for a 200- μm copper-layer thickness, and it is 35% of the measured time constant. I can conclude that this is either due to the lower thermal conductivity of the copper layer or due to a lower thermal conductivity of the LTCC substrate compared to the specified values. This disparity requires further investigation.

The Zernike coefficients $C_0 - C_{35}$ (cf. Figure 73(a)) are evaluated for a 100% duty cycle at different power levels. The largest contribution is due to defocus (C_3) and the influence of astigmatism is negligible. The second strongest factor is spherical aberration and both comae magnitudes are also significant. Therefore, the inhomogeneous loading causes mainly symmetrical wavefront deformation

(C_3 , C_8), and very little asymmetrical wavefront deformation (C_6 , C_7). Further, it is noteworthy that all the Zernike coefficients change in proportion to the absorbed power and the Zernike coefficients C_9 – C_{35} are negligible. The density plot of the measured coefficients C_1 – C_8 without considering defocus is shown in Figure 73 (b). This plot reveals a non-symmetric membrane deformation, thereby indicating a slight misalignment of the laser load and its non-concentric incidence. A better alignment of the laser load can result in smaller deviation from defocus.

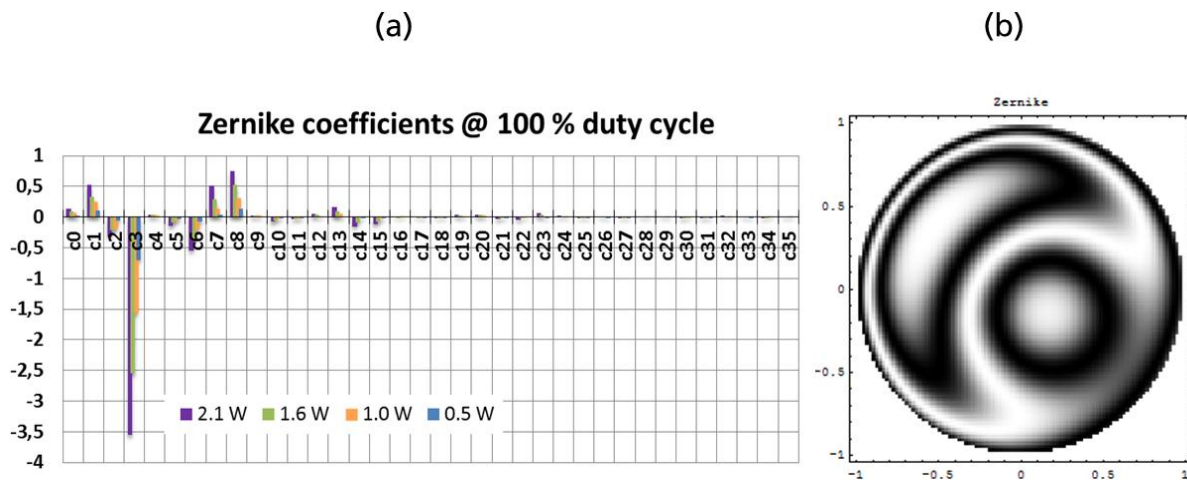


Figure 73 (a) Zernike coefficients with 100% duty cycle for different absorbed laser powers. Zernike coefficients scale in proportion to the absorbed laser power. (b) Mirror surface reconstructed from Zernike coefficients C_1 – C_8 without defocus.

6.4.5 Thermally-induced changes: compound loading

The induced mirror membrane bending for homogeneous loads is opposite to that under inhomogeneous thermal loads. A homogeneous load induces focusing of the mirror while an inhomogeneous load induces defocusing of the mirror. This suggests the possibility of the pre-compensation of laser-induced deformations by heating of the deformable mirror (compound loading). Two sets of compound loading measurements ((A) and (B)) are carried out; these measurements evaluate the thermally-induced mirror deflection and the change in defocus. The piezoelectric stroke at optimum compound loading is also analysed.

Figure 74 shows the measured P-V mirror membrane deformation induced by the absorbed power for different homogeneous pre-loadings along with the reference behaviour in the absence of pre-loading. In the absence of homogeneous pre-loading, the P-V mirror membrane deformation again increases linearly at a rate of $3.4 \mu\text{m}/\text{W}$. This behaviour changes according to the homogeneous pre-loading of the mirror. A pre-heating of 16 K (to 35°C) increases the P-V mirror deformation to $2.6 \mu\text{m}$ and $1.7 \mu\text{m}$ for (A) and (B), respectively, in the absence of high-power laser loading. An increase in absorbed power decreases the P-V mirror membrane deformation to a minimum at around 0.5 W for both measurements. With further increase of the absorbed power, the P-V mirror membrane deformation again increases. A polynomial trend line (of the third power) fits these characteristics.

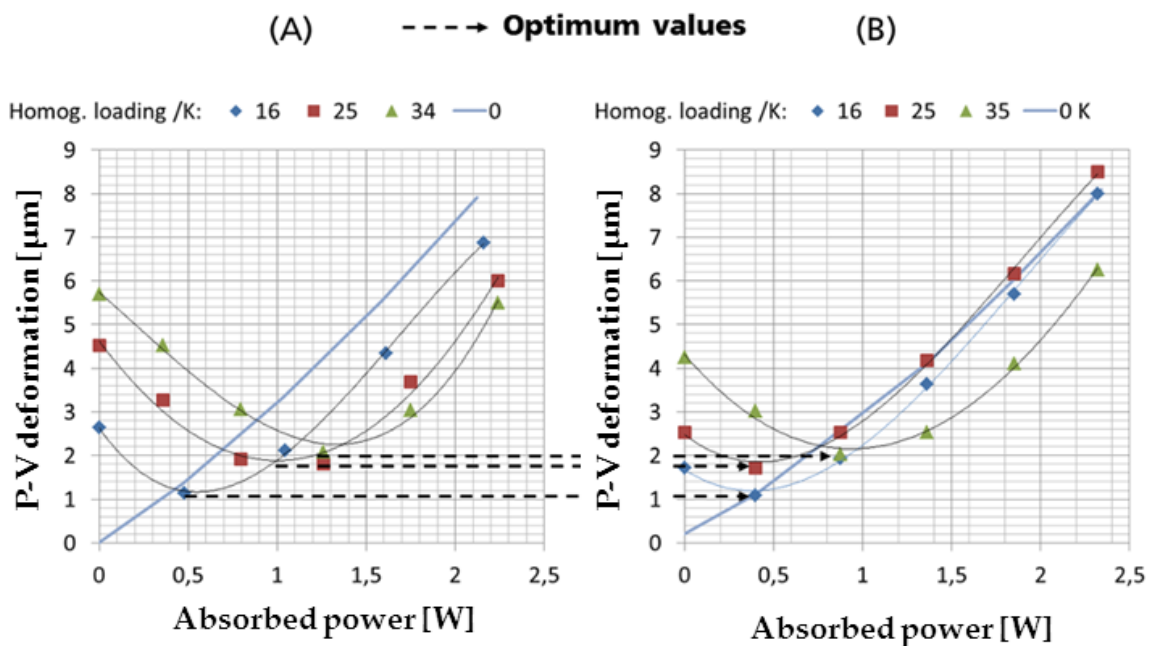


Figure 74 P-V membrane deformation for two sets of measurements, (A) and (B). The measurements reveal an optimum homogeneous pre-heating for minimal membrane deformation.

A similar behaviour is observed for every pre-heating temperature for both sets of measurement. The maximum P-V membrane deformation occurs at a maximum absorbed power of 2.3 W . Further, this maximum P-V membrane deformation decreases with homogeneous pre-heating. In addition, the

measurements show a minimum P-V membrane deformation of 1.1 μm , 1.7 μm , and 2 μm for homogeneous loadings of 16 K, 25 K, and 35 K, respectively. The minimum values are comparable for both measurements (A) and (B), and they define the optimum compound loading. The deformation settling time is measured as 1 s, and this value is in accordance with that for inhomogeneous loading.

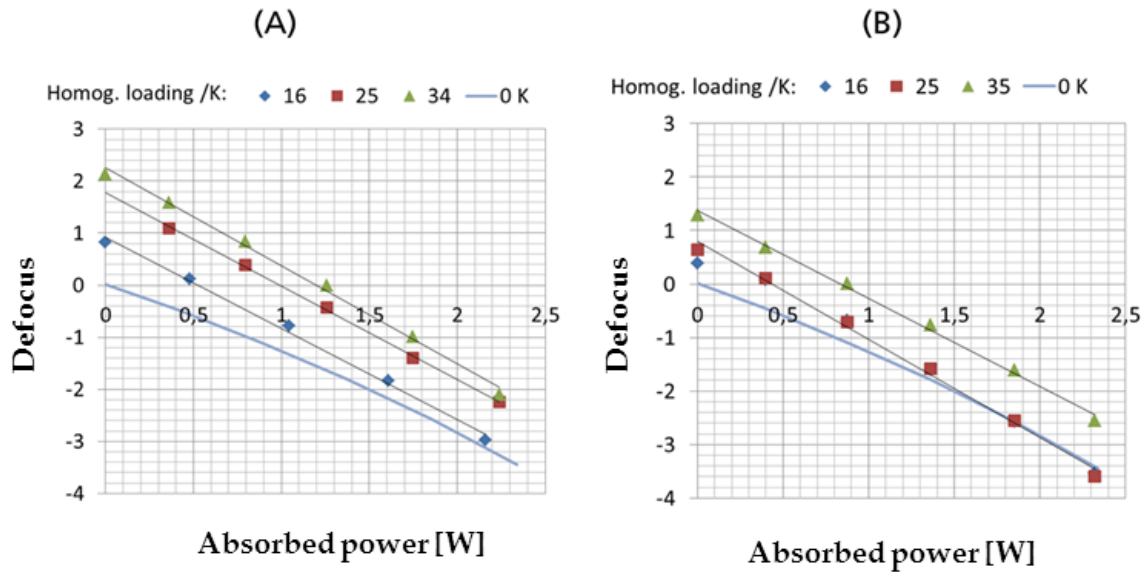


Figure 75 Zernike coefficients of defocus in measurements (A) and (B). The measurements reveal an optimum homogeneous loading that compensates for the defocus term under different inhomogeneous loads.

Defocusing is used as figure of merit for evaluating the pre-compensating properties. Figure 75 shows the defocus values for measurements (A) and (B) under compound loading. Inhomogeneous heating without homogeneous loading induces a negative defocus (represented by C_3). The homogeneous pre-loading increases the defocus in absence of power absorption. The defocus increases linearly down to negative defocusing with increasing power absorption. The measurements reveal the compensation of the inhomogeneously generated defocus by homogeneous loading. Measurement (A) suggests the ability to compensate for the defocus induced by 1.25 W of absorbed power by 34 K of homogeneous loading. Measurement (B) suggests a compensation of less than 1 W for a comparable homogeneous loading of 35 K.

Piezoelectric characterization

I also evaluate the piezoelectric stroke for the optimized compound loads for measurement (B) for an electric field of 2 kV/mm that is applied to all the actuators. The results show an increase in piezoelectric stroke for compound loading. A similar tendency has been observed for homogeneous loading.

Table 13 provides the values for the increase in piezoelectric stroke under compound loading. The measured P-V values are smaller than those obtained by the LTS total stroke measurements (cf. 6.4.3). This difference is caused by the smaller measured mirror aperture of the WFS. The mirror characteristic of increasing stroke under compound loading is suitable for high-power laser applications in which compound loading is necessary.

Table 13 Piezoelectric stroke at optimized compound loading.

Thermal loading		0K / 0W	17 K / 0.6 W	25 K / 1.0 W	34 K / 1.4 W
piezoelectric activation	C3		-5.7	-6.3	-6.7
	P-V [μm]	11.2	12.6	13.9	14.8

6.4.6 Comparison with simulated values

The simulations reveal a membrane deformation rate of $-0.2 \mu\text{m}/^\circ\text{C}$ and $1.3 \mu\text{m}/\text{W}$. This corresponds to a pre-compensation of 6 W by homogeneous heating of 40 K under the compound loading regime. An absorbed laser power of 6 W corresponds to a reflected laser load of 600 W for 1% absorption. In particular, high-power coatings enable a very high reflection of up to 1%, thereby corresponding to a reflected laser power of 6 kW. This shows the theoretical suitability of the mirror for high-power applications (cf. Figure 76).

The measurements show a lower membrane deformation rate of $-0.12 \mu\text{m}/^\circ\text{C}$ and a higher laser-induced deformation rate of $3.4 \mu\text{m}/\text{W}$. The manufactured mirrors show a lower heat dissipation that might be attributed to the reduced thermal conductivity of the electroplated copper compared to the bulk material. If the electroplating of copper reduces the material heat conductivity, the copper-layer

thickness requires to be increased. This effect should be investigated by measurements of the thermal conductivity of the electroplated copper layers.

Theory (200 μm Cu, CE7 mount)			➔	Experiment (200 μm Cu, CE7 mount)		
rate	load	deflection	rate	load	deflection	
-0.2 $\mu\text{m}/\text{K}$	x 40 K	= - 8.0 μm	-0.12 $\mu\text{m}/^\circ\text{C}$	x 34 K	= - 4.1 μm	
+1.3 $\mu\text{m}/\text{W}$	x 6 W	= +7.8 μm	+3.4 $\mu\text{m}/\text{W}$	x 1.3 W	= +4.4 μm	
		-0.2 μm			+0.3 μm	

Figure 76 Comparison between theoretical and experimental characteristics of compound loading.

6.5 Application: Compensation of static wavefront aberrations

The DM proposed in the study can (pre-) compensate for thermal lensing. The amplitudes of the abovementioned aberrations can be of the order of several μm . The ability of the screen-printed DM to compensate for such large aberrations is shown in the next experiment. The AO set-up as shown in Figure 57 is used with an aberration generator that is positioned after the first beam expander and before the beam splitter cube. The aim is the correction of the wavefront by compensating for the deviations from the plane, thereby leading to highest spot intensities. Figure 77 shows the mirror aperture in relation to the actuator layout for measurement apertures between 15.4 mm and 22.5 mm. The next two columns show the Strehl ratio and the aberrated wavefront with the corresponding Strehl ratio values, and the wavefront P-V and rms values. This information is also shown for the compensated wavefronts. The aberration generator introduces a P-V wavefront deformation between 3.2 μm and 6.1 μm (cf. Figure 77).

The wavefront deformation before compensation is mainly due to astigmatism (C_4 and C_5), and this results in a very low Strehl ratio. In contrast, the measurements of the compensated wavefront reveal a clear improvement over the original wavefront with aberrations. The best results are achieved if actuators are placed outside the mirror aperture (for apertures of 15.4 mm and 18.0 mm). The P-V wavefront deformation is improved by a factor of 5.8 and 5.3 and the rms deviation by a factor of 6.4 and 6.9 for mirror apertures of 18.0 mm and

15.4 mm, respectively. This deviation from the diffraction-limited Strehl ratio can be explained by the small number of actuators used. A higher actuator density could improve the rms deviation and consequently lead to higher Strehl ratios. The presented measurement for the aperture of 15.4 mm shows an rms deviation of <100 nm; this deviation can result in diffraction-limited Strehl ratios for laser systems emitting radiation at 1400 nm. The mirrors could also be used in laser systems emitting at 1070 nm for the corresponding Strehl ratio of 0.65. It is significant that the high piezoelectric stroke can compensate for multiple micrometer wavefront deviations.

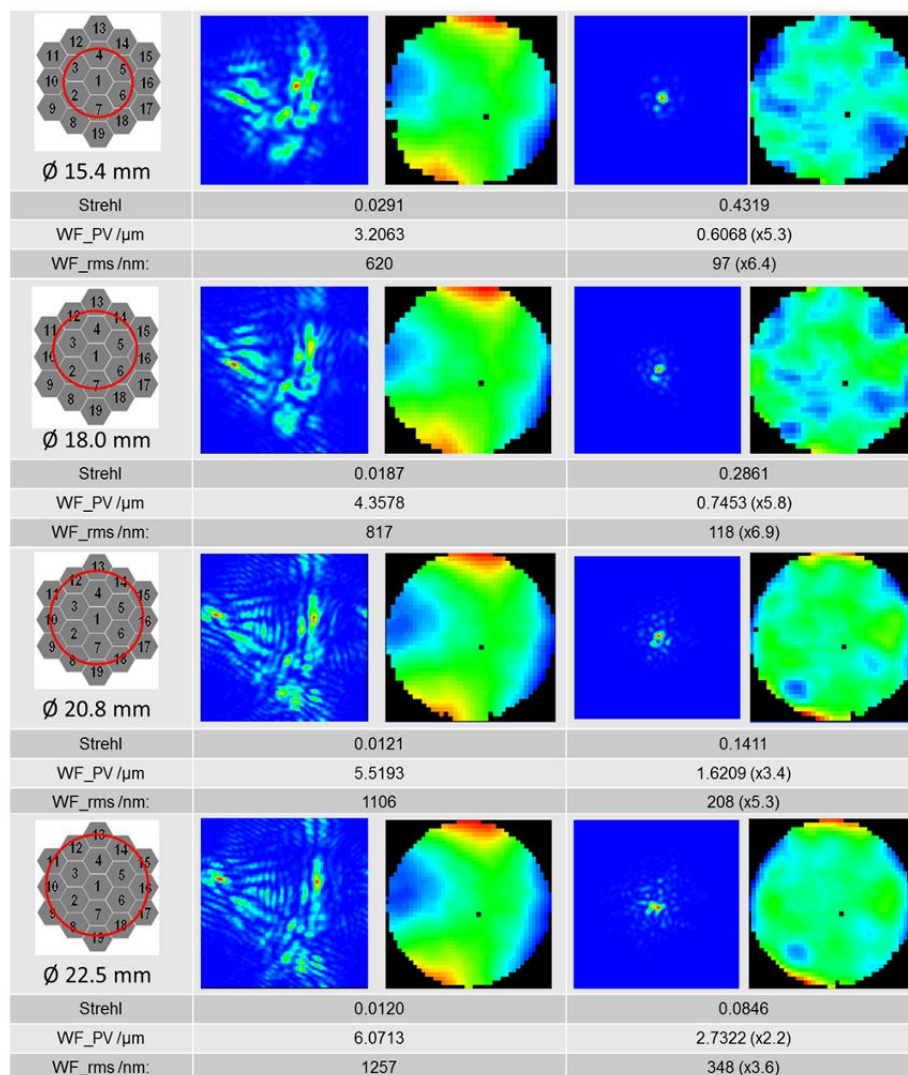


Figure 77 Compensation of static wavefront aberrations for different mirror apertures.

7 Summary and discussion of the results

This thesis discusses new designs for non-cooled deformable unimorph mirrors in order to improve their applicability in high power laser chains. In general, the labour costs involved in the fabrication of deformable mirrors can be reduced by the application of batch fabrication; the design mentioned in the thesis can be easily batch-fabricated. The applicability in high power laser chains can be enabled by the suppression of laser induced mirror deformation.

The thesis presents a novel manufacturing regime mainly based on batch-fabrication. Detailed thermo-mechanical investigations, based on experimentally evaluated material parameters of screen printed tick films, and analytical and finite element modelling are made. As a result, construction guidelines for homogeneous and inhomogeneous thermal mirror loading are formulated. The designed screen printed unimorph deformable mirror is manufactured and tested. The experimental results give evidence of a large piezoelectric stroke and thermo-mechanical mirror characteristics that are comparable with the simulation. Therewith, the novel compensation regime “compound loading” for the suppression of laser induced deformations is developed and proofed. The results of the single chapters are discussed below.

Firstly, a review of active mirrors and their properties is realized in chapters 3.1 to 3.5. This review describes the modes of operation and various configurations of active mirrors, such as segmented mirrors, mirrors with discrete actuators, and DMs. Modular/hybrid mirrors are introduced and MEMS mirrors are separately analysed due to their miniaturized set-up. Subsequently, the limitations of the state-of-the-art solutions are analysed (cf. 3.6) and the scope of the thesis is deduced (cf. 3.7).

The screen printed piezoelectric DM manufacturing concept and set-up is developed in chapter 3. The piezoelectric actuation regime is introduced (cf. 4.1) and the process of layer deposition using batch-fabrication techniques is discussed (cf. 4.2). The screen printing process is chosen for mirror fabrication

due to its (i) accurate processibility that results in the exact layout of structural patterns (film thickness, lateral resolution, etc.), (ii) release of manufacturing costs from actuator patterns and the applicability of different actuator mirror layouts in parallel on a single substrate, (iii) availability of thick (10–150 μm) piezoelectric layers and metallization layers, (iv) excellent actuating characteristics of screen-printed piezoelectric material, and (v) their applicability by screen printing on LTCC substrates. LTCC substrates are particularly suitable as mirror substrates due to their potential integration of mechanical cavities for mounting aids and cooling channels. Further, LTCC substrates can enable integration of screen-printed flat metallization and sensor elements into the multi-layered mirror membrane. Sensor elements such as strain gauges or temperature sensors can facilitate mirror deformation control. The manufacturing process is developed, and comprises six steps out of which five are batch-fabrication techniques. The SPDT process alone does not involve batch fabrication. In contrast to state-of-the-art deformable mirror technologies, the electric wiring is also batch-fabricated. Moreover, the mirror set-up is monolithic. The mirror mount is monolithically joined with the mirror membrane by Solderjet Bumping and copper electroplating, thereby leading to reliable mounting conditions. The material characteristics of the screen-printed layers are also discussed (cf. 4.3). Based on the density and nanoindentation measurements along the layer thickness and the layer surface, the complete stiffness matrix of the piezoelectric layer are evaluated. These results are based on manufacturing-imposed porosity that changes the material parameters of the screen-printed layers.

The detailed technological analysis is further elaborated into the manufacturing concept of the deformable mirror. In this section of the thesis, the structural dimensions are to be optimized by simulations in chapter 5. The simulations chapter is divided into two sections—analytical modelling and FEM. The analytical modelling evaluates the thermally-induced changes in the mirror's ML under homogeneous thermal loading conditions and in the piezoelectric stroke (cf. 5.1). The thermal considerations define the optimum copper-layer thickness

that minimizes the thermally-induced deflections of the mirrors ML (cf. 5.1.1). Consequently, a *zero deflection* design conceptualized; this design leads to balance of the thermally-induced strains in the monolithic single layers, thereby preventing a membrane that is insensitive to homogeneous temperature loading. The *zero deflection* copper-layer thickness for the simply-supported sample membrane is between 12 μm and 24 μm depending on the CTE of the piezoelectric layer. The discussion of the boundary conditions and copper-layer discontinuity proves the concept of thermal self-balancing, which can be realized by copper-layer thickness variations under fixed rim boundary conditions. The thermally-induced deflection can be determined by copper layer discontinuity (or copper-layer thickness variations). The static piezoelectric considerations define the working range of the piezoelectric layer's thickness and layer's diameter for large piezoelectric stroke (cf. 5.1.2). The relative thickness a is optimally thin, and the practical working range is found to be between $a = 1.7$ and $a = 3.1$. The optimal piezoelectric layer diameter is 13.2 mm ($\text{Ø}_{\text{substrate}} = 17.5$ mm), this value is insensitive to changes in the copper-layer thickness. The number of actuators is preferably >15 with 9 actuators being positioned external to the mirror aperture; this choice and positioning of the actuators is based on the effective correction of the Zernike modes.

The FEM simulations evaluated the static and dynamic properties of the membrane for piezoelectric activation and different thermal loadings in chapter 5.2. A CoventorWare™ based FEM model of the mirror assembly is configured, and the piezoelectric stroke is evaluated depending on copper-layer thickness (cf. 5.2.1). The FEM model is populated with the complete stiffness matrix of the piezoelectric layer (4 mm non-oriented polycrystalline material poled in third direction) and also with simplified piezoelectric parameter based on an isotropic material model. The simulations reveal insensitivity of the mirror's piezoelectric stroke to the completeness of stiffness matrix. A simplified database based on the properties of isotropic materials provides simulation results similar to those of the material model for Perovskite crystalline structures poled along z -direction. A comparison of the FEM results and a closed form solutions with simplified isotropic material behaviour revealed a good agreement for copper-layer

thicknesses below 80 μm . The differences between FEM and closed form solution rely not on material property simplifications but more likely on discretization issues of the FEM model or assumptions of the closed form solution.

The dynamic ML properties are evaluated by Ansys based FEM being subject to copper-layer thickness and piezoelectric stiffness variations (cf. 5.2.2). Two sets of material parameters were comparatively simulated; set 2 comprises a proper material data set. A reference system (a system that does not utilize copper metallization) is configured to evaluate the influence of the initial curvature of the mirror membrane on the dynamic behaviour. Further, the influence of residual stress in the piezoelectric layer on resonance behaviour is also evaluated. A computer-based FEM simulation proves that the types of curvature (convex, concave) and not the curvature radius determine the natural frequency shift induced by the initial curvature. A positive (convex) curvature of +40% of the substrate thickness results in a relative change of less than 2% in the first resonance frequency. In contrast, a concave curvature of -40% of the substrate thickness induce +10% relative change in the first resonance frequency. The residual stress in the piezoelectric layer cause membrane bowing. It is shown that the stress-induced bowing depends on the type of stress. A similar magnitude of tensile stress in piezoelectric thick films induces lower membrane deflection than that due to compressive stresses. The changes in the resonance frequency are not attributed to the magnitude of the stress, but to the variations in the membrane shape; in particular, the variations in the direction of curvature determine the resonance frequency shift for the present ML model. These results are important if the resonance frequency is critical to the mirror's operation. Minor tensile stresses in the piezoelectric layer deform the membrane by a small margin and induce only weak resonance shifts; therefore, these stresses can compensate for tensile stresses (such as stresses in dielectric mirror coatings) in other layers.

The thermally-induced changes were also evaluated by FEM. First, simulations of the homogeneous loading and their comparison with the results evaluated by an analytical method proves the existence of a *zero deflection* configuration in 5.2.3. An ML set-up consisting of a homogeneous piezoelectric layer that is

placed between sandwiching Au-electrodes and bonded on a LTCC substrate, requires a *zero deflection* copper-layer thickness of 14 μm . These results are summarized into a construction guideline for such optimized ML membrane mirrors, based on mounting by discrete compliant membrane support (cf. Figure 50). Subsequently, structural inhomogeneity of the piezoelectric layer and two different boundary conditions are integrated—the simply-supported and fixed rim conditions. These results lead to the formulation of new construction guidelines for homogeneous thermal loading of deformable mirrors depending on their boundary conditions. The *zero deflection* copper-layer thickness is approximately 10 μm and 150 μm for the simply supported and fixed rim conditions, respectively. The examination of a suitable metallic mount and the technical mount geometries for application in the mirror system in 5.2.4 reveals an optimal copper-layer thickness between 150 μm and 225 μm for W85Cu15 and CE7 with a thermally-induced deflection of $-0.2 \mu\text{mK}^{-1}$. The study of the technical mount geometries provides a relaxed *zero deflection* copper-layer thickness value in terms of sensitivity to thickness variations and machinability (due to the large thickness of the copper layer). The simulation results also indicate the existence of a *zero deflection* mount material with a CTE between $9 \times 10^{-6}/\text{K}$ and $11 \times 10^{-6}/\text{K}$, thereby leading to a *zero deflection* copper-layer thickness between 150 μm and 225 μm . Mount materials with CTE values in the abovementioned range include CE9 (Al40Si60), W72Cu28, and CE11 (Al50Si50). The ML temperature and the ML deformation caused by inhomogeneous laser loading were also simulated (cf. 5.2.5). A Gaussian intensity distribution of a laser is implemented in the simulation model by using a Gaussian-shaped heat flux. The simulations reveal deformation insensitivity to the mount material and deformation sensitivity to the copper-layer thickness. The laser-induced deformation is between 2.5 $\mu\text{m}/\text{W}$ and 1.1 $\mu\text{m}/\text{W}$ for copper-layer thicknesses between 150 μm and 225 μm , respectively. The temperature distribution of the mirror membrane is radially decreasing with peak values between 5.3 K and 2.8 K for copper-layer thicknesses between 150 μm and 225 μm , respectively. The mirror mount shows temperature changes below 1 K for all investigated copper-layer thicknesses. The deformation and temperature time constants were also

evaluated. The deformation time constant is between 0.7 s and 0.4 s, while the peak temperature time constants are between 1.6 s and 1.4 s for copper-layer thicknesses between 150 μm and 225 μm , respectively.

The thesis formulates two possible methods to compensate for the laser-induced mirror deformation. The compensation can be achieved either by manufacturing-imposed mirror curvature that is balanced by the laser-induced mirror deformation or by homogeneous thermal loading (cf. 5.4.2). The homogeneous thermal loading can compensate for laser-induced deformation as the deformation caused by the loading opposes the laser-induced deformation. This approach is referred as compound loading, and it is investigated in a practical mirror set-up.

The designed ML set-up for compensation of laser induced deformation by compound loading was practically fabricated as reported in chapter 6.1. The developed manufacturing concept is implemented and a deformable unimorph mirror with 19 hexagonally shaped actuators is fabricated (cf. 6.2). The initial mirror shape, the piezoelectrically-generated membrane shape variations, and the Zernike polynomials of the DM assembly are demonstrated in chapter 6.4.1 and chapter 6.4.2, respectively. The thermally-induced changes in the mirror membrane are also considered (cf. 6.4.3). The machined mirror offers an increased total stroke between 17 μm and 20 μm for temperatures between 21.5 K and 58.5 K. The resonance frequency linearly decreases with a rate of -3.3 Hz/ $^{\circ}\text{C}$. These changes are attributed to the temperature-dependent material parameters and not to the variations in the mirror curvature. The mirror curvature changes at a rate of -0.12 $\mu\text{m}/^{\circ}\text{C}$; this value is lower than the theoretical value of -0.2 $\mu\text{m}/^{\circ}\text{C}$.

The laser-induced mirror curvature is 3.4 $\mu\text{m}/\text{W}$ and the deformation time constant is approximately 0.9 s for the absorption of a 1-W cw laser (cf. 6.4.4). The theoretically evaluated laser-induced mirror curvature is 1.3 $\mu\text{m}/\text{W}$ with a deformation time constant of 0.5 s for a power absorption of 1 W for a copper-layer thickness of 200 μm . Therefore, we can conclude that the copper layer has

lower thermal conductivity compared to copper bulk material. This effect (reduction in the thermal conductivity of copper) can be induced by the galvanic deposition of copper, and it required further investigation.

The successful application of the compound loading of the mirror system is shown in this thesis. Different laser-induced mirror deformations are compensated for by additional homogeneous loading (cf. 6.4.5). A 1.3 W absorbed laser power is compensated by a 34 K homogeneous loading. This absorbed laser power corresponds to a reflected laser load of 130 W for 1% absorption. In particular, high power coatings provide a very high reflection of up to 1%, this corresponds to a reflected laser power of 1.3 kW or a power density of 0.4 kW/cm². The simulations reveal a manageable power density of the designed mirror of 1.9 kW/cm² (in case of bulk thermal conductivity of the copper layer). This shows the suitability of the mirror for high-power applications. The piezoelectric activation under compound loading shows an increase in piezoelectric stroke with thermal loading. This is suitable for high-power laser applications where compound loading is necessary.

A typical application of deformable mirrors is considered in the thesis, i.e., compensation for static wavefront deformation (cf. 6.5). It was shown that the P-V wavefront deformation can be improved by a factor of 5.8 and of 5.3 for 18 mm and 15 mm mirror aperture, respectively. The Strehl ratio increases by 0.43 for a 15 mm mirror aperture. These experiments prove the applicability of the developed DM for thermal lensing compensation in high-power laser systems.

Outlook on future developments

The application of the developed deformable mirrors in high power laser chains relies on the application of highly reflective coatings. These tailored coatings should be developed in the next step according to the wavelength and to be shaped power density of the application.

Another task is the optimization of actuator pattern on application challenges, e.g. the efficient compensation for thermal lensing through large mirror deformation range of defocus, astigmatism and spherical.

The LTCC substrate allows for the integration of temperature and deformation sensors. The number and position of sensors in the LTCC substrate should be

evaluated in the next step. The manufacturing regime of the deformable mirrors needs to be adapted and sensor sensitivity can be determined based on the present mirrors and further simulations.

Thesen zur Disputation

Thermo-mechanisches Design, dessen Umsetzung und Erprobung für
unimorphe Spiegel mit siebgedruckter Aktorstruktur

Claudia Bruchmann

1. Die steigende Leistungsdichte in Lasersystemen führt zum Auftreten einer thermischen Linse und der Notwendigkeit zum Ausgleich der selbigen beispielsweise durch aktiv optische Komponenten (Deformierbare Spiegel) im Strahlengang.
2. Unimorphe deformierbare Spiegel werden bereits zur Kompensation thermischer Linsen eingesetzt, jedoch erfordert ein weiterer Anstieg der Laserleistungsdichten neuartige thermo-mechanische Designs dieser Spiegel, um das Auftreten laser-induzierter Deformation auf dem Spiegel zu verhindern.
3. Das entwickelte Mehrlagendesign integriert mehreren Schichten in das Spiegel-setup mit thermo-mechanischen Parametern, die sich vom Substrat und der piezoelektrischen Schicht unterscheiden. Dadurch können thermisch-induzierte Deformationen der Spiegelfläche gezielt beeinflusst und verhindert werden.
4. Thermisch-induzierte Deformation können durch eine homogene Änderung der Spiegeltemperatur oder durch absorbierte und in Wärme umgewandelte Laserstrahlung induziert werden. Abhängig von der Art der thermischen Last und der Applikation müssen die Schichtdicken der einzelnen Lagen angepasst werden. Im vorliegenden Mehrlagendesign wird das thermo-mechanische Verhalten über die Variation der Kupferschichthöhe angepasst.
5. Eine thermisch induzierte Deformation durch eine homogene Temperaturveränderung des Spiegels, kann durch eine sog. zero deflection Konfiguration verhindert werden. Im vorliegenden Beispiel ist die Höhe der Kupferschicht so designt, dass die thermisch induzierte Dehnung der

Dickschichtmetallisierungen zur Kontaktierung der piezoelektrischen Schicht ausgeglichen werden können.

6. Der Ausgleich laserinduzierter Deformationen im deformierbaren Spiegel wird über eine homogene Erwärmung erzielt, deren induzierte Deformation gegenläufig zur laserinduzierten Deformation ist. Diese neuartige Kompensationstechnik wird als „compound loading“ (Kombinierte Belastung) eingeführt.
7. Der Herstellungsprozess der entwickelten deformierbaren Spiegel mit siebgedruckter piezoelektrischer Aktorstruktur besteht aus sechs Arbeitsschritten von denen fünf Schritte auf Waferlevel prozessierbar sind. Einzig die Bearbeitung der Spiegelfläche mittels eines ultrapräzisen Drehprozesses ist kein Waferlevelprozess.
8. Im Gegensatz zum Stand der Technik für deformierbare unimorph Spiegel ist die elektrische Verdrahtung der strukturierten Elektroden auch auf Waferlevel prozessierbar und das Spiegelsetup ist monolithisch.
9. Die entwickelten und vorwiegend mit parallelen Fertigungstechnologien hergestellten Spiegel sind für Hochleistungslaseranwendungen geeignet.
10. Für das vorliegende Mehrlagensubstrat wird gezeigt, dass thermisch induzierte Änderungen der Resonanzfrequenz nicht stressinduziert sind, sondern durch Formänderungen der Spiegelmembran oder durch Temperaturabhängigkeit der thermo-mechanischen Materialparameter hervorgerufen werden.
11. Die thermisch induzierten Änderungen der Resonanzfrequenz können zur Detektion von Temperaturänderungen genutzt werden. Der thermisch induzierte Frequenzshift kann hierbei über die abgeschiedene Kupferhöhe angepasst werden und beträgt zwischen $1.1 \text{ Hz/}^\circ\text{C}$ und $-3.3 \text{ Hz/}^\circ\text{C}$ für Kupferschichtdicken zwischen 0 und $200 \mu\text{m}$.

Appendix

A1. Definition of the Zernike polynomials, their normalization factor and description.

i	N	m	Polynomial	Normalization factor n	description
0	0	0	1	1	Piston
1	1	1	$\rho \cos[\theta]$	2	Tilt X
2	1	1	$\rho \sin[\theta]$	2	Tilt Y
3	1	0	$-1 + 2\rho^2$	$\sqrt{3}$	Defocus
4	2	2	$\rho^2 \cos[2\theta]$	$\sqrt{6}$	Astigmatism 0°
5	2	2	$\rho^2 \sin[2\theta]$	$\sqrt{6}$	Astigmatism 45°
6	2	1	$\rho(-2 + 3\rho^2) \cos[\theta]$	$2\sqrt{2}$	Coma X
7	2	1	$\rho(-2 + 3\rho^2) \sin[\theta]$	$2\sqrt{2}$	Coma Y
8	2	0	$1 - 6\rho^2 + 6\rho^4$	$\sqrt{5}$	Spherical
9	3	3	$\rho^3 \cos[3\theta]$	$2\sqrt{2}$	Trefoil 0°
10	3	3	$\rho^3 \sin[3\theta]$	$2\sqrt{2}$	Trefoil 30°
11	3	2	$\rho^2(-3 + 4\rho^2) \cos[2\theta]$	$\sqrt{10}$	Sec. Astigm. 0°
12	3	2	$\rho^2(-3 + 4\rho^2) \sin[2\theta]$	$\sqrt{10}$	Sec. Astigm. 45°
13	3	1	$\rho(3 - 12\rho^2 + 10\rho^4) \cos[\theta]$	$2\sqrt{3}$	Sec. Coma X
14	3	1	$\rho(3 - 12\rho^2 + 10\rho^4) \sin[\theta]$	$2\sqrt{3}$	Sec. Coma Y
15	3	0	$-1 + 12\rho^2 - 30\rho^4 + 20\rho^6$	$\sqrt{7}$	Sec. Spherical
16	4	4	$\rho^4 \cos[4\theta]$	$\sqrt{10}$	Tetrafoil X
17	4	4	$\rho^4 \sin[4\theta]$	$\sqrt{10}$	Tetrafoil Y
18	4	3	$\rho^3(-4 + 5\rho^2) \cos[3\theta]$	$2\sqrt{3}$	Sec. Trefoil 0°
19	4	3	$\rho^3(-4 + 5\rho^2) \sin[3\theta]$	$2\sqrt{3}$	Sec. Trefoil 30°
20	4	2	$\rho^2(6 - 20\rho^2 + 15\rho^4) \cos[2\theta]$	$\sqrt{14}$	
21	4	2	$\rho^2(6 - 20\rho^2 + 15\rho^4) \sin[2\theta]$	$\sqrt{14}$	
22	4	1	$\rho(-4 + 30\rho^2 - 60\rho^4 + 35\rho^6) \cos[\theta]$	4	
23	4	1	$\rho(-4 + 30\rho^2 - 60\rho^4 + 35\rho^6) \sin[\theta]$	4	
24	4	0	$1 - 20\rho^2 + 90\rho^4 - 140\rho^6 + 70\rho^8$	3	
25	5	5	$\rho^5 \cos[5\theta]$	$2\sqrt{3}$	
26	5	5	$\rho^5 \sin[5\theta]$	$2\sqrt{3}$	

i	N	m	Polynomial	Normalization factor n	description
27	5	4	$\rho^4(-5 + 6\rho^2)\text{Cos}[4\theta]$	$\sqrt{14}$	
28	5	4	$\rho^4(-5 + 6\rho^2)\text{Sin}[4\theta]$	$\sqrt{14}$	
29	5	3	$\rho^3(10 - 30\rho^2 + 21\rho^4)\text{Cos}[3\theta]$	4	
30	5	3	$\rho^3(10 - 30\rho^2 + 21\rho^4)\text{Sin}[3\theta]$	4	
31	5	2	$\rho^2(-10 + 60\rho^2 - 105\rho^4 + 56\rho^6)\text{Cos}[2\theta]$	$3\sqrt{2}$	
32	5	2	$\rho^2(-10 + 60\rho^2 - 105\rho^4 + 56\rho^6)\text{Sin}[2\theta]$	$3\sqrt{2}$	
33	5	1	$\rho(5 - 60\rho^2 + 210\rho^4 - 280\rho^6 + 126\rho^8)\text{Cos}[\theta]$	$2\sqrt{5}$	
34	5	1	$\rho(5 - 60\rho^2 + 210\rho^4 - 280\rho^6 + 126\rho^8)\text{Sin}[\theta]$	$2\sqrt{5}$	
35	5	0	$-1 + 30\rho^2 - 210\rho^4 + 560\rho^6 - 630\rho^8 + 252\rho^{10}$	$\sqrt{11}$	

A2. Material data PIC 151 based on M. Rauer, personal communication, October 30, 2009.

Complete material data set PIC151					
Coefficient	Unit	Value	Coefficient	Unit	Value
Density	kg/m ³	7,76E+03	N1	Hzm	1384
			N3	Hzm	1817
Qm		88	N5	Hzm	1050
			Np	Hzm	1915
ε 11T		1936	Nt	Hzm	2118
ε 33T		2109			
ε 11S		1110	d31	m/V	-2,14E-10
ε 33S		852	d33	m/V	4,23E-10
tan δ		15,7E-3	d15	m/V	6,10E-10
k31		0,382	g31	Vm/N	-1,15E-02
k33		0,697	g33	Vm/N	2,18E-02
k15		0,653	g15	Vm/N	3,65E-02
kp		0,663			
kt		0,528	e31	N/Vm	-9,60
			e33	N/Vm	15,10
Poisson (σ)		0,34	e15	N/Vm	12,00
s11E	m ² /N	1,683E-11	c11E	N/m ²	1,076E+11
s33E	m ² /N	1,900E-11	c33E	N/m ²	1,004E+11
s55E	m ² /N	5,096E-11	c55E	N/m ²	1,962E+11
s12E	m ² /N	-5,656E-12	c12E	N/m ²	6,312E+10
s13E	m ² /N	-7,107E-12	c13E	N/m ²	6,385E+10
s44E	m ² /N	5,096E-11	c44E	N/m ²	1,962E+10
s66E	m ² /N	4,497E-11	c66E	N/m ²	2,224E+10
s11D	m ² /N	1,436E-11	c11D	N/m ²	1,183E+11
s33D	m ² /N	9,750E-11	c33D	N/m ²	1,392E+11
s55D	m ² /N	2,924E-11	c55D	N/m ²	3,420E+10
s12D	m ² /N	-8,112E-12	c12D	N/m ²	7,376E+10
s13D	m ² /N	-2,250E-12	c13D	N/m ²	4,436E+10
s44D	m ² /N	2,924E-11	c44D	N/m ²	3,420E+10
s66D	m ² /N	4,497E-11	c66D	N/m ²	2,224E+10

Values are only for information - no specification!
Simulation purpose

The data in the table was determined using test bodies with geometries and dimensions in accordance with European Standard EN 50324 2, and are typical values.

Singular parameters can deviate from catalogue values, because they were measured at samples which were taken from one block of ceramics according to the sequence of IEC483 to get maximum consistency.

Catalogue values reflect the statistical distribution of each individual specification in production and therefore also take into account spreading from material batch to material batch.

A3. Material data PIC 255 based on M. Rauer, personal communication, October 30, 2009.



Material coefficients PIC255					
Coefficient	Unit	Value	Coefficient	Unit	Value
Density	kg/m ³	7,80E+03	N1	Hzm	1420
Qm		80	N3	Hzm	1710
			N5	Hzm	1125
ε 11Tr		1649	Np	Hzm	2000
ε 33Tr		1750	Nt	Hzm	2000
ε 11Sr		930			
ε 33Sr		857	d31	m/V	-1,74E-10
			d33	m/V	3,94E-10
β 11T	Vm/As	6,85E+07	d15	m/V	5,35E-10
β 33T	Vm/As	6,45E+07			
β 11S	Vm/As	1,21E+08	g31	Vm/N	-1,13E-02
β 33S	Vm/As	1,32E+08	g33	Vm/N	2,54E-02
			g15	Vm/N	3,66E-02
tan δ		20,0E-3			
			e31	N/Vm	-7,15
k31		0,351	e33	N/Vm	13,70
k33		0,691	e15	N/Vm	11,90
k15		0,661			
kp		0,620	h31	N/As	-9,43E+08
kt		0,471	h33	N/As	1,81E+09
			h15	N/As	1,45E+09
Poisson (σ)		0,36			
s11E	m ² /N	1,590E-11	c11E	N/m ²	1,230E+11
s33E	m ² /N	2,097E-11	c33E	N/m ²	9,711E+10
s55E	m ² /N	4,492E-11	c55E	N/m ²	2,226E+10
s12E	m ² /N	-5,699E-12	c12E	N/m ²	7,670E+10
s13E	m ² /N	-7,376E-12	c13E	N/m ²	7,025E+10
s44E	m ² /N	4,492E-11	c44E	N/m ²	2,226E+10
s66E	m ² /N	4,319E-11	c66E	N/m ²	2,315E+10
s11D	m ² /N	1,393E-11	c11D	N/m ²	1,298E+11
s33D	m ² /N	1,096E-11	c33D	N/m ²	1,220E+11
s55D	m ² /N	2,532E-11	c55D	N/m ²	3,949E+10
s12D	m ² /N	-7,660E-12	c12D	N/m ²	8,345E+10
s13D	m ² /N	-2,945E-12	c13D	N/m ²	5,729E+10
s44D	m ² /N	2,532E-11	c44D	N/m ²	3,949E+10
s66D	m ² /N	4,319E-11	c66D	N/m ²	2,315E+10

Values are only for information - no specification!

Simulation purpose

The data in the table was determined using testbodies with geometries and dimensions in accordance with European Standard EN 50324 2, and are typical values.

Singular parameters can deviate from catalogue values, because they were measured at samples which were taken from one block of ceramics according to the sequence of IEC483 to get maximum consistency.

Catalogue values reflect the statistical distribution of each individual specification in production and therefore also take into account spreading from material batch to material batch.

A4. Material data mount materials

Copper thickness / μm	Deformation @point 1 / μm		
	CE7	WCu	CE11
100	2.52	2.50	2.59
150	1.89	1.92	1.94
200	1.32	1.37	1.36
225	1.09	1.15	

List of figures

Figure 1 (a) Wavefront aberration $W(\varrho, \varphi)$, (b) Compensation for wavefront aberration by variation of the optical path length by a deformable mirror.	9
Figure 2 The lens array focuses discrete parts of the aberrated wavefront onto a CCD array with 4 pixel underneath every lens.	11
Figure 3 Zernike Polynomials Z1 to Z15.....	12
Figure 4 Optical classification of active optical elements.....	15
Figure 5 Active segmented mirror composed of sixty-one hexagonal segments. Each hexagonal mirror can be controlled via a piston, tip and tilt mechanism. Credit: Picture and text taken from the ESO website.	17
Figure 6 Prototype of Hamelinck's mirror system with 61 actuators in one of its assembly steps. Credit: Picture and text by Roger Hamelinck.....	19
Figure 7 Cross-section of a unimorph deformable mirror. One segmented electrode is activated (shown in red). The activation causes the piezoelectric material between activated electrode and ground electrode to contract.....	21
Figure 8 Silicon wafer (\varnothing 150 mm, thickness = 700 μm) with 91 screen printed piezoelectric actuators and an active optical aperture of 65 mm; (a) Soldered wires, (b) Mirror surface, and (c) modular mirror comprising silicon wafer with screen-printed thick film.	24
Figure 9 (a) Diagram of a single mirror segment. Engineered stress in the bimorph flexure lifts the mirror segment. The three electrodes enable piston plus tip/tilt movement. (b) Scanning electron microscopy image of the Iris AO 37-segment deformable mirror. Credit: Pictures taken from	29
Figure 10 Addressing electrodes with four configurations of electrical wiring. Each configuration covers one-fourth of a piezoelectric mirror's rear surface. (1) Glued/soldered wires, (2) drawing-out of the electrodes, (3) flexible copper-clad laminates, and (4) 3D-structuring by lithographic processes or screen printing..	33
Figure 11 Piezoelectric sample with definition of the axes. Reverse piezoelectric effect: application of an electric field results in an expansion in the direction of the field and contraction perpendicular to the field axis.	39
Figure 12 Polarization: (a) electric field curve and (b) strain-electric field curve.	40

Figure 13 Mechanical hysteresis: hysteresis width is the difference between the rising and falling curves.....	42
Figure 14 Screen-printed sample structures: (a) singularized piezoelectric cantilever with different cantilever lengths on Al ₂ O ₃ substrate and (b) different screen-printed cantilever and circular membrane structures on LTCC before singularization.....	53
Figure 15 Schematic of the screen-printed sample structures: surface and cross-section.....	54
Figure 16 Microscopic images of polished piezoelectric thick film samples on Al ₂ O ₃ and LTCC substrates.....	56
Figure 17 Schematic of the evaluation of the material characteristics of piezoelectric thick films based on measurements and comparison with piezoelectric bulk data.....	57
Figure 18 Measured indentation modulus in cross-section.....	60
Figure 19 Identification of suitable material by comparison of measured data of PZT thick film (TF) with available material.....	62
Figure 20 Comparison of measured stiffness of PZT thick films (TF) with material characteristics of bulk materials. Poisson's ratio is assumed to be 0.3...	62
Figure 21 Comparison of calculated stiffness ratio.....	64
Figure 22: Definition of the stress level in the piezoelectric layer	66
Figure 23 The mirror manufacturing concept is comprised from six steps. Schematic shows the cross-section of a mirror membrane.....	72
Figure 24 Mirror mounting options: (a) loose mounting, (b) central clamping, (c) fixed mounting, and (d) discrete compliant membrane support.....	73
Figure 25 Mirror design concept. (a): cross section of mounted mirror membrane; (b): detail with mounting aid structures, mount and solder filled conical bores.	75
Figure 26 Model of a circular multilayer mirror membrane.....	77
Figure 27 Thermally-induced curvature and deflection for copper-layer thicknesses t_s between 0 μm and 100 μm at a thermal loading of up to 30 K. The CTE of the piezoelectric material varies from 4 to 8 $\times 10^{-6}\text{K}^{-1}$. Left: Curvature. Right: Deflection for 10 K (blue, dashed) and 30 K (red line) loads. The <i>zero deflection</i> copper-layer thickness is insensitive to the temperature load.....	81

Figure 28 Deflection of a circular plate. Two cases are examined: circular and annular top layer (blue) with simply-supported and fixed-rim boundary conditions. Ratio A/S is the coverage ratio of the substrate.....	82
Figure 29 Active layer mirror set-ups.	85
Figure 30 Comparison of different piezoelectric layer set-ups. Highest stroke is induced by unimorph and cooperative set-ups within the working range.	86
Figure 31 Optimization of piezoelectric layer diameter for different copper-layer thicknesses. (a) Model and (b) simulated deflection of the membrane centre for different copper-layer thicknesses.	88
Figure 32 Influence of the copper-layer thickness on the piezoelectric stroke.....	89
Figure 33 (a) 3D model using CoventorWare™. The fixed boundary condition is highlighted (yellow). (b) Simulation results of both finite element method and closed-form solutions. The deviation between both methods increases with increasing copper-layer thickness.....	93
Figure 34 ANSYS model of the piezoelectric membrane. Boundary conditions suppress the membrane movement at its rim. The membranes centre can freely move along the y-direction.	94
Figure 35 Resonance frequency as a function of the copper-layer thickness for two different sets of piezoelectric material properties.	96
Figure 36 (a) Mechanical model with fixed rim and applied prestress on the top electrode, (b) Modeled change in resonance frequency by initial curvature of the membrane.....	97
Figure 37 Membrane deflection for different tensile and compressive stress levels.....	99
Figure 38 (a) Stress-induced resonance shift for stress levels between -100 MPa and +100 MPa, (b) Resonance shift for low stress levels.....	99
Figure 39 Comparison of the induced frequency shift depending on the membrane deflection.	100
Figure 40 Comparison of dilatation and stress S_x for tensile and compressive pre-tension of the piezoelectric membrane. The arrows represent the forces in the mirror membrane.	101

Figure 41 (a) Mechanical model and boundary conditions, (b) P-V membrane deformation for copper-layer thicknesses up to 200 μm at 10-K and 30-K homogeneous loadings. (c) Mirror membrane deformation along membrane radius. Zero deflection multilayer set-up requires 14 μm of copper-layer thickness.	103
Figure 42 (a) S_x calculated by FEM for temperatures of 10 K and 30 K. Positive values indicate tensile stress and negative values indicate compressive stress. (b) Comparison between FEM and closed-form solution reveal good agreement of the results.	104
Figure 43 ML membrane's centre deflection for CTE values of (4, 6 and 8) $\times 10^{-6} \text{K}^{-1}$ for (a) simply-supported mirror membrane and (b) fixed rim boundary conditions.	106
Figure 44 Simulation model with mount and boundary conditions (figure not drawn to scale).	108
Figure 45 (a) Thermally-induced P-V mirror deformation for different mount materials. (b) Comparative representation of the simulation results of membrane deformation for CE7 and WCu.	109
Figure 46 Simulation model of inhomogeneous loading with measurement points 1-3 (not drawn to scale).	111
Figure 47 Induced deformation at measurement point 1 for different mount materials.	112
Figure 48 Laser-load-induced deformation and temperature change at measurement point 1 for different mount materials.	113
Figure 49 Simulated temperature increase on measurement points 1-3.	114
Figure 50 (a) Multilayer membrane with <i>zero deflection</i> design and simply-supported from underneath on a base plate. (b) The assembly is homogeneously loaded (heated) and the ML expands laterally ($\text{CTE}_{\text{ML}} = \text{CTE}_{\text{base}}$). The radial expansion of the mount (base plate) is equal to the radial expansion of the ML. The thermally-induced deflection is zero.	117
Figure 51 Thermo-mechanical design approaches for deformable mirrors.	119
Figure 52 Cross-sectional view of the deformable mirror assembly.	123

Figure 53 Comparison between (a) mesh design and (b) screen-printed sample mirror.	124
Figure 54 Design of the mounting and attached mirror including a detailed view of the conical joining geometry that allows the solder to form a joint between the mirror and the mount.	126
Figure 55 Single point diamond turning (SPDT) tool path generation. Dashed lines indicate the design tool path and solid lines indicate the membrane shape. The tool path is generated with respect to the filler-induced deformation and the mechanical load of the SPDT tool.	129
Figure 56 (a) Cross-sectional view of the deformable mirror mount with integrated Peltier element for thermal control of the mirror. (b) Image of the mounted mirror with applied gold coating.	130
Figure 57 Adaptive optical measurement and control set-up: The collimated beam of a laser diode (LD) is expanded by a beam expander (BE 1), and it is incident on the deformable mirror. The DM reflects the light that passes through a beam splitter cube (BSC). A second beam expander (BE 2) adapts the light diameter to the aperture of the wavefront sensor (WFS).	131
Figure 58 Experimental set-up for inhomogeneous and compound loading. High power laser beam is expanded to 20 mm whereat the hard stop ensures the beam diameter. Peltier element and piezoelectric actuators (PZT) are hot-wired during inhomogeneous loading and controlled during compound loading.	132
Figure 59 Initial mirror membrane shape: (a) Tencor FLX-2320 measurements reveal a radius of approximately 2.5 m. The WFS aperture of the adaptive optical set-up is also shown. (b) Measurement of the AO set-up. (c) Mirror shape without piston, tip, tilt, and defocus.	134
Figure 60 Measured actuator influence function for machined screen printed DM.	136
Figure 61 Graphical representation of the calculated P-V values of the AIFs measured by WFS and vibrometer. The comparison reveals good agreement between the two measurement set-ups. P-V values decrease with radial distance from the mirror centre. Some actuators have not been measured by the scanning vibrometer.	137

Figure 62 Image of the screen-printed actuator patterns with corresponding apertures between 15.3 mm and 24.5 mm. Comparison between uncompensated and actively levelled mirror membrane by activation of $\pm 10\%$ of the piezoelectric working range. The P-V and rms deviation of the mirror membrane without accounting for the defocus term are also shown.....	138
Figure 63 (a) Examples for adjustable Zernike polynomials C_3 to C_{10} . (b) P-V membrane deformation [μm] for Zernike polynomials in (a).....	139
Figure 64 Rms deviation from adjusted Zernike coefficients. (a) Positive Zernike coefficients. (b) Negative Zernike coefficients.....	140
Figure 65 Examples for Zernike polynomials C_3 to C_{10} . Mirror aperture 22.5 mm and 100 V Offset applied to all actuators.	141
Figure 66: Total stroke of the deformable mirror for different temperatures and copper-layer thicknesses.....	142
Figure 67 (a) Frequency of the first resonance, and (b) quality of resonance depending on temperature.....	143
Figure 68 Temperature-induced P-V deflection of the mirror membrane. Slope of the linear fit is $-0.1 \mu\text{mK}^{-1}$	145
Figure 69 (a) Changes in the Zernike coefficients C_3 – C_7 for temperature differences up to 30 K. (b) Zernike coefficients C_1 – C_{20} of the mirror membrane at 35 K.....	146
Figure 70 Image of the experimental measurement set-up for homogeneous, inhomogeneous, and compound loading of the mirror system. The red line indicates the path of the high-power laser beam and the thin white lines indicate the monitoring beam's path from the laser diode to the WFS.	147
Figure 71 Plot of the absorbed power against the P-V deformation. The laser-load-induced membrane deformation is $3.4 \mu\text{m/W}$. There is no detectable difference between the cw laser and modulated laser loads.....	148
Figure 72 Transient behaviour of the mirror deformation for different cw and modulated laser loads. The table on the right summarizes the measured time constants.....	149
Figure 73 (a) Zernike coefficients with 100% duty cycle for different absorbed laser powers. Zernike coefficients scale in proportion to the absorbed laser	

power. (b) Mirror surface reconstructed from Zernike coefficients C_1 – C_8 without defocus.	150
Figure 74 P-V membrane deformation for two sets of measurements, (A) and (B). The measurements reveal an optimum homogeneous pre-heating for minimal membrane deformation.	151
Figure 75 Zernike coefficients of defocus in measurements (A) and (B). The measurements reveal an optimum homogeneous loading that compensates for the defocus term under different inhomogeneous loads.	152
Figure 76 Comparison between theoretical and experimental characteristics of compound loading.	154
Figure 77 Compensation of static wavefront aberrations for different mirror apertures.	155

References

- ¹ Björn Wedel, "Anforderungen an Laserbearbeitungsköpfe beim Schweißen mit hoher Strahlqualität," Proc. 5. Laser-Anwendungsforum Bremen, (2006).
- ² H. Hügel, T. Graf, *Laser in der Fertigung – Strahlquellen, Systeme, Fertigungsverfahren* (Vieweg+Teubner, 2009).
- ³ N. Hodgson, H. Weber, *Laser Resonators and Beam Propagation – Fundamentals, Advanced Concepts and Applications* (Springer, 2005).
- ⁴ M. Yu. Loktev, V. N. Belopukhov, F. L. Vladimirov, G. V. Vdovin, G. D. Love, A. F. Naumovb, "Wave front control systems based on modal liquid crystal lenses," *Rev. Sci. Instrum.* **71**, 3290-3297 (2000).
- ⁵ J. M. Geary, *Introduction to Wavefront Sensors* (SPIE, 1995).
- ⁶ R. K. Tyson, *Principles of Adaptive Optics* (Academic, 1991).
- ⁷ E. Hecht, *Optik* (Oldenbourg Verlag München, 5. improved edition, 2009).
- ⁸ F. Zernike, "Beugungstheorie des Schneidensverfahrens und seiner verbesserten Form, der Phasenkontrastmethode," *Physica* **1**, 689-704, (1934).
- ⁹ International Organization for Standardization, *ISO 10110-5 Part 5 Surface form tolerances* (First edition, 1996-03-15).
- ¹⁰ DIN Deutsches Institut für Normung e.V., *Augenoptik und ophthalmische Instrumente – Verfahren zur Darstellung von Abbildungsfehlern des menschlichen Auges (ISO 24157:2008); Deutsche Fassung EN ISO 24157:2008*, (Beuth Verlag, 2008).
- ¹¹ R. J. Noll, "Zernike polynomials and atmospheric turbulence," *J. Opt. Soc. Am.* **66**, 207–211 (1976).
- ¹² M. Born, E. Wolf, *Principles of optics: electromagnetic theory of propagation, interference and diffraction of light*, (Pergamon Press, Oxford, 1993).
- ¹³ J. C. Wyant, K. Creath, *Basic Wavefront Aberration Theory for Optical Metrology*, Chap. 1 in *Applied Optics and Optical Engineering*, Vol. XI, RR Shannon and JC Wyant, Eds., 1–53 (1992). <http://www.optics.arizona.edu/jcwyant/Zernikes/Zernikes.pdf>
- ¹⁴ K. Strehl, "Über Luftschlieren und Zonenfehler," *Zeitschrift für Instrumentenkunde* **22**, 213-217 (1902).
- ¹⁵ W. Singer, M. Totzeck, H. Gross, *Handbook of Optical Systems – Vol. 2*, (Wiley-VCH, 2005).
- ¹⁶ R. H. Freeman and J. E. Pearson, "Deformable mirrors for all seasons and reasons," *Appl. Opt.* **21**, 580-588 (1982).
- ¹⁷ F. G. Gebhardt, J. F. Kendall, J. F. Jaminet, E. D. Hasselmark, and G. S. Bar-Tal, *United Technologies Research Center Report N911771-11* (1974).

- ¹⁸ J. W. Hardy, "Instrumental limitations in adaptive optics for astronomy," *Proc. SPIE* **1114**, 2-13 (1989).
- ¹⁹ B. Hulburd, D. Sandier, "Segmented mirrors for atmospheric compensation," *Opt. Eng.* **29**, 1186-1190 (1990). doi:10.1117/12.55713
- ²⁰ D. S. Acton and R. C. Smithson, "Solar imaging with a segmented adaptive mirror," *Appl. Opt.* **31**, 3161-3169 (1992).
- ²¹ F. Gonté, C. Dupuy, B. Luong, C. Frank, R. Brast, and B. Sedghi, "Active hexagonally segmented mirror to investigate new optical phasing technologies for segmented telescopes," *Appl. Opt.* **48**, 6392-6399 (2009).
- ²² F. Gonté, C. Dupuy, C. Frank, C. Araujo, R. Brast, R. Frahm, R. Karban, L. Andolfato, R. Esteves, M. Nylund, B. Sedghi, G. Fischer, L. Noethe, F. Derie, "The First Active Segmented Mirror at ESO," *The Messenger* **128**, 23-24 (2007).
- ²³ R. K. Tyson, *Principles of Adaptive Optics* (Academic, 1991).
- ²⁴ M.A. Ealey and J.F. Waheba, "Continuous facesheet low voltage deformable mirror," *Opt. Eng.* **29**, 1191-1198 (1990).
- ²⁵ Patent US000004657358A: cooled deformable mirror. filed 23.08.1985, date of publication 14.04.1987, US 4,657,358. Assignees: Itek Corporation, Textron Inc., Inventors: Frank M. Athony, Ralph E. Aldrich, Steven M. Daigneault
- ²⁶ http://www.as.northropgrumman.com/products/aoa-xin_deformable_mirror/index.html
- ²⁷ R. Hamelinck, R. Ellenbroek, N. Rosielle, M. Steinbuch, M. Verhaegen, N. Doelman, "Validation of a new adaptive deformable mirror concept," *Proc. SPIE* **7015**, 70150Q, (2008). doi:10.1117/12.787755
- ²⁸ http://alpao.fr/products_deformable_mirrors.html (10.08.2011)
- ²⁹ Currents flow through solenoids creating Laplacian forces.
- ³⁰ J. Feinleib, S. G. Lipson, P. F. Cone, "Monolithic piezoelectric mirror for wavefront correction" *Appl. Phys. Lett.* **25**, 311-313 (1974). doi:10.1063/1.1655486
- ³¹ C. A. Primmerman and D. G. Fouche, "Thermal-blooming compensation: experimental observations using a deformable-mirror system," *Appl. Opt.* **15**, 990-995 (1976).
- ³² E. Steinhaus and S. G. Lipson, "Bimorph piezoelectric flexible mirror," *J. Opt. Soc. Am.* **69**, 478-481 (1979).
- ³³ C. Schwartz, E. Ribak, and S. G. Lipson, "Bimorph adaptive mirrors and curvature sensing," *J. Opt. Soc. Am. A* **11**, 895-902 (1994).
- ³⁴ J. -C. Siquin, J. -M. Lurcon, C. Guillemard, "Monomorph large aperture deformable mirror for laser applications," *Proc. 6. Int. Workshop on ADAPTIVE OPTICS FOR INDUSTRY AND MEDICINE*, 130-135 (2007).

- ³⁵ A. G. Safronov, "Bimorph adaptive optics: elements, technology, and design principles," Proc. SPIE **2774**, 494-504 (1996). doi:10.1117/12.246729
- ³⁶ A. V. Kudryashov, V. I. Shmalhausen, "Semipassive bimorph flexible mirrors for atmospheric adaptive optics applications," Opt. Eng. **35**, 3064-3073 (1996). doi:10.1117/1.601044
- ³⁷ J. C. Dainty, A. V. Koryabin, and A. V. Kudryashov, "Low-Order Adaptive Deformable Mirror," Appl. Opt. **37**, 4663-4668 (1998).
- ³⁸ A. L. Rukosuev, A. Alexandrov, V. Y. Zavalova, V. V. Samarkin, and A. V. Kudryashov, "Adaptive optical system based on bimorph mirror and Shack-Hartmann wavefront sensor," Proc. SPIE **4493**, 261-268 (2002). doi:10.1117/12.454721
- ³⁹ <http://www.cilas.com/adaptative-mirrors.htm> (26.05.2010)
- ⁴⁰ <http://www.turn.ru/products/at26.htm> (06.07.2011)
- ⁴¹ <http://www.nightn.ru/> (06.07.2011)
- ⁴² T. R. Möller, *Ein Beitrag zur Untersuchung von Bimorphspiegeln für die Präzisionsoptik*, (Shaker, 2002).
- ⁴³ G. Rodrigues, R. Bastait, S. Roose, Y. Stockman, S. Gebhardt, A. Schoenecker, P. Villon, A. Preumont, „Modular bimorph mirrors for adaptive optics,” Opt. Eng. **48**, 034001- 034001-7 (2009). doi:10.1117/1.3099716
- ⁴⁴ Pictures taken from http://www.ulb.ac.be/scmero/optic_bimorph.html;
- ⁴⁵ Patent US000003904274A: monolithic piezoelectric wavefront phase modulator. filed 27.08.1973, date of publication: 09.09.1975, US 3,904,274. Assignees: Itek Corp, Inventors: Julius Feinleib, Stephen G. Lipson
- ⁴⁶ Patent US000004298247A: thick optical element having a variable curvature. Filed 01.04.1980, date of publication: 03.11.1981, US 4,298,247. Assignee :Quantel, Inventors: Guy Michelet, Jean-Pierre Treton
- ⁴⁷ Patent US000004257686A: multiple layer piezoelectric wavefront modulator. filed: 14.12.1978, date of publication: 24.03.1981, US 4,257,686. Assignee: Itek Corp, Inventors: Nedo P. Albertinetti, Ralph E. Aldrich
- ⁴⁸ Patent EP000000793120A1: Bimorpher, adaptiver Mosaikspiegel. Date of filing: 06.05.1996, Date of publication: 03.09.1997, EP 0 793 120 A1. Applicant: Yalstown Corp N.V, Inventor: Andrei Gennadievich Safronov
- ⁴⁹ Patent DE102004051838A1: Spiegelanordnung, Verfahren zum Herstellen einer solchen, optisches System und lithographisches Verfahren zur Herstellung eines miniaturisierten Bauelements. Date of filing: 25.10.2004, date of publication: 25.05.2005, DE 10 2004 051 838 A1. Applicant: Carl Zeiss SMT AG, Inventors: Dr. Timo Möller, Dr. Martin Ross-Messemer, Dr. Frank, Höller, Sascha Bleidistel

- ⁵⁰ Patent WO002006046078A1: heat dissipating layers in de formable mirrors. Date of filing: 13.09.2005, date of publication: 04.05.2006, WO 2006/0406078 A1. Applicant: Bae Systems Plc, Inventors: Michael Stewart Griffith, Leslie Charles Laycock
- ⁵¹ Patent WO002009007447A3: deformable mirror. Date of filing: 11.07,2008, Date of publication: 15.01.2009, WO 2009/007447 A3. Applicant: Univ. Bruxelles, Invetors: Andre Preumont, Goncalo Rodrigues
- ⁵² M. Griffith, L. Laycock, N. Archer, I. Sardharwalla, R. Myers, P. Doel, "Progress on the development of a zonal bimorph deformable mirror," Proc. SPIE **7476**, 74760L-1 – 74760L-11 (2009).
- ⁵³ G. Rodrigues, *Adaptive Optics With Segmented Deformable Bimorph Mirrors*, PhD (Active Structures Laboratory, ULB, Belgium, 2010).
- ⁵⁴ G. Vdovin, P. M. Sarro, "Flexible mirror micromachined in silicon," Appl. Opt. **34**, 2968-2972 (1995). doi:10.1364/AO.34.002968
- ⁵⁵ <http://www.okotech.com/mmdm> (07.04.2010)
- ⁵⁶ G. Vdovin, V. Kiyko, "Intracavity control of a 200-W continuous-wave Nd:YAG laser by a micromachined deformable mirror," Opt. Letters **26**, 798-800 (2001).
- ⁵⁷ S. Bonora, I. Capraro, L. Poletto, M. Romanin, C. Trestino, and P. Villorresi, "Wave front active control by a digital-signal-processor-driven deformable membrane mirror," Rev. Sci. Instrum. **77**, 093102-1 - 093102-5 (2006). doi:10.1063/1.2337096
- ⁵⁸ S. Bonora, L. Poletto, "Push-pull membrane mirrors for adaptive optics," Opt. Express **14**, 11935-11944 (2006). doi:10.1364/OE.14.011935
- ⁵⁹ <http://www.edmundoptics.com/onlinecatalog/DisplayProduct.cfm?productid=3258> (22.06.2010)
- ⁶⁰ T. G. Bifano, J. Perreault, R. K. Mali, M. N. Horenstein, "Microelectromechanical Deformable Mirrors," IEEE J. of Sel. Topics in Quantum Electronics **5**, 83-89 (1999).
- ⁶¹ <http://www.bostonmicromachines.com/deformable-mirrors.htm> (07.04.2010)
- ⁶² http://www.thorlabs.de/newgrouppage9.cfm?objectgroup_id=3208 (22.06.2010)
- ⁶³ D. Dagel, W. Cowan, O. Spahn, G. Grossetete, A. Grine, M. Shaw, P. Resnick, and B. Jokiel, Jr., "Large-stroke MEMS deformable mirrors for adaptive optics," J. Microelectromech. Syst. **15**, 572–583 (2006).
- ⁶⁴ M. A. Helmbrecht, T. Juneau and M. Hart, and N. Doble, "Segmented MEMS deformable mirror technology for space applications," Proc. SPIE **6223**, 622305-1 - 622305-7 (2006).
- ⁶⁵ <http://www.irisao.com/products.html> (07.04.2010)
- ⁶⁶ <http://www.laser2000.de/index.php?id=374537> (29.10.2011)

- ⁶⁷ S. A. Cornelissen, P. A. Bierden, T. G. Bifano, C. V. Lam, "4096-element continuous face-sheet MEMS deformable mirror for high-contrast imaging," *J. Micro/Nanolith. MEMS MOEMS* **8**, 031308-1 – 031308-8 (2009). doi:10.1117/1.3158067
- ⁶⁸ J. D. Mansell, S. Sinha, R. L. Byer, "Deformable Mirror Development at Stanford University," *Proc. SPIE* **4493** (2002).
- ⁶⁹ http://www2.dupont.com/Pyralux/en_US/products/laminate/ (02.11.2011)
- ⁷⁰ EMES consulting LTD, *UK ADAPTIVE OPTICS MARKET AND SUPPLY CHAIN STUDY* (A report for the STFC astronomy technology centre, 2009).
- ⁷¹ D. J. Jendritza, *Technischer Einsatz neuer Aktoren* (expert, 2008).
- ⁷² B. Jaffe, W.R. Cook Jr. and H. Jaffe, *Piezoelectric Ceramics* (Academic Press, 1971).
- ⁷³ <http://www.piceramic.de/piezoeffekt.html> (22.06.2010)
- ⁷⁴ W. Heywang, K. Lubitz, W. Wersing, *Piezoelectricity: Evolution and Future of a Technology* (Springer Series in Material Science **114**, 2008).
- ⁷⁵ K. R. Ruschmeyer, *Piezokeramik-Grundlagen, Werkstoffe, Applikationen* (expert Verlag, 1995)
- ⁷⁶ H. S. Nalwa, *Ferroelectric polymers: chemistry, physics, and applications* (Marcel Dekker, 1995).
- ⁷⁷ I. Tichy, G. Gautschi, *Piezoelektrische Messtechnik* (Springer, 1980).
- ⁷⁸ A. Lenk, *Elektromechanische Systeme-Band 1 und II* (VEB Verlag Technik, 1971).
- ⁷⁹ T. K. Gupta, *Handbook of Thick- and Thin-Film Hybrid Microelectronics* (John Wiley & Sons, 2003).
- ⁸⁰ N. J. Conway, Z. J. Traina and S.-G. Kim, "A strain amplifying piezoelectric MEMS Actuator," *J. Micromech. Microeng.* **17**, 781–787 (2007). doi:10.1088/0960-1317/17/4/015
- ⁸¹ A. Schroth, M. Ichiki, J. Akedo, M. Tanaka, R. Maseda, "Properties and Application of Jet Printed Piezoelectric PZT Film for Actuation Purposes," *Proc. Int. Sympos. Micromechatronics and Human Science*, 67-72 (1997).
- ⁸² D. H. Lee, B. Derby, "Preparation of PZT suspensions for direct ink jet printing," *J. Europ. Ceram. Soc.* **24**, 1069–1072 (2004.)
- ⁸³ S. Zhang, Z. Liang, Q. Wang, Q. M. Zang, "Ink-Jet printing of ferroelectric poly(vinylidene fluoride-trifluoroethylene) copolymers," *Proc. Mat. Research Soc. Symp.* **889**, 167-186 (2006).
- ⁸⁴ J. E. Sergent, C. A. Harper, *Hybrid Microelectronics Handbook* (McGraw-Hill, 1995).
- ⁸⁵ <http://www.koenen.de/> (14.11.2011)
- ⁸⁶ W. Wolny „Piezoceramic Thick Films - Technology and Applications. State of the Art in Europe," *Proc. of 12th IEEE Int. Symp. Appl.Ferroelectrics* **1**, 257-262 (2000).
- ⁸⁷ M. Hrovat, J. Holc, S. Drnovsek, D. Belavic, J. Cilensek, S. Macek, M. Santo-Zarnik, and M. Kosec "Processing and Evaluation of Piezoelectric Thick Films on Ceramic Substrates," *Proc. of 4th Europ. Microelectronics and Packaging Symp. EMPS*, 3-8 (2006).
- ⁸⁸ E.S. Thiele, D. Damjanovic, N. Setter, "Processing and Properties of Screen-Printed Thick Films on Electroded Silicon" *J. Am. Ceram. Soc.* **84**, 2863-2868 (2001).

- ⁸⁹ R. N. Torah, S. P. Beeby, M. J. Tudor, N. M. White, "Thick-film piezoceramics and devices," *J. Electroceram* **19**, 95-110 (2007). DOI: 10.1007/s10832-007-9040-7
- ⁹⁰ H. Baudry, "Screen printing piezoelectric devices," *Proc. 6th European Microelec. Conf.*, 456–463 (1987).
- ⁹¹ S. Gebhardt, L. Seffner, F. Schlenkrich, A. Schönecker „PZT thick films for sensor and actuator applications," *J. Europ. Ceram. Soc.* **27**, 4177–4180 (2007).
- ⁹² IEEE Standard on Piezoelectricity ANSI/IEEE Std 176-1987
- ⁹³ M. S. Zarnik, D. Belavic, H. Ursic, S. Macek, "Numerical modelling of ceramic mems structures with piezoceramic thick films," *J. Electroceram* **20**, 3-9 (2008). DOI: 10.1007/s10832-007-9329-6
- ⁹⁴ M. S. Zarnik, D. Belavica, S. Macek „Evaluation of the constitutive material parameters for the numerical modelling of structures with lead–zirconate–titanate thick films," *Sensors and Actuators A* **136**, 618-628 (2007).
- ⁹⁵ V. Walter, P. Delobelle, P. Le Moal, E. Joseph, M. Collet, „A piezo-mechanical characterization of PZT thick films screen-printed on alumina substrate," *Sensors and Actuators A* **96**, 157–166 (2002).
- ⁹⁶ V. Walter, *Characterization and modelling of PZT thick film screen-printed on alumina substrate – application to shape control and active damping of cantilever bimorph* (PhD Université de France-Comté, 2001).
- ⁹⁷ J.G. Smits, W.S. Choi, "The constituent equations of piezoelectric heterogeneous bimorphs," *Proc. of IEEE Transactions on Ultra., Ferro. And Freq. Cont.* **38**, (256-270) 1991.
- ⁹⁸ K. Sivanandana, A. T. Achuthana, V. Kumara, I. Kannob "Fabrication and transverse piezoelectric characteristics of PZT thick-film actuators on alumina substrates," *Sensors and Actuators A* **148**, 134–137 (2008). doi:10.1016/j.sna.2008.06.031
- ⁹⁹ R.N. Torah, S.P. Beeby, N. M. White, "Experimental investigation into the effect of substrate clamping on the piezoelectric behaviour of thick-film PZT elements," *Appl. Phys.* **37**, 1074–1078 (2004).
- ¹⁰⁰ L. Simon, S. Le Dren, P. Gonnard "PZT and PT screen-printed thick films," *J. Europ. Ceram. Soc.* **21**, 1441-1444 (2001).
- ¹⁰¹ H. Banno, "Effects of shape and volume fraction of closed pores on dielectric, elastic, and electromechanical properties of dielectric and piezoelectric ceramics—a theoretical approach," *Am. Ceram. Soc. Bull.* **66**, 1332–1337 (1987).
- ¹⁰² T. Zeng, X. Dong, C. Mao, Z. Zhou, H. Yang, "Effects of pore shape and porosity on the properties of porous PZT 95/5 ceramics," *J. Europ. Ceram. Soc.* **27**, 2025-2029 (2007).
- ¹⁰³ J. Kováčik, „Correlation between Young’s modulus and porosity in porous materials," *J. of Mat. Sci. Let.* **18**, 1007-1010 (1999).

- ¹⁰⁴ S. Nazare, G. Ondracek, „Zum Zusammenhang zwischen Eigenschaften und Gefuegestruktur mehrphasiger Werkstoffe. Teil IV: Gefuegestruktur und thermischer Ausdehnungskoeffizient,“ Zeitschr. f. Materialwissenschaft und Werkstofftechnik **9**, 140–147(1978).
- ¹⁰⁵ J. Müller, M. Mach, H. Thust, D. Schwanke and C. Kluge, “Thermal design considerations for LTCC microwave packages,” Europ. Microelectronics and Packaging Symp., (2006).
- ¹⁰⁶ J. E. Sergent, *Thermal Management Handbook: For Electronic Assemblies* (McGraw-Hill Education Electronic Packaging and Interconnection Series, 1998).
- ¹⁰⁷ S. Gebhardt, L. Seffner, F. Schlenkrich, A. Schönecker “PZT Thick Films for Microsystems Applications,” Proc. EMPS 2006 - 4th European Microelectronics and Packaging Symposium, 9-13 (2006).
- ¹⁰⁸ R. Gerbach, M. Bernasch Instrumentierte Eindringprüfung an PZT Schichten (Fraunhofer IWM, Berichtsnummer V 134/2008, 2008).
- ¹⁰⁹ A. Schönecker, S. Gebhardt, F. Schlenkrich, I. Endler, T. Mayer-Uhma, S. Uhlig, “Development of Functional Ceramic Films for Nano and Microsystems Technology,” Proc. 2006 Electronics System Integration Technology Conference, Dresden Germany, (2006)
- ¹¹⁰ S.N. Gwirc, C.A. Negreira, “Evaluation of the effect of porosity and substrate on the piezoelectric behaviour of thick-film PZT elements,” Appl. Phys. **39**, 4215–4221 (2006). doi:10.1088/0022-3727/39/19/014
- ¹¹¹ CeramTec AG, Multifunctional Ceramics Division, *Materials for actuators* (product brochure, 2011). www.ceramtec.com/downloads/mf_materials-actuators.pdf
- ¹¹² CeramTec AG, Multifunctional Ceramics Division, *Special Materials* (product brochure, 2011). www.ceramtec.com/downloads/mf_materials-special.pdf
- ¹¹³ Morgan Electro Ceramics, Technical Publication TP-226 Properties of Piezoelectricity Ceramics, (www.morgan-electroceramics.com, 2011); <http://www.morganelectroceramics.com/resources/technical-publications/> (25.11.2011)
- ¹¹⁴ S. Gebhardt, A. Schönecker, C. Bruchmann, E. Beckert, G. Rodrigues, R. Bastaits, A. Preumont, “Active Optical Structures by Use of PZT Thick Films,” Proc. 4th Int. Conf. on Ceramic Interconnect and Ceramic Microsystems Technologies CICMT 2008, 87-93 (2008).
- ¹¹⁵ http://www.piceramic.de/pdf/piezo_material.pdf (08.07.2011)
- ¹¹⁶ J. Juuti, *Pre-stressed piezoelectric actuator for micro and fine mechanical applications* (PhD ACTA UNIVERSITATIS OULUENSIS C Technica **235**, 2006).
- ¹¹⁷ G. H. Haertling “Rainbow ceramics – a new type of ultra-high-displacement actuator,” Am. Ceram. Soc. Bulletin **73**, 93-96, (1994).
- ¹¹⁸ B. W. Barron, G. Li and G. H. Haertling “Temperature dependent characteristics of Cerambow actuators,” Proc. IEEE Int. Symp. Appl. of Ferroelectrics ISAF’96, IEEE, 305–308 (1996).

- ¹¹⁹ S. Lee, T. Tanaka, K. Inoue, J.-M. Kim, Y.-E. Shin, M. Okuyama, "Stress influences on the ultrasonic transducers," *Sensors and Actuators A* **119**, 405-411 (2005).
- ¹²⁰ C.-C. Lee, G.Z. Cao and I.Y. Shen, "Effects of residual stresses on lead–zirconate–titanate (PZT) thin-film membrane microactuators," *Sensors and Actuators A* **159**, 88-95 (2010).
- ¹²¹ Q.-M. Wang, Q. Zhang, B. Xu, R. Liu, L. E. Cross, "Nonlinear piezoelectric behaviour of ceramic bending mode actuators under strong electric fields," *Appl. Phys.* **86**, 3352-3360 (1999).
- ¹²² L. J. Golonka, "Technology and applications of Low Temperature Cofired Veramic (LTCC) based sensors and microsystems," *Bull. Polish Acad. Sci.* **54**, 221-231 (2006).
- ¹²³ J. S. Massa, C. Paterson, "Development of low cost deformable bimorph mirrors for use in adaptive optics," *Proc. SPIE* **6018**, 601810-1 - 601810-6 (2005).
- ¹²⁴ US6568647B2: Mounting apparatus for a deformable mirror. Date of filing: 25.01.2001, date of publication: 27.05.2003, US 6,568,647 B2. Assignee: AOptix Technologies Inc., Inventors: J. Elon Graves, Malcolm J. Northcott
- ¹²⁵ Patent US7019888B1: Deformable mirror with perimeter wiring. Date of filing: 16.10.2003, date of publication: 28.03.2006, US 7,019,888 B1. Assignee: AOptix Technologies Inc., Inventors: J. Elon Graves, Malcolm J. Northcott, J. Christopher Shelton
- ¹²⁶ Q. Sun, Z. Jiang, "Double-layer PMN bimorph deformable mirror system optimization design and fabrication technology," *Proc. SPIE* **7513**, 75131K-1 - 75131K-10 (2009).
- ¹²⁷ Patent WO002005040885A3: improvements relating to deformable mirror holders. Date of filing: 20.10.2004, date of publication: 06.05.2005, WO 2005/040885 A3. Applicant Bae Systems Plc, Inventors: Griffith Michael Stewart, Laycock Leslie Charles, Archer Nicholas John, Mccarthy Andrew Graham
- ¹²⁸ Patent EP000002189832A1: Verformbare Spiegelaufhängung. Date of filing: 20.11.2008, date of publication: 26.05.2010, EP 2 189 832 A1. Applicant: Bae Systems Plc. , Inventors: n/a
- ¹²⁹ M. Griffith, L. Laycovk, N. Archer, R. Myers, A. Kirby, P. Doel, D. Brooks, "Integrated dual-stage deformable mirrors," *Proc. SPIE* **7736**, 77365M-77365M-11 (2010).
- ¹³⁰ P. R. Yoder, Jr., *Mounting optics in optical instruments* (2nd printing in SPIE press, 2004).
- ¹³¹ thermally conductive, electrically insulating, un-reinforced gap filling material; http://www.bergquistcompany.com/thermal_materials/gap_pad/gap-pad-2500.htm (20.10.2011)
- ¹³² E. Beckert, T. Oppert, G. Azdasht, E. Zakel, T. Burkhardt, M. Hornaff, A. Kamm, I. Scheidig, R. Eberhardt, A. Tünnermann, F. Buchmann, „Solder Jetting - A Versatile Packaging and Assembly Technology for Hybrid Photonics and Optoelectrical Systems," *IMAPS 42nd International Symposium on Microelectronics*, 406 (2009).
- ¹³³ T. Burkhardt, A. Kamm, M. Hornaff, E. Beckert, R. Eberhardt, A. Tünnermann, „Precision photonic packaging using laser-based Solderjet Bumping," *Proc. 4th Europ. Conference Smart Systems Integr.*, (2010).

- ¹³⁴ M. J. Riedl, *Optical Design Fundamentals for Infrared Systems* (2nd Ed. SPIE Tutorial Texts in Optical Engineering **TT48**, 2001.)
- ¹³⁵ R. Steinkopf, A. Gebhardt, S. Scheiding, M. Rohde, O. Stenzel, S. Glied, V. Giggel, H. Löscher, G. Ullrich, P. Rucks, A. Duparre, S. Risse, R. Eberhardt, A. Tünnermann, "Metal mirrors with excellent figure and roughness," Proc. SPIE **7102**, 71020C- 71020C-12 (2008).
doi:10.1117/12.797702
- ¹³⁶ J. S. Kim, K. W. Paik, J. H. Lim, Y. Y Earmme, "Thermomechanical stress analysis of laminated thick-film multilayer substrates," Appl. Phys. Lett. **74**, 3507- 3509 (1999).
- ¹³⁷ G. G. Stoney, Proc. R. Soc. Lond. A **82**, 172-175 (1909). doi: 10.1098/rspa.1909.0021
- ¹³⁸ S. Timoshenko, "Analysis of bi-metal thermostats," JOSA **11**, 233-255 (1925).
doi:10.1364/JOSA.11.000233
- ¹³⁹ C.H. Hsueh, "Thermal stresses in elastic multilayer systems," Thin Solid Films **418**, 182–188 (2002).
- ¹⁴⁰ Product information DuPont Microcircuit Materials 951 Green Tape™, downloaded 15.10.2010 (www2.dupont.com/MCM/en_US/assets/downloads/prodinfo/GreenTape_Design_Layout_Guidelines.pdf)
- ¹⁴¹ C. Hsu, W. Hsu, "A two-way membrane-type micro-actuator with continuous deflections," J. Micromech. Microeng. **10**, 387–394 (2000).
- ¹⁴² S.A. Kokorowski, "Analysis of adaptive optical elements made from piezoelectric bimorphs," J. Opt. Soc. Am. **69**, 181-187 (1979)
- ¹⁴³ X. Li, W. Y. Shih, I. A. Aksay, and Wei-Heng Shih, "Electromechanical Behavior of PZT-Brass Unimorphs," J. Am. Ceram. Soc. **82**, 1733-1740 (1999).
- ¹⁴⁴ S. Li, S. Chen, "Analytical analysis of a circular PZT actuator for valveless micropumps," J. Sensors and Actuators A **104**, 151–161 (2003).
- ¹⁴⁵ C. Mo, R. Wright, W. S. Slaughter, W. W. Clark, "Behaviour of a unimorph circular piezoelectric actuator," J. Smart Mater. Struct. **15**, 1094–1102 (2006). doi:10.1088/0964-1726/15/4/023
- ¹⁴⁶ G. Pfeifer, *Piezelektrische lineare Stellantriebe* (Wiss. Zeitschrift der TH Karl-Marx-Stadt, 1982).
- ¹⁴⁷ E. M. Ellis, *Low-cost Bimorph Mirrors in Adaptive Optics* (PhD Imperial College of Science, Technology and Medicine, University of London, 1999).
- ¹⁴⁸ Y. Ning, W. Jiang, N. Ling, C. Rao, "Response function calculation and sensitivity comparison analysis of various bimorph deformable mirrors," Opt. Express **15**, 12030-12038 (2007).
doi:10.1364/OE.15.012030
- ¹⁴⁹ M. Deshpande, L. Saggere, "An analytical model and working equations for static deflections of a circular multi-layered diaphragm-type piezoelectric actuator," Sensors and Actuators A **136**, 673–689 (2007).

- ¹⁵⁰ J.N. Reddy, "Chapter 5: classical and first-order theories of laminated composite plates," in *Mechanics of Laminated Composite Plates: Theory and Analysis* (CRC Press, 1997).
- ¹⁵¹ M. Loktev, D. W. de Lima Monteiro, G. Vdovin, "Comparison study of the performance of piston, thin plate and membrane mirrors for correction of turbulence-induced phase distortions," *J. Opt. Comm.* **192**, 91-99 (2001).
- ¹⁵² G. Vdovin, O. Soloviev, A. Samokhin, M. Loktev, "Correction of low order aberrations using continuous deformable mirrors," *Optics Express* **16**, 2859-2866 (2008).
<http://dx.doi.org/10.1364/OE.16.002859>
- ¹⁵³ S. Verpoort, U. Wittrock, "Actuator patterns for unimorph and bimorph deformable mirrors," *J Appl Opt.* **49**, G37-G46 (2010). <http://dx.doi.org/10.1364/AO.49.000G37>
- ¹⁵⁴ P. Frank, *Piezoresponse Force Microscopy and Surface Effects of Perovskite Ferroelectric Nano-structures* (PhD Schriften des Forschungszentrums Jülich, Reihe Informationstechnik **11**, 2006).
- ¹⁵⁵ W. Schätzing, *FEM für Praktiker* (Expert Verlag, 2003).
- ¹⁵⁶ Release 11.0 Documentation for ANSYS,
http://www.kxcad.net/ansys/ANSYS/ansyshelp/theory_toc.html
- ¹⁵⁷ DuPont Microcircuit Materials 951 Green Tape™ Thick Film Composition Product Description, downloaded 05.10.2011
(www2.dupont.com/MCM/en_US/assets/downloads/prodinfo/951LTCCGreenTape.pdf)
- ¹⁵⁸ GreenTape™ Design & Layout Guide, downloaded 05.10.2011
(www2.dupont.com/MCM/en_US/assets/downloads/prodinfo/GreenTape_Design_Layout_Guidelines.pdf)
- ¹⁵⁹ S. Verpoort and U. Wittrock, "Unimorph deformable mirror for telescopes and laser applications in space," *Proc. Int. Conf. Space Optics*, Rhodes, Greece (2010).
- ¹⁶⁰ Y. Miyamoto, W. A. Kaysser, B. H. Rabin, A. Kawasaki, R. G. Ford, *Functionally graded materials: design, processing and applications* (Kluwer Academic Publishers, 1999).
- ¹⁶¹ L.P. Zhou and D.W. Tang, "A functionally graded structural design of mirrors for reducing their thermal deformations in high-power laser systems by finite element method," *Optics & Laser Techn.* **39**, 980-986 (2007).
- ¹⁶² R. Lawrence, D. Ottaway, M. Zucker and P. Fritschel, "Active correction of thermal lensing through external radiative thermal actuation," *Optics Letters* **29**, 2635-2637 (2004).
- ¹⁶³ J. Degallaix, C. Zhao, L. Ju and D. Blair, "Thermal lensing compensation for AIGO high optical power test facility," *Class. Quantum Gravity* **21**, 903-908 (2004). doi: 10.1088/0264-9381/21/5/079
- ¹⁶⁴ <http://www.surtec.com/Kataloge/Galvanotechnik.html> (downloaded 23.03.2011)
- ¹⁶⁵ M. Appelfelder, *Mounting and characterization of a Unimorph deformable mirror* (Master thesis FH Jena, Fachbereich SciTec, 2011).

¹⁶⁶ H. A. C. Tilmans, M. Elwenspoek and J. H. J. Fluitman, "Micro resonant force gauges," *Sensors and Actuators A* **30**, 35-53 (1992).

¹⁶⁷ Y. Ning, H. Zhou, H. Yu, C. Rao, and W. Jiang, "Thermal stability test and analysis of a 20-actuator bimorph deformable mirror," *Chin. Phys. B* **18**, 1089-1095 (2009).